Experimental and CFD Study of Wind-Induced Response for Bridge Cables with Ice accretion

by

Songyu Cao

A thesis submitted to the
Faculty of Graduate and Postdoctoral Studies
in partial fulfilment of the requirements for the degree of
Master of Applied Science in Civil Engineering

uOttawa

Department of Civil Engineering
Faculty of Engineering
University of Ottawa
Ottawa, Ontario, Canada

Acknowledgement

This is a great opportunity to show my deepest gratitude to my supervisor Dr. Elena Dragomirescu, who is a responsible and considerate professor, who helped me greatly since I entered the University of Ottawa graduate program. She is not only the supervisor of my studies, but also a mentor for my life, she has given me many useful and inspiring advices when I meet difficulties; hence I would like to express my great appreciation for her support.

I would like to present my gratitude to Mr. John Perrins, who assisted me in making the cable models, to Mr. Hassan Shaban who helped me to become familiar with the equipment in the wind tunnel and to Mr. Mark Lapoint who lent me the equipment to use in the wind tunnel.

I owe a great gratitude to my friends, I am grateful for what they have done to help me conquering all the problems I encountered. I would like to thank to Xi Chen, Fan Feng, Hongyu Tu, Xiangwen Zuo, Haoran Deng, Yichong Ren and Yongheng Zhang, they helped me with valuable advices for finishing the experiment and the CFD simulation.

I would like to express my acknowledgement to my parents and my girlfriend, without their support, I would not get through the hard times.

Abstract

Cable-stayed bridges are massive structures which rely on their structural elements such as deck girder, towers and stay-cables for their stability. The bridge stay-cables can be considered as the most flexible elements of the cable-stayed bridges, and thus their structural stability integrity is verified for several phenomena which might affect them. Wind and wind/rain induced vibrations for bridge stay-cables were comprehensively studied by researchers worldwide; however recent projects have identified a new type of cable vibrations caused by ice accretion formed around the cable circumference. The current research proposed two ice accretion profiles for inclined bridge cables and has experimentally investigated the wind-induced vibrations of the two models for the bridge stay-cables with ice accretion, under different vertical (inclination) and horizontal (yaw) angles, and for different wind speeds. Initially, three models of the bridge cable with 1.0 cm and 2.0 cm ice profile were tested in the wind tunnel of cross-section 61 cm × 90 cm, and a maximum wind speed of 30 m/s. In total 6 cases with 1.0 cm ice thickness and 3 cases with 2.0 cm ice thickness were investigated and the vertical and torsional oscillatory displacements were recorded for wind speeds from 1.5 m/s to 15 m/s at intervals of 1.5 m/s. The wind-induced vibrations were analyzed and were compared with the response reported for cables without ice and with the rain-induced response for stay-cables.

Computational Fluid Dynamics (CFD) simulations were performed to observe the drag, lift and pressure coefficients around the surface of the accreted cable models yawed and inclined at $\alpha = 0°$, $\beta = 0°$ and $\alpha = 60°$, $\beta = 15°$ under the effect of 10 m/s and 15 m/s wind speed applied for both cases. A verification for galloping divergent instability was conducted based on the Den Hartog formulation and the vertical vibrations obtained from the wind tunnel experiment.

List of symbols

A_y	Initial amplitude (m)
B	The width normal to the free stream velocity (m) (Eq. 3.1)
C_D	Drag coefficient (no dimension)
C_L	Lift coefficient (no dimension)
C_M	Moment coefficient (no dimension)
C_y	The coefficient of vertical force (no dimension)
c_p	Heat capacity (J/m^3)
c_P	Pressure coefficient (no dimension) (Eq. 4.19)
c_s	The volume concentration of S (V/V)
D	Cable diameter (m) (Eq. 2.2)
D	Displacement (m) (Eq.3.4)
$D_{average}$	Average displacement (m)
D_s	The diffusion coefficient (no dimension)
F	The fraction of water in the air contained in the droplets
F_D	Drag force (N)
F_L	Lift force (N)
F_M	Moment force (N)
f	The vibration frequency of the structure section (Hz)
f_n	Free vibration frequency (Hz)
f_θ	The frequency for the section and flow (Hz)
G	Mass of water in air (kg)
I_θ	The polar moment of inertia for the section and flow (m^4)
I_u	Turbulence level (no dimension)
K	Conduction coefficient (no dimension) (Eq.2.31)
k	Elastic constant of springs (N/m)
k_y	Spring stiffness (N/m)
k_θ	Torsion stiffness (N/m)

L_w	Wind load function (N)
L_{sp}	The elongation in the spring due to the applied torsion force
L_1, L_2, L_3	Length of model 1, model 2, and model 3 (m)
m_1, m_2, m_3	Mass of model 1, model 2, and model 3(kg)
n	Number of points recorded in the test (no dimension)
P	Precipitation (mm/m^2)
p_0	Local and far upstream pressure (Pa)
r_d	The radius of the ice
S_c	Scruton number (no dimension)
S_s	The mass produced by chemical process (kg)
S_T	The initial heat source (J)
t	Time (s)
U	Wind velocity (m/s)
U_r	Relative flow velocity (m/s)
Z	The distance from ground (m)
α	Horizontal inclination angle(°)
β	Vertical inclination angle (°)
γ	The correction angle (°)
$\gamma_{average}$	The average of correction angle (°)
δ	Ice density (g/cm^3)
ξ	Damping ratio (no dimension)
ζ_T	The sum of structure damping component and aerodynamic force component (no dimension)
ζ_θ	Damping factor (no dimension)
ρ	Air density (g/cm^3)
ω_y	The inherent frequency (Hz)
ρc_s	The mass concentration (kg/cm^3)
θ	Relative inclined angle (°)
$\theta_{average}$	Average relative inclined angle (°)
θ_{ice}	Relative angle with ice (°)

ϕ	The initial phase angle (°)
ΔR	The increase ice thickness on transmission line (m)

List of Contents

List of Figures

List of Tables

Chapter 1 Introduction

1.1 Background

Long-span cable-stayed bridges are slender and complex structures that can span large distances and thus are used in geographical areas with wide water openings and high vehicular traffic. The Port Mann Cable-stayed Bridge, constructed in 2012 between Coquitlam and Surrey in British Columbia, is the second-longest cable-stayed bridge in North America. With its 470 m main span, a total length of 2,020 m and 10 lanes opened to traffic, the bridge itself is very elegant and efficient for commuting [1], however, recently this bridge brought more challenges for the engineers designing the stay-cables, especially during the winter season.

Figure 1.1. Port Mann Bridge, Vancouver, Canada [1]

In general, cable-stayed bridges can achieve long spans of up to 1,500 m. Like other relatively complex structural systems, cable-stayed bridges have many uncertain design problems that need to be solved, otherwise imminent bridge failure might occur and thus it would become a real disaster [2]. The difference between cable-stayed bridges and suspension bridges is that they transfer loads differently; thus for cable-stayed bridges, the deck loads are directly transferred to the pylons through the stay-cables, while for suspension bridges, the main cables carry the deck loads through the vertical cables

called hangers. For most cases, the main spans of suspension bridges are longer than the spans of cable-stayed bridges, hence the number of structural elements (cables) for the cable-stayed bridges is lower than that of the suspension bridges. In addition, the construction process is more complicated for the suspension bridge, which is why most cable local failures happen for suspension bridges. For instance, the Tacoma Narrows Bridge which was opened in 1940 in the U.S. state of Washington, it was a suspension bridge, and was the third-longest suspension bridge in the world at that time [3]. However, due to wind effects the bridge collapsed and the structural elements which ruptured first were the hanger cables of the bridge. Moreover, the deck flutter was observed as the failure mode of the bridge, and it is the main reason for the Tacoma Bridge collapse [3]. Critical failures were not reported, however numerous cable – stayed bridges reported unexpected wind-induced vibrations of stay-cables. For example, Fred Hartman Bridge in Houston, Texas, has experienced large amplitude cable vibrations, which could be critical for the bridge stability. Zuo et al 2005 [4] reported the field measurements for the Hartman Bridge to observe the large amplitude vibrations due to wind and rain effects. Results have shown that kind of vibration occurs occasionally, so it is very important to understand the vibration mechanism of the stay-cables, which can be considered as a serviceability criterion failure. Therefore the vibrations of bridge stay-cables became a major research topic for bridge designers. To clarify the aerodynamic phenomena associated with the inclined stay-cables and to improve the design recommendations in order to avoid potential failure problems that might occur during the life service of the bridge the research related to cable-stayed bridges needs to be further expanded and the effect of ice accretion in combination with strong winds must be detailed [5].

The cable-stayed bridges, due to the slenderness and the light weight, both the lateral and torsional stiffness are much lower than regular continuous bridges, however, they can achieve longer spans and are also usually built in open and vast areas such as rivers, coasts and valleys where strong winds are registered. The turbulence of the wind speed is unpredictable, therefore, wind fluctuations are often characterized as a long period signal; for regular bridges, the natural period is lower, which means their vibrations do not become resonant in wind, but for cable-stayed bridges, the natural vibration period is

longer, which might coincide with the wind signal period and thus tends to be resonant in the wind, becoming a major reason of concern for many of the wind-induced vibrations registered for cable-stayed bridges [6].

1.2 Research motivation

From the wind design perspective, usually the inclined stay-cables are verified for the wind drag and lift forces, which are transferred to both the pylons and the deck; however, the bridge designers realized that the cables are dynamically responding elements, and significant vibrations were observed in the past couple of years, which could not be clearly explained [6].

Several bridge-inclined cable models were used and improved with the purpose of predicting the aerodynamic cable instabilities in different aspects of wind-induced behaviour however the vibrations of the stay-cables due to wind and ice accretion received less attention. For electricity transmission lines, in the 1930s, Davison [7] analyzed the iced cable galloping and attributed the occurrence of cable vibrations during the freezing rainstorms, in the order of change in the lift aerodynamic force, while the wind was blowing across the conductor. Also, Den Hartog [8] made a series of calculations and proposed a mathematical description about the boundary for galloping, which is broadly used nowadays for galloping verification of any type of structure exposed to wind action. In the 1960s, Davenport [7] introduced the expression for the aerodynamic damping of a cylinder submerged in flow, for both along-wind and across-wind directions, and the instability criterion is nowadays referred to as the drag crisis as presented by Martin et al, 1999 [9]. At the same time, torsional galloping vibrations were observed by Nigol and Buchan, 1999 [10] and they concluded that if the iced conductor is eccentric, the instability is imminent; they also obtained the corresponding critical condition, after which Macdonald and Larose, 2009 [11] proposed a general expression for verifying the galloping instability occurrence, based on the quasi-steady aerodynamic damping of an inclined cylinder, however without the ice accretion or rain conditions.

The fluid flow field formed around the bridge cable elements interact with the surface of the cable and can lead to a significant cable response. To determine the flow field, the shape of the real structure and the characteristics of the oncoming flow, Leihhard, 1966

[12] classified six different flow regimes corresponding to the Reynolds number; these regimes can also be recorded as maps with the change in the Strouhal number, which is a very important parameter for obtaining the vortex shedding frequency of the structure. In reality, the flow field around the stay-cables on bridges or around transmission lines could be altered when exposed to a freezing condition because the smoothness and the form of the cable is modified by the ice profile, which could potentially make the cable prone to various types of wind-induced vibrations. The majority of the research conducted up to the present for aerodynamic phenomena of the bridge stay-cables considered the circular shape of the cable but the inclined cable cross-section is an ellipse. However, no results have been presented for the bridge stay-cables affected by different types of ice profiles, with circular or ellipse cross-section considered, and the wind loading conditions that could lead to a drastic drop of the Strouhal number, as an indirect indicator for the evolution of the drag and lift-force coefficients [13].

As the bridge span increases, the vibrations for the cable tend to accentuate, especially under the combined effect of the wind load, the traffic load and the self-weight of the bridges. The wind-induced vibrations occur differently, for the three different cable surface conditions, which are dry cables, wet cables and ice-accreted cables. In particular, the ice accretion accumulates with rain or snow falling, which is deposited on its surface, and it can change the shape of the cables, causing aerodynamic instability. Thus the ice accretion can be considered as a time-dependent modification factor of the shape of the exposed objects, and in general there are three different forms of ice formations that could affect the accretion at the surface of an object: hoar frost, in-clouds or fogs and precipitation icing. Research indicates that the ice accretion from the light precipitation at low temperatures could accumulate more than other ice formations, thus it could lead to large-amplitude vibrations for cable-stayed bridges [11].

Several experimental and numerical researches were conducted to analyze the influence of the ice accretion on the aerodynamics of transmission lines, for which the stability criteria were formulated [14], however, there is scarce knowledge about the aerodynamic vibrations of the ice-accreted stay-cables of cable-stayed bridges. It should be emphasized that the diameter of the transmission lines is much smaller than that of the bridge cables, and the two conditions cannot be directly compared because of very

different characteristics for ice accretion, such as the shape and thickness of the ice, etc. Also field measurements are difficult to conduct for ice accretion on bridge cables, due to the high-altitude location of the cable and due to the complexity of installing measuring devices along the stay-cable, in order to get wind-induced vibration modes. The shape of ice accretion could accentuated the wind-induced vibrations; for example, galloping vibration can occur for the cable with ice accumulation, when usually the galloping is not expected for circular-section cylinders or cables, as Den Hartog criterion specifies [14].

Papers also indicate that, besides the modification of the cross-sectional shape, the difference between a simple cable and a cable with ice accretion or rain-induced rivulet is the alteration of the surface roughness, which influences the aerodynamics of the cable, especially in the proximity of the critical Reynolds (Re) number; observations for various wind excitation mechanisms of cables, in the critical Re number range, could also help in understanding the wind-induced vibrations of the stay-cable with ice accretion [15]. For cables located both on the middle span or on the side span of the bridge, the vertical inclination angle and the horizontal inclination angle vary, determining a relative angle of attack with the wind direction, and the cable vibrations might occur simultaneously, despite the wet or dry condition of the cable[16][17].

An important experiment was conducted by Demartino et al, 1999 [10] to investigate the aerodynamic behaviour of ice-accreted cables, in the climatic wind tunnel of the DTU/Force Technology collaborative climatic wind tunnel, demonstrating that the ice accretion has a tendency to form on the windward part of the cable, and the ice profile has a rectangular configuration rather than the cone geometry reported for the airfoil ice accretion.

In 2014, just two years after completion, The Port Mann Bridge was closed to traffic because of the ice falling from the stay-cables which became dangerous for the traffic and people on the bridge; actually due to wind effects, the cables vibrations increased, which made it easier for the ice to detach from the cable and fall. Therefore, the stay-cables aerodynamic behaviour and the wind-induced vibrations for different thicknesses of ice accretions were not sufficiently studied, thus the stability criteria for different wind-loading conditions are not yet established. Moreover, most of the research has considered the windward ice accretion, but the actual case of wind speed changing direction with 90°

or more, which would place the ice profile on the downward side of the cable, when the wind speed increases, was never considered.

1.3 Scope of Research

Wind and wind/rain-induced vibrations for bridge cables were comprehensively studied by researchers worldwide; however, recent projects have identified a new type of cable vibration caused by ice accretion formed around the stay-cable circumferences. The current research has experimentally investigated three inclined stay-cable models, each with two ice accretion profiles for inclined bridge cables. In order to identify both the vortex-induced and galloping vibrations, the wind-induced vertical and torsional vibrations of the two bridge cables with ice accretion scaled (1:45) models were measured under 0 and 15 vertical inclination angles and 0, 15, 30 and 60 horizontal yawed angles for different wind speeds. Three scaled models of the bridge stay-cable with ice profiles of 1.0 cm and 2.0 cm were tested in a suction wind tunnel of cross-section 61 × 92 cm which can achieve a maximum wind speed of 30 m/s. In total, six cases with 1.0 cm ice thickness and three cases with 2.0 cm ice thickness were investigated, and the vertical and torsional vibrations were recorded for wind speeds increasing from 1.5 m/s to 15 m/s at intervals of 1.5 m/s. The measured wind-induced vibrations were analyzed and compared with results available in the literature review for cable models without ice and the rain-induced vibration of a stay-cable. For the present experiments conducted in the wind tunnel of the University of Ottawa, the shape of the ice accretion was approximately the same and only the ice thickness varied. The main purpose of conducting the dynamic wind tunnel experiments was to observe the wind-induced vibrations of the stay-cable models with different ice accretion thicknesses and different vertical and horizontal inclination angles in regard to the wind speed direction.

In order to determine the changes in the aerodynamic behaviour of the ice-accreted cables, the frequency analysis was performed through Fast Fourier transform which was applied to the recorded displacements, to observe the frequency of the model under critical vibrations.

The drag and lift force coefficients were not measured during the wind tunnel experiments due to equipment malfunction; therefore, a Computational Fluid Dynamics

(CFD) simulation using the ANSYS commercial software was performed. The cable model perpendicular to wind, with the vertical and horizontal inclination angles $\alpha = 0°$, $\beta = 0°$ and the cable model horizontal and vertical inclination at $\alpha = 60°$, $\beta = 15°$, angles were developed for the ice accretion of 1.0 cm thickness. The drag and lift coefficients are very important for the static design of the bridge stay-cables and also for the verification of the galloping instability through the Den Hartog formulation. Also the CFD simulation provided the pressure coefficient distribution on the surface of the cable and on the surface of the ice accretion. Moreover, the wind flow behaviour around both the cable and ice accretion profile could be identified at several distances along the cable model length. Finally, the effect of the ice accretion on the cable aerodynamic properties was analyzed based on the essential drag, lift and pressure information obtained from the CFD simulation, completed with the displacement vibrations observed in the wind tunnel experiment.

1.4 Thesis layout

The motivation of the performed wind tunnel experiment and of the CFD simulations were outlined in Chapter 1, along with the purpose of this study of clarifying the effect of ice accretion on stay-cables under the wind loading. The concepts and the principles employed to support this experiment are reviewed in Chapter 2; also, the latest experimental and numerical work reported for wind-induced vibrations of vertically and horizontally inclined cables was presented in Chapter 2. The experiment setup details were described in Chapter 3, which includes the details of the wind tunnel and the cable models, the experiment procedures for vertical and torsional vibrations, and the details of the CFD simulation process. Chapter 4 presents the results obtained from the wind tunnel experiment, and compares different cases to discuss the vertical vibration frequencies obtained through the Fast Fourier Transform. The CFD simulation results for drag, lift and pressure coefficients are also detailed in Chapter 4 along with the velocity profiles around the ice-accreted cable model. This research concluded with the interpretation of the effect of the ice profile on the cable model aerodynamics and recommendations for future work, which were formulated in Chapter 5 of this thesis.

Chapter 2 Literature Review

2.1 Bridge wind-induced vibrations

A considerable number of bridges collapsed or were partially damaged due to wind-induced vibrations over time. The Dryburgh Abbey Bridge in Scotland was one of the earliest bridge collapses that occurred due to the wind load effect [18]. However, the most famous bridge collapses caused by wind-induced vibrations were the Tacoma Bridge in the U.S., which collapsed in 1940, and the Tay Bridge in Scotland in 1874. Upon studying these two collapses, bridge engineers realized the potential danger of wind-induced vibration for the bridges, and began to analyze the aerodynamic effect of the wind as a crucial factor for dynamic vibrations of bridges; meanwhile, referring to the available data showed that since the 19th century, 12 bridges collapsed due to structural vibrations; Table 2.1 lists the 12 bridges. Because many bridges vibrate dramatically under the effect of wind, researchers observed and evaluated the Golden Gate Bridge in U.S., and their results showed that the maximum vertical displacement was 17.0 m. This massive structure displacement could be very harmful for the service life of the bridge and people's safety, so the vibration of the stay-cable is very important to analyze [19].

As the span of cable-stayed bridges increases, the bridge becomes more flexible, and since the cable-stayed bridge is relatively light, having a small damping ratio, the vibration is more likely to occur due to wind effect; sometimes the vibration could be large enough and could overpass the critical stability limits of bridges [20]. In general, due to the increasing span of cable-stayed bridges, the length of the cables became longer and bigger oscillations were noticed. Large-amplitude vibrations for stay-cables were also observed for the bridges constructed in China; wind-induced vibrations of the stayed-cables of the Yangpu Bridge were reported several times in 1990s , and the vibration amplitudes of the Baishazhou long-span Cable-stayed Bridge was recorded as 1.0 m due to rain-induced vibrations [21]. However, the service life can be reduced when the length of the cable increases, and modifications for improving the stay-cables design should be taken into consideration, when it comes to long-span bridges [22].

The most known collapses of bridges registered until the present are reported in Table 2.1. The last wind-caused collapse of a bridge was registered in 1940 (Tacoma Bridge),

and after the introduction of bridge aerodynamics only wind-induced vibrations of bridges were registered but no other collapse was encountered.

Table 2.1 Bridge collapses due to wind [23]

Bridge name	Location	Span(m)	Time of collapse
Dryburgh Abbey	Scotland	80	1818
Union Bridge	England	140	1821
Nassau Bridge	Germany	75	1834
Brughon Bridge	England	80	1836
Montrose Bridge	Scotland	130	1838
Menai Straits Bridge	Welsh	180	1839
Roeche Bemard Bridge	France	195	1852
Wheeling Bridge	America	310	1854
Niagara-Lewiston Bridge	America	320	1864
Tay Bridge	Scotland	74	1874
Niagara-Cloifton Bridge	America	380	1889
Tacoma Narrows Bridge	America	853	1940

A number of aerodynamic mechanisms can lead to vibrations of bridge stay-cables as summarized below [24] [25]:

1. Vortex excitation of a single cable or groups of cables：When exposed to wind flow, the cables or group of cables encounter vortex shedding detaching from the rear side of the cylinder, which generates an oscillation of the object when the air overpasses the bluff body; these vortices are formed at the back of the body and separate periodically from its surface.

2. Wake galloping for group of cables: Wake flow galloping for stay-cables occurs when the downstream cables are situated in the wake flow of upstream cables. The impact of the wind flow on the downstream cables induces vibrations that can be avoided by installing crossties connecting the cables.

3. Dry galloping for a single cable: Dry galloping is a self-excitation vibration phenomenon caused by high wind speeds, with large amplitude and small frequency, and is usually one of the main aerodynamic verifications considered in bridge design. Theoretically, galloping cannot be encountered by circular-section bodies perpendicular

to the flow [24]; however, for certain relative angles of attack, the cross-section of the cable becomes an ellipse and galloping vibration might occur.

4. Galloping of cables with ice accretion: During the winter season, precipitations accumulate on the surface of the cable, forming an ice profile. This accumulation can change the shape of the cable's cross-section; hence, the galloping vibrations of the bridge cables with ice accretion are different than the dry galloping for a single cable; however, this was not clearly defined until the present.

5. Rain-wind induced vibrations: The difference between the rain-wind induced vibration and the single-cable vibration is that the rain affects the cable's surface by forming water rivulets attached onto the surface and streaming along the cable, which can lead to vibrations of cables due to wind.

7. Wind buffeting: Buffeting refers to the random wind loads due to fluctuations from incoming turbulent wind speeds, and is not a major concern for the bridge stay-cables but mostly affects the girder deck of the bridge [24].

Table 2.2 [23] presents the main types of vibrations triggered by wind, in association with other phenomena, such as rain, ice accretion, etc. Moreover, the main structural elements of the bridge affected by these vibrations are specified for each case.

Table 2.2 Types of vibrations for long-span bridges caused by wind [23]

Vibration type	**Girder**	**Towers**	**Cables**
Buffeting	yes	no	no
Vortex shedding	yes	yes	yes
Galloping	yes	yes	yes
Bending-torsional coupling	yes	no	no
Ice-accretion vibration	no	no	yes
Separated flow torsional vibration	yes	no	no
Rain-induced vibration	no	no	yes

In some cases, the erosion and fatigue combined with the strong wind effect could be critical for stay-cables of cable-stayed bridges [26]; for example, the Guangzhou Haiyin Bridge, which was built in 1989, has four layers of protection that are used from inside to outside for the stay-cables. While the material used seems tight at that time, due to some chemical effects, the some of the stay-cables still ruptured and fell down in 1995 [27].

2.2 Rain-wind induced vibrations

The combination of rain and moderate wind speeds can cause a large-amplitude vibration, and this phenomenon has been observed for many cable-stayed bridge cases.

Rain/wind-induced vibrations were first presented by Hikami and Shiraishi (1987). Then several observations were conducted in the following years, for bridges such as the Fred Hartman Bridge in Texas, U.S, the Sidney Lanier Bridge in Georgia U.S., the Aratsu Bridge in Japan, and the Nanpu and Yangpu Bridges in China. These vibrations typically occurred under the same conditions, namely both the rain and wind speeds were moderate (8.0 to 15.0 m/s) and the frequency was low, below 3.0 Hz [28]. The characteristics for the rain/wind-induced vibration are as follows:

1. The vibrations normally occur in rain conditions with a wind speed range from 7.0 m/s to 14.0 m/s.
2. The frequency for the rain/wind-induced vibration on cables is between 1.0 Hz and 3.0 Hz, and the modal amplitude vibration increases as the length of the cable increases. Hikami, 1999 [28] found the effect of waterline on the cable changes the shape of the cable cross-section.
3. Rain/wind-induced vibration is the result of the coupling effect between vortex vibration and galloping instability [29].

The principle for rain-wind induced vibration is very complicated and is still not well understood. The two main ways to reduce the rain-wind induced vibration are structural modifications and aerodynamic countermeasures for the cable. The structural modifications can increase the stiffness and damping of stay-cables, such as auxiliary cables, and can be used in the cable plane, while dampers can be installed at the end of the cables [30]. The aerodynamic countermeasures consist in optimization of the shape; for instance, the helical wires wrapped around the cable are a very popular method to help the cables system have better aerodynamic characteristics. The resistance for the helical lines is larger than that for cables; when helical lines need to be designed for real cases, the design should be comprehensively considered [31]. Also if the range of angles between the water rivulet and incoming wind speed is from 70° to 90°, rain-induced vibration is more likely to occur [32].

He et al. (2000) [29] conducted an experiment about rain/wind-induced vibrations on

stay-cables to analyze the effect of the water rivulet formed by the rain droplets. He used oil to replace water rivulets and to set it along the cable model in the wind tunnel. The results showed that the embossment on the model was the reason why large-amplitude vibrations occurred, under the wind effect. Additionally, helical lines with certain heights around the cable could have a significant effect on reducing the rain/wind-induced vibration, but also the Scruton number, which is a parameter describing the weight, mass, damping, and dimension of the model, as it can be seen from Eq. 2.1, has a very high impact on the magnitude of vibrations.

$$S_c = m\zeta/\rho D^2 \qquad \text{(Eq. 2.1)}$$

Where,

m is the mass of unit length of cable

ζ is logarithmic decrement (damping as ratio of critical damping)

ρ is air density

D is cable diameter

S_c is the Scruton number and as mentioned above, it is an important parameter for controlling the vortex shedding and rain-wind induced vibration.

The Scruton number is inverse proportional to the amplitude of oscillation. As per the Federal Highway Administration (FHWA) bridge stay-cables design recommendations, when the Scruton number is bigger than 10, the rain-wind vibrations can be reduced to safe levels.

2.3 Vortex-induced vibrations

In fluid dynamics, vortex-induced vibrations (VIV) are motions of bodies caused by external flows producing an external force on the surface of cylinders. The most visual experiment for vortex-induced vibrations is putting a cylinder into the water and moving it around an axis perpendicular to the water plane. The fluid can be observed on the surface of the cylinder due to its viscosity. While the fluid is slowed down, the boundary layer is formed and the vortices are formed, which could change the force distribution around the cylinders. This could change the lift force on each side of the cylinders, causing an asymmetric motion [33]. This motion alters the nature of the vortex formation, and at very low wind speeds, the flow becomes symmetric; as the wind speed increases,

the flow becomes asymmetric, and the Karman Vortex street occur [34].

The Strouhal number is a very important parameter relating to the frequency of the vortex shedding to the velocity of flows [34]:

$$S_t = f_{st}D/U \quad \text{(Eq. 2.2)}$$

Where

f_{st}: Vortex shedding frequency

D: Diameter of the cylinder

U: The velocity of ambient flows

The blockage ratio and the aspect ratio could have a significant impact on the flow passing the model as well.

The blockage ratio is defined as [34]:

$$\frac{\text{Total surface area of the model normal to the free stream velocity}}{\text{Total area of the wind}} \quad \text{(Eq. 2.3)}$$

The aspect ratio is [34]:

$$\frac{\text{Model length}}{\text{model width normal to the flow velocity}} \quad \text{(Eq. 2.4)}$$

Wes and Apelt (1982) [35] conducted a study on smooth cylinders with a range of aspect ratios from 4 to 10; the study indicated that the Strouhal number was not affected by the blockage ratios up to 6%, while for the blockage ratio of 9%, a maximum of 3% increase in the Strouhal number was observed. The aspect ratio depends only on the model itself and the angle of attack.

2.4 Galloping vibrations

Galloping vibrations mostly occur for rectangular-type, square-type and perpendicular-to flow structures. The principle of galloping vibration occurrence is that the lift coefficient variation has a negative slope, so that the air lift force will have a negative damping

effect, which causes energy to be absorbed from the outside flow into the structure. According to different principles, galloping instability can be divided into two types: wake-flow galloping and cross-flow galloping [36].

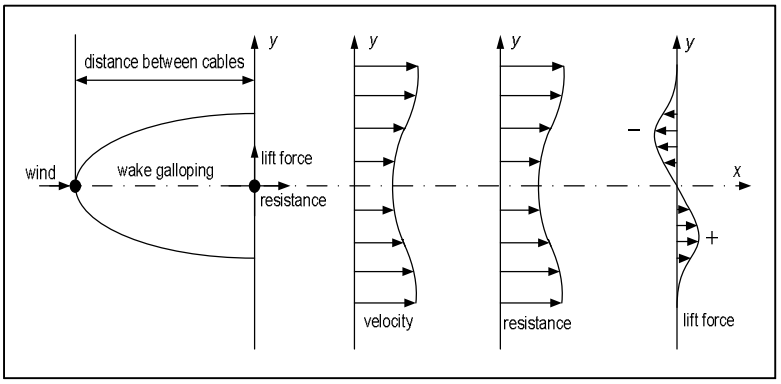

Figure 2.1 Distribution of the wake wind velocity, drag and lift acting on downstream cables [36]

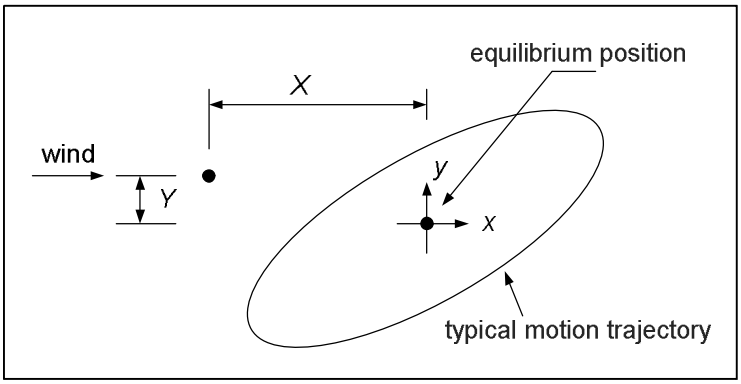

Figure 2.2 Wake galloping phenomenon [36]

Wake-flow galloping for stay-cables occurs when the downstream cables are in the wake flow of the upstream cables, causing vibration of the downstream cables. When the cable axis is along the incoming flow, the cables in the front rows will form an unstable galloping area, because the natural frequencies of the front and of the back cables are very close. If the cables in the back rows are in the galloping area, the amplitude is going to increase until it reaches a stable limit cycle with a large amplitude [36]. However, because the diameters of the cables are relatively small, and the distances between the

cables are considerable compared with the diameters, it is not very evident when the wake-flow galloping occurs on stay-cables, and this vibration can be attributed to other causes.

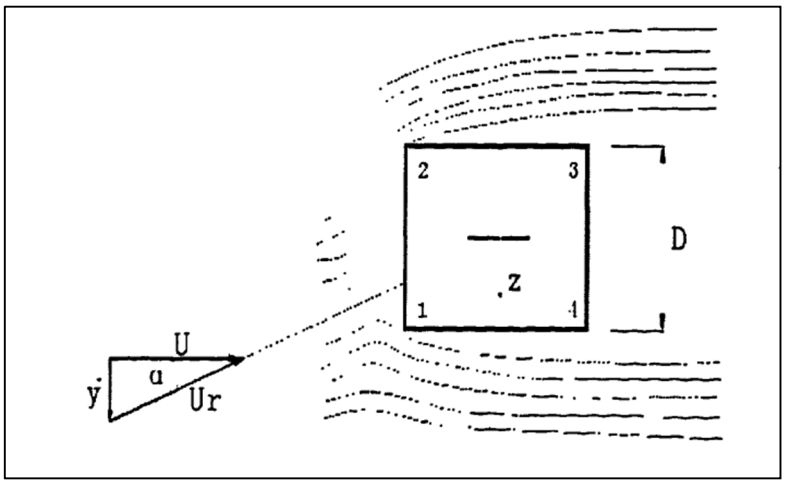

Figure 2.3 Cross-section of the structure under uniform upcoming flow [36]

When the structure is moving perpendicular to the flow direction U, as shown in Figure 2.3, and the flow velocity of the air is $\dot{y} = \frac{dy}{dt}$, so that the relative velocity of the section is U_r, the angle between the motion of the structure and the flow direction is $a = \arctan(\frac{\dot{y}}{U})$. The streamlines produced by the flow detached from point 2, are very close when the flow passes the structure. The wake flow area behind the structure is a turbulent flow area.

Therefore, results showed that the transverse lift force is the most important factor for the galloping instability of the structures. When the incoming flow forms a positive angle of attack with the windward side of the structure, a negative transverse force is produced [37].

Generally, the frequency for which the galloping occurs is as follows [37]:

$$\frac{fD}{U} \leq 0.05 \qquad \text{(Eq. 2.5)}$$

Where,

f is the vibration frequency of the structure, D is the diameter of the structure and U is the mean wind speed.

$\frac{fD}{U}$ in Eq. 2.5 is also the equation for scaling the models to be tested in dynamic wind tunnel experiments, as presented in Fig. 2.4; based on this equation, the scaling parameter can be obtained so that the scaled geometrical dimension and the frequency of the model can be determined through this equation.

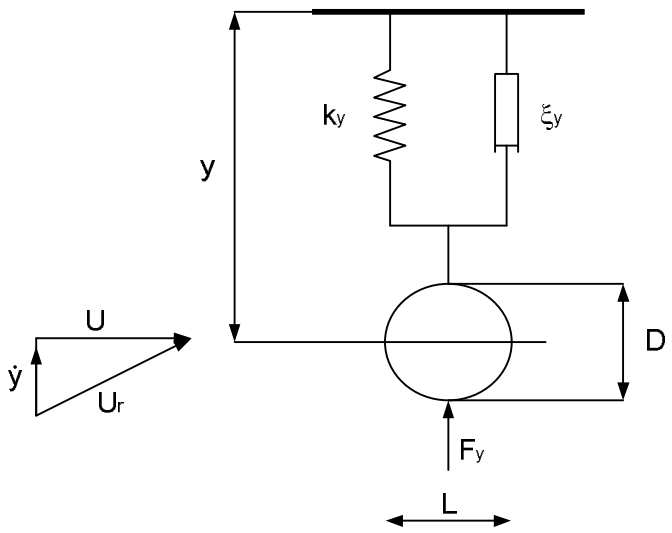

Figure 2.4 Transversal stability of vibration model [37]

The parameters in Figure 2.4 are as follows:

U: velocity of the flow

K: spring stiffness

ξ: damping factor

m: mass of unit length

The angle between the direction of the flow and the direction of the structure model is as follows:

$$\partial = -\mathrm{tg}^{-1}\left(\frac{y'}{U}\right) \qquad \text{(Eq. 2.6)}$$

The attack angle α can be defined according to the aerodynamic mechanics; that is, when the flow moves from left to right, the attack angle is increasing when the structure rotates clockwise. So the relative flow velocity can be presented as follows:

$$U_r^2 = y'^2 + U^2 \quad \text{(Eq. 2.7)}$$

The vertical force can be described as

$$F_y = \frac{1}{2}\rho U^2 D C_y \quad \text{(Eq. 2.8)}$$

C_y : The coefficient of F_y

$$C_y = \frac{U_r^2}{U^2}(C_l \cos a + C_D \sin a) \quad \text{(Eq. 2.9)}$$

The vibration equation for the section

$$my'' + 2m\zeta_y \omega_y y' + ky = \frac{1}{2}\rho U^2 D C_y \quad \text{(Eq. 2.10)}$$

In the equation, ω_y is the inherent frequency, and the unit is rad/s.

$$\omega_y = \left(\frac{k_y}{m}\right)^{\frac{1}{2}} \quad \text{(Eq. 2.11)}$$

Taylor transformation can be used at α = 0 when not much change occurs for the attack angle. Then the equation is obtained as following [37]:

$$y = A_y e^{-\zeta_t \omega_D t} \sin(\omega_D t + \phi) \quad \text{(Eq. 2.12)}$$

$$\omega_D = \omega_y (1 + \zeta_T^2)^{\frac{1}{2}} \quad \text{(Eq. 2.13)}$$

Where,

ζ_T is the sum of the structure damping component and aerodynamic force component.

A_y is the initial amplitude.

ϕ is the initial phase angle.

When ζ_T becomes negative, structure instability occurs so the minimum flow velocity of the point where instability starts is

$$\frac{U}{f_y D} = -\frac{\frac{4m(2\pi\zeta_T)}{\rho D^2}}{(\frac{\partial C_L}{\partial \alpha}+C_D)} \quad \text{(Eq. 2.14)}$$

Substituting $f_y = \frac{\omega_y}{2\pi}$ into the equation above, the following equation is obtained：

$$U = -\frac{4m\omega_y\zeta_T}{\rho D(\frac{\partial C_L}{\partial \alpha}+C_D)} \quad \text{(Eq. 2.15)}$$

When $(\frac{\partial C_L}{\partial \alpha} + C_D) \geq 0$ the model is stable, only when $\left(\frac{\partial C_L}{\partial \alpha} + C_D\right) < 0$ and $U > -\frac{4m\omega_y\zeta_T}{\rho D(\frac{\partial C_L}{\partial \alpha}+C_D)}$, the model could encounter galloping instable, and this is the well-known Den-Hartog criterion [37].

The critical velocity for torsional instability is defined as:

$$\frac{U}{f_\theta D} = -\frac{\frac{4I_\theta(2\pi\zeta_\theta)}{\rho D^3 R}}{\frac{\partial C_M(\alpha=0)}{\partial \alpha}} \quad \text{(Eq. 2.16)}$$

$$f_\theta = \frac{\omega}{2\pi} \quad \text{(Eq. 2.17)}$$

Where, C_M: Torque coefficient

α: Attack angle

I_θ：The polar moment of inertia for the section and flow.

ζ_θ：Damping factor

2.5 Wind effect on cables with and without ice accretion

2.5.1. Experimental work

The thickness and shape of the ice are very important when analyzing the ice-accreted bridge cables. However, because of the variety of climates, no regularity can be found in regards to the shape and thickness of the ice. The weight of the ice is an additional static load, which vary with different climates as well. As mentioned before, the rain/wind-induced vibration changes the shape of the cable by forming water rivulets at the surface of the model, causing complicated and unpredictable vibrations of the stay-cables. The principles for the vibrations of ice-accreted cables are similar to those of the rain/wind-induced vibrations. Pierre et al. [38] made a two-degree-of-freedom model to analyze the galloping phenomenon of a cable with ice, and the schematic diagram of the two-degree-of-freedom model is presented in Figure 2.5, where k_y represents the spring stiffness, k_θ represents the torsion stiffness, and A and B are used for describing the cable axes. The simulation of galloping phenomenon for the cable with thin ice thickness was conducted by an integration of an uncoupled two-dimensional system. After a series of calculations and mathematical functions were applied, results indicated that for cables with very thin ice thickness, the Den Hartog criterion may not apply for the case, but it could be possible to gain vertical galloping due to the lift and torsional vibrations; besides, torsional energy could be transferred to vertical vibration, and that could amplify the vertical vibration. Koss et al. (2012) [39] conducted an experiment about the ice accretion on cylinders under different climatic conditions and he obtained three different stages for ice accretion as indicated in Figure 2.6.

.

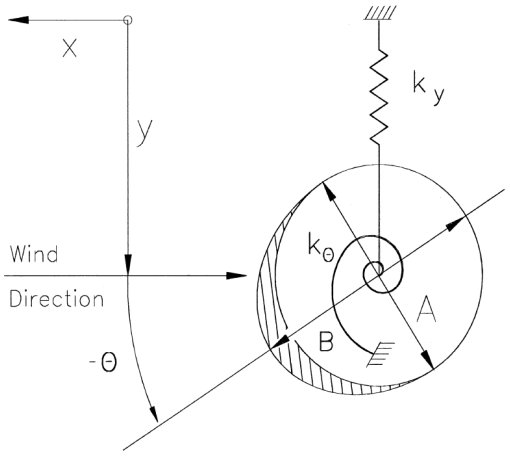

Figure 2.5 Schematic diagram of the two-degree-of-freedom model [38]

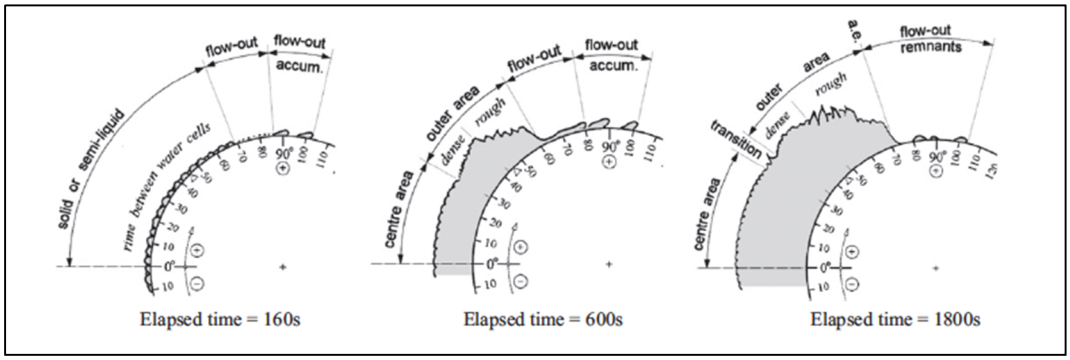

Figure 2.6 Ice accretion under different climatic conditions [39]

Table 2.3 Test boundary condition [39]

Boundary condition	Variation range
Fluid Flow parameter	~
Airspeed	10, 20, 30 m/s
Air temperature	-5,-4,-3,-2,-1 °C
Liquid water content (LWC)	0.4
Droplet mean volume diameter (MVD)	10, 20, 30, 50 μm
Exposure time	5, 10, 15, 30, 60 s

Different wind tunnel climate conditions, such as the values for the airspeed, air temperature, liquid water content, droplet mean volume diameter and exposure time are presented in Table 2.3. With different climate conditions various ice shapes and

roughness can be formed, as it can be observed in Figure 2.7.

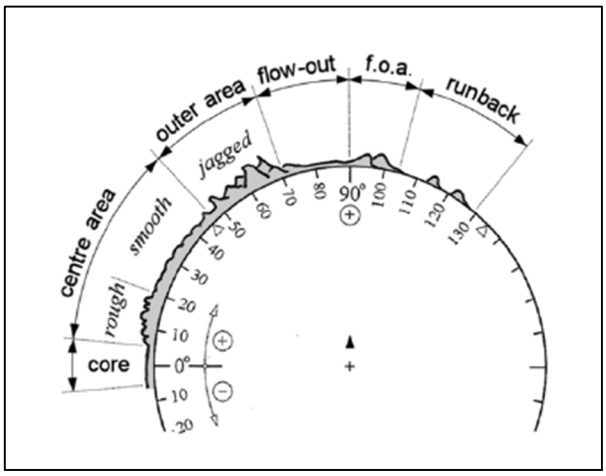

Figure 2.7 Ice accretion area with different roughness zones [39]

The core area was formed due to a long exposure time to freezing conditions; the thickness of the core was accumulated when the exposure time increased. The centre area consisted of two parts, the rough area and the smooth area; the rough area is jagged while the smooth area is flat.

The ice of the outer area is jagged (Figure 2.8) and it tends to be more irregular than the rough part of the centre area. For the flow-out area, the thickness depends on the droplet coming from the downstream edge of the cylinder. For the flow-out area, the ice was not very stable; also this could either be solid or liquid over time. The shape was resembling more a rivulet in a runback area.

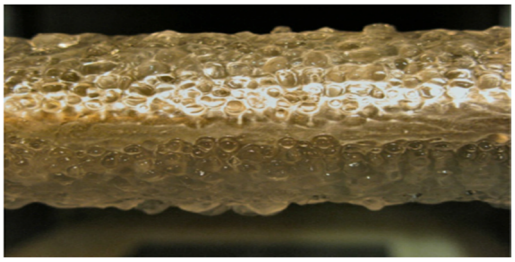

Figure 2.8 A close-up for ice accretion in core [39]

Demartino et al., 2015 [10] conducted an experiment to investigate the aerodynamic

behaviour of ice-accreted cables. This experiment was conducted in the climatic wind tunnel, of the DTU/Force Technology Institute and the setup for the experiment is shown in Figure 2.9. In this wind tunnel temperatures can be changed, and the lowest temperature achieved was -5°C. The drag and lift coefficients were measured under different temperatures and angle-inclined conditions. The spray bar was used to create an in-cloud condition to form the ice accretion; a Plexiglas half-circle nose with a diameter of 4.0 cm was used in order to reduce the flow turbulence generation (Figure 2.9); the length of the cable model was 1.42 m and the diameter was 160 mm. The results showed that the main factors affecting in-cloud ice accretion were, firstly, the evolution of the particle dynamics with the change of the shape for the ice accretion objects; secondly, the pathway of the droplets of their impact; and thirdly, the thermodynamics of the freezing growth process.

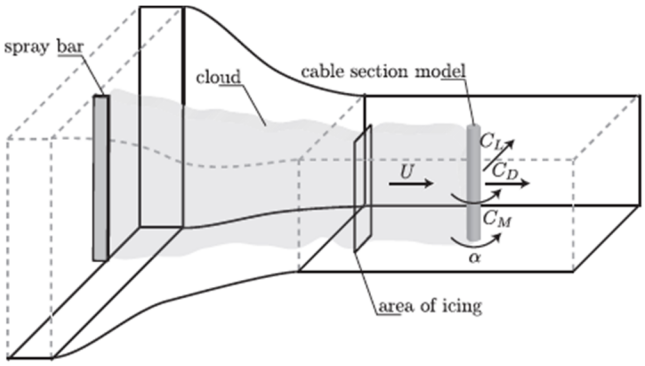

Figure 2.9 Cable model experiment setup [10]

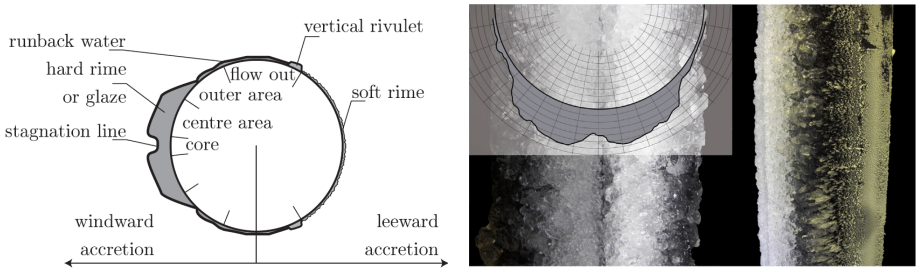

Figure 2.10 Ice shape a) Schematic representation b) Simulated ice accretion [10]

The description of the ice accretion zone for the cable model, which was placed vertically in the wind tunnel, is presented in Figure 2.10. The figure shows that the ice was prone to form on the windward side of the cable, and the shape of the ice was more like a rectangle than a cone.

Luo et al. (2013) [31] conducted an experiment for simulating the rain-induced vibrations of the bridge cables in the wind tunnel of the South-West Jiaotong University in China. The bridge model was Edong Yangtze River Bridge, which has three spans of lengths 270 m, 926 m and 270 m. The material for the cable was high density polyurethane (HDPE), and there were three different diameters for the cable models used in the wind tunnel: 235 mm, 260 mm and 280 mm, respectively. Smooth and spiral cable forms were used for the test. The section for the wind tunnel was 1.34 m × 1.54 m, and the range of the tested wind speeds was from 0.5 m/s to 20 m/s. The cable models were horizontally and vertically inclined in the wind tunnel: α was the horizontal inclination angle and β was the vertical inclination angle.

Wu et al. (2004) [40] conducted an experiment about reducing the vibration of stay-cables with dampers installed. A 7.16 m long stay-cable with a scale ratio of eight was set up for this vibration test.

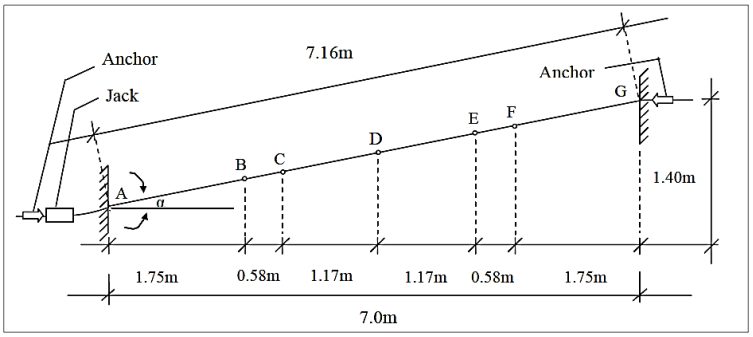

Figure 2.11 Experiment set-up [41]

Figure 2.11 shows the setup of the cable model for the wind tunnel experiment, which used dampers at points A, B, C, D, E and F along the cable. The frequencies were measured and were compared with the frequencies calculated for the ropes. The results have shown that the dampers could be very efficient in reducing the vibration of the stay-

cables; moreover, if the tension force is changed, the natural frequency is also changed, and as the stiffness of the damper increases, the natural frequency of the cable system becomes larger.

Table 2.4 Parameters for the cable models tested [31]

Parameter	Diameter 235 mm	Diameter 260 mm	Diameter 280 mm
Frequency	0.76 Hz	0.75 Hz	0.75 Hz
Damping ratio	0.143%	0.103%	0.117%
Scruton number	0.45	0.30	0.29
Mass	44.46 kg	49.35 kg	49.14 kg

The parameters for the cable models used in the rain-induced vibration test are presented in Table 2.4; the frequency, damping ratio, Scruton number and mass are listed in for different cases of cable diameters, correspondingly.

The results indicated that the rain-induced vibration increased as the angles α and β increased, and the critical wind speed depends to the diameter of the cables. The helical lines were very effective in changing the rain induced rivulets; therefore, the helical lines can reduce the rain-induced vibration, however, when these are used for the design of stay-cables, the damping ratio for helical lines are larger than the damping ratio of the smooth lines. Thus, when it comes to the design perspective, this effect should be taken into consideration.

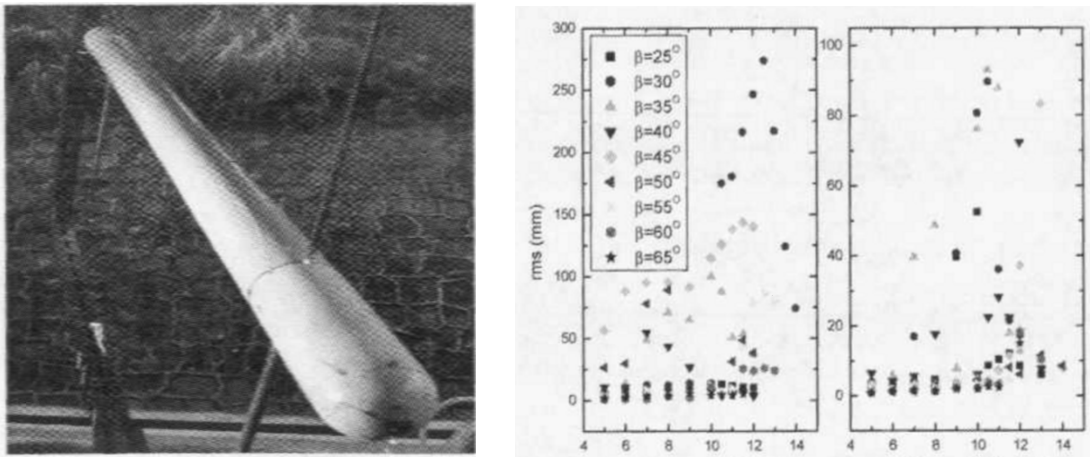

Figure 2.12 The cable model with 169 mm diameter and the vertical vibration for the wind and rain-induced vibration experiment with α = 36° [29]

He et al. (2001) [29] conducted an experiment simulating the rain-induced vibration of stay-cables models of 2.0 m length and diameters for the models were 139 mm, 169 mm, using a boundary layer wind tunnel with a cross-section of 1.34 m × 1.54 m, for wind speeds in the range of 0.5 m/s to 20 m/s; the damping coefficient has been taken into consideration for this experiment, but compared with other cases, the damping coefficient was very small, only 0.3%, and it can be ignored. The precipitation which simulated the rain in the wind tunnel had an incoming speed of around 85 mm/h. The tested stay-cable cases which were indicated as critical cases for rain precipitations at 85 mm/h were listed in Table 2.5, and the vertical vibration amplitude results were plotted in Figure 2.12. The helical lines made of polyurethane (PE), had heights of 2 mm, 4 mm and 6 mm, respectively, and were installed at a distance of 30 mm between them, along the cable are 30 mm reduced the stay-cable vibrations. The Scruton number for the cases which were reported as critical, were are all below 10. The horizontal inclination angle $\alpha = 36°$ was used for the cable case with a diameter of 139 mm, and $\alpha = 21°$ was used for the cable case with a diameter of 169 mm. The damping ratio was approximately 0.1%.

Table 2.5 The critical cases for precipitation of the rain is around 75 mm/h [29]

	Mass (kg)	Frequency (Hz)	Damping ratio (%)	Scruton number
Diameter (139mm)	23.2	0.91	0.1 to 1.0	0.93 to 9.9
Diameter (169mm)	31.5	0.63	0.09 to 0.9	0.9 to 8.3

For the cable case with a bigger diameter, the value of the mass was bigger than for the cable case with a smaller diameter, while the frequency, damping ratio and Scruton number were smaller than those for the cable case with a smaller diameter.

Cheng et al. (2008) [41] conducted an wind tunnel experiment for simulating the vibration of dry-inclined cables, in the boundary layer wind tunnel of the Institute for Aerospace Research, National Research Council Canada. The experiment setup is shown

in Figure 2.13; the vertical vibration for one of the cable cases is plotted in Figure 2.14, and the frequency determined for this vibration is presented in Figure 2.15. The wind tunnel has an open-circuit section with 3 m (W) × 6 m (H), and the maximum wind speed of the wind tunnel is 39 m/s. A 25% reduction scale for the models was applied due to the dimensions limits of the wind tunnel. The material used for making the models was steel, and the models were covered with smooth polyethylene sheets for protection, as used for the full scale bridge stay-cables; the total length for the cable was 6.7 m, and the external diameter was 160 mm while the linear density was 60.8 kg/m.

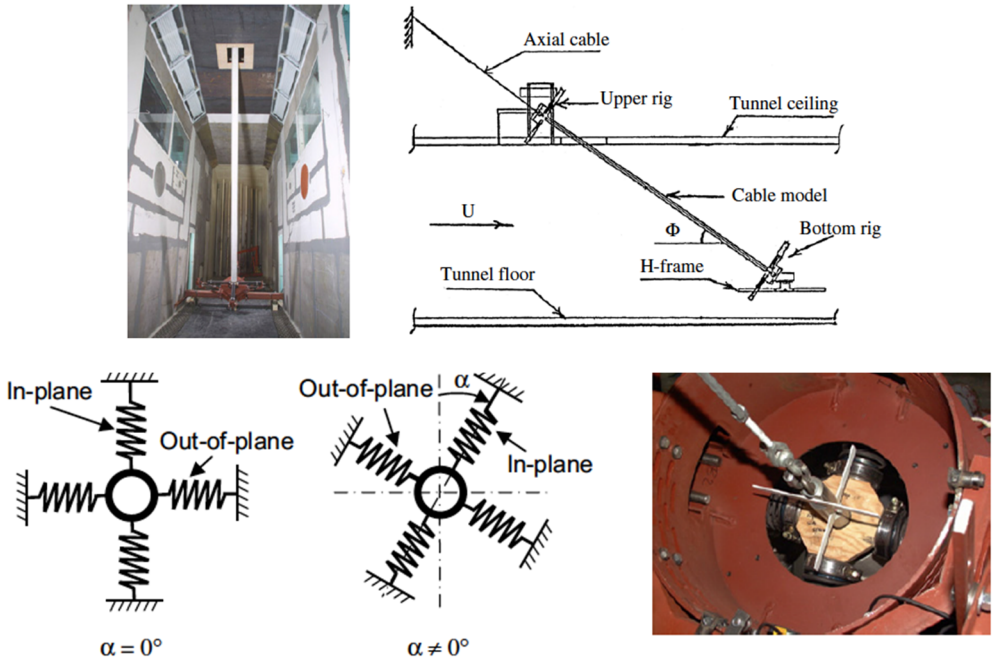

Figure 2.13 Dynamic setup [41]

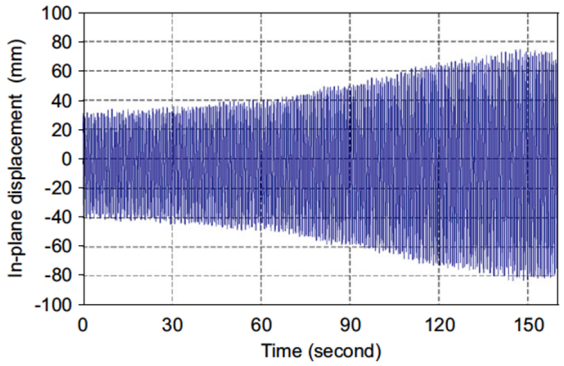

Figure 2.14 Time history of displacement for the dry-inclined cable with α = 54.7° and β = 35.3°, at 32 m/s wind speed (at upper end) [41]

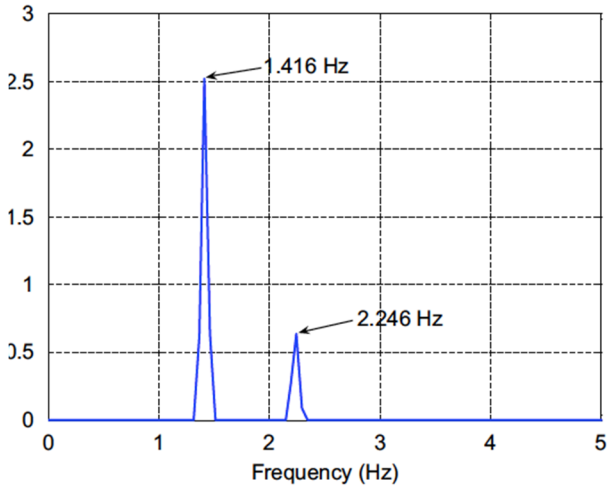

Figure 2.15 The frequency of inclined cable [41]

2.5.2 CFD simulations for inclined cables

Hoftyzer (2013) [42] conducted a CFD simulation for determining the wind effect on inclined cable without ice or rain conditions. A diameter of 8.9 cm was used for the cable model with a length of 2.67 m; the horizontal inclination angles α ranged from 50° to 60°, and the vertical inclination angles β ranged from 0° to 40°, as shown in Figure 2.16 (a). The mesh details used for the CFD simulation are also shown in Figure 2.16 (b).

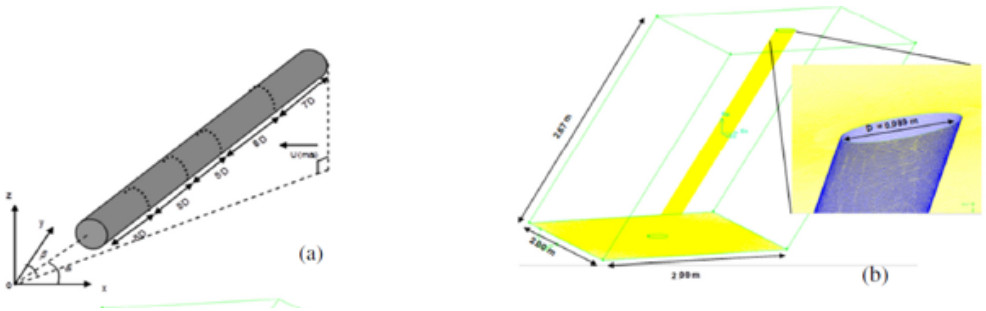

Figure 2.16 Inclined cylinder orientation: a) Geometric dimensions, b) Mesh details [38]

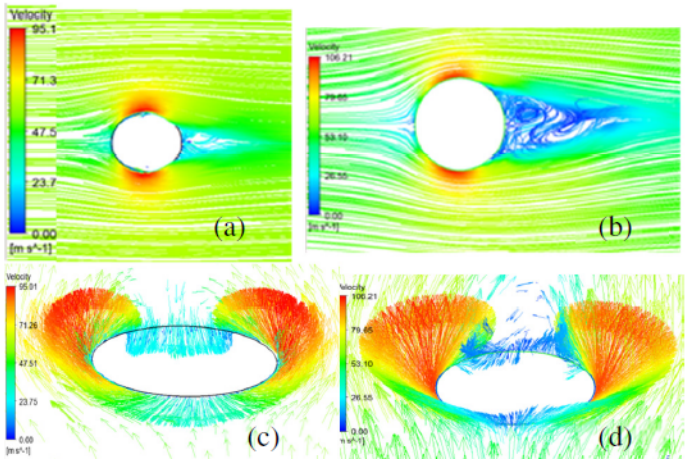

Figure 2.17 Velocity streamlines and distribution at $R_e = 6.7 \times 10^5$ for a) α = 60°, b) α = 0°, c) α = 60°, d) α = 0° [38]

The velocity streamlines and the distribution of the velocity vectors around the inclined stay-cable is shown in Figure 2.17 for two of the critical cable cases indicated in this study. The maximum velocity was 95.1 m/s at the bottom and top surface of the cable model, for the cable model inclined at α = 60°, while for α = 0°, the maximum velocity was 106.21 m/s on the bottom surface and top surface of the stay-cable model. Also Hoftyzer (2013) [42] pointed out that for the α = 60° critical angle, an axial flow which remains attached on the back of the cable is formed and this might influence the occurrence of galloping instability.

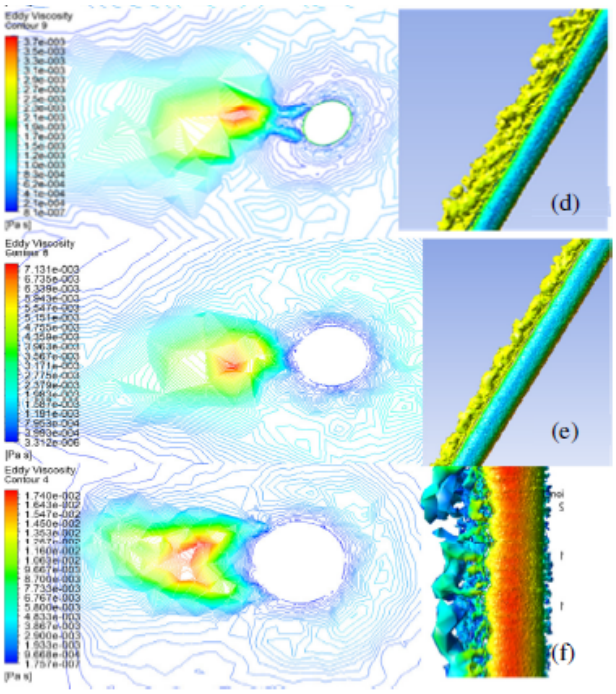

Figure 2.18 Eddy viscosity profiles for d) α = 64°, e) α = 60°, f) α = 0°

The pressure on the surface of the cable model is presented in Figure 2.18; wind-induced pressure was formed on the left side of the cable model and the maximum pressure was 7.131×10^{-3} for the cable case inclined at α = 60°.

2.5.3 The mathematical model of the ice accretion profile

Rodgers (1976) [12] developed a mathematical formulation for estimating the ice formation at the circumference of the cable model. The formulation he proposed for the droplets spectrum is as follows:

$$1 - F = \exp[-(2r_d/a)^k],\ G = Aa^p \qquad \text{(Eq. 2.18)}$$

Where,

F: The fraction of the water to air contained in the droplets with a radius smaller than r_d.

G: The mass of super-cooled water in air at freezing conditions (g/m^3). G typically is $0.3\ g/m^3$.

K, A, p: Coefficients describing ice accretion profile. The suggested values were 3.27, 1.1×10^{-3}, and 1.79, respectively.

d: The diameter range of droplets is 5 to 25μ.

The density of the ice is 0.55 g/cm^3, of super-cooled ice is 1.0 g/cm^3.

Nonlinear first order equation governing the evolution of ice accretion was [12]:

$$\frac{\partial C}{\partial t} = \frac{2kG}{\rho}\int_{r_d}^{\infty} v_i^*(r_d; x_B, y_B) \cdot \nabla C dF(r_d) \qquad \text{(Eq. 2.19)}$$

$r_d > 0$ and $v_i^*(r_d; x_B, y_B)$ is the impaction velocity of a droplet with radius r_d at the point (x_B, y_B).

The vectorial equation of motion for a droplet was expressed as：

$$\frac{4}{3}\pi r_d^3 \rho^* \frac{dv^*}{dt} = 6\pi\eta r_d (v - v^*)\frac{C_D R^*}{24} \qquad \text{(Eq. 2.20)}$$

Turbulence level according to the manual of Japan [12]:

$$I_u = A\left(\frac{Z}{H}\right)^{-\beta-0.05} \qquad \text{(Eq. 2.21)}$$

Where

Z: The vertical distance from ground (m)

H: The height of the building

B: The value corresponding to different relief categories, for example, for category A (Urban zone), β = 0.12, for category B (Rural Zone), β = 0.16.

For H = 30, the condition $A = B$ is recommended.

The aerodynamic static force coefficients, on the across-wind direction (lift coefficient), along wind direction (drag coefficient) and torsion coefficient are defined as [43]：

$$C_D = \frac{F_D}{0.5\rho U^2 Ld}; C_L = \frac{F_L}{0.5\rho U^2 Ld}; C_M = \frac{M_M}{0.5\rho U^2 Ld}; \qquad \text{(Eqs. 2.22)}$$

Where

F_D, F_L and M_M are the drag, lift forces and the moment

U is the mean wind speed

L is the length of the model

D is the diameter of the model

ρ is the density of the air

The ice thickness can be determined according to the weather model developed by Swedish Meteorological and Hydrological Institute [43] for calculating the reliability of the transmission line under freezing conditions.

The basic model to describe the wind load and ice load on transmission lines is:

$$f(x,y) = A \times \exp\left(-\frac{1}{2}\left(\left(\frac{x-x_{center}}{\sigma_x}\right)^2 + \left(\frac{y-y_{center}}{\sigma_y}\right)^2\right)\right) \qquad \text{(Eq. 2.23)}$$

Where

A is the amplitude that represents the severity of the centre of the weather model.

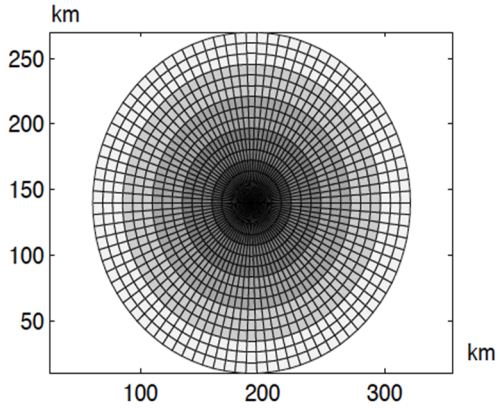

Figure 2.19 The first weather model [43]

The severity of the proposed weather model is decreasing from the centre of the circle towards the circumferences as is shown Figure 2.19; this is the first weather model used for calculating the wind speed and the droplets accumulation on transmission lines.

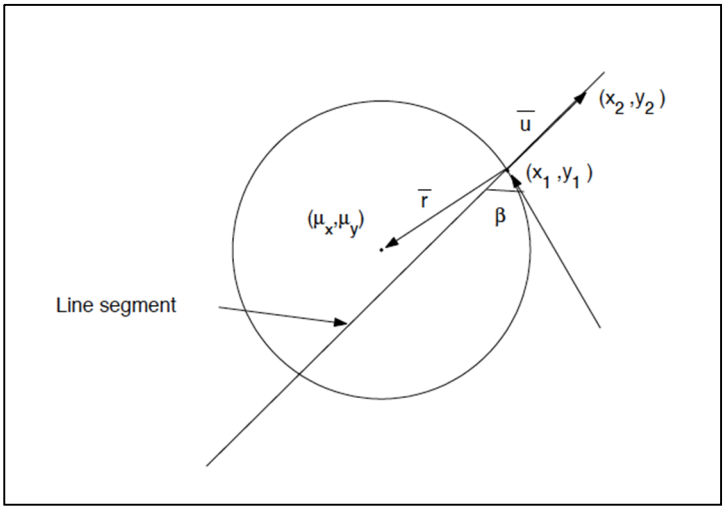

Figure 2.20 The angle β between the model axis and the wind speed vector [43]

Wind speed is often treated as the mean value taken for a certain period; for example, observations can be made in the first ten minutes, after which the wind speed can be recorded every ten seconds and then the average value can be calculated. The direction of the wind speed is also important and for the transmission lines [43] this was determined based on the angle β between the incoming wind speed and the axis of the model, as presented in Figure 2.20.

The wind loading function for a line segment represented by a point in the weather model can be estimated as per the following equation [43]:

$$L_w(x_j, y_j, t)[m/s] = \omega_\beta[A_1 \exp(-\frac{1}{2}\left(\frac{x_j - x_{center}}{\sigma_{x_1}}\right)^2 + \left(\frac{y_j - y_{center}}{\sigma_{y_1}}\right)^2) - A_2 \exp(-\frac{1}{2}((\frac{x_j - x_{center}}{\sigma_{x_2}})^2 + (\frac{y_j - y_{center}}{\sigma_{y_2}})^2)] \quad \text{(Eq. 2.24)}$$

Where

$\omega_\beta(t)$ is the wind factor for considering the impact of angles, and $\omega_\beta(t) \in [0,1]$

With the help of the weather model, the increased ice thickness on the circumferences of the transmission lines is given by:

$$\Delta R = \frac{1}{\delta\pi}\sqrt{P\delta^2 + (3.6V_{mean}\nu)^2} \quad \text{(Eq. 2.25)}$$

Where δ is the density of ice (g/cm^3), P is the precipitation rate according to the weather model, Vmean is mean wind speed (m/s) and ν is the liquid water content (g/cm^3)

2.6 Basic formulation of CFD algorithms

2.6.1 Background of the CFD

Finite element analysis is widely used in engineering for determining the stability of structures and it is already implemented in many engineering software. Midas/CIVIL and ANSYS are the most popular software used to analyze the loads and the vibrations of structures. However, in the finite element analysis perspective, the method for static load is not applied for the surrounding fluid which can cause the dynamic vibration of the structures [44]. For non-linear vibrations, the natural frequency is not significant, because the concept of resonance is not applied [45] and the effect of bending stiffness is different [46]. These kinds of vibrations are not taken into consideration for the current study because the forces induced by the wind flow to the analysed structure, must be determined.

Computational Fluid Dynamics (CFD) analyzes the structure system including the fluid flow, heat conduction and the relevant behaviours affected by different factors, such as wind-induced pressure. Complex calculations can be performed to determine the pressure coefficients at the surface of the structure, the flow formations around the cylinders can be determined. The basic concept for the CFD which uses a large amount of limited variable values on discrete points that could replace the original velocity, pressure fields, and by applying certain principles the relating equations between the values can be set.

The process of performing a CFD simulation is described in Table 2.6 below [47]:

Table 2.6. CFD Router chart [47]

1	Set up the governing equation
2	Set up the initial and boundary conditions
3	Divide the calculation grid; generate calculation nodes
4	Set up discrete equation
5	Disperse the initial and boundary conditions
6	Determine governing parameters
7	Solve the equation

The general process is to set up the governing equations, initial conditions and boundary conditions, then to select the input parameters needed for the software to analyze the effect of the factors, which has been set up in initial and boundary conditions. This process will be described in detail in Chapter 3.

2.6.2 Main algorithms used in CFD

Any fluid problem should satisfy the law of conservation of mass. The law can be described as the increasing mass of the fluid in unit time equals the net mass of the inflow in unit time [47]:

$$\frac{\partial \rho}{\partial t} + \frac{\partial (\rho u)}{\partial x} + \frac{\partial (\rho v)}{\partial y} + \frac{\partial (\rho w)}{\partial z} = 0 \qquad \text{(Eq. 2.26)}$$

ρ: Density (kg/m^3)

t: Time (sec)

u: Velocity vector and u, v, w are the velocity vector in x,y,z axis.

The law of conservation of momentum is also a basic principle; the equations are derived for the three directions as follows：

$$\frac{\partial (\rho u)}{\partial t} + \frac{\partial (\rho uu)}{\partial x} + \frac{\partial (\rho uv)}{\partial y} + \frac{\partial (\rho uw)}{\partial z} = \frac{\partial}{\partial x}\left(\mu \frac{\partial u}{\partial x}\right) + \frac{\partial}{\partial y}\left(\mu \frac{\partial u}{\partial y}\right) + \frac{\partial}{\partial z}\left(\mu \frac{\partial u}{\partial z}\right) - \frac{\partial p}{\partial x} + S_u \qquad \text{(Eq. 2.27)}$$

$$\frac{\partial (\rho v)}{\partial t} + \frac{\partial (\rho vu)}{\partial x} + \frac{\partial (\rho vv)}{\partial y} + \frac{\partial (\rho vw)}{\partial z} = \frac{\partial}{\partial x}\left(\mu \frac{\partial v}{\partial x}\right) + \frac{\partial}{\partial y}\left(\mu \frac{\partial v}{\partial y} + \frac{\partial}{\partial z}\left(\mu \frac{\partial v}{\partial z}\right)\right) - \frac{\partial p}{\partial y} + S_v \qquad \text{(Eq. 2.28)}$$

$$\frac{\partial (\rho w)}{\partial t} + \frac{\partial (\rho wu)}{\partial x} + \frac{\partial (\rho wv)}{\partial y} + \frac{\partial (\rho ww)}{\partial z} = \frac{\partial}{\partial x}\left(\mu \frac{\partial w}{\partial x}\right) + \frac{\partial}{\partial y}\left(\mu \frac{\partial w}{\partial y}\right) + \frac{\partial}{\partial z}\left(\mu \frac{\partial w}{\partial z}\right) - \frac{\partial p}{\partial z} + S_w \qquad \text{(Eq. 2.29)}$$

Law of energy conservation is expressed as:

$$\frac{\partial(\rho T)}{\partial t} + \frac{\partial(\rho u T)}{\partial x} + \frac{\partial(\rho T v)}{\partial y} + \frac{\partial(\rho T w)}{\partial z} = \frac{\partial}{\partial x}\left(\frac{k}{c_p}\frac{\partial T}{\partial x}\right) + \frac{\partial}{\partial y}\left(\frac{k}{c_p}\frac{\partial T}{\partial y}\right) + \frac{\partial}{\partial z}\left(\frac{k}{c_p}\frac{\partial T}{\partial z}\right) + S_T \quad \text{(Eq. 2.30)}$$

Where

c_p is specific heat capacity, T is temperature and k is the conduction coefficient.

S_T is the internal heat source and the viscosity effect for the mechanical energy transferring to heat.

Additionally the law of chemical mass conservation can be included in the CFD algorithms. This is more likely to affect the chemical properties of the fluid, as the change of the chemical mass with respect to time which equals the flow diffusion and the chemical producing rate of the mass; such equation can be further modified if ice droplets must be directly simulated. Thus the equation can be described as follows:

$$\frac{\partial(\rho c_s)}{\partial t} + \frac{\partial(\rho c_s u)}{\partial x} + \frac{\partial(\rho c_s v)}{\partial y} + \frac{\partial(\rho c_s w)}{\partial z} = \frac{\partial}{\partial x}\left(D_s \frac{\partial(\rho c_s)}{\partial x}\right) + \frac{\partial}{\partial y}\left(D_s \frac{\partial(\rho c_s)}{\partial y}\right) + \frac{\partial}{\partial z}\left(D_s \frac{\partial(\rho c_s)}{\partial z}\right) + S_w \quad \text{(Eq. 2.31)}$$

Where c_s is the volume concentration of specimen s (V/V), ρc_s is the mass concentration of this specimen (m/m), D_s is the diffusion coefficient of this specimen (no dimension) and S_s is the mass produced by the chemical process (kg).

After comparing the above equations (Eq. 2.27 to Eq. 2.32), it can be learned that all these equations have shown the conservation properties for a general variable thus leading to the general form of governing equation. Therefore ϕ is used to represent the general variables and the equations above (Eq. 2.27 to Eq. 2.32) can be presented as the following:

$$\frac{\partial(\rho\phi)}{\partial t} \mathrm{div}(\rho u \phi) = \mathrm{div}(\Gamma \mathrm{grad}\phi) + S \quad \text{(Eq. 2.32)}$$

The expanded form of this equation is:

$$\frac{\partial(\rho\phi)}{\partial t} + \frac{\partial(\rho\phi u)}{\partial x} + \frac{\partial(\rho\phi v)}{\partial y} + \frac{\partial(\rho\phi w)}{\partial z} = \frac{\partial}{\partial x}\left(\Gamma\frac{\partial\phi}{\partial x}\right) + \frac{\partial}{\partial y}\left(\Gamma\frac{\partial\phi}{\partial y}\right) + \frac{\partial}{\partial z}\left(\Gamma\frac{\partial\phi}{\partial z}\right) + S \quad \text{(Eq. 2.33)}$$

The general formulations of the above described equations were employed in the current study, for simulating the wind-induced effect on the cable modeled covered with ice accretion.

In conclusion, the most known bridge failures caused by wind were discussed in this chapter; also the main vibrations types for bridge cables have been described, such as, rain-induced vibration, vortex-induced vibration and galloping phenomenon, and several experiments are presented to have a better comprehension about the rain/wind-induced and ice/wind-induced vibrations of cables. Also the general CFD concepts have been illustrated. According to the information gathered from the experiments and the CFD simulations reported in the literature, the basic concepts and assumptions have been learned for performing the current wind tunnel experiment and CFD simulation and for analysing the data obtained. Thus the experiments presented in this chapter can be footstone for this experiment, by comparing the vibrations between different cable models with ice or water rivulets. Also different mathematical methods for analyzing the vibrations of cables presented in this chapter, such as Den Hartog criterion, were later used for determining the galloping instability conditions for the currently performed experiments.

The ice accretion shape is an interesting aspect to analyze as well; several experiments reviewed above have shown different ice profiles obtained under different climate conditions. The vibration for transmission lines with ice accretion was also discussed in this chapter, and the reason for which these are not comparable with bridge accreted cables were detailed.

Chapter 3: Experimental setup and CFD modelling

3.1 Overview

The current research project aims to investigate the aerodynamic behaviour of ice-accreted bridge cables, and it was conducted in the wind tunnel experimental facility of the University of Ottawa, Mechanical Engineering Department. The springs supporting system was used to sustain the cable models, for the dynamic test, and measurements were performed for the vertical displacement and torsion vibrations, for the models positioned at horizontal inclination angles of 0°, 30°, 60° and vertical inclination angle of 0°, 15°, tested for wind speeds between 1.5 m/s and 15 m/s. The purpose of conducting this experiment is to clarify the effect of ice accretion on the aerodynamic properties of the inclined bridge stay-cables; based on the experimental data recorded, the frequency of the wind-induced vibrations and the potential galloping vibration, for each wind speed step was obtained. The critical cases for torsional and vertical displacements, at different vertical and horizontal inclination angles were identified and discussed. The overall wind-induced response of cables with ice accretion profiles of 1.0 cm and 2.0 cm height were discussed, for cables perpendicular to the wind flow and for inclined bridge cable models. The static force coefficients were obtained from the CFD simulation performed for the cable model with 1.0 cm ice profile, inclined at 15° and 60°, for wind speeds of 10 m/s and 15 m/s. The critical wind speed for galloping was determined for different inclination and ice profile cases.

3.2 Wind tunnel and mechanical room facilities

The testing took place in the wind tunnel experimental facility of the University of Ottawa, Mechanical Engineering Department, which is an open-circuit, suction wind tunnel with a fan inducing a maximum wind speed of 30 m/s (2,000 rpm). The testing cross-section of the tunnel is 61 cm × 91 cm, and has three openings on each side of the wood panels enclosing the tunnel, to install the test models and to coordinate the necessary vertical and horizontal inclination angles for the cable models. At the inlet, the

wind tunnel has a honeycomb filter to ensure a good quality flow coming into the wind tunnel testing section. The total length of the wind tunnel is approximately 3.6 m.

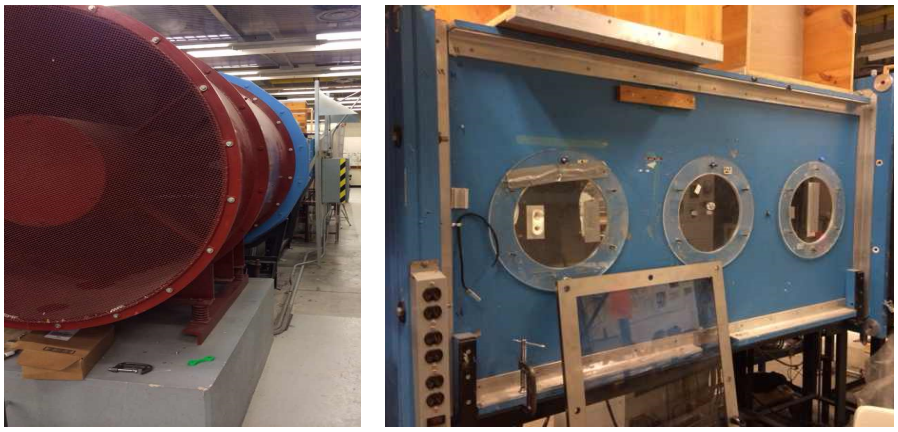

Figure 3.1 The University of Ottawa wind tunnel facility

By adjusting the wind speed controller, experiments can be conducted for wind speeds of up to 30 m/s; however, considering the vibrations observed under various testing conditions, for the current experiment the ice-accreted cable were tested for the maximum wind speed of 15 m/s.

3.2 Cable models with ice accretion

Prior to commencing the wind tunnel test, the cable models were designed and prepared in the mechanical room of the Structures Lab. Initially, each cable model had a diameter of 2.0 cm, following a scale of 1:45 from the prototype bridge cable used by Cheng et al (2008) [41] for the full-scale wind tunnel experiments they performed. To this diameter, 1.0 cm and 2.0 cm ice accretion profiles were added on one side of the cable model. Three cable models were made for reaching the lateral walls of the wind tunnel at the vertical/horizontal inclinations required: Model 1, which was the cable perpendicular to the flow, had a total length of 92 cm. When the model was inclined in regard to the wind direction, Model 2 and Model 3 were used with different lengths of 107 cm and 184 cm, respectively, in order to ensure the connection of the cable model extremities to the spring suspension system installed outside the testing section, as detailed in the following sections.

Figure 3.2 The mechanical room used for model preparation

In order to simulate the randomness of the ice profile, expandable foam was applied on the cable model, as shown in Figure 3.3. The ice accretion simulated by foam showed good geometrical agreement with the models obtained from the climatic wind tunnels reported in the literature [39] (Fig. 3.4), especially for the troughs and crests of the ice accretion. However, during expansion, the foam created very irregular openings, which needed to be filled, in order to respect the ice profile recommended by the available literature [39].

Figure 3.3 Cable model with foam-simulated ice accretion.

The full process of expanding and hardening the foam took approximately one day for each model; after hardening, a second layer of foam was applied for refilling the small openings in the ice accretion created in the first stage of the application. As mentioned above, the shape and thickness of the ice depend on the wind speed, air temperature,

liquid water content, droplet mean volume diameter and exposure time, but also depends on different stages of ice accretion; however, the shape mostly resembles a rectangular shape, for given segments along the cable as it can be noticed in Fig. 3.4 b) [39]. Therefore, for parts of the cable with smaller ice accretion, the shape was assumed to be rectangular, and the mass of the ice simulated by foam was very small; therefore, the inertia effect of the ice profile would not influence the vibration response of the entire cable model. Thus, the effect of the ice geometry could be separately studied to gain a better result of this experiment.

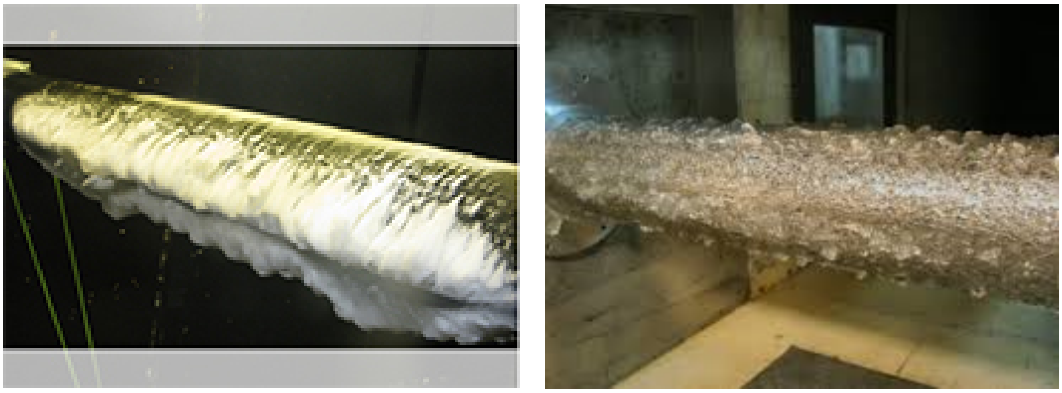

Figure 3.4 Ice accretion model in climatic wind tunnel experiment a) Non-uniform profile b) Uniform profile [39]

The shape of the ice accretion used in the current experiment, after refilling and correction, is presented in Figure 3.5. Additionally, two ice-accretion heights were constructed for the tested cable models of 1.0 cm and 2.0 cm, respectively. These dimensions correspond to the real cable ice accretion of 45.0 cm (D/2) and 90.0 cm (D) where D is the diameter of the real bridge stay-cable.

The climate wind tunnel studies showed that for bridge cables, ice accretion can reach profile heights of almost D/2, after 1,800 sec exposure time to precipitation [39]; therefore, to compare with the results reported in studies performed for ice-accreted cables, similar ice profile dimensions (1.0 cm after scaling) were considered for the current experiment, however, because the bridge cable's safety criteria was of concern, ice-accretion profiles were tested as high as 1D (2.0 cm after scaling) ice thickness were tested. The shape of the improved ice profile for 1.0 cm height is shown in Figure 3.5 a);

it must be mentioned that, to maintain the randomness of the ice profile, the height of the ice accretion was not 1.0 cm everywhere on the surface of the cable model; also, to rectify the foam's small imperfections and indentations, and to make the model better resemble ice surface smoothness, an aluminum foil was used for covering the entire ice profile and the cable model, as it can be seen in Fig. 3.5. b)

Figure 3.5 The bridge cable model with 2.0 cm ice accretion a) initial foam model b) improved model

For each cable model steel T-bars of 29 cm were welded at both ends of the cable model, in order to extend laterally and to ensure sufficient length for installing the supporting springs; also for achieving different angles of the models, the T-bars were welded at different horizontal inclinations with the models in order to place the cable models diagonally in the wind tunnel, between the entrance windows and exit windows, as it will be detailed in the following section. In total, three models were made for this experiment, with horizontal inclination angles α of 0°, 30°, 60° and vertical inclination angles β of 0°, 15°. The models had lengths of L_1 = 0.92 m， L_2 = 1.07 m， L_3 = 1.84 m，and the total masses of m_1 = 0.5 kg, m_2 = 0.7 kg, m_3 = 0.9 kg.

3.3 Experimental setup

For the current experiment, Reynolds numbers of up to 4×10^5 were used, corresponding to the maximum wind speed in the wind tunnel of 15.0 m/s; the testing cross-section was 61 cm × 91 cm, and thus for the model diameters, which were 1.0 cm and 2.0 cm, the blockage ratios were as follows [35]:

$$\text{BL} = \frac{\text{Total surface area of the model normal to the free stream velocity}}{\text{Total area of the wind tunnel}}$$

$$\text{BL} = \frac{1 \times 2}{61 \times 89} = 0.000368 \quad \text{for 1.0 cm ice profile} \qquad \text{(Eq. 3.1)}$$

$$\text{BL} = \frac{2 \times 2}{61 \times 89} = 0.000736 \quad \text{for 2.0 cm ice profile}$$

Because the blockage ratios were very small, and in general the Strouhal number is not affected by the blockage ratio when this is lower than 6% [35], no correction is needed to account for the blockage ratio. Moreover, the turbulence intensity would not be a significant concern. The wind speed was varied during the tests, from 1.5 m/s to 15.0 m/s at intervals of 1.5 m/s.

The detailed steps for performing the dynamic experiment for the above-mentioned test cases are as follows:

- Initially, the fan was set to 100 RPM corresponding to 1.5 m/s wind speed.
- The cable model was given an initial displacement of about 2.0 cm, which induced an initial vibration of the cable.
- For all the test cases, the vertical and torsional vibration data were measured and calibration was performed.
- If the critical aerodynamic instability is reached, under the effect of wind speed the initial vibration would amplify. If the vibrations do not increase under the effect of the currently tested wind speed, the model is stopped and the next wind speed case is initiated, as per the steps described above.

Cable model installation in the wind tunnel is indicated in Figure 3.6, for the ice-accreted cable Model 1 at $\alpha = 0°$, $\beta = 0°$ (Figure 3.6 a)), Model 2 at $\alpha = 30°$, $\beta = 15°$ (Figure 3.6

b)) and Model 3 at α = 60°, β = 15° (Figure 3.6 c)), as described in detail in the following sections. Because of the dimensions limitations of the wind tunnel, to meet the required inclination angles of the cable models for vertical and horizontal directions, different arrangements were used when installing the model between the entrance windows and exit windows of the test section. The windows that were not used during the experiment were covered with the original Plexiglas disc, so that the openings would not influence the quality of the flow in the test section.

Figure 3.6 The cable models in wind tunnel a) Model 1, case α = 0°, β = 0° b) Model 2, case α = 0°, β = 15° c) Model 3, case α = 30°, β = 15°

Outside the test section of the wind tunnel, the ice-accreted cable models were connected to the supporting system, consisting of 4 springs for each end of the model, 2 upper springs and 2 lower springs, to ensure a good vibration simulation test. The diameters of

the entrance and exit windows were 29 cm each, and by raising the middle axis of the spring's supporting system, the maximum vertical inclination angle β of 15° was reached, while by using the first entrance window and the last exit window for the cable model, the maximum horizontal inclination angle α of 60° was achieved. Some space was also considered between the cable model's neutral axis and the edge of the window, in order to avoid hitting the upper or lower margins of the windows, during the experiments, when the cable models vibrate.

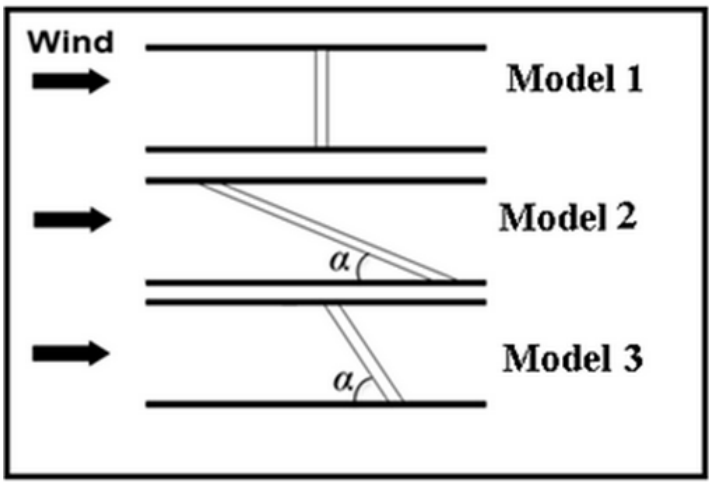

Figure 3.7 Top view of the models placed in the wind tunnel

Figure 3.7 shows the top view of the models placed in the wind tunnel under different horizontal inclination angles α. If the ice-accreted cable model is inserted from the right entrance window on one side of the wood panel and reached the middle exit window on the other side of the wood panel, the angle of horizontal inclination is α = 30° (Model 2); if the model is inserted from the middle entrance window and is taken out on the other side of the wind tunnel test section from the middle exit window, the angle of horizontal inclination is α = 0° (Model 1). Finally, if the model is inserted from the middle entrance window and is extended to the other side of the wind tunnel test section from the left exit window, the angle of horizontal inclination is α = 60° (Model 3). Also the maximum vertical inclination angle was β = 15° allowing sufficient space for the vertical vibration of each of the cable models.

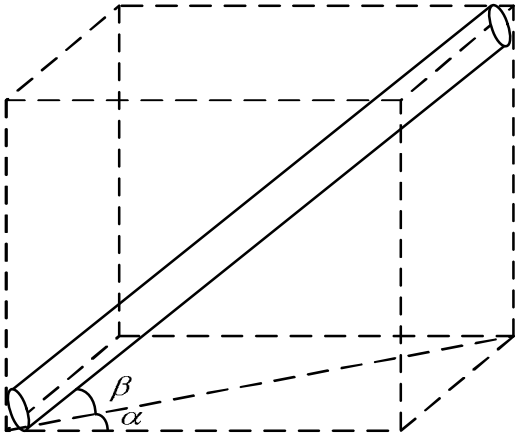

Figure 3.8 Schematic representation of the cable model configuration

For better conveying the geometrical configuration of the cable installed in the wind tunnel, Figure 3.8 schematically represents the vertical and horizontal inclination angles β and α for the cable model placed in the wind tunnel, where the same angle conventions as above were maintained, namely, α represents the angle of horizontal inclination and β represents the angle of vertical inclination. However, for estimating the angle formed between the wind speed direction and the cable axis, in the three-dimension perspective, the concept of relative angle is needed. Also, the relative angle convention is very useful when results are compared with other studies that use similar three-dimensional inclinations for the cable model.

Therefore, the wind-cable relative angle as defined by Cheng et al. [41] was employed:

$$\theta = \arccos(\cos\alpha\cos\beta) \qquad \text{(Eq. 3.2)}$$

In reality, the wind speed is always the decisive factor for the vibration of slender objects, and there is a critical direction between the impacting wind speed and the bridge cables, which would amplify the cable's vibration. The wind flow approaching the cable models always induces higher vibrations on the perpendicular direction of the wind flow, because the cable is more restrained along the flow direction, and because of the vortices formed on top and on the bottom of the models [48]. Thus, the model is always vibrating more in

the vertical direction, which is the direction perpendicular to the wind flow.

In order to realistically simulate the wind-induced vibrations for the cable models installed in the wind tunnel, supporting springs are needed for the vibration test; these were symmetrically installed along the vertical direction, on the top and bottom sides of the T-bars connected to the cable model, and were placed outside the wind-tunnel section, to have a similar wind effect for the cable vibration (Figure 3.9). The springs are needed on both top and bottom sides of the model because for simulating the wind-induced vibrations, the structure needs to move upwards and downwards, with a certain frequency that depends on the structural frequency of the model, and also on the wind speed; if the model is supported only by the top or bottom springs, then the model would vibrate asymmetrically, towards the top or bottom vertical directions. Hence, both top and bottom springs were installed for performing the vibration tests. Because the room accommodating the wind tunnel has relatively small dimensions, and there is not sufficient space around the test section, the massive steel frames used for supporting the springs of the model and for changing the inclination angles could not be brought inside the lab and could not be placed on each side of the wind tunnel. Therefore, the springs had to be set directly on the wind tunnel wall. The fasteners that usually keep the covering Plexiglas windows in place were used and the springs were attached on both sides of the entrance and exit windows (Figure 3.9).

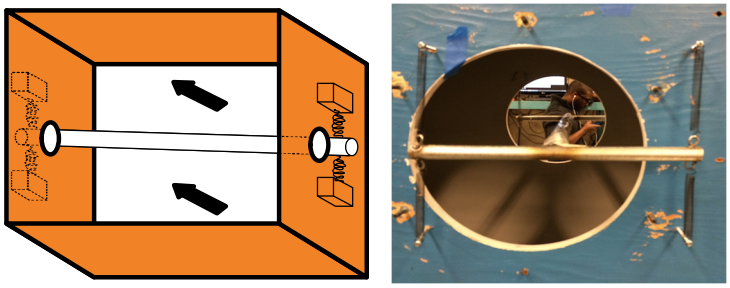

Figure 3.9 The springs supporting setup of the cable model

The 4 springs used on each side of the test section cannot be connected directly to the cable model; therefore, the models were rigidly welded at both ends to two T-bars of 29 cm length, and 4 hooks were welded on both ends of the T-bars, at top and bottom sides,

connecting the springs with the cable models.

Each spring has an elastic constant k (N/m), which is a very important parameter for performing the free vibration test and for determining the structural frequency and damping of the tested models. Each of the four springs had the same elastic constant on each side of the models; the elastic constant of the springs was 1.5 N/m, the elastic constant of the entire system is 3.0 N/m, which was calculated as per the Hook's law [48]:

$$k = \frac{F}{Lsp} \qquad \text{(Eq. 3.3)}$$

In Eq. 3.3, k is the elastic constant of the spring, F is the tension force applied on the spring, Lsp is the elongation of the spring due to the applied tension force, which was measured in the mechanical room presented in Figure 3.2. Several sets of springs were tested and the springs with the equivalent k = 3.0 N/m were selected because, as per Eq. 3.8 this value of k is required for an object, the tested cable model in this case, of mass 0.5 kg to achieve a natural frequency of f = 0.39 Hz. Actually as detailed in the later sections, the three tested cable models had masses of 0.5 kg, 0.7 kg and 0.9 kg, which correspond to natural frequencies of f = 0. 39 Hz, 0.33 Hz and 0.29 Hz respectively. These frequencies were estimated by scaling down the natural frequency of a real bridge cable of f = 1.4 Hz [41] by employing the Eq. 2.14.

Also the springs supporting system arrangement was used for varying the vertical angle β for each of the ice-accreted cable models. In order to adjust the β from 0° to 15°, the springs were lowered or raised by moving the position of the fasteners on one side of the wind tunnel test section.

After installing the springs, usually the windows cannot be covered with the usual Plexiglas disc; therefore, cardboard was used to partially shield the wind tunnel openings on both sides of the test section, without interfering with the motion of the cable model; some of the installation details can also be noticed in Figure 3.7. An initial test was performed for the maximum wind speed of 15.0 m/s to test the stability of the fasteners, springs and cardboard attachments, and because no mechanical failure was observed it could be concluded that the supporting system and cardboard coverings can perform well

for the wind tunnel testing.

3.4 The test cases for the ice-accreted cable models

To better comprehend the vibration tests performed, the wind tunnel experimental cases are listed and described below. In total, 90 cases for the three cable models with an ice profile of 1.0 cm and then with an ice profile of 2.0 cm were carried out, for wind horizontal inclination angles $\alpha = 0°$, 30° and 60° and vertical inclination angles $\beta = 0°$ and 15°, at wind speeds between 1.5 m/s to 15 m/s (Table 3.1). Because in the available literature more results are found for the ice profiles of dimensions equivalent to the 1.0 cm ice profile thickness used in the current test, more cases were performed for this ice profile model. Therefore, six cases with 1.0 cm ice thickness and three cases with 2.0 cm ice thickness were carried out. The settings and testing conditions for each case are briefly described below.

Table 3.1 The tested cases for the experiment

Model tested	Horizontal inclination angle α (°)	Vertical inclination angle β (°)	Relative angle θ (°)	Ice accretion 1.0 cm	Ice accretion 2.0 cm	Mass (kg)	Length (m)
Model 1	0	0	0	Yes	Yes	0.5	0.92
Model 1	0	15	15	Yes	Yes	0.5	0.92
Model 2	30	0	30	Yes	Yes	0.7	1.07
Model 2	30	15	33	Yes	No	0.7	1.07
Model 3	60	0	60	Yes	No	0.9	1.84
Model 3	60	15	61	Yes	No	0.9	1.84

Test case 1

The first test case performed was for the cable Model 1 with 1.0 cm ice thickness for $\alpha = 0°$, $\beta = 0°$; this case was used as a benchmark for comparison with other cases. Also, because of the limited time for which the wind tunnel was available, and because there is sufficient data for this case in the available literature, tests on the cable model perpendicular and inclined/yawed in regard to the flow, but without any ice accretion, were not performed.

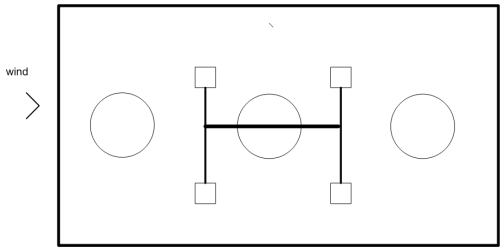

Figure 3.10 Front view for test case 1

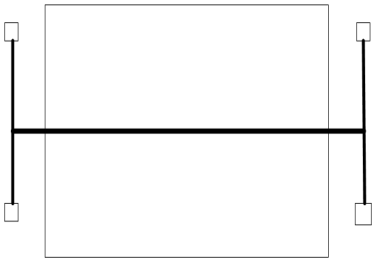

Figure 3.11 Side view for test case 1

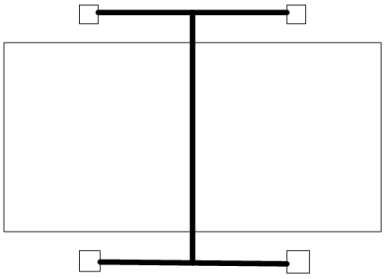

Figure 3.12 Top view for test case 1

For the test case 1, all the inclinations for vertical and horizontal directions were 0°, therefore the model is supported by the springs hanging on the middle entrance window and middle exit window, as it can be noticed in Figure 3.10 to Figure 3.12. In the side view representation of the model, the vertical angle $\beta = 0°$ can be noticed, and the top view plotted in Figure 3.17, $\alpha = 0°$ can be observed. The cable model was connected to the T-bars at each end, so the model can be hung on the springs to the wood panel on each side of the wind tunnel. Also, it is important to mention that the horizontal α angles were obtained by performing the welding between the cable model and the T-bar under the required horizontal angle.

Test case 2

Test case 2 was performed on Model 1 with 1.0 cm ice thickness as well, but for the angles of $\alpha = 0°$, $\beta = 15°$; for this case, the position of the springs was used to incline the model vertically. Thus the model was placed between the middle entrance window and the middle exit window as schematically represented in Figure 3.13, with some space between the cable model and the edges of the windows, so that the vibrations could occur without interfering with the window walls. From the side view in Figure 3.14, it can be observed that the model was rigidly welded to the T-bars, to form the vertical inclination angle $\beta = 15°$ and to connect the model to the wood panels at each side, as shown in the top view plotted in Figure 3.15.

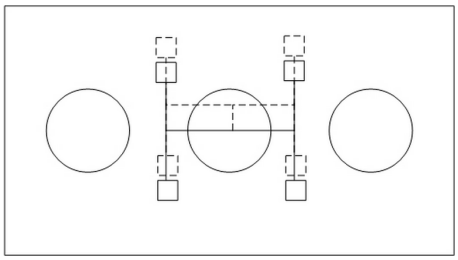

Figure 3.13 Front view for test case 2

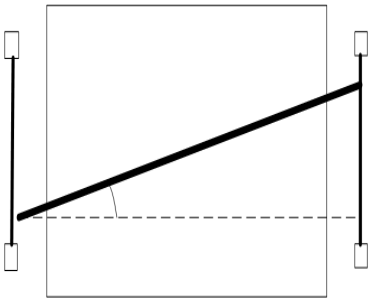

Figure 3.14 Side view for test case 2

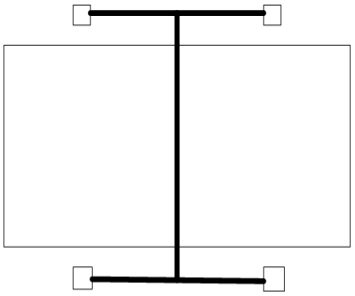

Figure 3.15 Top view for test case 2

The maximum wind speed of 15 m/s was initially carried out to observe if the cable model touches the edges of the windows when vibrating.

Test case 3

Test case 3 was performed on the cable Model 2 with 1.0 cm ice thickness and for the angles $\alpha = 30°$ and $\beta = 15°$; for this case, because of some unavoidable installation errors, a torsional angle exists before the vibration occurs; therefore, when the final torsional

vibration was calculated, the initial torsion was taken into consideration.

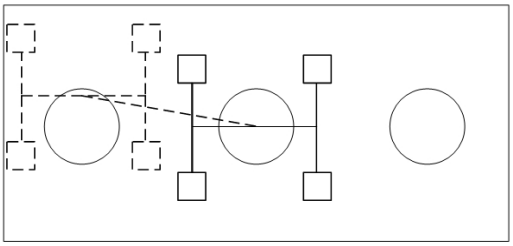

Figure 3.16 Front view for test case 3

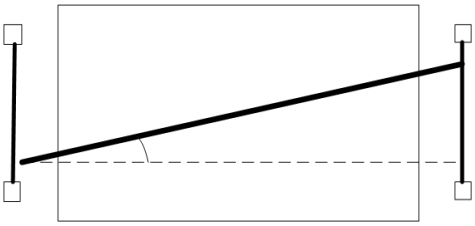

Figure 3.17 Side view for test case 3

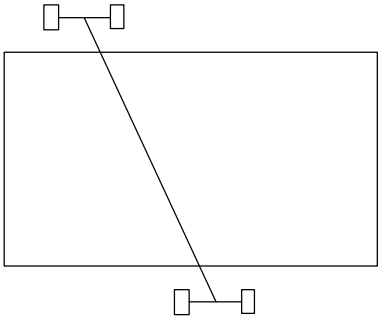

Figure 3.18 Top view for test case 3

Figure 3.16 shows the front view of the third case of the tested cable model 2 for which the model was placed between the middle entrance window and the exit left window, and the T-bars were welded to the cable model with the horizontal angle of 30°; by moving upwards the locations of the springs at the entrance windows, and the springs at the exit window downwards, the vertical angle of 15° was achieved, as presented in the top view and the side view of the model shown in Figure 3.17 and Figure 3.18.

Test case 4

Cable Model 2 was used for test case 4, with 1.0 cm ice thickness; the parameters for test case 4 were $\alpha = 30°$, $\beta = 0°$ and tested wind speeds were from 1.5 m/s to 15 m/s. This case was also used as a benchmark for analyzing the effect of the β angle on the vibration

of the cables.

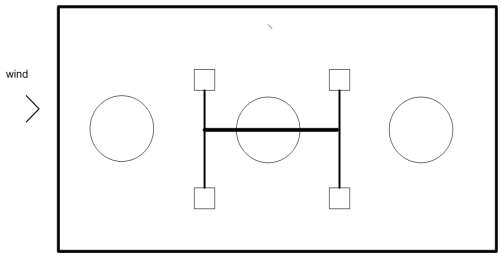

Figure 3.19 Front view for test case 4

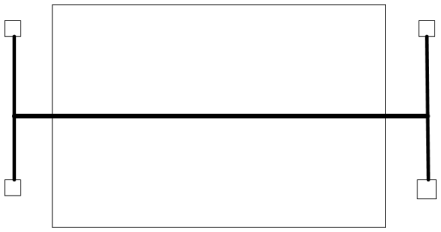

Figure 3.20 Side view for test case 4

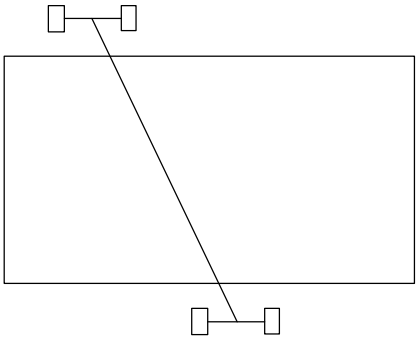

Figure 3.21 Top view for test case 4

Figure 3.19 to Figure 3.21 schematically represent the layout of the cable model for the test case 4, when the model was placed between the middle entrance window and the left exit window as it can be noticed in Figure 3.19 to Figure 3.21. Similar to the previous test cases, the horizontal angle of 30° was obtained by welding the cable model to the T-bars, which were welded to the cable model under a 30° angle, while the location of the springs was not altered because the vertical angle of 0° was required for this test case, as presented in the top and side view of the model shown in Figure 3.19, Figure 3.20 and Figure 3.21.

Test case 5

Cable Model 3, with 1.0 cm ice thickness, was used to observe the vibration motion for test case 5, which was conducted for horizontal and vertical angles of $\alpha = 60°$ and $\beta = 0°$,

respectively, and for the same wind speeds of 1.5 m/s to 15 m/s. In order to achieve the highest value for the horizontal angle of $\alpha = 60°$, the right entrance window and the left exit window were used for supporting the model. This configuration is represented in the front view of Figure 3.22, and the top view of Figure 3.23. It can also be noticed that the vertical angle β was 0° according to the side view in Figure 3.24.

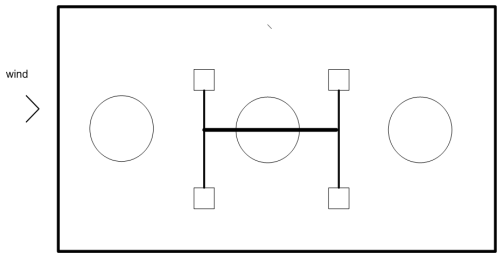

Figure 3.22 Front view for test case 5

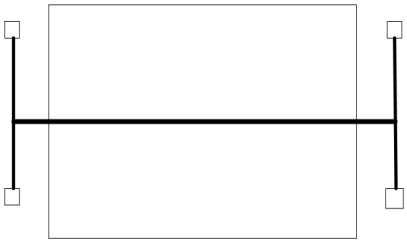

Figure 3.23 Side view for test case 5

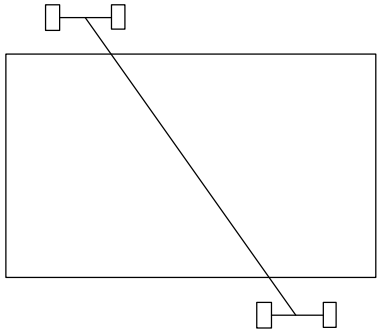

Figure 3.24 Top view for test case 5

Test case 6

Cable Model 3 with 1.0 cm ice thickness was used for test case 6, having the parameters of $\alpha = 60°$, $\beta = 15°$, and wind speeds between 1.5 m/s and 15 m/s. For this case, the initial torsion displacements should be taken into consideration, and also the initial vertical displacement for the two laser sensors should be carefully calibrated because there might be some differences when measurements are performed due to the alignment of the laser sensors.

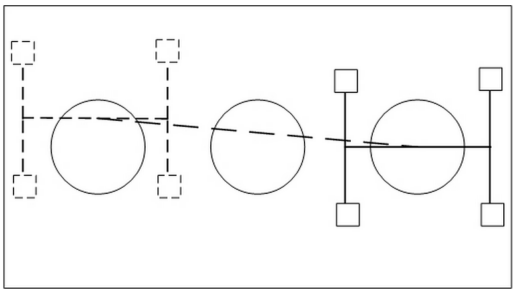

Figure 3.25 Front view for test case 6

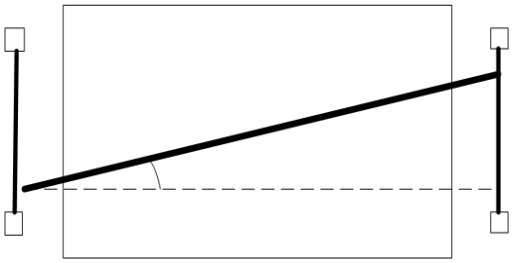

Figure 3.26 Side view for test case 6

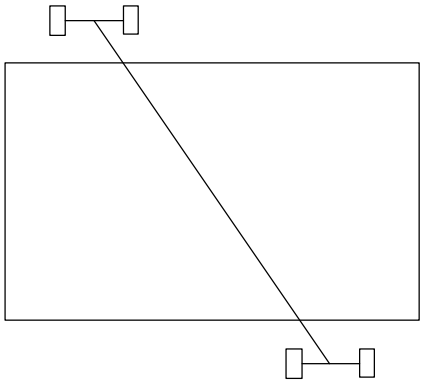

Figure 3.27 Top view for test case 6

Figures 3.25 and 3.27 represent the front and side views of the cable model in the wind tunnel, for the test case 6 configuration. Similar to the previous test cases, the horizontal and vertical angles $\alpha = 60°$ and $\beta = 15°$ were achieved by inclining the welded connection between the model and the T-bar, and by moving the location of the springs on both sides of the wind-tunnel testing section.

Test case 7

The tested specimen was cable Model 3; however, in this case the 2.0 cm ice thickness was modelled for the horizontal and vertical angles of $\alpha = 0°$, $\beta = 0°$. Actually, the cable model layout and the testing parameters are the same as those described at the test case 1 above, and only the ice-profile thickness was changed. Figures 3.15 to Figure 3.17 representing test case 1, are also representative for the configuration of the current case.

Also, test case 7 was also used as a benchmark for results comparison.

Test case 8

Test case 8 corresponds to the test case 4, for which Model 2 with inclinations of $\alpha = 30°$, $\beta = 0°$ was used, however for the test 8, the 2.0 cm ice thickness was tested. Therefore, reference from Figure 3.19 to Figure 3.21 can be made for the details describing the layout of the cable model in the wind tunnel. The reason for selecting the same configuration but with a different ice profile was to determine the effect of the ice-accretion dimensions, and to present more cases for a better comparison with 1.0 cm ice thickness cases.

Test case 9

Cable Model 3 was used for test case 9, after removing the initial ice profile and replacing it with 2.0 cm ice thickness. The testing angles were $\alpha = 0°$, $\beta = 15°$, which correspond to test case 2 described above; therefore, Figure 3.13 to Figure 3.15 can also represent the configuration described for the current test case. Due to the installation of the model, it was noticed that there is an initial difference in the vertical displacement and in the initial torsion, which was measured and taken into consideration when the plotting of the data was performed (Figure 3.28).

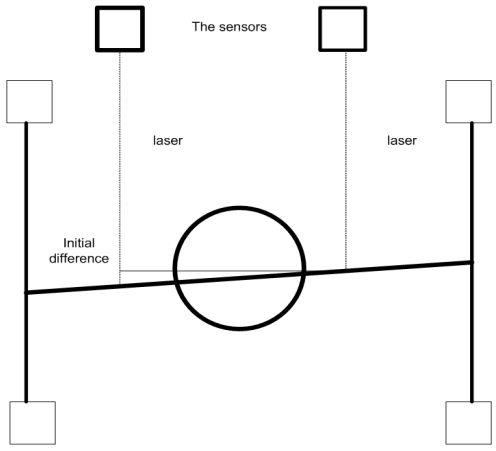

Figure 3.28 The initial difference for vertical displacement

3.5 Data collection and analysis

Data has been collected for the vertical and torsion displacements under various wind speed conditions. For better observation, the displacement units were chosen as ‘mm’ for the vertical displacement, and ‘degrees’ were used as the unit for the torsion; the unit of the wind speed is ‘m/s.’

Two displacement sensors were installed at the two ends of the T-bars that support the cable model; the distance between the two sensors was recorded before each individual case was performed, because each had a different distance between the sensors, and these distances are very important for the calculation of the torsional angle.

Figure 3.29 The displacement sensors used in the wind tunnel

Figure 3.29 shows the two types of laser sensors used in the wind tunnel test. For the best accuracy of the data recorded by the two sensors, calibration is needed at the beginning of each test, even after each test case was finished, because some unexpected factors could affect the reading distances between the model and the sensors. Therefore, the calibration was conducted before each case was performed and after each case was finished. Glue and adhesive plaster were used to attach the sensor on the edges of the wind tunnel wall, and to ensure the lasers are perpendicular to the reading plates mounted on the cable, paper was used to pad the sensors.

Table 3.2 Output at 15 m/s wind speed for α = 0° β = 0° with 2.0 cm ice thickness

	Displacement		Displacement		Displacement	Inclination
	Calibrated Values		Initial data		At centre	
	[26] mm	[27] mm	A	B	D	E
1	133.75	122.02	0.4302	-0.6119	-0.085	3.87
2	133.82	122.06	0.5002	-0.5719	-0.035	3.98
3	133.92	122.04	0.6002	-0.5919	-0.005	4.42
4	133.62	122.07	0.3002	-0.5619	-0.13	3.20
5	134.02	122.15	0.7002	-0.4819	0.11	4.38
6	133.83	121.72	0.5102	-0.9119	-0.2	5.27
7	133.79	122.07	0.4702	-0.5619	-0.09	3.83
8	133.88	122.11	0.5602	-0.5219	0.04	4.01
9	133.77	122.02	0.4502	-0.6119	-0.16	3.94
10	133.68	121.99	0.3602	-0.6419	-0.14	3.72

As an example, the output data for the measured vertical displacements, for the cable model with 2.0 cm ice thickness at α = 0° β = 0° and 15 m/s, is listed in Table 3.2. As mentioned above, the observation and record started from a wind speed of 1.5 m/s and was raised until 15 m/s at intervals of 1.5 m/s; for each case, each output had recorded at least 300 points. The calibrated value of the displacement measured by the sensors was obtained based on the original distance between the sensors and the vertical and torsional displacements obtained from the cable models for the free vibrations; therefore, the displacement was calculated by using the mathematical method from the calibrated value of the displacement and original distance presented below. Thus, for example, the initial data obtained for the displacements recorded by the sensors, as represented in Table 3.2 from A1 to A10, and from B1 to B10. Now notation ‘A’ is used to represent the data from A1 to A10 and ‘B’ is used to represent the data from B1 to B10. Only the first 10-point

values were considered here for the simplicity of the described example.
The displacement of the centre of the bar was determined as follows:

$$D=\frac{A+B}{2} \quad \text{(Eq. 3.4)}$$

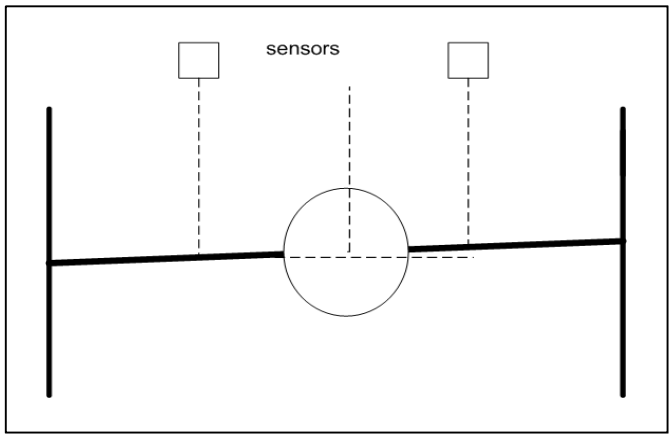

Figure 3.30 The point of average displacement for the cable model centre

The schematic configuration of the averaged displacement at the centre of the cable model is represented in Figure 3.30. The average value for the n number of data points that were recorded for the time history is estimated as follows:

$$D_{average} = \frac{D_1+D_2+\cdots D_n}{n} \quad \text{(Eq. 3.5)}$$

As mentioned before, the distance between the sensors is recorded separately for each case, and for the current case the distance between the two sensors was 7.7 cm.
Therefore, the correction angle γ was obtained as follows:

$$\gamma = \arctan\left(\frac{A-B}{7.7}\right) \quad \text{(Eq. 3.6)}$$

The average of γ was:

$$\gamma_{average} = \frac{\gamma_1+\gamma_2+\cdots+\gamma_n}{n} \quad \text{(Eq. 3.7)}$$

The recorded time history for the n of points for the calibrated averaged vertical displacement is represented in Figure 3.31.

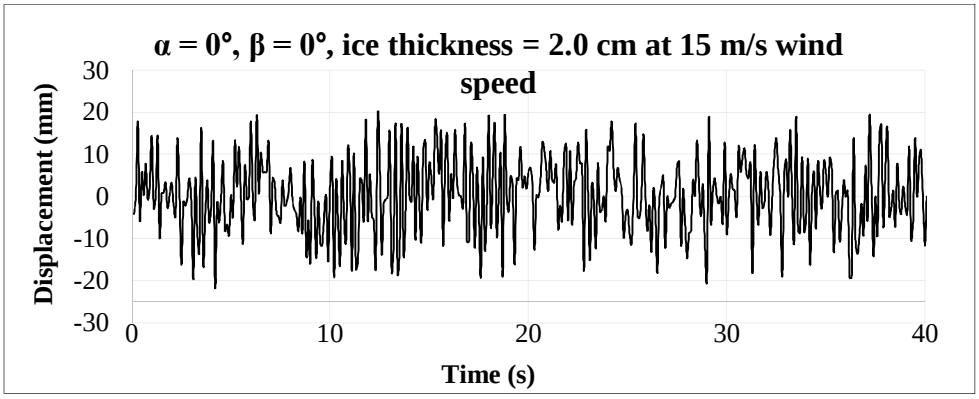

Figure 3.31 The calibrated vertical displacement at high wind speed with α = 0° β = 0°, 2.0 cm ice thickness

The maximum displacement could determine the critical instability of the cable model, and for the general case of data interpretation and in order to have a better analysis of the experiment, the average value of every time history was also plotted in Figure 3.32.

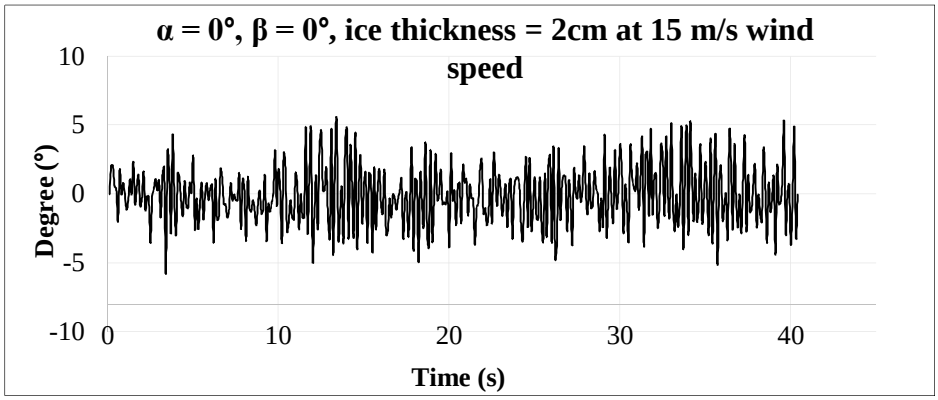

Figure 3.32 The calibrated torsional displacement at high wind speed for α = 0° β = 0° for 2.0 cm ice thickness.

3.6 Free vibration test

The model is supported on both ends with a total of eight springs on each side; two springs are hung on the top and bottom sides of the model, respectively, and the elastic constant k is 1.5 N/m for each spring. The mass for the Model 1 was 0.5 kg, and the thicknesses of the ice were 1.0 cm and 2.0 cm. therefore the natural frequency of the model could be determined by Eq. 3.8:

$$f_n = \frac{1}{2\pi}\sqrt{\frac{k}{m}} \qquad \text{(Eq. 3.8)}$$

Where k is the equivalent stiffness of the spring and m is the total mass of the model.
Also before conducting the test, the cable model was allowed to vibrate freely, in zero wind conditions. The Fast Fourier transformation (FFT) was used on the recorded time history, for further frequency analysis.

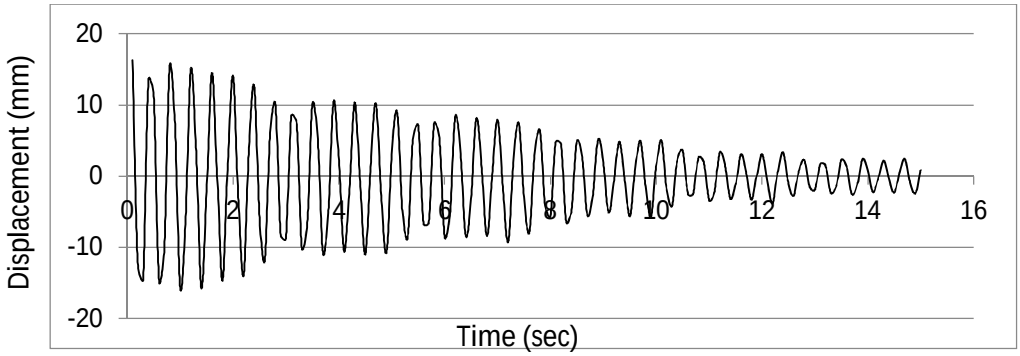

Figure 3.33 Free vibration for Model 1

The free vibration test performed for the vibration of the model placed in the wind tunnel, at 0 m/s wind speed. Based on the time history of the displacement recorded, FFT was performed through a Matlab code for Model 1 and the free vibration frequency was determined.

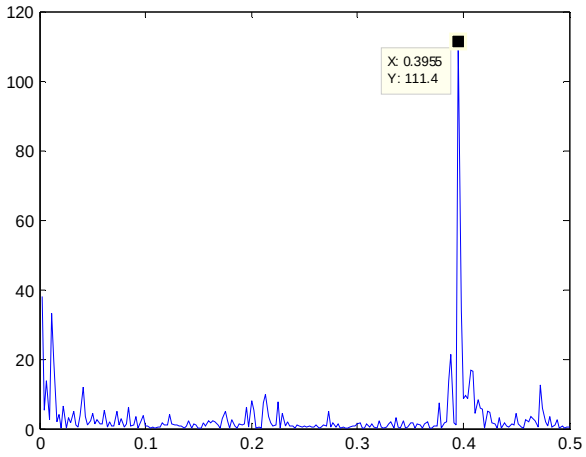

Figure 3.34 Free vibration frequency for Model 1 (Hz)

Figure 3.34 presented the free vibration frequency for the model; the frequency obtained through the FFT procedure was 0.3955 Hz. Using the mass of Model 1 as 0.5 kg in Eq. 3.8, the free vibration frequency of the model could be calculated as follows:

$$f_n = \frac{1}{2\pi}\sqrt{\frac{k}{m1}} = \frac{1}{6.28} \times \sqrt{\frac{3}{0.5}} = 0.39 \text{ Hz} \qquad \text{(Eq. 3.9)}$$

Thus the free vibration frequency Model 1, which is in good agreement with the value plotted in Figure 3.34 was 0.39 Hz.

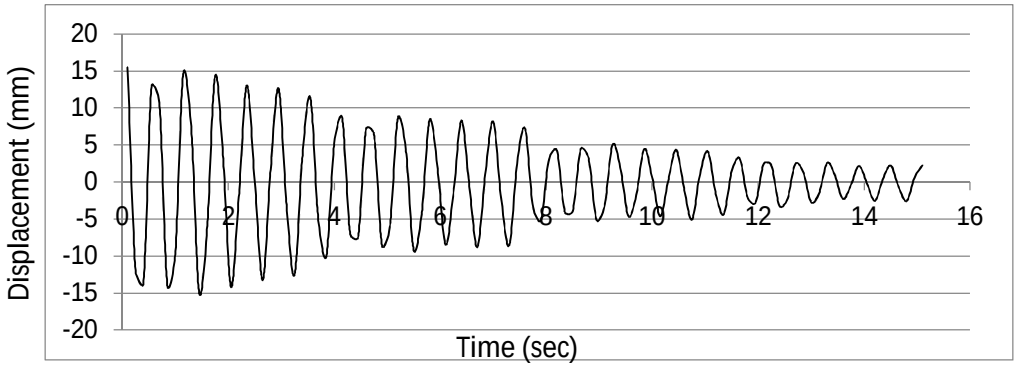

Figure 3.35 Free vibration for model 2

Based on FFT (Fast Fourier Transform) the free vibration frequency was determined for vertical displacement.

Matlab was used to analyze the FFT; the frequency of vortex shedding is gained. Figure 3.35 shows the free vibration for model 2, and the free vibration frequency can be gained through the value from Figure 3.36.

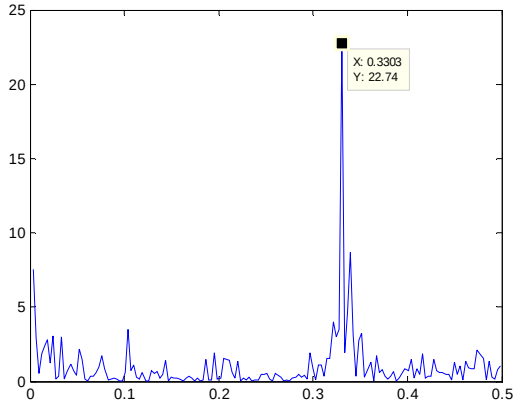

Figure 3.36 Free vibration frequency for Model 2

A similar procedure was undertaken for determining the free vibration frequency of the Model 2. The peak of the plot in Figure 3.36 is the frequency of the vertical displacement obtained after applying the FFT to the recorded time history of the vertical displacement. The free vibration frequency for the model 2 was 0.3303 Hz as shown in Figure 3.36. If Eq. 3.8 is applied, considering the mass of Model 2 as 0.7 kg, then the free vibration frequency can be calculated as follows:

$$f_n = \frac{1}{2\pi}\sqrt{\frac{k}{m2}} = \frac{1}{6.28} \times \sqrt{\frac{3}{0.7}} = 0.33 \text{ Hz} \qquad \text{(Eq. 3.10)}$$

The natural frequency value of 0.33 Hz calculated from the Eq. 3.10 is in good agreement with the measured free vibration frequency shown in Figure 3.36, which was obtained from the FFT transformation of the recorded vertical displacement data.

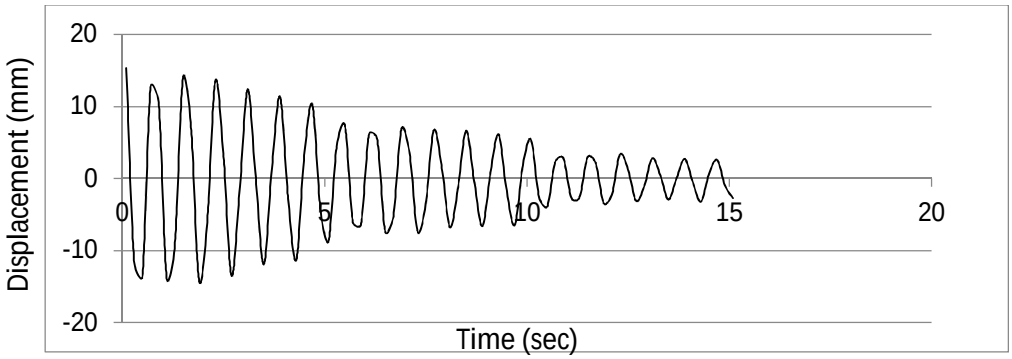

Figure 3.37 Free vibration for Model 3

Figure 3.37 presents the recorded displacement for the free vibration test of Model 3, which is the vibration motion at 0 m/s wind speed.

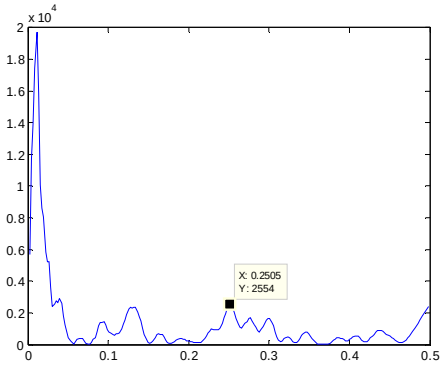

Figure 3.38 Free vibration frequency for model 3

The free vibration frequency for Model 3 is plotted in Figure 3.38. For this case it could be estimated that because of some installation or reading errors existing in the experiment, two peaks or even more could happen during the test, however, the free vibration frequency could be identified in Figure 3.38, and the recorded value of free vibration frequency for Model 3 was 0.2505 Hz.

The mass of Model 3 was 0.9 kg, and the natural frequency could be calculated as follows:

$$f_n = \frac{1}{2\pi}\sqrt{\frac{k}{m3}} = \frac{1}{6.28} \times \sqrt{\frac{3}{0.9}} = 0.29\ \text{Hz} \qquad \text{(Eq. 3.11)}$$

Therefore the frequency calculated as 0.29 Hz for the Model 3 is slightly different than the frequency obtained from the FFT transformation.

In order to establish if the natural frequencies reported for the currently tested cable models are in good agreement with other bridge cable models tested in the wind tunnel, these were compared with the natural frequency reported for other cases [10, 17].

Table 3.3 Comparison of free vibration frequency for the different cable models

Cable without ice (160 mm diameter) [17]	Cable with rain rivulet (139 mm diameter) [10]	Cable with ice (Model 1) (20 mm diameter)
1.414 Hz	0.91 Hz	0.39 Hz

Table 3.3 lists the different free vibration frequencies for several experimental cases reported in the literature for bridge cables tested under dry conditions [17] and rain conditions [10] and these were compared with the natural frequency obtained for the Model 1 tested in the current experiment. It was noticed that the largest natural frequency was reported for a simple cable without ice, which had the biggest diameter as well, while the lowest natural frequency was recorded for the case presented in this study, which had the smallest diameter as well. Therefore the difference in the natural frequency was expected, however it is important to notice that all the natural frequencies of the cable models tested in the wind tunnel were in the close range of 0.39 Hz to 1.414 Hz.

3.7 CFD computational details and simulation procedure

The CFD simulation is used to analyze the effect of incoming wind, at various speeds, on the cable model; the drag and lift coefficients of the aerodynamic static drag and lift forces, are obtained through this process, and the details of the wind flow formations impacting the surface of the cable model can be studied. Wind-induced pressure coefficients on different planes around the model or perpendicular to the model can be visually determined by the figures plotted through the simulation process and the pressure

distribution on the surface of the ice-accreted cable model is thus well understood. The complete description of the CFD simulation results are presented in Chapter 4, only the simulation initial conditions and cable model are described below. The purpose for conducting this simulation is to have a better understanding for the vibrations of the ice-accreted cables due to wind effects. As it will be presented in Chapter 4, the experimental results pointed out that the worst case for the vertical and torsional displacements of the cable model with 1.0 cm ice thickness, was the Test case 6 conducted on Model 3 inclined at $\alpha = 60°$, $\beta = 15°$; the best case for torsional and vertical displacements of the cable with 1.0 cm ice thickness, was the Test case 1 testing the Model 1 inclined at $\alpha = 0°$, $\beta = 0°$. These two cases are selected for performing the CFD simulation at 10 m/s wind speed and 15 m/s wind speed.

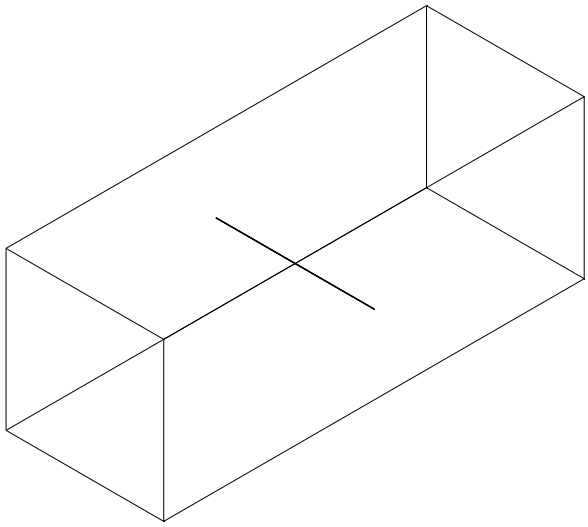

Figure 3.39 The AutoCAD model for case 1 $\alpha = 60°$, $\beta = 15°$, 1.0 cm

The ice-accreted cable model and the simulation domain surrounding the model were created in AutoCAD as shown in Figure 3.39. In order to avoid the influence of the walls, the dimensions of the domain must be much higher than the diameter of the cable. For reproducing the experimental conditions, the cable diameter was modeled as 20 mm, and the dimensions of the domain were 700 mm by 920 mm by 1330 mm as the width, depth and length of the domain. Problems occurred when the model was converted into ANSYS

Fluent for the CFD simulation, and not all the details of the cable and ice profile could be generated; for this reason, it was difficult to model the irregular ice profile attached to the body as an extension, which is the option of drawing the irregular ice in AutoCAD, but is not working when converted to ANSYS Fluent. However, if the ice profile is created by creating an area, of a shape similar to the ice profile, which is then rotated around the a part of the circumference of the cable, then the ice accretion attached on the cable is formed as a solid; merging this solid with the cable model initially developed, would finally create the three-dimensional body of the ice accreted cable, that can be converted to ANSYS Fluent. This was the solution employed for creating the current ice-accreted models and for converting them to ANSYS software. Therefore, to further analyze the ice accretion profiles in ANSYS, the body obtained by rotating certain area in AutoCAD gave better results for creating the initial models, which were used for the input into ANSYS.

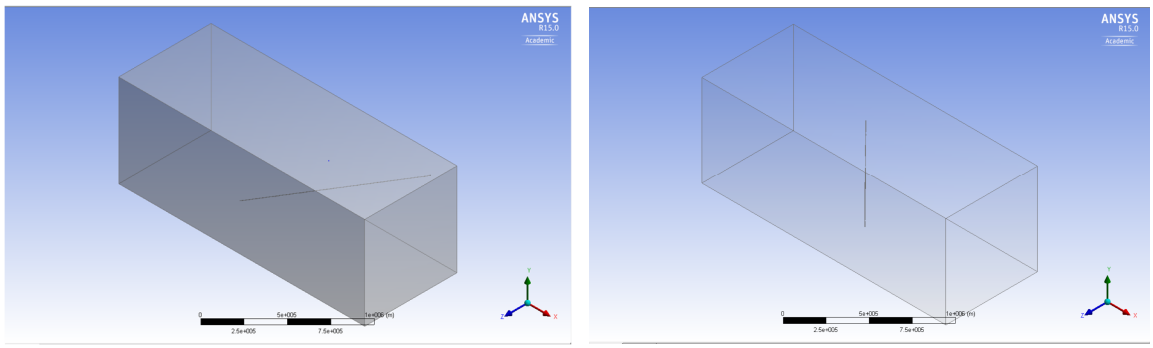

Figure 3.40 The models for case 6 $\alpha = 60°$, $\beta = 15°$ and case 1 $\alpha = 0°$, $\beta = 0°$ in ANSYS before meshing

The ice-accreted cable model was inclined in the box of the domain, and the concept of CFD simulation is to simulate the incoming wind speed starting from one end of the box, overpassing the model and exiting from the other end of the box. With certain modifications applied in AutoCAD, the cable model inside the box was subtracted, so that the cable and the box can become an entire body, with a void shaped as the cable model inside. Thus the flow equations will not be calculated for the interior or on the surface of the model and the ANSYS software will treat it as a solid cable immerged in a fluid. Each side of the domain was named as inlet, outflow, symmetry, cable, each with a

different function and boundary condition. The inlet and outflow planes are where the wind enters and exits the domain, the symmetry is the lateral wall of the domain around the cable has the property of absorbing the fluid, without bouncing back towards the model, and the cable which is the model inside the box and has no-slip, no-penetration conditions defined at its surface; additionally, 10 m/s and 15 m/s wind speeds are selected as input velocities for the CFD simulation.

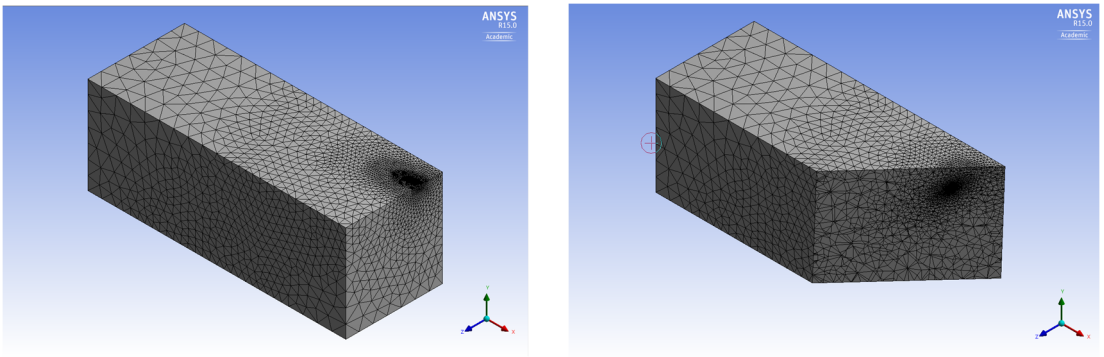

Figure 3.41 The model for case 6 α = 60°, β = 15° after meshing

Around 1.7 million tetrahedral cells were used for the mesh process of case 6, and 1.5 million tetrahedral cells are used for case 1. It should be mentioned that the number of the cases was preserved as per the test cases number described in section 3.4 above. The mesh at the surface of the cable model was much thinner than the mesh for the rest of the domain. Thus, on the top of the box, where the cable intersects the domain, an area of denser mesh can be noticed (Figure 3.41). Also Figure 3.41 shows the inside of the box, and the trace of the cable at a given cross-section.

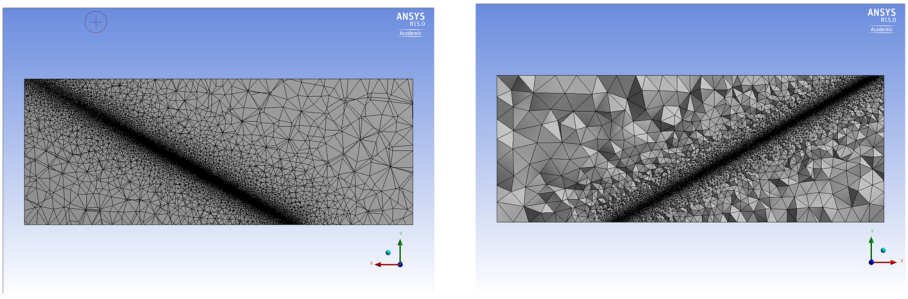

Figure 3.42 The cable detail for case 6 α = 60°, β = 15°

Material has been chosen as steel for the cable, shown in the cross-section taken along the length of the cable model in Figure 3.42; more mesh elements were used around the entire circumferences of the cable to obtain more accurate pressure results in this area.

Table 3.4 The CFD simulation cases

Cases	The inclination angle (°)	Number of elements (10^7)	10 m/s wind speed	15 m/s wind speed
Case 6	$\alpha = 60°, \beta = 15°$	1.7	Yes	Yes
Case 1	$\alpha = 0°, \beta = 0°$	1.5	Yes	Yes

Table 3.4 lists the cases performed in the CFD simulation for both 10 m/s wind speed and 15 m/s wind speed.

In conclusion, the main purpose of this chapter is to describe the experiment setup and CFD simulation procedure. The illustrations of this chapter have shown the ice profiles around the cable for 1.0 cm and 2.0 cm ice thickness, the wind tunnel and the mechanical room. The test cases and the steps carried out for performing the experiment along with the procedure employed for the CFD simulation were shown; the model created in AutoCAD for the CFD simulation was described in detail, and free vibration frequency was verified with the FFT transform employed through the Matlab code.

The analysis of the measured data from the experiments and the interpretation of the results obtained from the CFD simulations constitute the foundation of Chapter 4.

Chapter 4 Wind-induced response for ice-accreted cables

The incoming wind flow acting on ice-accreted bridge cables induces a response of the model, which is identified as vertical and torsional vibrations. For most of the wind speeds, the vibrations do not register high amplitudes, however when the wind speeds increase and reaches a critical value, the vertical vibration, in the across-wind direction also increases and tends to become develop into unstable aerodynamic phenomena such as galloping divergent vibration. Besides the wind speed, several other factors can influence the magnitude of the wind-induced vibration response of the ice-accreted bridge cables, namely the angle of attack between the cable and the tested model, the cable damping and natural frequency, and for the case of the current project, the shape of the ice-accreted cable cross-section. Thus the present study has focused on clarifying the effect of the ice profile formed around the cable, and the effect of the relative angle of attack, obtained as a combination between the vertical inclination angle and the horizontal inclination angle of the cable model, in regard to the vertical and horizontal axis of the wind tunnel respectively. Because it was not possible to use the force balance measuring device, the drag and lift aerodynamic coefficients were determined by employing a CFD analysis through the ANSYS commercial software. The vertical and torsional vibrations measurements are presented in the following sections along with their interpretation. From the CFD study, several parameters such as pressure distribution along three planes perpendicular to the ice-accreted cable and the aerodynamic drag and lift coefficients were collected and the galloping verification was conducted based on the DenHartog criterion. The critical galloping on-set wind speeds were obtained and were compared with those obtained from the experimental vibration results.

4.1 Vertical and torsional vibrations

The torsional and vertical vibrations for all the investigated cases, are presented in Figures 4.1 to 4.9, starting with the cable model with ice accretion profile of 1.0 cm and following with the 2.0 cm ice profile. The vibrations were recorded for wind speeds from 1.5 m/s to 15 m/s at intervals of 1.5 m/s, however due to the high number of figures

required, only the results for 4.5 m/s and for 15 m/s are discussed in detail in this chapter, while the results for the rest of the tested wind speeds are included in Appendix A. The natural frequency of each of the three cable models were determined through the free-vibration tests conducted at 0 m/s wind speed, as presented in section 3.5 above. The average value for the vibration amplitudes is considered from each vertical and rotational vibration time history, and by summarizing the displacements at different times, the average vertical and torsional displacement was determined, and these were presented in Figures 4.1 to 4.9, for all the investigated cases.

4.1.1 Case 1 $\alpha = 0°$, $\beta = 0°$ with 1.0 cm ice thickness

Figures 4.1. a)-d) represent the vertical and torsional vibration displacements for the case $\alpha = 0°$, $\beta = 0°$ with 1.0 cm ice thickness, tested at both a low wind speed of 4.5 m/s and a high wind speed of 15 m/s.

The maximum vertical displacement of the ice-accreted cable with ice thickness of 1.0 cm, tested at 4.5 m/s wind speed was 9.08 mm and was registered towards the end of the time history, as it can be noticed in Figure 4.1 a), while for the beginning of the recorded displacement time history the values of the vertical vibrations tended to be smaller, registering some sudden increments only at specific points, but finally the vibrations become stable, and the average value for the entire time history could be considered based on the entire data recorded. For Figure 4.1 b) the maximum vertical amplitude of the same model at 15 m/s wind speed was 23.924 mm and was registered at 8.4 s. From 13.7 s to 16.4 s, the amplitudes for the vertical displacements are relatively small compared with other time intervals, however the vibration is stable, and the average value for the vertical displacement of the model at 15 m/s wind speed can be determined as 14.48 mm.

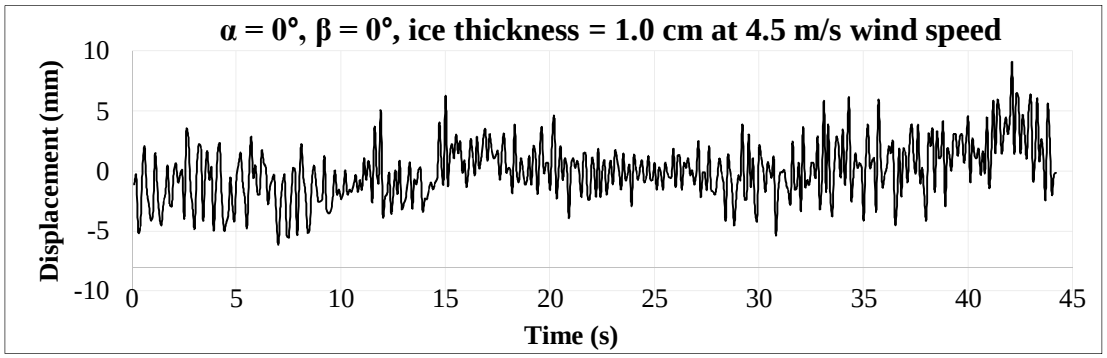

a) Vertical displacement for ice-accreted cable model α = 0°, β = 0°, 1.0 cm ice thickness at 4.5 m/s

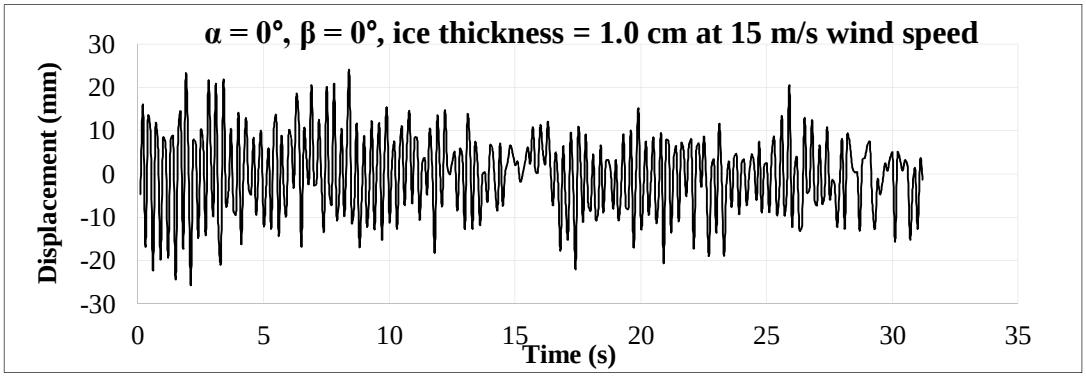

b) Vertical displacement for ice-accreted cable model α = 0°, β = 0°, 1.0 cm ice thickness at 15 m/s

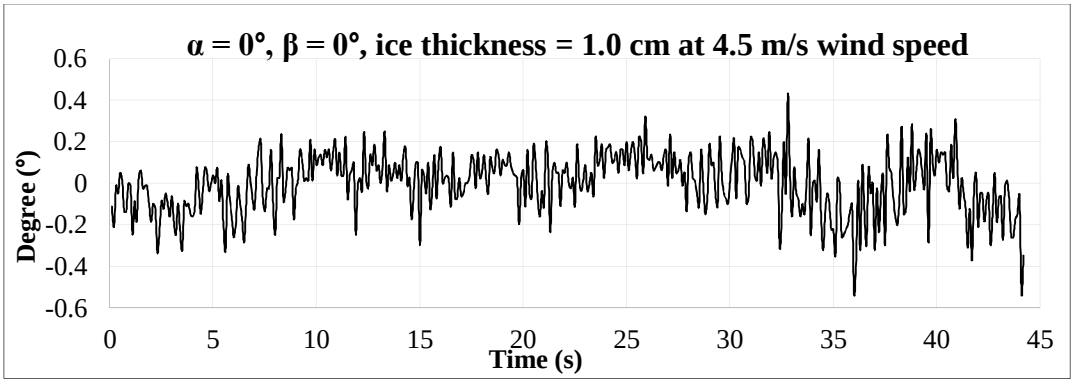

c) Torsional displacement with α = 0°, β = 0°, 1.0 cm ice thickness at 4.5 m/s

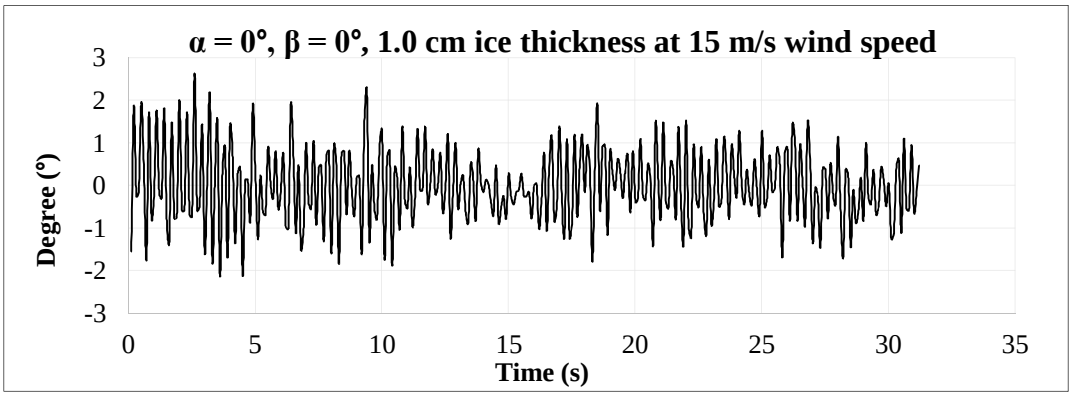

d) Torsional displacement with α = 0°, β = 0°, 1.0 cm ice thickness at 15 m/s wind speed

Figure 4.1 Time displacement history for vertical and torsional displacements for case 1: α = 0°, β = 0° with 1cm ice thickness

The maximum torsional displacement is shown in Figure 4.1 c) as 1.3° at 32.8 s; the general trend of the vibration is fluctuating, however the sudden increase of amplitude registered are very low in magnitude, thus the average amplitude for 4.5 m/s wind speed is only 0.59°. In Figure 4.1 d), the maximum displacement for torsional vibrations registered at 15 m/s wind speed can be noticed as having much higher amplitudes, of maximum 2.63° at 2.6 s; the vibration tends to occur in waves, with periods of high amplitudes which stabilize temporarily and then increase immediately after. These type of vibrations are called "beats" and are specific for the galloping response encountered at high wind speeds [48]. During the test for this case, the average value of the torsional vibration amplitudes at 15 m/s wind speed was 1.95°. In general, the structures with circular cross-section do not encounter galloping, however, as pointed out in the previous chapter the ice accretion attached at the surface of the cable changed the geometry of the cross-section [11], and thus, as the current experimental results indicated, galloping can be encountered.

4.1.2 Case 2 α = 0°, β = 15° with 1.0 cm ice thickness

The vertical and torsional displacement vibrations for Case 2 when the cable model was inclined at α = 0°, β = 15° and had 1.0 cm ice thickness are presented for both wind speeds of 4.5 m/s and 15 m/s in Figures 4.2 a) to 4.2 d)

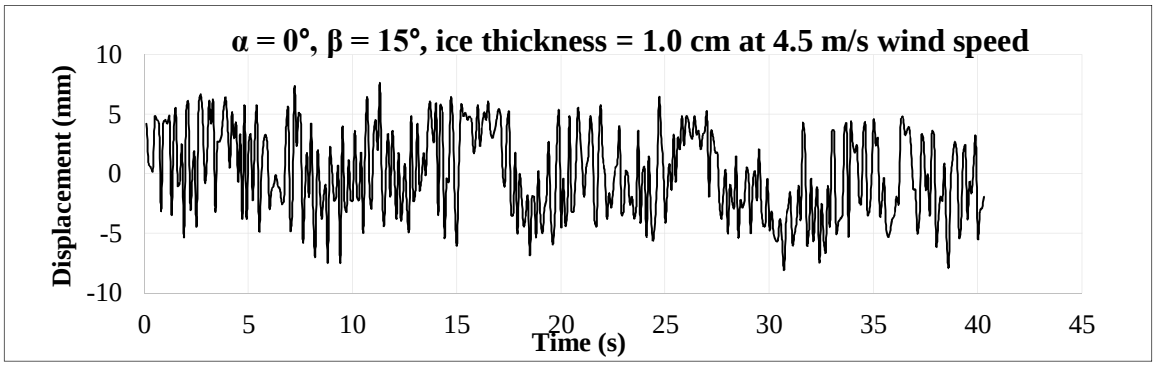

a) Vertical displacement for ice-accreted cable model α = 0°, β = 15°, 1.0 cm ice thickness at 4.5 m/s

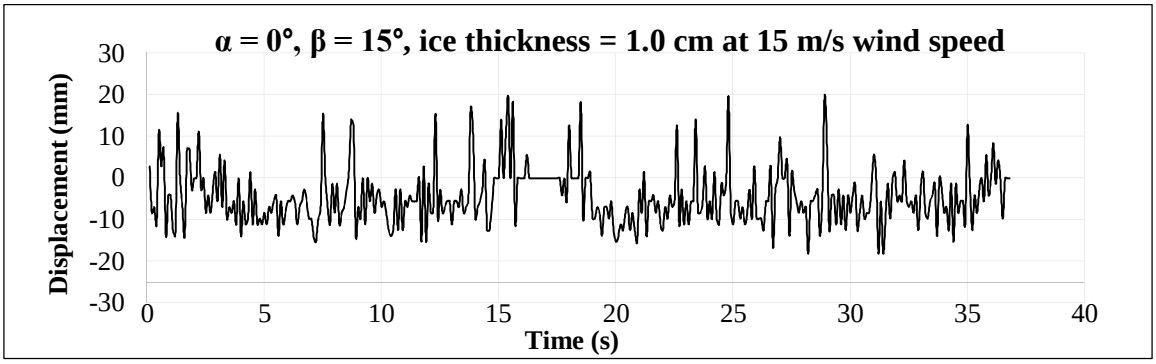

b) Vertical displacement for ice-accreted cable model α = 0°, β = 15°, 1.0 cm ice thickness at 15 m/s

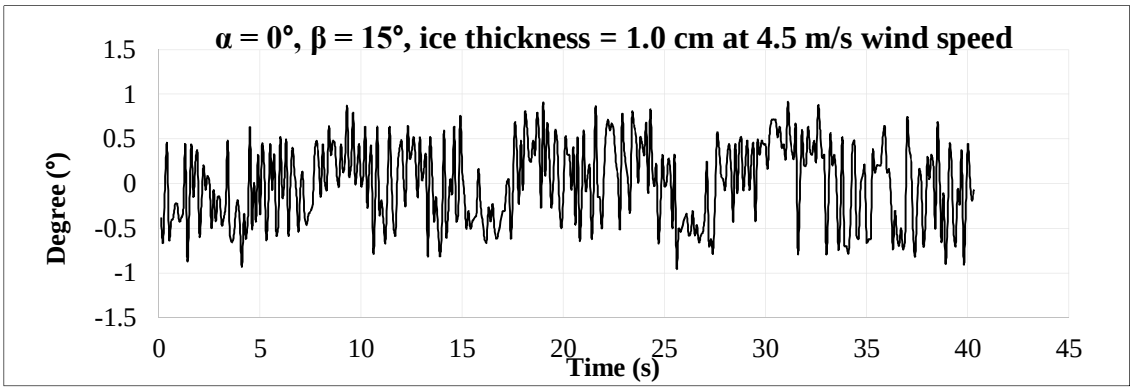

c) Torsional displacement for ice-accreted cable model α = 0°, β = 15°, 1.0 cm ice thickness at 4.5 m/s wind speed

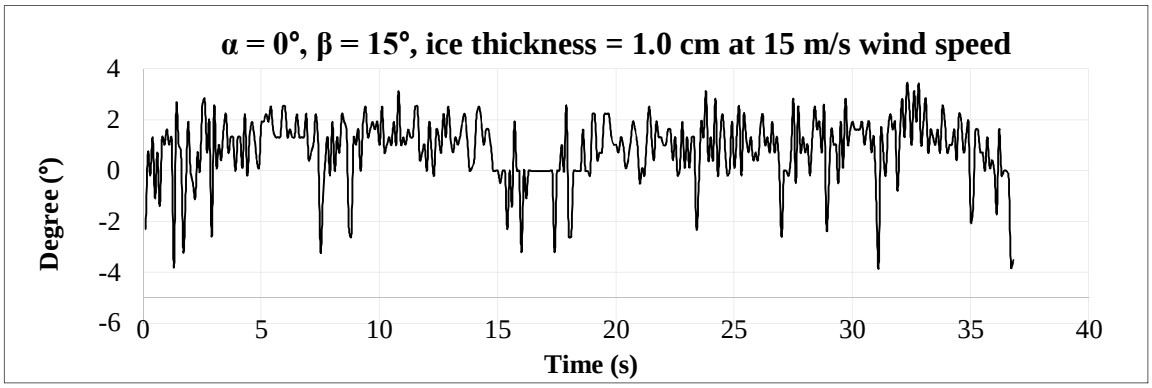

d) Torsional displacement for ice-accreted cable model α = 0°, β = 15°, 1.0 cm ice thickness at 15 m/s wind speed

Figure 4.2 Time displacement history for vertical and torsional modes of case: α = 0°, β = 15° with 1.0 cm ice thickness

For Case 2, for α = 0°, β = 15°, ice thickness = 1.0 cm at 4.5 m/s wind speed, Figure 4.2 a) shows several sudden vibration amplitude increments which occurred during the test, and could be noticed that the maximum displacement of the vertical vibration was 7.6 mm at 11.3 s. The average vertical displacement was 4.39 mm. In Figure 4.2 b) the vertical vibration for the same case but tested at 15 m/s wind speed shows that from time 16 s to time 18 s, the vibration does not occur, but several high peaks occurred for the vertical vibration during the experiment; thus the vibrations resemble the beats vibrations, however it cannot be clearly concluded that this was the galloping response. The maximum value of the displacement for the vertical vibration recorded at 15 m/s was 19.656 mm, and the average value was 16.23 mm. In Figure 4.2 c) the maximum torsional displacement for case 2 at α = 0°, β = 15°, 1.0 cm ice thickness at 4.5 m/s wind speed, can be noticed as 0.79°at 9.6 s, and the average value which was considered for the displacement comparison was 0.91° at 19 s. In Figure 4.2 d) drastic increments were noticed during the test, for case 2 at α = 0°, β = 15°, ice thickness of 1.0 cm at 15 m/s wind speed, with the maximum value for torsional displacement of 3.79° at 31.1 s, and mean value for the displacement for this case of 2.23°. As it can be noticed in Figures 4.2 b) and d) for some parts of the signal the measurements showed zero displacement; this was caused by the beams emitted by the lasers which, temporarily, were unable to reach

the reading sensor installed on the T-bar of the cable, due to exceeding vertical and torsional motions .

4.1.3 Case 3, α = 30°, β = 15° with 1.0 cm ice thickness

Figures 4.3 a) to Figure 4.3 d) represent the vertical and torsional displacements for the test case 3, recorded for the cable model inclined at α = 30°, β = 15° with 1.0 cm ice thickness at both 4.5 m/s and 15 m/s wind speed.

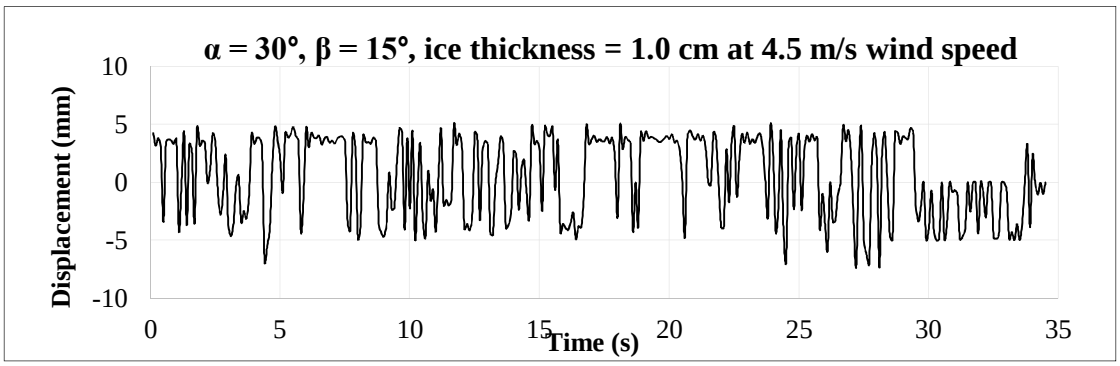

a) Vertical displacement for ice-accreted cable model α = 30°,β = 15°, 1.0 cm ice thickness at 4.5 m/s wind speed

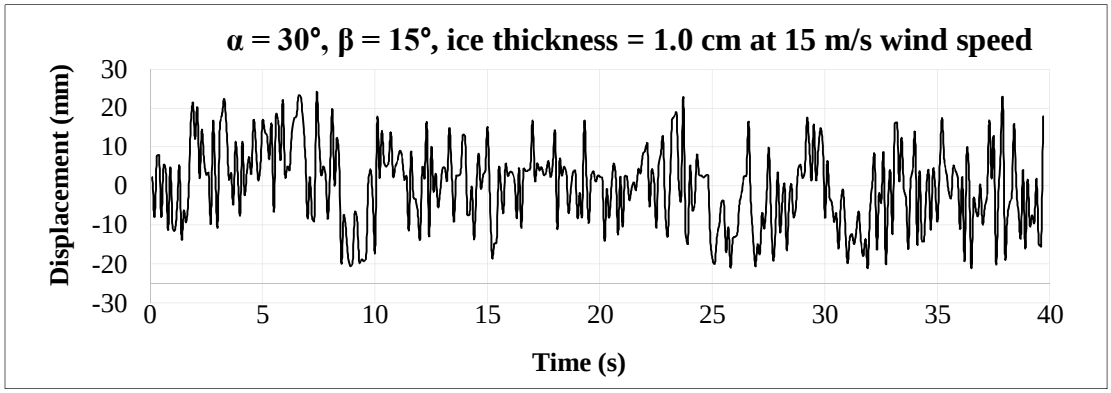

b) Vertical displacement for ice-accreted cable model α = 30°, β = 15°, 1.0 cm ice thickness at 15 m/s wind speed

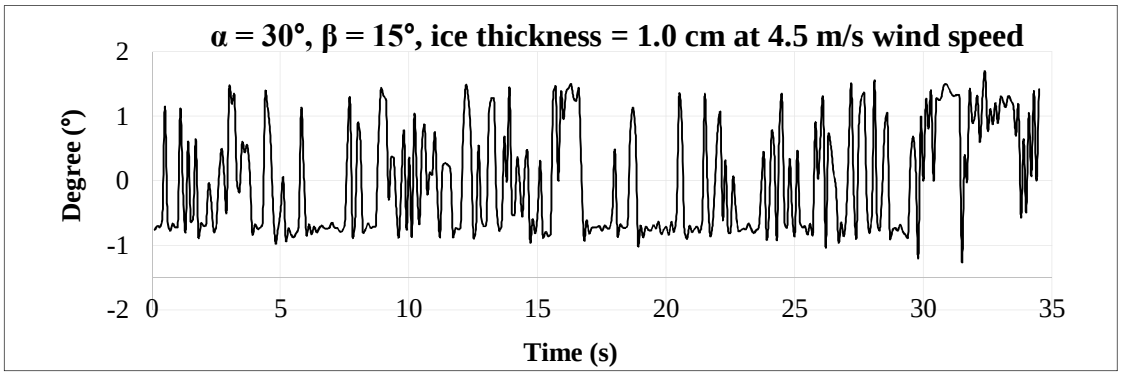

c) Torsional displacement for ice-accreted cable model α = 30°, β = 15°, 1.0 cm ice thickness at 4.5 m/s wind speed

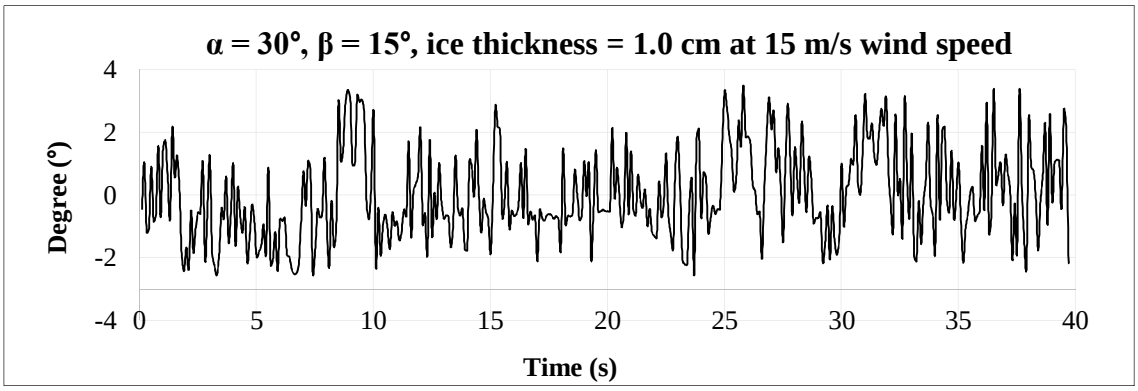

d) Torsional displacement for ice-accreted cable model α = 0°, β = 15°, 1.0 cm ice thickness at 15 m/s wind speed

Figure 4.3 Time displacement history for vertical and torsional modes of case:α = 30°，β = 15° with 1.0 cm ice thickness

In Figure 4.3 a), the results for Case 3, of the model inclined at α = 30°, β = 15°, having an ice thickness of 1.0 cm are presented for 4.5 m/s wind speed; it was noticed that the maximum value for the vertical vibration was 7.06 mm at 27.7 s, and the average value for this case was 4.87 mm. In Figure 4.3 b) the vertical vibrations for the same model (Case 3 at α = 30°, β = 15°, ice thickness = 1.0 cm) but tested at 15 m/s wind speed, showed that the maximum value for the vertical displacement was 22.88 mm at 23.7 s, and the mean value for this case was 18.23 mm. In Figure 4.3 c), the Case α = 30°, β = 15°, with ice thickness of 1.0 cm tested at 4.5 m/s wind speed, several peaks can be observed with the maximum value for torsional displacement of 1.68° recorded at 32.4 s.

The mean value for this case was 1.1°. Figure 4.3 d) shows the torsional response for the cable model inclined at α = 30°, β = 15°, with ice thickness = 1.0 cm and tested at 15 m/s wind speed, for which the maximum value for the torsional displacement was 3.5° at 25.8 s; the mean value for this case was 2.83°. Thus for the last two cases presented, Case 3 and Case 2, no beats vibrations could be noticed, however highly fluctuating vibrations were recorded for both low and high wind speeds, which might indicate that no galloping but another type of aerodynamic instability, such as "high-amplitude vibrations" (Cheng et al, 2008 [41]) might take place for these horizontally and vertically inclined cables at α = 0°, β = 15° (Case 2), and α = 30°, β = 15° (Case 3).

4.1.4 Case 4 α = 30°, β = 0° with 1.0 cm ice thickness

Vertical and torsional displacements for Case 4, which were measured on the cable model inclined at α = 30°, β = 0°, with 1.0 cm ice thickness at both 4.5 m/s and 15 m/s wind speed are presented in Figures 4.4 a) to 4.4 d).

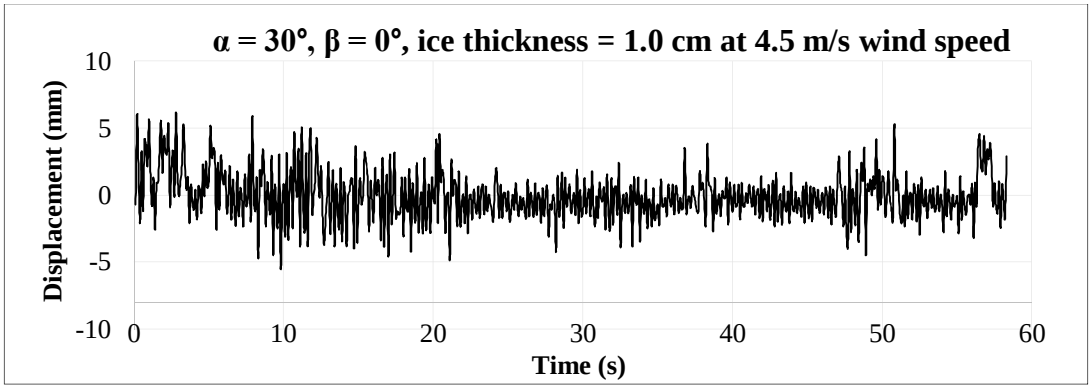

a) Vertical displacement for ice-accreted cable model α = 30°, β = 0°, 1.0 cm ice thickness at 4.5 m/s wind speed

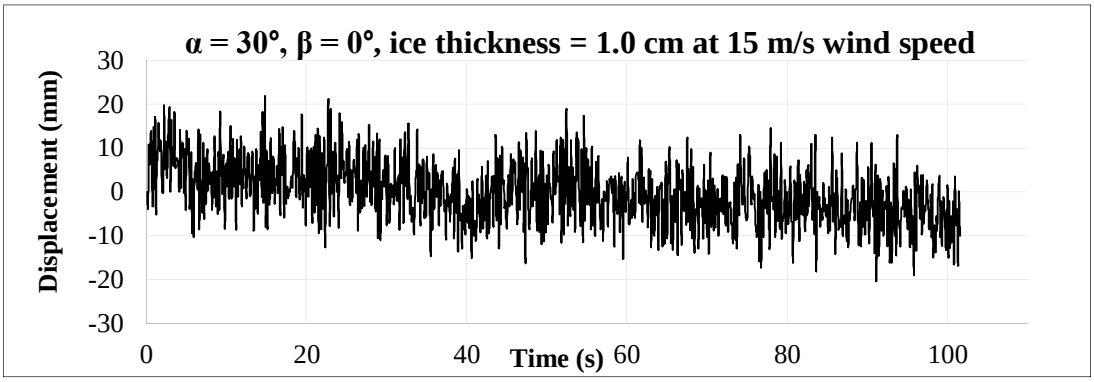

b) Vertical displacement for ice-accreted cable model α = 30°, β = 0°, 1.0 cm ice thickness at 15 m/s wind speed

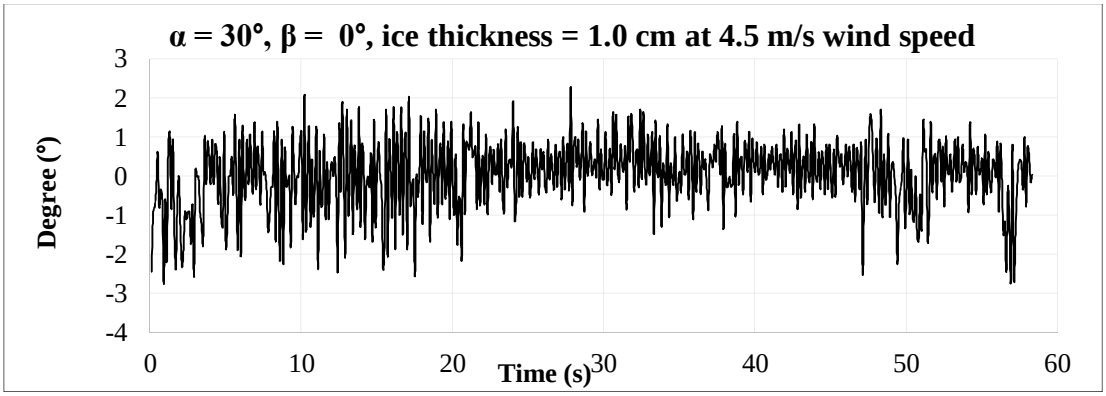

c) Torsional displacement for ice-accreted cable model α = 30°, β = 0°, 1.0 cm ice thickness at 4.5 m/s wind speed

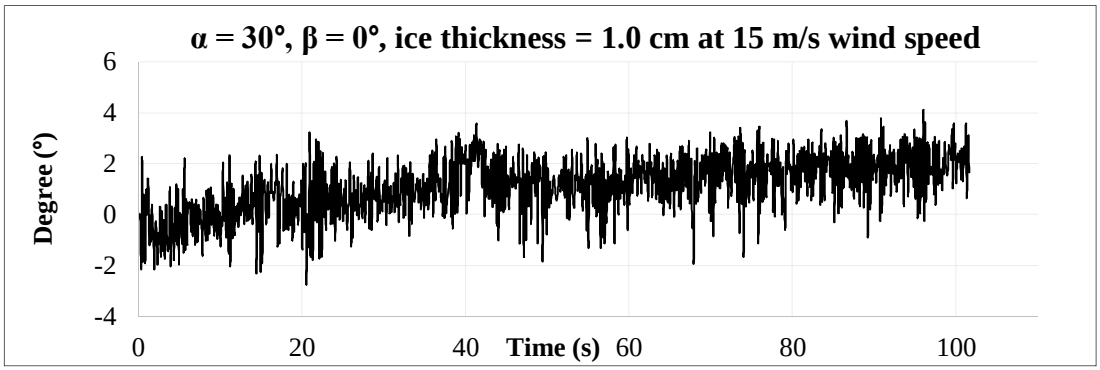

d) Torsional displacement for ice-accreted cable model α = 30°, β = 0°, 1.0 cm ice thickness at 15 m/s wind speed

Figure 4.4 Time displacement history for vertical and torsional modes of case α = 30°, β = 0° with 1.0 cm ice thickness

The maximum vertical displacement recorded for Case 4 at 4.5 m/s wind speed was 5.93 mm, and the average value for the vertical displacements was 5.11 mm, as it can be noticed in Figure 4.4 a). In Figure 4.4 b) is shown the vertical displacement for the same model, at 15 m/s wind speed, for which the maximum amplitude was 21.94 mm at 14.8 s; the vibrations were stable and the average value for the amplitudes was 15.25 mm. For the torsional vibrations, shown in Figure 4.4 c) for 4.5 m/s the maximum amplitude was 2.28 mm at time 27.8 s, with a decreasing tendency thus the average value was 1.13 mm. In Figure 4.4 d), the maximum vibration amplitude for torsional displacement at 15 m/s

was 4.09° at 96 s, and the average torsional vibration displacement was 2.7°. The vibration is steadily increasing, but no strong fluctuations were noticed for this case. The magnitude of the amplitudes was different, however the general trend of the vibrations was similar for both 4.5 m/s and 15 m/s, with small fluctuations and no beats vibrations occurring at higher wind speeds. Thus the aerodynamic instability occurring in this case is the "high-amplitude vibrations" as described by Cheng et al, 2008 [41].

4.1.5 Case 5 α = 60°, β = 0° with 1.0 cm ice thickness

Figures 4.5 a) to Figures 4.5 d) represent the vertical and torsional vibrations for test Case 5 conducted at α = 60°, β = 0° with 1.0 cm ice thickness, for both 4.5 m/s and 15 m/s wind speed.

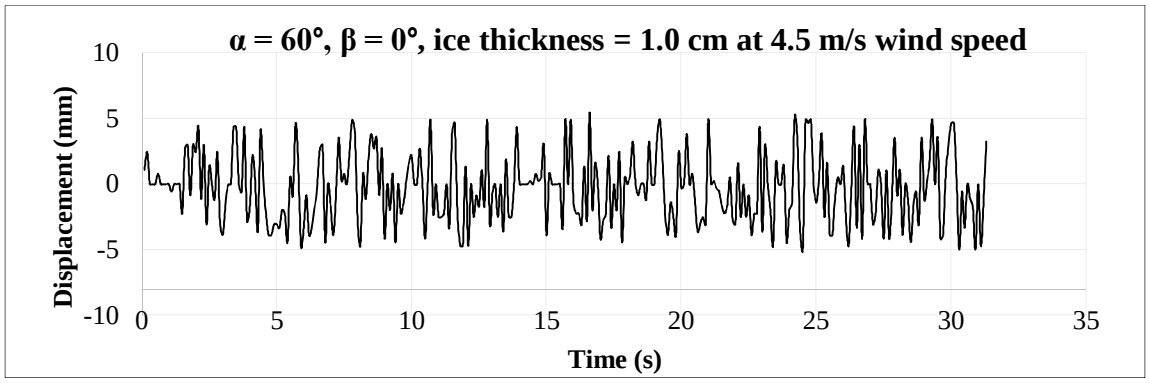

a) Vertical displacement for ice-accreted cable model α = 60°, β = 0°, 1.0 cm ice thickness at 4.5 m/s wind speed

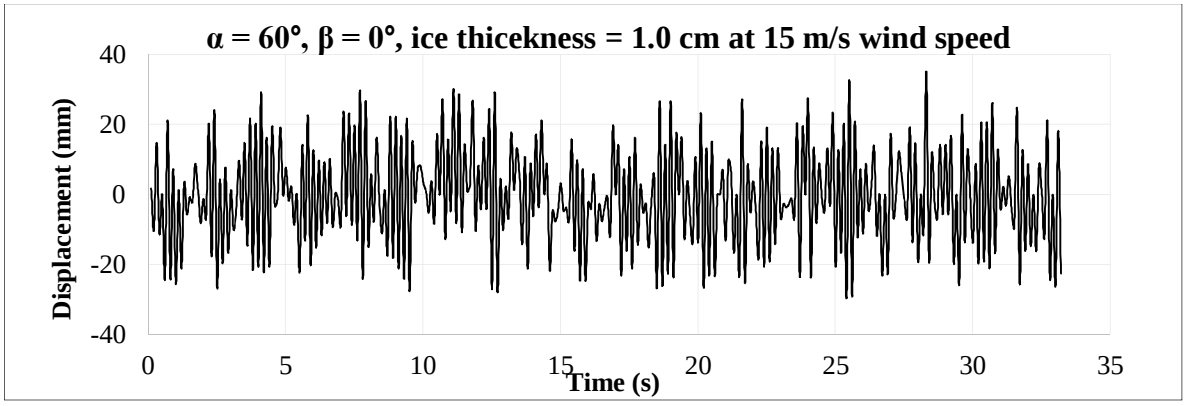

b) Vertical displacement for ice-accreted cable model α = 60°, β = 0°, 1.0 cm ice thickness at 15 m/s wind speed

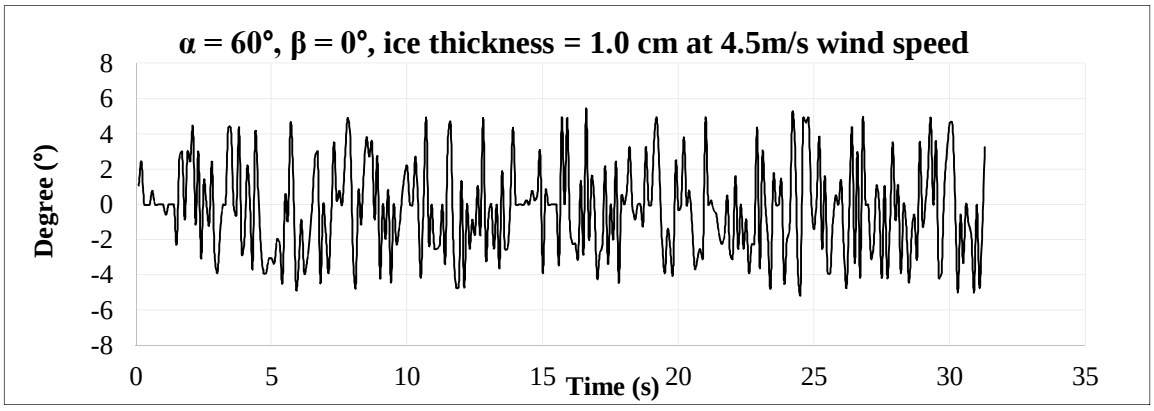

c) Torsional displacement for ice-accreted cable model α = 60°, β = 0°, 1.0 cm ice thickness at 4.5 m/s wind speed

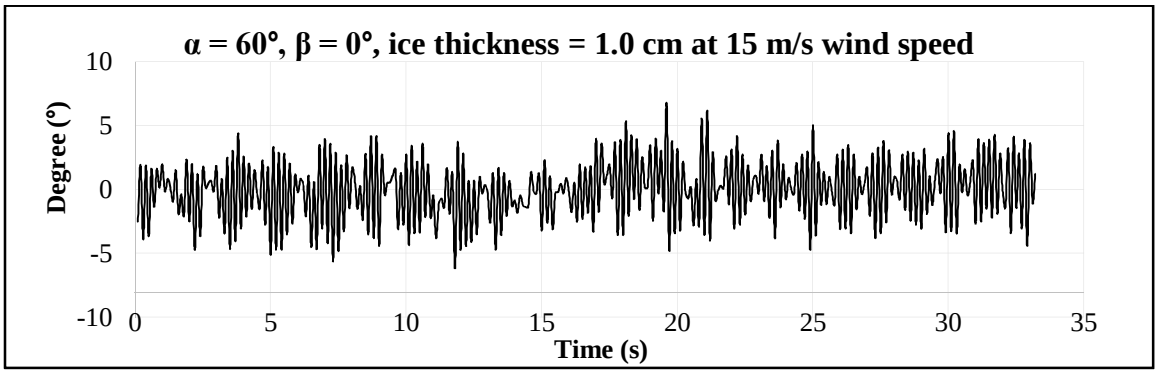

d) Torsional displacement for ice-accreted cable model α = 60°, β = 0°, 1.0 cm ice thickness at 15 m/s wind speed

Figure 4.5 Time displacement history for vertical and torsional modes of case α = 60°, β = 0° with 1.0 cm ice thickness

In Figure 4.5 a) is shown that the maximum vertical vibration amplitude for Case 5 of the model inclined at α = 60°, β = 0° with 1.0 cm ice thickness at 4.5 m/s wind speed was registered as 5.47 mm at 16.6 s, while the average value of the vertical displacement was 5.59 mm. For higher wind speeds of 15 m/s, Figure 4.5 b) shows that the maximum vertical vibration amplitude for Case 5, α = 60°, β = 0° with 1.0 cm ice thickness was 35.3 mm at 28.3 s, and the average value was 17.93 mm. The maximum torsional vibration for test Case 5 at α = 60°, β = 0° with 1.0 cm ice thickness at 4.5 m/s wind speed was 5.4703° and the average value was only 1.1°, as it can be noticed in Figure 4.5 c). From Figure 4.5 d) can be seen that the maximum torsional displacement for the same

case 5 at 15 m/s wind speed was 6.8° registered at 19.6 s. The average value of torsional displacement for the same model tested at 15 m/s wind speed was 3°. It is interesting to note that for this case the vibrations highly fluctuate at low wind speeds, and also beats vibrations, specific to galloping response, can be noticed for high wind speeds of 15 m/s. In general, for bridge stay-cables without ice accretion the inclination of 60° is reported to be critical for wind-induced vibrations [41].

4.1.6 Case 6 α = 60°， β = 15° with 1.0 cm ice thickness

The following Figures 4.6 a) to 4.6 d) show the vertical and torsional displacements for test Case 6 conducted on a cable model at α = 30°, β = 0° with 1.0 cm ice thickness for both wind speeds of 4.5 m/s and 15 m/s.

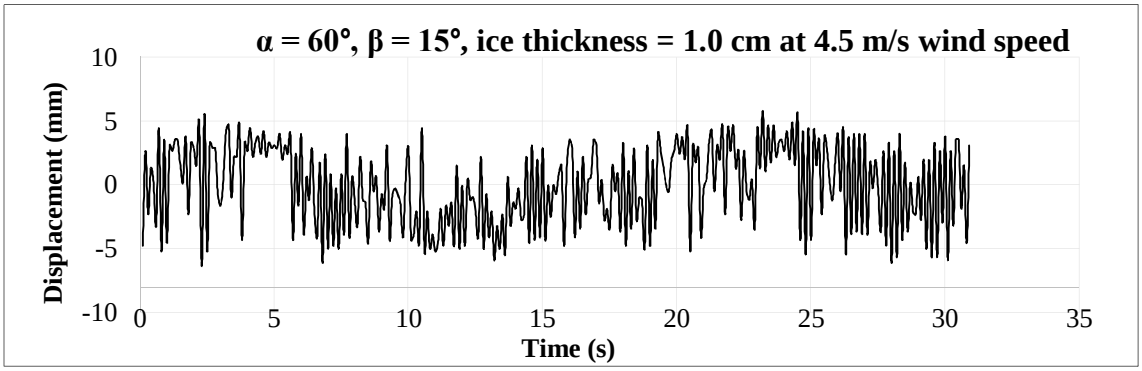

a) Vertical displacement for ice-accreted cable model α = 60°, β = 15°, 1.0 cm ice thickness at 4.5 m/s wind speed

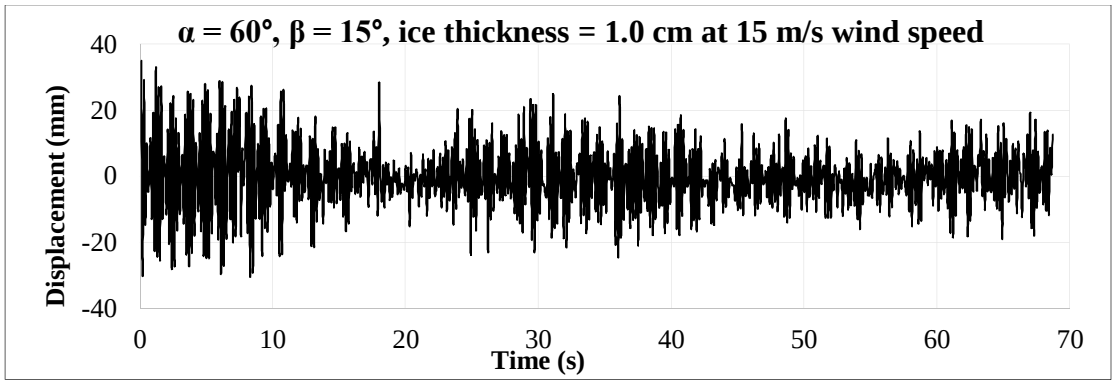

b) Vertical displacement for ice-accreted cable model α = 60°, β = 15°, 1.0 cm ice thickness at 15 m/s wind speed

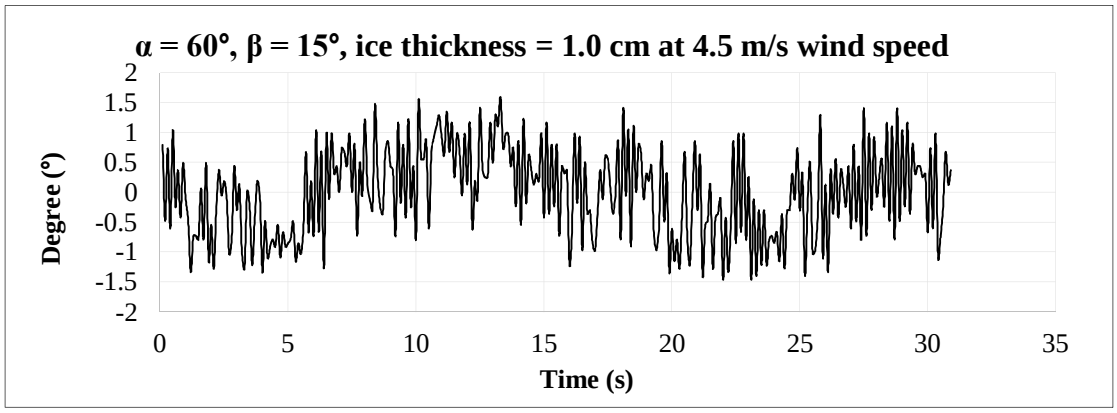

c) Torsional displacement for ice-accreted cable model α = 60°, β = 15°, 1.0 cm ice thickness at 4.5 m/s wind speed

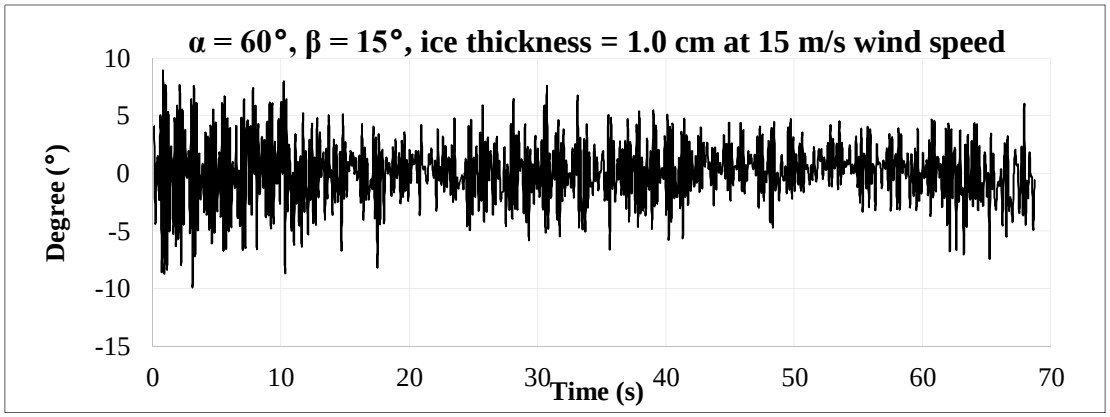

d) Torsional displacement for ice-accreted cable model α = 30°, β = 15°, 1.0 cm ice thickness at 15 m/s wind speed

Figure 4.6 Time displacement history for vertical and torsional modes of case: α = 60°， β = 15° with 1.0 cm ice thickness

In Figure 4.6 a) it can be noticed that the maximum value of the vertical displacements registered for Case 6 (α = 60°, β = 15°, ice thickness of 1.0 mm) was 6.1 mm at 23.2 s, and the mean value of the vertical displacements was 5.89 mm at 4.5 m/s. Figure 4.6 b) shows vertical displacements for the same Case 6 α = 60°, β = 15°, ice thickness of 1.0 cm but tested at 15 m/s wind speed; the maximum vertical displacement value was 33.17 mm at 1.2 s and the average value for this case was 22.94 mm. The maximum value of the torsional displacement for case 6 of α = 60°, β = 15°, ice thickness of 1.0 cm recorded at 4.5 m/s, was 1.59° at 13.3 s and the mean value for torsional displacement was 1.46°,

as it can be noticed in Figure 4.6 c). From Figure 4.6 d), it can be observed that the torsional response for the same Case 6 but tested at 15 m/s wind speed registered a maximum value of 8.9° at 0.8 s. A clear difference was noticed between the trends of vibrations for 4.5 m/s, where no aerodynamic instability was noticed and the 15 m/s, where obvious beats vibrations, at higher density (low frequency), associated with galloping were reported. Case 6 of the model inclined at $\alpha = 60°$, $\beta = 15°$, is also a critical case for the bridge stay-cables, without ice accretion [41].

4.1.7 Case 7 $\alpha = 0°$, $\beta = 0°$ with 2.0 cm ice thickness

Figures 4.7 a) to 4.7 d) represent the vertical and torsional displacements for the cable model tested at Case 7 , for inclinations of $\alpha = 0°$, $\beta = 0°$, at both 4.5 m/s and 15 m/s wind speeds, but with 2.0 cm ice thickness,.

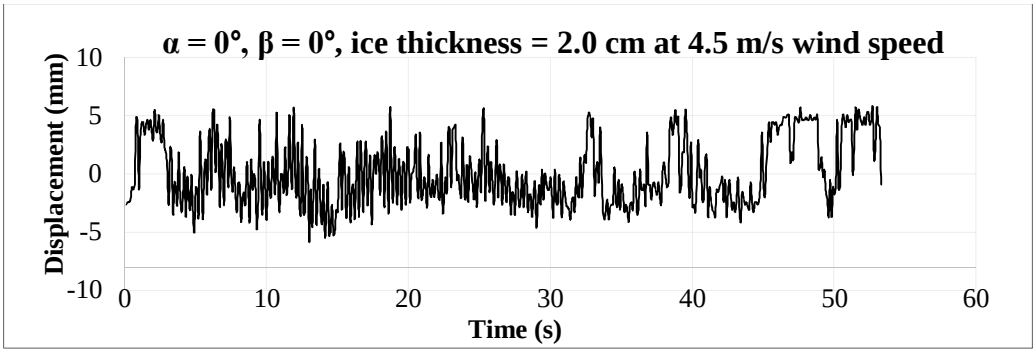

a) Vertical displacement for ice-accreted cable model $\alpha = 0°$,$\beta = 0°$, 2.0 cm ice thickness at 4.5 m/s

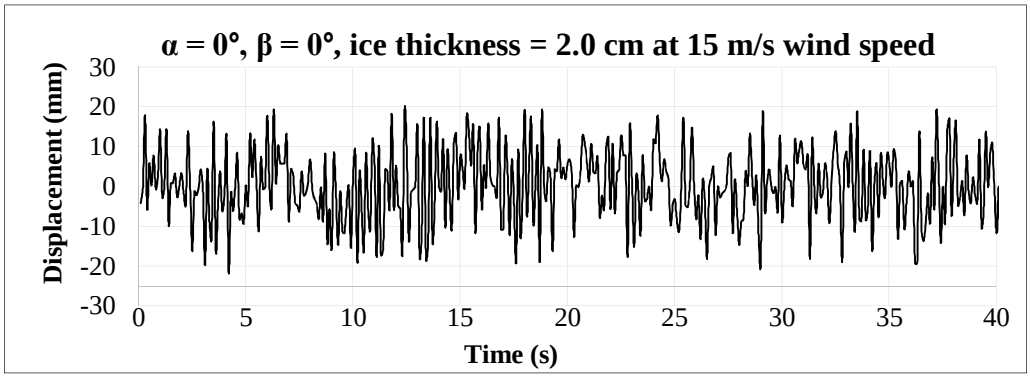

b) Vertical displacement for ice-accreted cable model $\alpha = 0°$, $\beta = 0°$, 2.0 cm ice thickness at 15 m/s

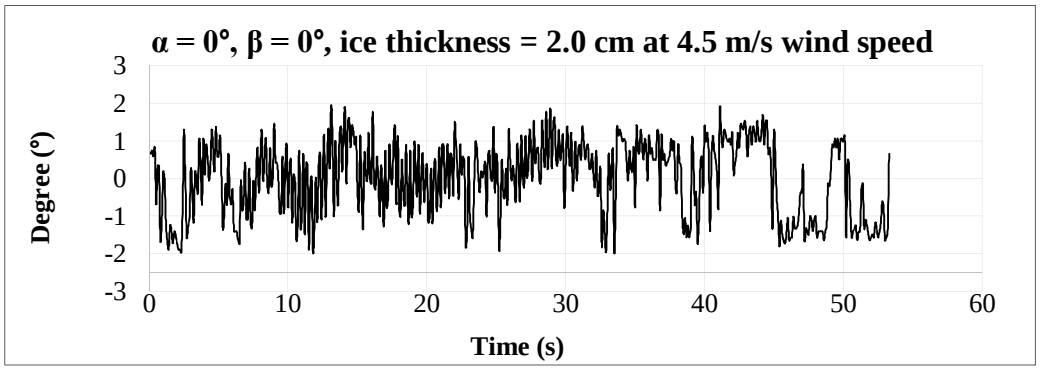

c) Torsional displacement for ice-accreted cable model α = 0°, β = 0°, 2.0 cm ice thickness at 4.5 m/s wind speed

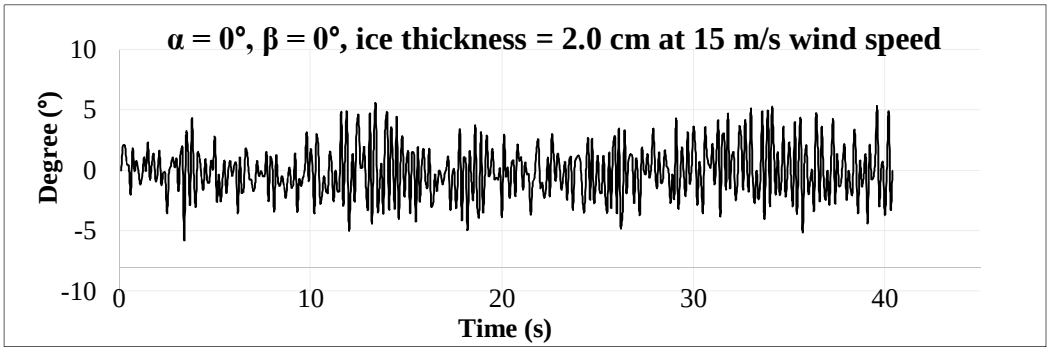

d) Torsional displacement for ice-accreted cable model α = 0°, β = 0°, 2.0 cm ice thickness at 15 m/s wind speed

Figure 4.7 Time displacement history for vertical and torsional modes of case:α = 0°， β = 0° with 2.0 cm ice thickness

In Figure 4.7 a) the vertical displacement for the Case 7 at α = 0°, β = 0°, ice thickness of 2.0 cm tested at 4.5 m/s wind speed is presented and it was noticed that the maximum value for the vertical vibrations was 5.72 mm at 18.7 s, while the mean value for this case was 3.4 mm. In Figure 4.7 b) the vertical displacement at 15 m/s wind speed for the same case of α = 0°, β = 0°, ice thickness of 2.0 cm is presented, with the maximum value of 21.95 registered at 4.2 s, and the mean value of 3.4 mm. The torsional displacement had a maximum value of 1.9°, and the average value for this case was 1.1° for 4.5 m/s (Figure 4.7 c)). For the same model, tested at 15 m/s wind speed, the maximum torsional displacement was 5.8° at 3.4 s, and the mean value for the case was 2.58°, as it can be noticed in Figure 4.7 d). For this case both the vertical and torsional responses registered

at 4.5 m/s wind speed changed their period of vibration after 30 s, which might indicate an equipment or model connection malfunction. For high wind speeds of 15 m/s however, besides the increase of amplitude, the beats vibrations were noticed especially for the torsional response, thus the association with galloping instability can be made.

4.1.8. Case 8 α = 30°， β = 0° with 2.0 cm ice thickness

The following Figures 4.8 a) to 4.8 d) represent the vertical and torsional displacements for the test Case 8 conducted on the cable model inclined at α = 30°, β = 0° with 2.0 cm ice thickness at both 4.5 m/s and 15 m/s wind speed.

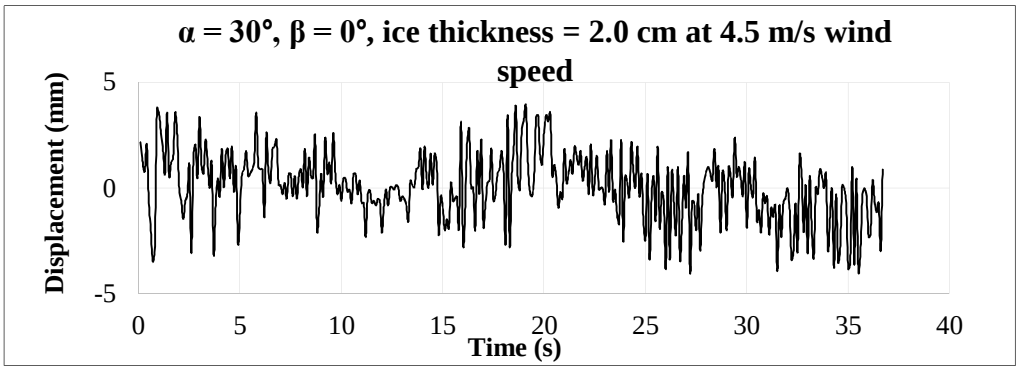

a) Vertical displacement for ice-accreted cable model α = 30°, β = 0°, 2.0 cm ice thickness at 4.5 m/s wind speed

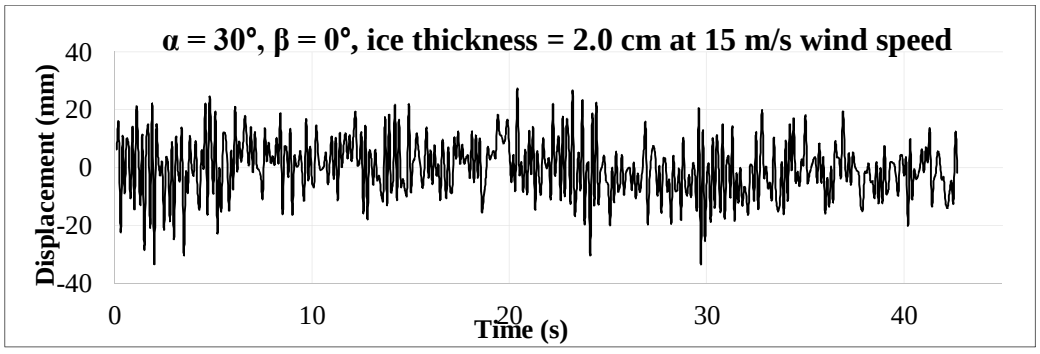

b) Vertical displacement for ice-accreted cable model α = 30°， β = 0° with 2.0 cm ice thickness at 15 m/s wind speed.

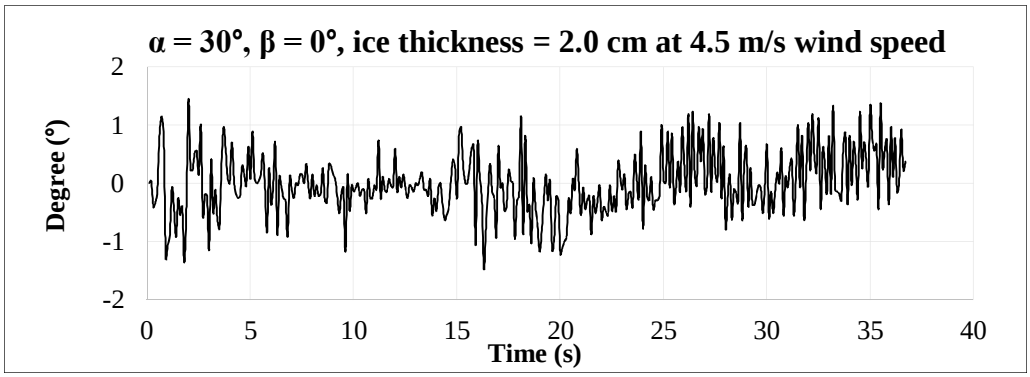

c) Torsional displacement for ice-accreted cable model α = 30°, β = 0°, 2.0 cm ice thickness at 4.5 m/s wind speed

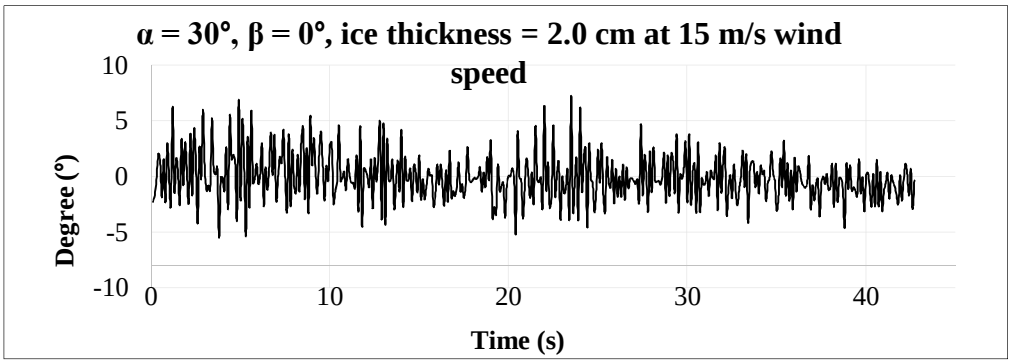

d) Torsional displacement for ice-accreted cable model α = 30°, β = 0°, 2.0 cm ice thickness at 15 m/s

Figure 4.8 Time displacement history for vertical and torsional modes of case: α = 30°， β = 0° with 2.0 cm ice thickness

For Figure 4.8 a) the results for Case 8, α = 30°, β = 0°, 2.0 cm ice thickness at 4.5 m/s wind speed are presented. The maximum value for the vertical vibration was 4.2 mm at 27.2 s, and the mean value for this case was 3.0 mm. In Figure 4.8 b) the rotational displacement is plotted for the same case of α = 30°, β = 0°, ice thickness of 2.0 cm tested at 15 m/s wind speed; the maximum recorded value for the vertical displacement was 33.27 mm at 29.7 s, while the mean value for this case was 20.66 mm. The maximum amplitude of the torsional vibration was 1.5° at 16.3 s, for the case α = 30°, β = 0°, ice thickness of 2.0 cm at 4.5 m/s wind speed (Figure 4.8 c)), and the average value for this case was 1.03°. For Figure 4.8 d) the torsional vibration displacements for the same Case 8 α = 30°, β = 0°, ice thickness of 2.0 cm at 15 m/s wind speed were presented,

and the maximum value was 7.3° at 23.5 s, while the mean value for this case was 3.3°. Similar to the previous cases, the response for high wind speed of 15 m/s, could not be clearly identified as the galloping instability, however the "high-amplitude vibrations" was noticed and this can be associated with the aerodynamic instability as described by Cheng et al, 2008 [41].

4.1.9. Case 9 α = 0°, β = 15° with 2.0 cm ice thickness

The Figures 4.9 a) to 4.9 d) represented the vertical and torsional displacements for the test Case 9 of α = 0°, β = 15° with 2.0 cm ice thickness at both 4.5 m/s and 15 m/s wind speeds.

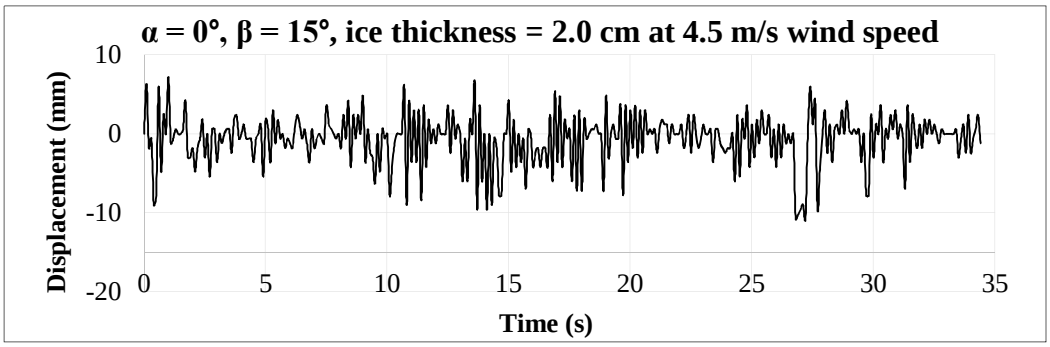

a) Vertical displacement for ice-accreted cable model α = 0°, β = 15°, 2 cm ice thickness at 4.5 m/s wind speed

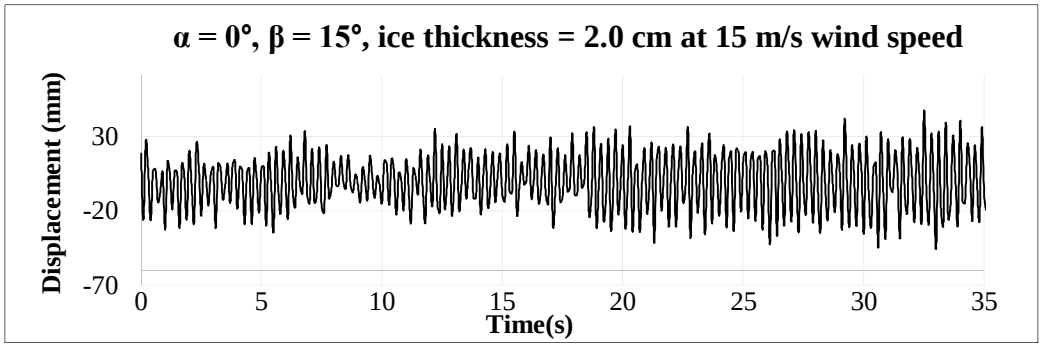

b) Vertical displacement for ice-accreted cable model α = 0°, β = 15°, 2.0 cm ice thickness at 15 m/s wind speed

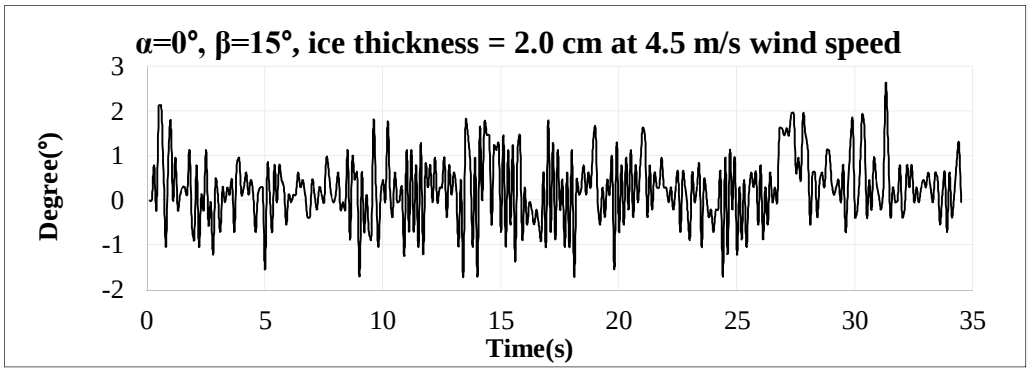

c) Torsional displacement for ice-accreted cable model α=0°, β=15°, 2 cm ice thickness at 4.5 m/s wind speed

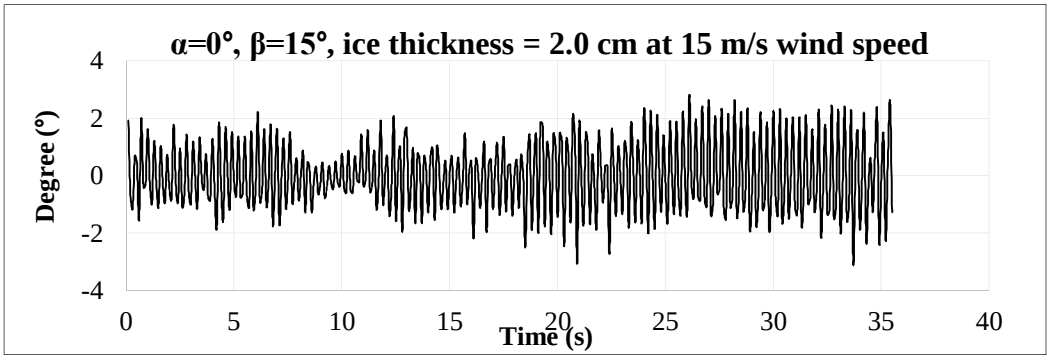

d) Torsional displacement for ice-accreted cable model α = 0°, β = 15°, 2 cm ice thickness at 15 m/s wind speed

Figure 4.9 Time displacement history for vertical and torsional modes of case: α = 0°, β = 15° with 2.0 cm ice thickness

In Figure 4.9 a) the vertical response for the cable tested at Case 9 at α = 0°, β = 15°, with ice thickness of 2.0 cm at 4.5 m/s wind speed is shown; the maximum value for the vertical displacement was 6.0 mm at 0.6 s, and the mean value for this case was 5.55 mm. For 15 m/s wind speed, for the same case, the maximum value of the vertical vibration was 47.8 mm at 32.5 s, and the mean displacement of vertical vibration was 22.43 mm (Figure 4.9 b)). As it can be seen in Figure 4.9 c), for α = 0°, β = 15°, ice thickness of 2.0 cm at 4.5 m/s wind speed, the maximum value for the torsional displacement was 2.62° at 31 s, and the mean value for this case was 1.2°. For 15 m/s wind speed, the maximum displacement for the torsional vibration was 3.1° at 33.7 s, the average value was 2.82°, for the same case of α = 0°, β =15°, ice thickness of 2.0 cm (Figure 4.9 d)). High-

amplitude response was noticed, rather than clear galloping instability, for both torsional and vertical vibration recorded at 15 m/s were noticed for the currently tested cable model.

Because of the lack of recording devices and because of the limited availability time of the wind tunnel, the drag and lift coefficients were not measured in this experiment. The dynamic wind tunnel test was performed, which showed that the wind-induced vibrations were more irregular at low wind speeds than at high wind speeds, while for high wind speeds the vibrations of the model increased and two types of aerodynamic instabilities were noticed: the galloping divergent vibrations and the high-amplitude vibrations. For the later there is no further model of verification, however for the galloping instability a verification can be performed by applying the Den Hartog criterion, if the drag and lift coefficients are known. Therefore the CFD simulation was employed for determining the drag and lift coefficients as detailed in the following sections.

Performing an analysis of the change of frequency registered for the displacements time history responses might also provide the information regarding the critical wind speeds for which both aerodynamic instabilities, the galloping and the high-amplitude frequency would commence.

Also it should be mentioned that some disparity in the recorded data was noticed during the experiment, especially for very low wind speeds. The first reason which might cause this phenomenon is the possible error of the reading sensors and the potential connection failure between the models and the support system. Thus initial displacement and torsion could be triggered by low wind speed and depending on the case, data correction can be done, or tests were re-made. The second reason could be formulated in relationship with the randomness of the geometrical shape of the ice profile and cables tested. For irregular shape models, low wind speed had more irregular vibrations. It can be imagined as if a car is running at low speed on a road with rough and irregular surface, the car will be jolty, and the time spent is longer, but if the car is driving across the same road, but at a much higher speed, then the trend of the motion tends to be smooth, and the time spent is shorter. In this case, as the wind speed is increasing, it would be easier for the wind to

slip across the irregular surface of the ice-accreted models, and this could make the vibration more regular.

4.2. The average vibration amplitude comparison for vertical and torsional displacements:

Reporting and discussing the vertical and torsional responses for all the tested wind speeds between 1.5 m/s and 15 m/s is extensive and would be beyond the limitations of the current section of this chapter. Instead, the average values described above for each recorded vertical and torsional vibrations for all the tested cases were summarized in Figures 4.10 to 4.24. Also, because the galloping divergent vibration can be identified from the vertical response, and the variation of the torsional response cannot be directly related to the galloping occurrence [17], in section 4.3 below, the frequency analysis was performed for the time history of the vertical response.

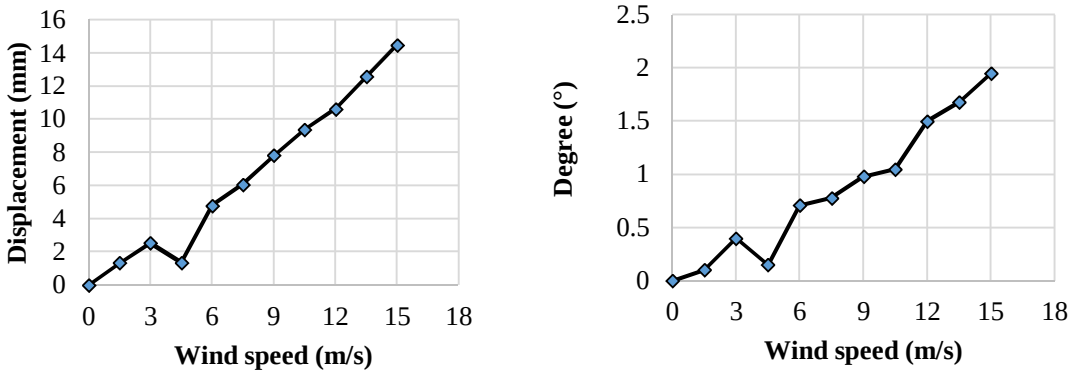

Figure 4.10 Average torsional and vertical vibration amplitudes for α = 0°, β = 0° with 1.0 cm ice thickness

The average of torsional and vertical vibration amplitudes for the Case 1 at α = 0°, β = 0° with 1.0 cm ice thickness are shown in Figure 4.10. As expected, the torsional and vertical vibrations amplitudes increased gradually in direct proportion with the increase of the wind speed applied in the tests. The highest torsion recorded for the highest wind speed tested of 15 m/s was 1.95°, and the highest vertical displacement was 14.48 mm. A

decrease of the wind-induced response can be noticed at 4.5 m/s followed by a sudden increase at 6.0 m/s (Fig. 4.10).

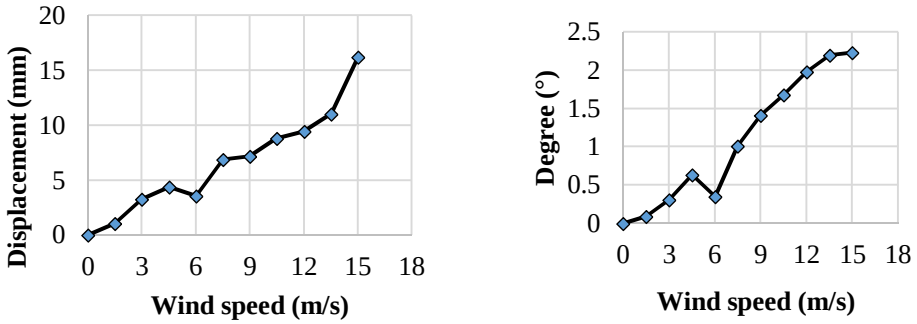

Figure 4.11 Average torsional and vertical vibration amplitude for $\alpha = 0°$, $\beta = 15°$ with 1.0 cm ice thickness

Average torsional and vertical vibration amplitudes for Case 2, at $\alpha = 0°$, $\beta = 15°$ with 1.0 cm ice thickness are presented in Figure 4.11, for all the tested wind speeds. The torsional and vertical vibrations are proportional to the wind speed and the maximum torsion was 2.23°, while the maximum displacement is 16.23 mm. The particularity of the wind-induced response for this case is that a slight displacement decrease can be noticed for 6.0 m/s for both the vertical and the torsional responses, followed by an increase at 7.5 m/s. Also the sudden increase in the amplitude of vibration for the vertical response at 15 m/s represents a characteristic of the aerodynamic instability.

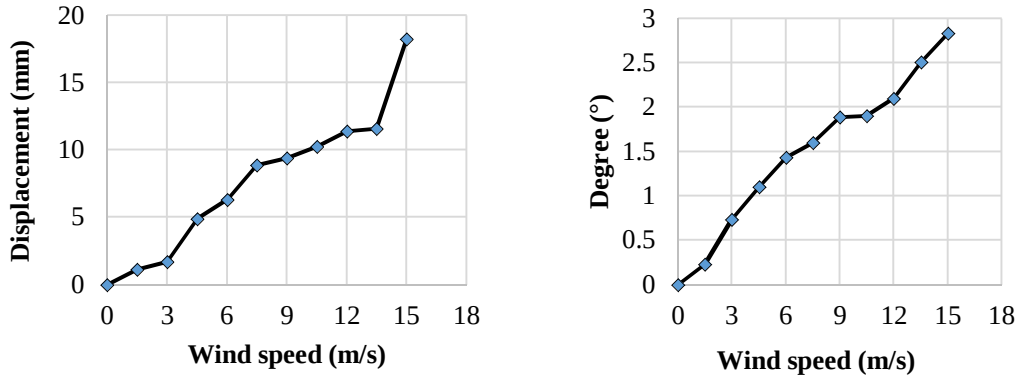

Figure 4.12 Average torsional and vertical vibration amplitude for α = 30°, β = 15° with 1.0 cm ice thickness

For Case 3, at α = 30°, β = 15° with 1.0 cm ice thickness, the average vibration amplitudes plotted in Figure 4.12, show that the vertical response registered a decrease at around 3.0 m/s, followed by a sudden increase at 4.5 m/s and then again at 15.0 m/s, while the torsional response decreased briefly at 10.5 m/s. Similar to the previous case, the sudden increase of the vertical response at 15 m/s can indicate the aerodynamic instability. In general, the torsional and vertical vibrations are proportional to the wind speed and the highest torsion was of 2.83°, while the maximum vertical displacement was 18.23 mm, both registered at 15 m/s.

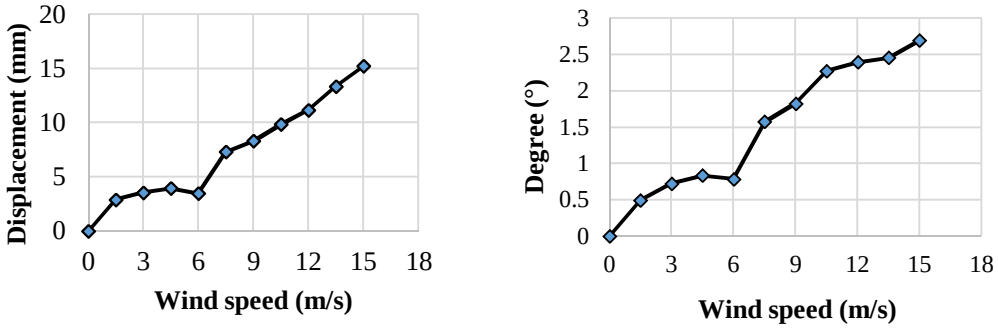

Figure 4.13 Average torsional and vertical vibration amplitudes for α = 30°, β = 0° with 1.0 cm ice thickness

In Figure 4.13 the average torsional and vertical vibration amplitudes for α = 30°, β = 0° with 1.0 cm ice thickness (Case 4) were plotted as a function of wind speed. For this case a slight decrease in the amplitude of vibration can be noticed at 6 m/s for both torsional and vertical vibrations, followed by a sudden increase at 7.5 m/s. Similar to the previous case, the torsional and vertical vibrations are proportional to the increase of wind speed during the tests, and the highest torsion was 2.7°, while the highest vertical displacement was 15.25 mm.

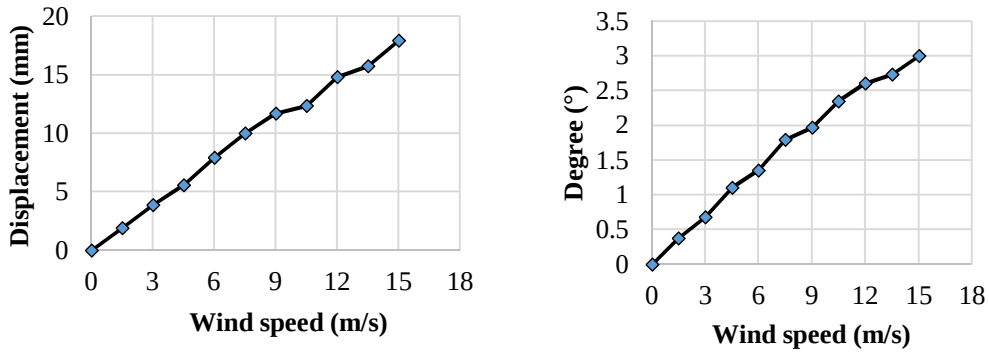

Figure 4.14 Average torsional and vertical vibration amplitudes for α = 60°, β = 0° with 1.0 cm ice thickness

Torsional and vertical vibration amplitudes at α = 60°, β = 0° with 1.0 cm ice thickness (Case 5), which in general is a critical case for the bridge stay-cable without ice [41] are shown in Figure 4.14. For this case a slight stagnation tendency was noticed for the vertical vibration at 10.5 m/s, but for the torsional vibration this decrease occurred at 9 m/s, however the value of the response change was very small. The torsional and vertical vibrations are proportional with the increase of the wind speed and the highest torsion was 3°, while the maximum vertical displacement was 17.93 mm, both registered at 15 m/s.

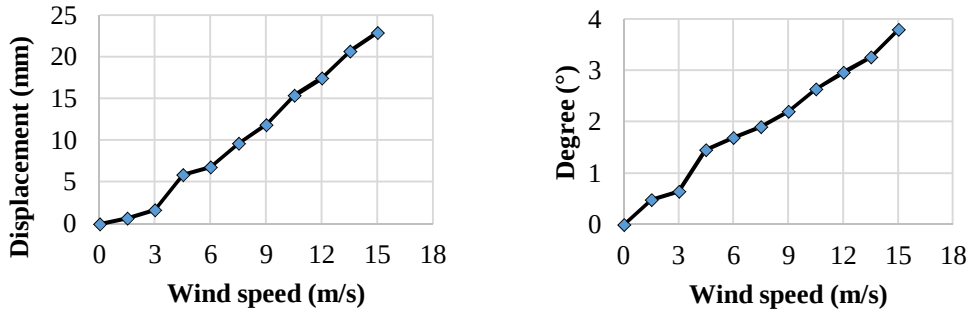

Figure 4.15 Average torsional and vertical vibration amplitudes for α = 60°, β = 15° with 1.0 cm ice thickness

The average torsional and vertical vibration amplitudes for Case 6 at α = 60°, β = 15° with 1.0 cm ice thickness are plotted in Figure 4.15. This is the second case which was reported as having critical vibrations for bridge stay-cables without ice accretion [41]. In the current experiment, for the cable model with 1.0 cm ice accretion profile, was noticed that the brief stagnation followed by a jump in the response was recorded at 3.0 m/s and 4.5 m/s respectively, for both vertical and torsional vibrations. Otherwise, the torsional and vertical vibrations increased with the increase of the wind speed during the experiments, and the highest torsion was registered as 3.8°, while the highest displacement was 22.94 mm, both at 15 m/s.

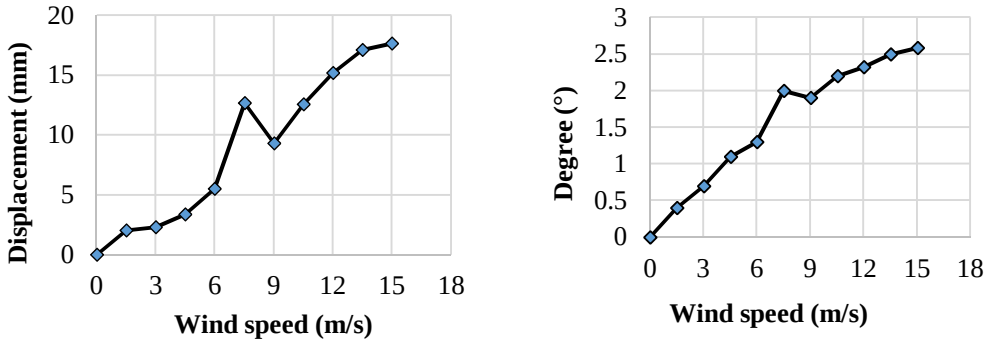

Figure 4.16 Average torsional and vertical vibration amplitudes for α = 0°, β = 0° with 2.0 cm ice thickness

Figure 4.16 presents the torsional and vertical vibrations amplitudes for Case 7 at α = 0°, β = 0° with 2.0 cm ice thickness. For this case, only the vertical response registered a slight stagnation at 3.0 m/s, while the general trend of the torsional and vertical vibrations was proportional to the increase of the wind speed. A sudden increase in both vertical and torsional vibrations were noticed for 7.5 m/s. At 15 m/s the highest recorded torsion was 2.58°, and the highest vertical displacement was 17.66 mm.

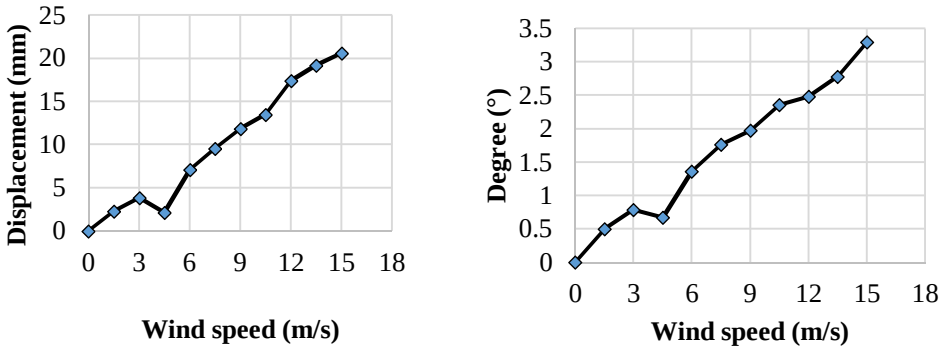

Figure 4.17 Average torsional and vertical vibration amplitudes for α = 30°, β = 0° with 2.0 cm ice thickness

For test Case 8, at α = 30°, β = 0° with 2.0 cm ice thickness, the average torsional and vertical vibrations are increasing with the increase of the wind speed, until 4.5 m/s where a decrease was noticed for the vertical and torsional vibrations, however from 6 m/s the responses increased again until reaching the maximum the maximum value of 20.66 mm at 15 m/s. The torsional vibration increased steadily, reaching the highest magnitude of rotation of 3.3° at 15.0 m/s. The details for the torsional and vertical vibration amplitudes at α = 30°, β = 0° with 2.0 cm ice thickness can be observed in Figure 4.17.

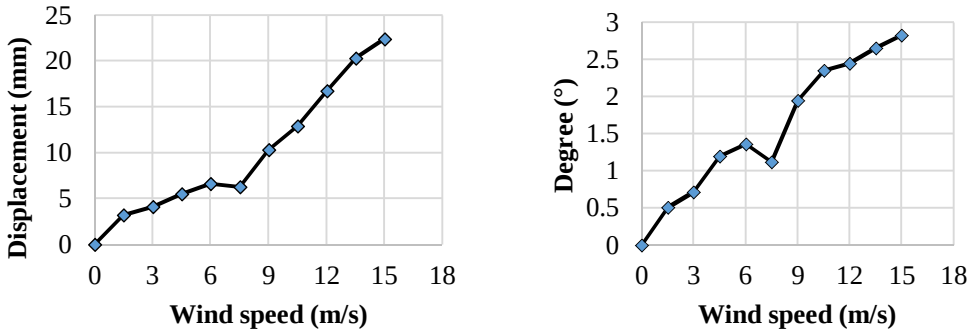

Figure 4.18 Average torsional and vertical vibration amplitude for α = 0°, β = 15° with 2.0 cm ice thickness

For the last test Case 9, at α = 0°, β = 15° with 2.0 cm ice thickness it can be observed from Figure 4.18 that the torsional and vertical vibrations were proportional with the wind speed and that the highest torsion recorded at 15 m/s was 2.83°; the highest vertical displacement was 22.43 mm, for the same wind speed. At 7.5 m/s a sudden decrease in the vertical and torsional responses was noticed.

Table 4.1 Vertical and torsional vibrations registered at maximum wind speed of 15 m/s

Cases	Case 1 at α=0° β=0° 1.0 cm	Case 2 at at α=0° β=15° 1.0 cm	Case 3 at α=30° β=15° 1.0 cm	Case 4 at α=30° β=0° 1.0 cm	Case 5 at α=60° β=0° 1.0 cm	Case 6 at α=60° β=15° 1.0 cm	Case 7 at α=0° β=0° 2.0 cm	Case 8 at α=30° β=0° 2.0 cm	Case 9 at α=0° β=15° 2.0 cm
Maximum displacement (mm)	14.48	16.23	18.23	15.25	17.93	22.94	17.66	20.66	23.10
Maximum torsion (°)	1.95	2.23	2.83	2.7	3.0	3.8	2.58	3.3	2.65

For the same wind speed of 15.0 m/s, the maximum vertical and torsional vibrations increased with the relative angle of attack from 14.48 mm to 22.94 mm for the vertical response and from 1.95° to 3.8° for the torsional response registered for the cable model with 1.0 cm ice accretion profile (Table 4.1). For the same ice profile model of 1.0 cm, the case of 60° stands out as a critical case, registering very high vertical and torsional responses of 17.93 mm and 3.0° respectively. Similarly, for the cable model with 2.0 cm

ice profile, the wind-induced response increased with the relative angle of attack, from 17.66 mm to 23.10 mm for the vertical vibration and from 2.54° to 3.3° for the torsional response, as it can be noticed in Table 4.1.

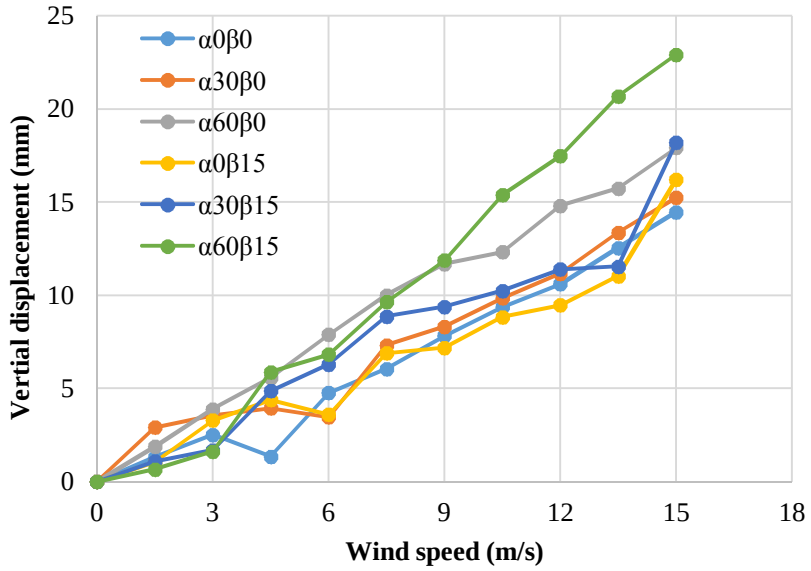

Figure 4.19 Average vertical amplitudes for cable models with 1.0 cm ice thickness

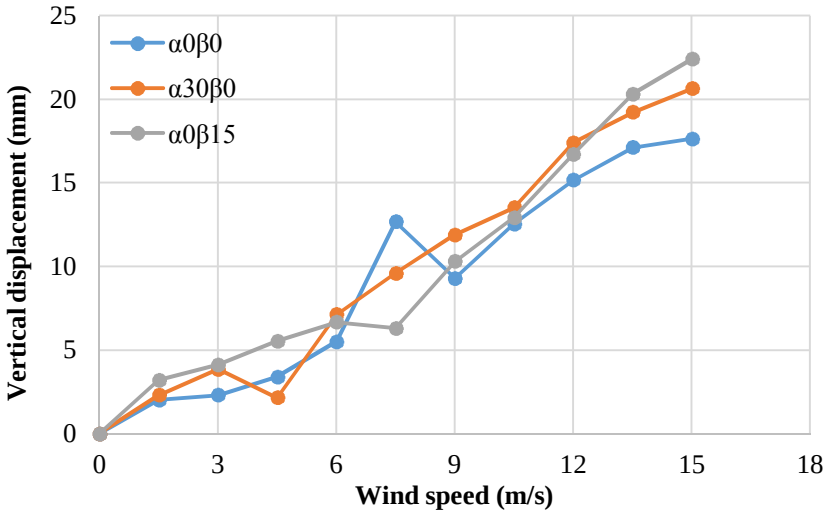

Figure 4.20 Average vertical amplitudes for cable models with 2.0 cm ice thickness

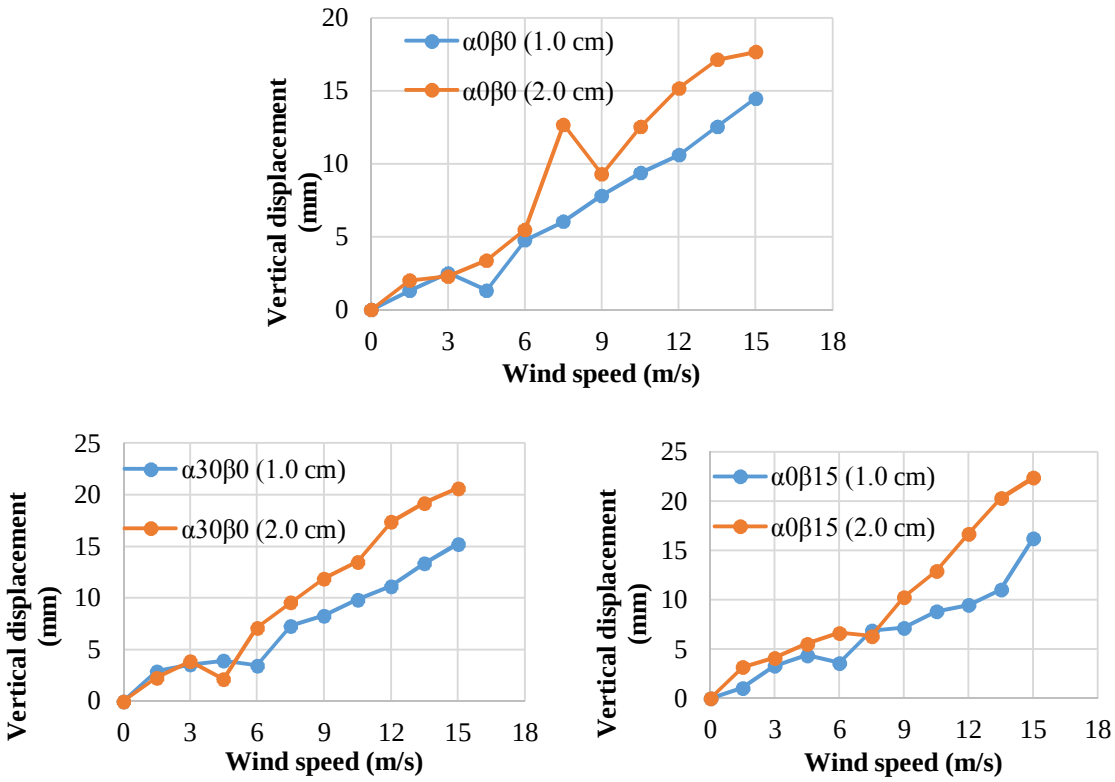

Figure 4.21 Vertical response for the cases with 1.0 cm and 2.0 cm ice thickness

In order to determine the critical cases for the horizontally and vertically inclined bridge cables with ice accretion of 1.0 cm and 2.0 cm, a comparison of the average vertical and torsional wind-induced vibrations was conducted in Figures 4.19 to 4.21, as discussed below.

For the cable models with 1.0 cm ice accretion, the critical cases for which higher vertical vibrations response compared with the other cases, were registered for the $\alpha = 60°$, $\beta = 15°$ and $\alpha = 60°$, $\beta = 0°$ (Fig. 4.19), which coincide with the critical cases reported by Cheng (2008) [41] for vertically and horizontally inclined stay-cables without ice accretion.

For the cable models with 2.0 cm ice thickness, all the investigated cases of $\alpha = 0°$, $\beta = 15°$, $\alpha = 0°$ $\beta = 0°$ and $\alpha = 30°$, $\beta = 0°$ showed a very similar response variation with the increase of the wind speed, with the exception of the cable perpendicular to the flow ($\alpha = 0°$ $\beta = 0°$) which showed a sudden increase of response at 7.5 m/s. For higher wind speeds the cable inclined at $\alpha = 0°$, $\beta = 15°$ registered a bigger response but for the

lower wind speeds the case of $\alpha = 30°$, $\beta = 0°$ the vertical response was higher (Figure 4.20).

Also, as it can be noticed from Figures 4.19 to 4.21, the vertical vibration response is proportional with the wind speed, and the general trend for the cable models with 1.0 cm ice thickness, is that the displacement depends more on the horizontal inclination angle α; for example when $\beta = 0°$, and α is increasing, the maximum displacement is increasing as well, however it does not mean that the displacement for the cases with higher horizontal angle (α angle) the response is larger than that of the models with lower α angle, but higher β, for the wind speeds tested. Also it was noticed that, for lower wind speeds, the vertical displacement of the cable model with 1.0 cm ice accretion, tested for $\alpha = 60°$, $\beta = 0°$, (Case 5) is much higher than the case of $\alpha = 30°$, $\beta = 0°$ (Case 4), as it can be noticed in Fig 4.20. Also the vertical displacement for Case 2 at $\alpha = 0°$, $\beta = 15°$ is larger than the vertical displacement for Case 1 at $\alpha = 0°$, $\beta = 0°$ (Fig. 4.20), and it can indicate that the wind-induced displacement of the ice-accreted cables increases with the increase of the vertical inclination angle β. However, more cases need to be performed to fully support this conclusion. As per the testing conditions of the current experiment, it was noticed that in general, for the cases with the same α but with different β, the cases with greater β had larger vertical vibration than the cases with lower β.

For the Case 4 of $\alpha = 30°$, $\beta = 0°$, before reaching the wind speed of 15 m/s, the vertical vibration was larger than that of the Case 2 of $\alpha = 15°$, $\beta = 0°$, but as shown in Figure 4.20, at higher wind speed, the vertical vibration increase rate for the case $\alpha = 15°$, $\beta = 0°$ was greater than that of the Case 5 of $\alpha = 60°$, $\beta = 0°$. Therefore an initial conclusion can be formulated that the vertical inclination angle has more effect on the vertical vibration than the horizontal inclination angle.

For clarifying the effect of the ice accretion effect on the vertical displacement of the tested cable, the cases with the same vertical and horizontal inclination angles were compared in Figures 4.21 a-c), and it was noticed that the vertical vibration amplitudes for the cables with 2.0 cm ice thickness were larger than those of the cable with 1.0 cm ice thickness, especially for higher wind speeds.

An interesting phenomenon was for the case of α = 0°， β = 0° (Case 1), and the case of α = 0°， β = 15° (Case 2), when the wind speed reached a higher value of 13.5 m/s, both cases seemed to encounter an increase for the vertical vibration, which might be an indication of galloping. Actually, for cables, without ice formations, the circular cross-section shape is symmetrical, therefore, as per the Den Hartog criterion, the galloping is not supposed to occur; the reason why galloping might happen in the current experiment is the vertical and horizontal inclination angles, which would determine an elliptical cross-section of the cable inclined to the wind direction. However this reason cannot support the case α = 0°, β = 0° because this case does not have any inclined angle. Therefore, a second assumption was formulated in regard to the ice accretion which could change the shape of the cross-section of the cable, and thus would make the cable asymmetric.

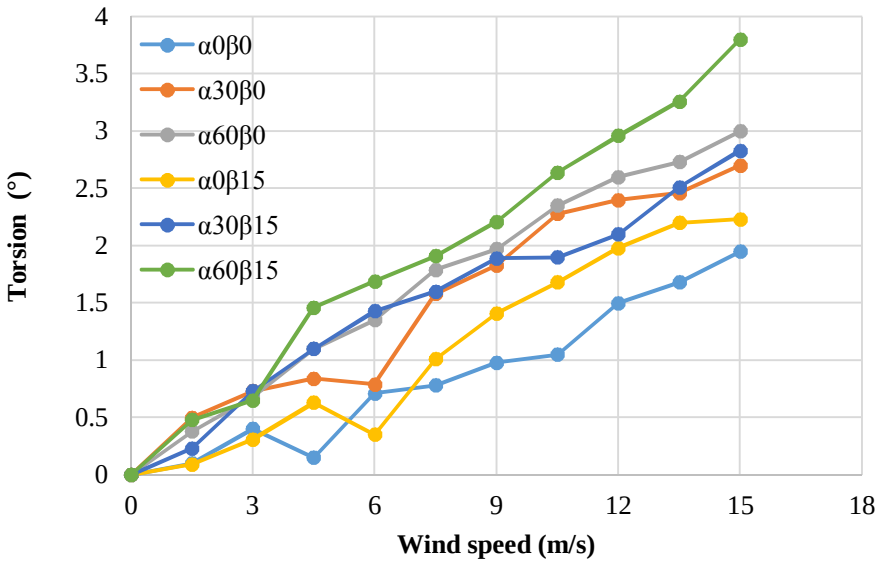

Figure 4.22 Average torsional amplitudes for cable models with 1.0 cm ice thickness

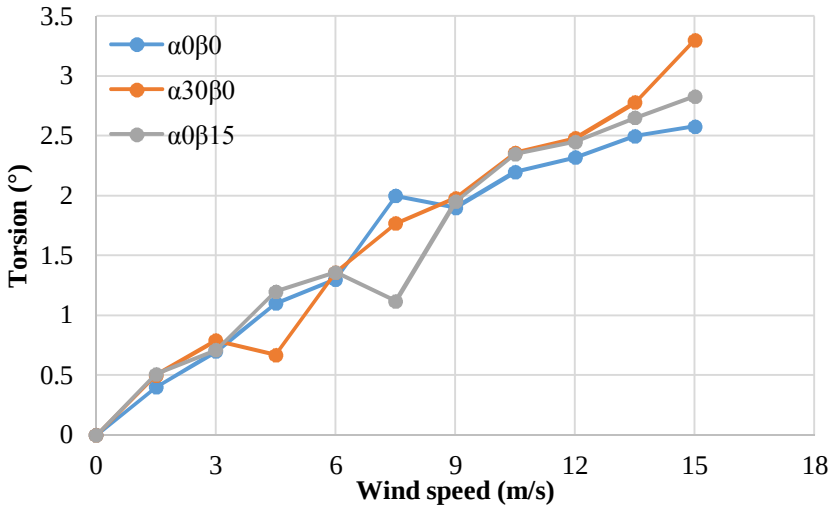

Figure 4.23 Average torsional amplitudes for cable models with 2.0 cm ice thickness

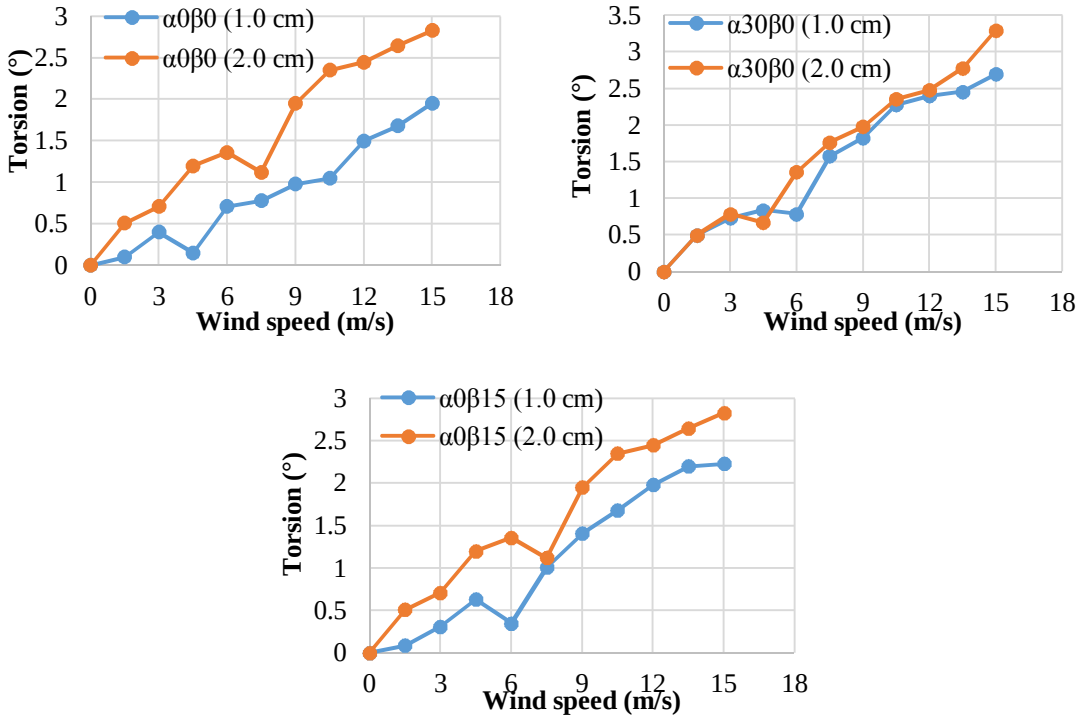

Figure 4.24 Torsional response for the cases with 1.0 cm and 2.0 cm ice thickness

The torsional amplitude variation with the wind speed, for all the investigated cases is presented in Figures 4.22 and 4.23, and the comparison for torsional vibration for the two

different ice thicknesses is plotted in Figure 4.24. The torsional vibration amplitudes were consistent with the vertical vibrations amplitudes reported in Figures 4.20 to 4.22, namely for the same cases for which high vertical vibrations were noticed, torsional vibrations were also high. Thus, the highest torsional vibrations were noticed for the two cases of $\alpha = 60°$, $\beta = 15°$ (Case 6) for the cable with 1.0 cm ice thickness, and of $\alpha = 30°$, $\beta = 0°$ (Case 8), for the cable model with 2.0 cm ice thickness; the lowest magnitude of torsional response was noticed for the case of $\alpha = 0°$, $\beta = 0°$ (Case 1) and the case of $\alpha = 0°$, $\beta = 15°$ (Case 3) both for cable with 1.0 cm ice thickness (Fig. 4.20).

Therefore the conclusion that the β angle has more effect on the vertical vibration increment than the α angle formulated previously for the vertical vibrations results, it is not applicable for the torsional vibrations, because the case of $\alpha = 0°$, $\beta = 15°$ (Case 2) is one of the lowest response cases for torsional response.

For the torsional vibrations, the effect of the dimensions of the ice thickness is greater, because the case of 2.0 cm ice thickness at $\alpha = 30°$, $\beta = 0°$, was one of the worst two cases in terms of vertical responses, and the best two cases, with the lowest wind-induced responses, are both cable models with 1.0 cm ice thickness. Due to time and equipment limitations, only three cases of cables with 2.0 cm ice thickness were performed in this experiment, thus the higher inclination angles for cable models with 2.0 cm ice profile case were not tested. Also in the current experiment, a foam material was used for developing the ice profile and for the cable steel was used. Thus the mass ratio between the simulated ice and the cable is bigger than that in real cases, in other words, the effect of the ice accretion simulated in this experiment might be smaller than the effect for the real case of an ice accreted cable; however, the ice profile thickness is still playing a very important role for both torsional and vertical vibrations in this experiment, which means that for real cases, the ice profile thickness is a very important parameter to analyze the wind-induced vibrations of cables.

4.3. Frequency analysis by Fast Fourier transform

The Fast Fourier transform was used to analyze the frequency of the vertical and torsional vibrations measured; a Matlab software code was employed to transform the measured

displacements time histories to frequency time histories. The purpose of conducting the Fast Fourier transform (FFT) analysis is to observe the difference of the response frequency under various wind speeds. The horizontal 'x' axis represents the frequency in Hz and the vertical 'y' axis represents the energy corresponding to each frequency. The frequencies obtained from the vertical vibration time history at 4.5 m/s and 15 m/s wind speeds are presented in Figures 4.25 to 4.30. In general the frequency of the vertical response did not change very much and it registered values slightly lower or higher than 0.30 Hz as shown in Figures 4.25 to 4.30 below. After applying the FF transform, several additional spikes were noticed in some of the frequency plots; the reason why such frequency spikes occurred might be related to the model setup; because each cable model had two supporting bars, some of the spikes might indicate the frequency of the bars, but this assumption is not confirmed, however, the frequencies which belong to the vertical response of the ice accreted cable model can be identified as being much higher than the additional spikes. Therefore, these additional spikes were not taken into consideration in this analysis. It should be mentioned that in spite of the drastic variation, which can be noticed in the frequency plots in Figure 4.25 to Figure 30, the actual difference between adjacent frequency values was not higher than 0.02 which is very small. However studying the changes of the response frequency is very important, because this can indicate the change in the aerodynamic response of the cable model, under the effect of the increasing wind speed.

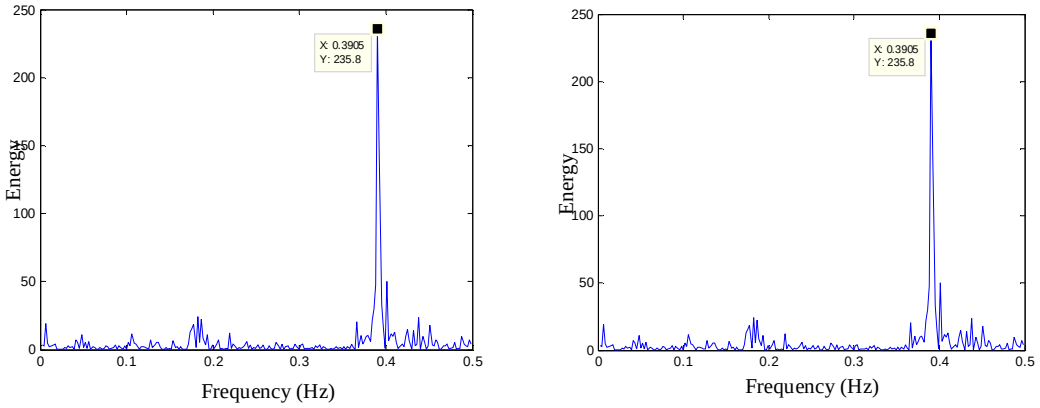

Figure 4.25 a) FFT of the vertical displacement for Case 1 α = 0°, β = 0° 1.0 cm ice thickness at 4.5 m/s and 15 m/s

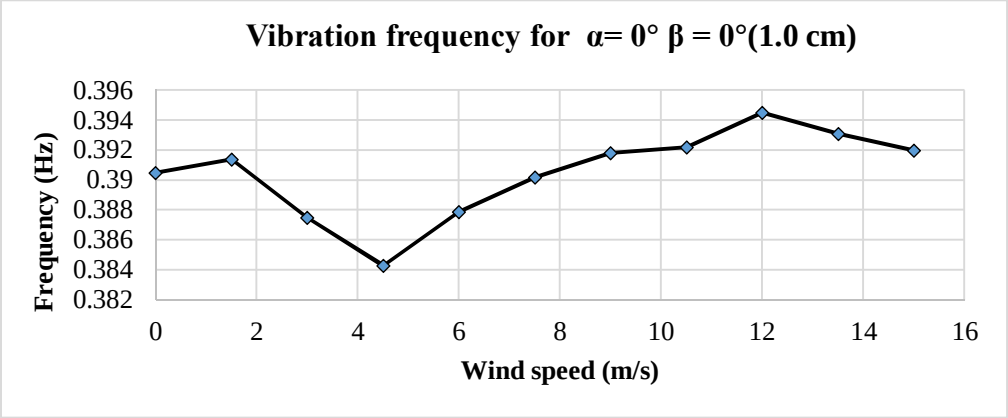

Figure 4.25 b) Vertical displacement frequency variation for Case 1, α = 0°, β = 0° with 1.0 cm ice thickness

The frequency obtained by the FFT transformation, for the wind speeds of 4.5 m/s and 15.0 m/s are presented in Figure 4.25 a). The frequencies of the vertical response for the test Case 1, α = 0°, β = 0° with 1.0 cm ice thickness, plotted in Figure 4.25 b), have shown a variation between the minimum value of 0.384 Hz, and the maximum vertical frequency of 0.395 Hz. After a slight increase at low wind speed, a drop occurs at 4.5 m/s wind speed, after which the frequency begins to increase again. At higher wind speeds after 12 m/s, a slight decrease occurs until 15 m/s wind speed, from 3.945 Hz to the final frequency of 3.92 Hz. Therefore, it can be concluded that for the wind speeds of 4.5 m/s and for 12 m/s a change in the dynamic response of the model would occur, however the average vertical response of the cable presented in the Figure 4.12 a) above indicated a decrease in the amplitude of vibration at 4.5 m/s follwoed by a sudden increase at 6.0 m/s; thus the same critical response was pointed put by the change in frequency plotted in Figure 4.25.

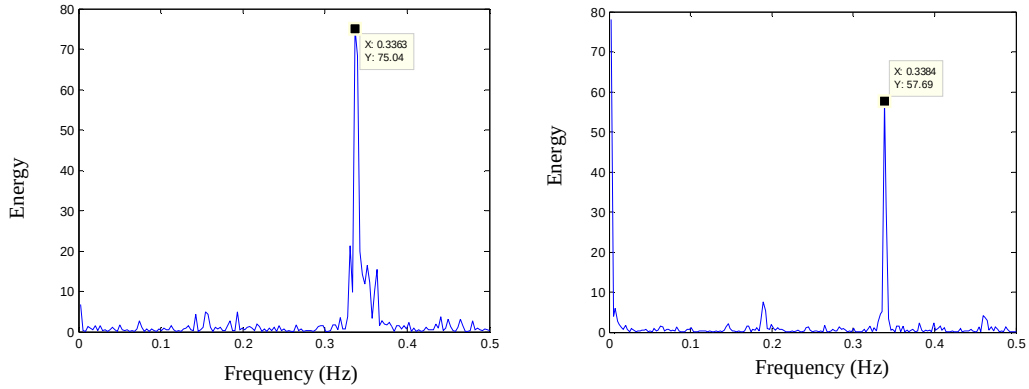

Figure 4.26 a) FFT of the vertical displacement for case 2 α = 0°, β = 15° , 1.0 cm ice thickness at 4.5 m/s and 15 m/s

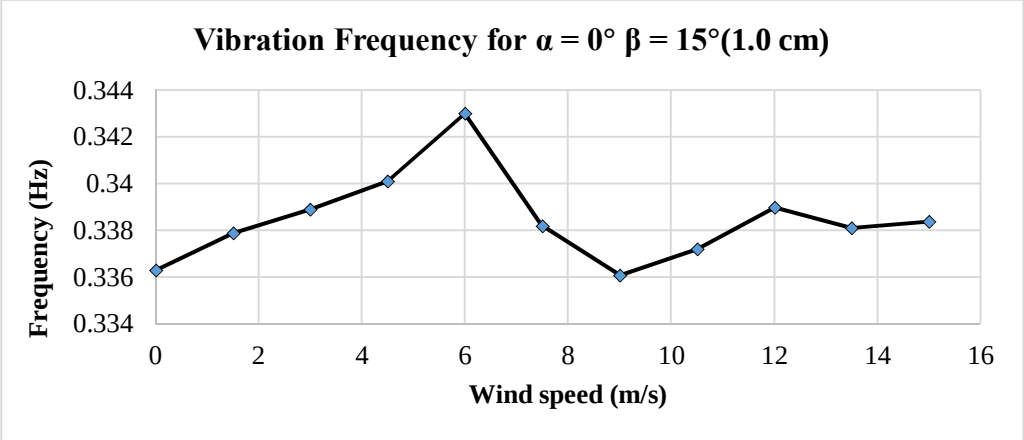

Figure 4.26 b) Vertical displacement frequency variation for Case 2, α = 0°, β = 15° with 1.0 cm ice thickness

For the Case 2 α = 0°, β = 15° with 1.0 cm ice thickness, the minimum vertical vibration frequency was 0.336 Hz, and maximum vertical frequency was 0.343 Hz, which was registered as a sudden increase at 6.0 m/s, as it can be noticed in Figure 4.26 b). The frequency decreases until 0.3361 Hz at 9.0 m/s wind speed, only to increase again until 12.0 m/s, from where this becomes stable. The vertical vibration amplitudes shown in Figure 4.14 showed the decrease for 6.0 m/s, however no distinct change in the vertical vibration was noticed for the wind speed of 9.0 m/s.

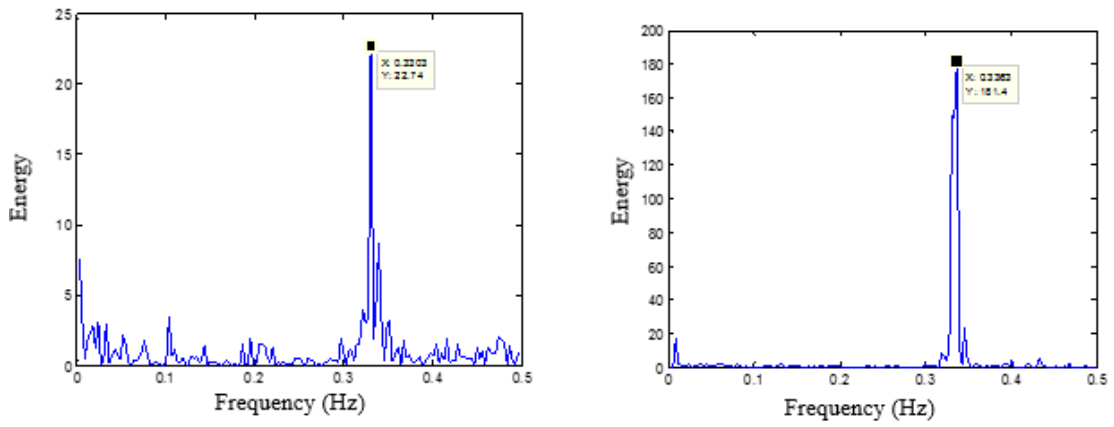

Figure 4.27 a) FFT of the vertical displacement for case 4 α = 30°, β = 0° , 1.0 cm ice thickness at 4.5 m/s and 15 m/s

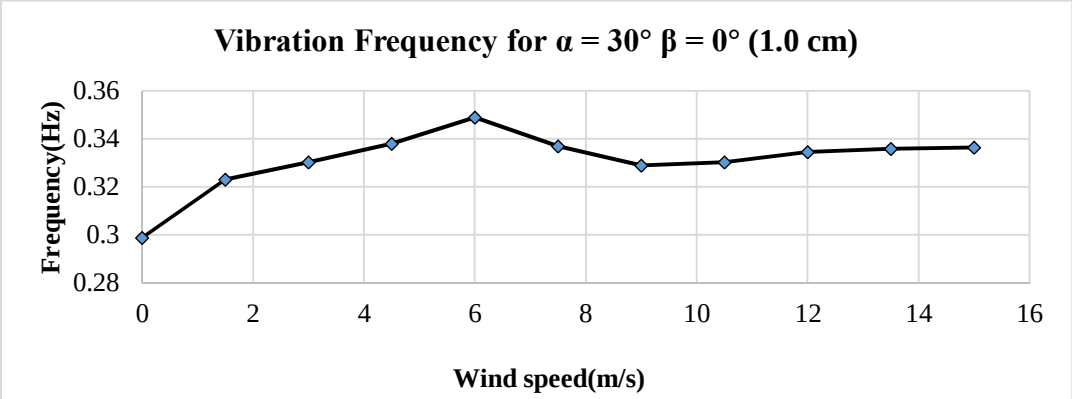

Figure 4.27 b) Vertical displacement frequency variation for Case 4, α = 30°, β = 0° with 1.0 cm ice thickness

Figure 4.27 b) presents the frequency variation for the vertical displacement for the Case 4 α = 30°, β = 0° with 1.0 cm ice thickness. The frequency varied between the minimum frequency of 0.3 Hz, and maximum frequency of 0.35 Hz, which was registered at 6.0 m/s wind speed, thereafter the frequency values decreased again until 0.338 Hz, registered at 9.5 m/s, maintaining a consistent trend afterwards until the maximum tested wind speed of 15.0 m/s. For the Case 4 of α = 30°, β = 0° with 1.0 cm ice thickness, the vertical vibration amplitudes reported in Figure 4.13 showed a slight decrease for the wind speeds of 6.0 m/s which confirmed a critical instability indicated for this case.

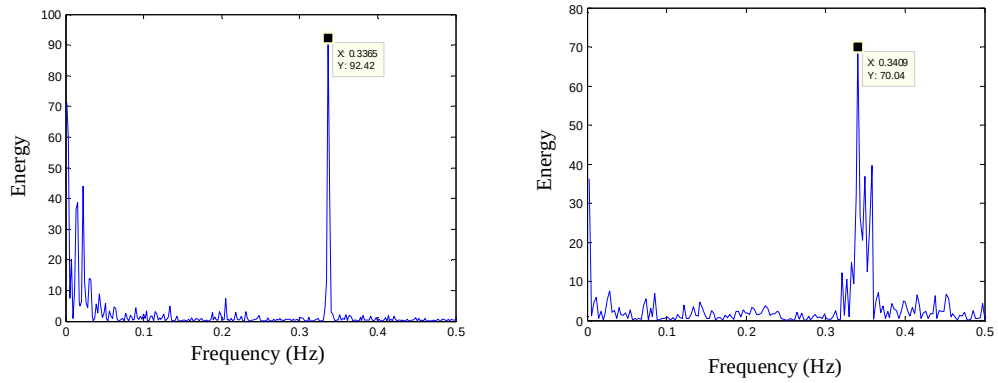

Figure 4.28 a) FFT of the vertical displacement for case 7 α = 0°, β = 0° , 2.0 cm ice thickness at 4.5 m/s and 15 m/s

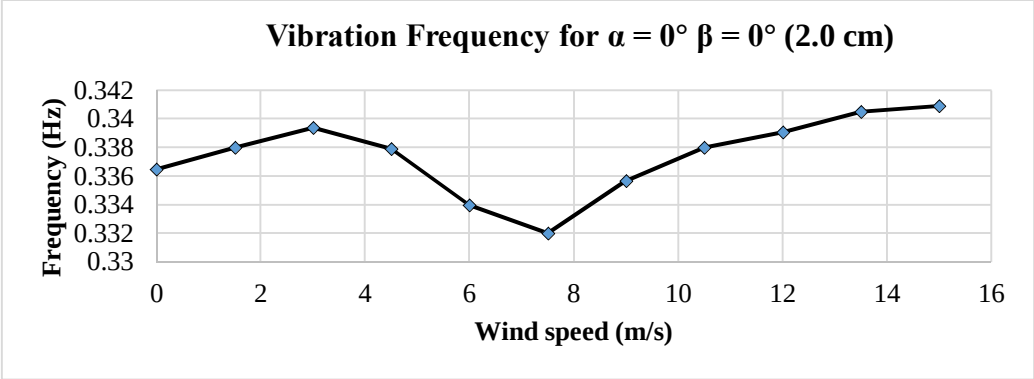

Figure 4.28 b) Vertical displacement frequency variation for Case 7, α = 0°, β = 0° with 2.0 cm ice thickness

Figure 4.28 shows the frequency variation for the vertical displacement for Case 7 of α = 0°, β = 0° with 2.0 cm ice thickness. The minimum vertical vibration frequency was 0.332 Hz, and maximum vertical frequency was 0.341 Hz; at low wind speeds, the vibration frequency is increasing until 3 m/s wind speed, then a significant drop occurred up to 7.5 m/s wind speed, after which the vibration frequency started to increase again, until the maximum tested wind speed of 15 m/s. In Figure 4.16, a stagnation of the vertical response was reported at 3.0 m/s and a sudden increase was noticed at 7.5 m/s. Thus the frequency analysis confirmed the aerodynamic response registered in the wind tunnel and it can be concluded that a critical instability could be registered from 7.5 m/s, for this test case.

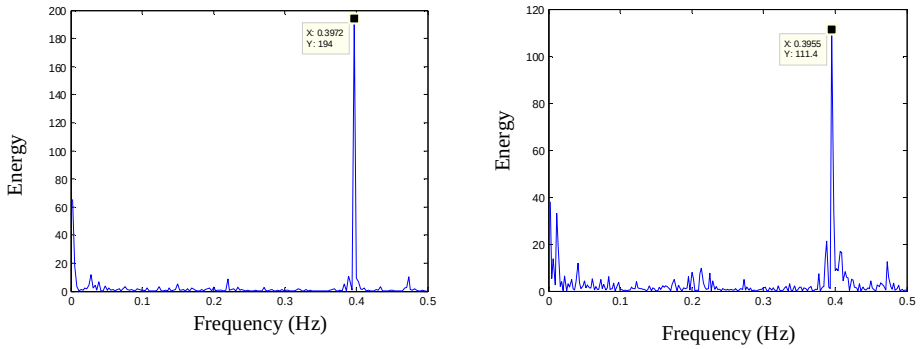

Figure 4.29 a) FFT of the vertical displacement for case 8 α = 30°, β = 0° , 2.0 cm ice thickness at 4.5 m/s and 15 m/s

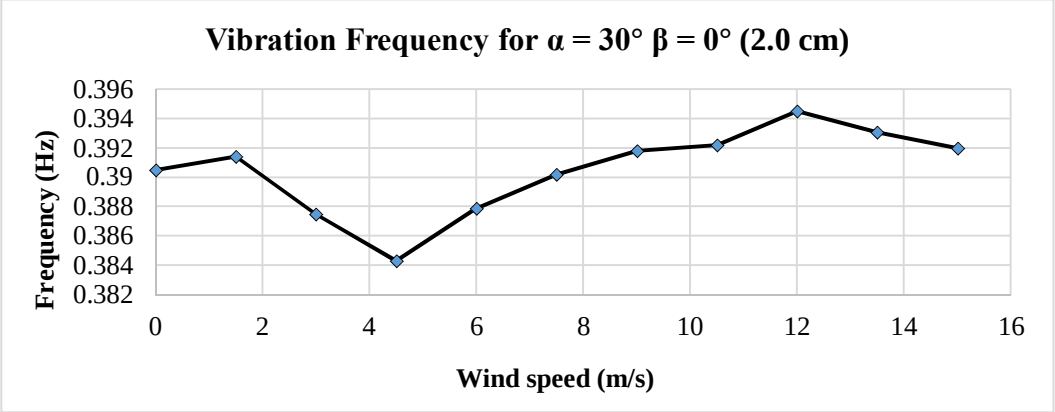

Figure 4.29 b) Vertical displacement frequency variation for Case 8, α = 30°, β = 0° with 2.0 cm ice thickness

The frequencies at different wind speeds obtained from the vertical responses recorded for the case 8 of α = 30°, β = 0° with 2.0 cm ice thickness are plotted in Figure 4.29 b). The minimum vertical vibration frequency was 0.384 Hz, and maximum vertical frequency was 0.395 Hz; after a slight increase at the beginning, the vibration frequency dropped until 0.384 Hz at 4.5 m/s wind speed, after which this started to increase until higher wind speeds of 12.0 m/s, from where the frequency became stable. The vertical response presented in Figure 4.17 showed a decrease at the same wind speed of 4.5 m/s.

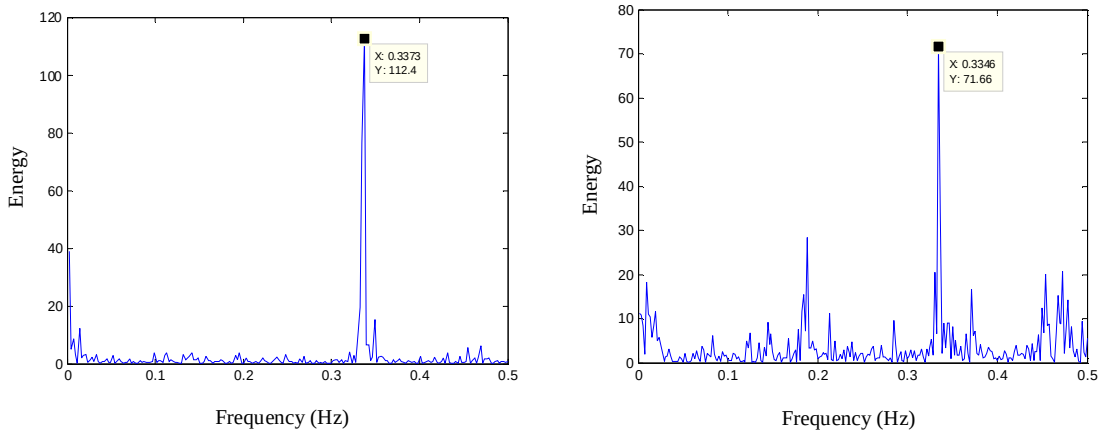

Figure 4.30 a) FFT of the vertical displacement for case 9 α = 0°, β = 15° , 2.0 cm ice thickness at 4.5 m/s and 15 m/s

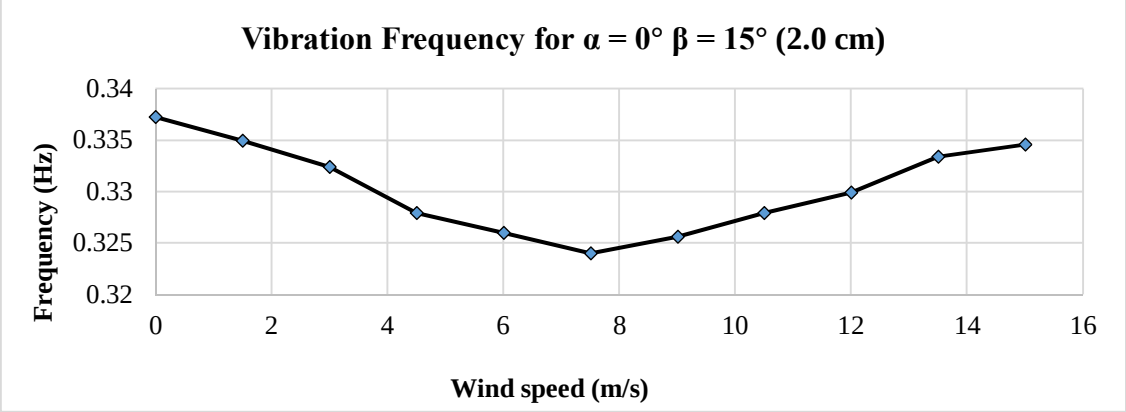

Figure 4.30 b) Vertical displacement frequency variation for Case 9, α = 0°, β = 15° with 2.0 cm ice thickness

Figure 4.30 shows the frequency variation for the vertical displacement recorded for the test case 9 of α = 0°, β = 15° with 2.0 cm ice thickness. The minimum vertical vibration frequency was 0.324 Hz, and maximum vertical frequency was 0.337 Hz. A drop occurs when the wind speed reaches 7.5 m/s wind speed and the frequency begins to increase to finally become stable at higher wind speeds. The vertical response for the Case 9 showed a sudden decrease in amplitude for the same wind speed of 7.5 m/s.

In order to compare the frequency variation at different wind speeds for the cable models with 1.0 cm ice accretion (Cases 1, 2 and 4) and with 2.0 cm ice accretion (Cases 7, 8 and

9), the Strouhal formulation was applied, for normalizing the frequencies with the wind speed and the diameter of each cable model. The Eq. 2.2 was used, as $S_t = f_{st}D/U$, where f_{st} was the frequency of the vertical response reported in Figures 4.20 to 4.30 above, U was the wind speed for each and D was the diameter of the cable model exposed to the wind direction.. The cable model geometry which is directly exposed to the incoming wind speed includes the ice accretion profile, as schematically represented for the cable model with 1.0 cm ice accretion in Figure 4.31; therefore the height of the ice profile was added to the diameter of the cable model for normalizing the frequencies as per the Eq. 2.2 above. Also the relative angle of attack was considered when calculating the dimensions of the diameter and the ice profile exposed to wind as per Eq. 2.2 in Chapter 2. Thus the total cable diameter was considered as:

$$Dtot = (Dcable + Height\ ice\ profile)*\cos(q) \qquad \text{(eq. 4.1)}$$

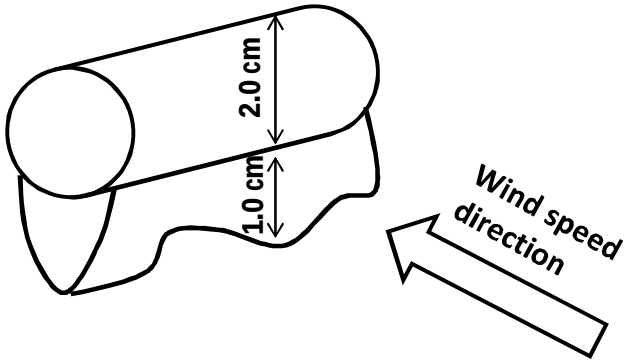

Figure 4.31 Schematic representation of the cable model with 1.0 cm ice profile exposed to wind direction

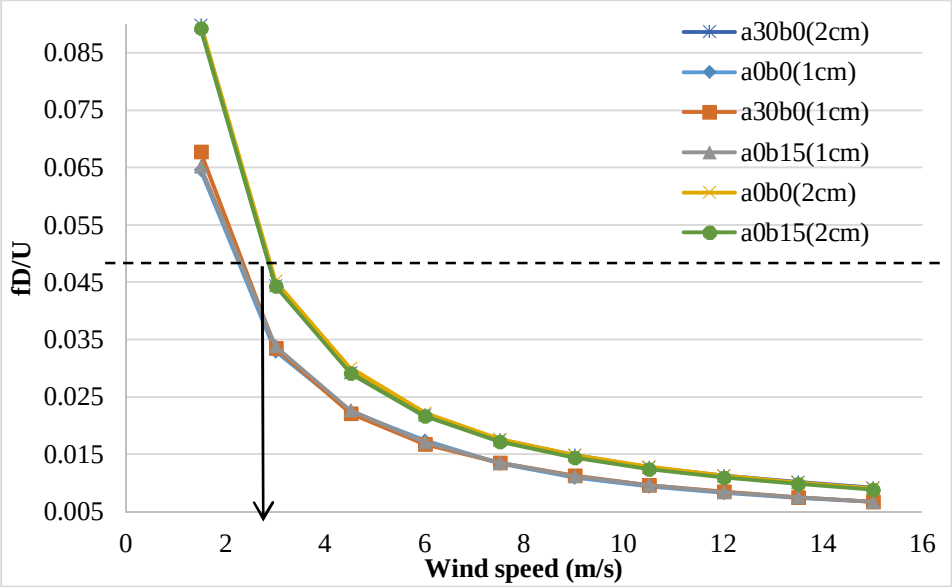

Figure 4.32 Variation of the fD/U normalized frequency for the vertical response

By normalizing the frequency of the vertical response by the diameter of the model, Dtot and the wind speed, which is a standard data interpretation method for the wind tunnel results, a better comparison can be made for the tested cases. As it can be noticed in Figure 4.32 the normalized frequencies fD/U of the vertical response are decreasing with the increase of the wind speed, which is expected from the application of the normalization formula. Also, in spite of the frequencies variations presented in the Figures 4.20 to 4.30, when normalized, the fD/U frequencies for the cable model with 1.0 cm ice profile were consistent for all the relative angles tested, while the fD/U frequencies for the cable model with 2.0 cm ice profile were completely overlapping.

The logarithmic decrement ζ can be calculated as [49]:

$$\zeta = \frac{1}{\sqrt{1+\left(\frac{2\pi}{\ln(x_0/x_1)}\right)^2}} \qquad \text{(Eq. 4.2)}$$

x_0 is the left peak and x_1 is the first peak to its right registered in the free vibration test.

$$\zeta = \frac{1}{\sqrt{1+\left(\frac{2\times 3.14}{\ln(1.04)}\right)^2}} = 0.0076 \qquad \text{(Eq. 4.3)}$$

Based on Eq. 2.1 and Eq. 2.2, the critical Scruton number S_c can be obtained. Thus, for cable Model 1:

$$S_c = \frac{0.5 \times 0.0076}{2 \times 3.14 \times 1.29 \times 0.02 \times 0.02} = 2.1 \quad \text{(Eq. 4.4)}$$

Therefore critical wind speed Ucr can be obtained as (Eq 2.2):

$$Ucr = 0.39 \times 0.2 \times 40 \times \sqrt{2.1} = 4.5 \text{ m/s} \quad \text{(Eq. 4.5)}$$

For cable Model 2:

$$\zeta = \frac{1}{\sqrt{1+(\frac{2 \times 3.14}{\ln(1.15)})^2}} = 0.024 \quad \text{(Eq. 4.6)}$$

$$S_c = \frac{0.7 \times 0.024}{2 \times 3.14 \times 1.29 \times 0.02 \times 0.02} = 5.1 \quad \text{(Eq. 4.7)}$$

$$Ucr = 0.33 \times 0.2 \times 40 \times \sqrt{5.1} = 6.0 \text{ m/s} \quad \text{(Eq.4.8)}$$

For cable Model 3:

$$\zeta = \frac{1}{\sqrt{1+(\frac{2 \times 3.14}{\ln(1.27)})^2}} = 0.038 \quad \text{(Eq. 4.9)}$$

$$S_c = \frac{0.9 \times 0.038}{2 \times 3.14 \times 1.29 \times 0.02 \times 0.02} = 10.5 \quad \text{(Eq. 4.10)}$$

$$Ucr = 0.29 \times 0.2 \times 40 \times \sqrt{10.5} = 7.5 \text{ m/s} \quad \text{(Eq. 4.11)}$$

Therefore the critical wind speeds Ucr determined based on the experiments performed for the ice-accreted cables for Model 1, Model 2 and Model 3 are 4.5 m/s, 6.0 m/s and 7.5 m/s, respectively which indicates that the galloping phenomenon can occur when wind speed reaches these corresponding wind speeds; a second galloping instability verification can be carried out by employing the Den Hartog criterion once the drag and lift coefficients results from the CFD simulation are introduced. Thus the validation of the CFD model for the currently performed experiment can also be done.

Moreover the Eq. 2.2 presented in section 2.3 states that the galloping divergent vibration can occur for frequencies fD/U lower than 0.05. Therefore, Figure 4.32 indicates that the galloping divergent vibration could occur, for both cable models, with 1.0 cm ice accretion and with 2.0 cm ice accretion, from wind speeds as low as 3.0 m/s, however the sudden changes in the vertical response frequencies presented in Figures 4.20 to 4.30 showed that the high-amplitudes wind-induced vibrations occurred at different wind speeds, depending on the angle of attack and the height of the ice profile tested: 4.5 m/s for Model 1- test Cases 1, for Model 2 – Test Cases 3 and 8, and for Model 3 – Test Case 6, 6.0 m/s for Model 1- test Cases 2 and for Model 2- test Cases 4, and 7.5 m/s for Model 1-test Cases 7, and for Model 3-test Cases 9. These critical wind speeds identified in the wind tunnel correspond to 30 m/s, 38 m/s and 44 m/s respectively, using the similarity scaling Eq. 2.2

4.4 Comparison of vertical displacements with other experiments.

Numerous experimental studies for bridge stay-cables perpendicular and inclined in regard to the wind speed direction are available in the literature, but these studies were performed on cable models without the ice profile accretion. In order to clarify the effect of the ice accretion attached to the cable circumferences, two experimental results conducted in similar test conditions as the current experiment, were selected from the available literature for comparing the wind-induced vertical response.

He et al [29] conducted a wind tunnel experiment for simulating rain-induced vibration of a bridge stay-cable model vertically and horizontal inclined in regard to the wind speed

direction. The diameters of the cable models were 139 mm and 136 mm and the tests were performed for the wind speeds in the range of 0.5 m/s to 20 m/s, considering incoming rain precipitations at 85 mm/h. Several inclined angles of the cable models were considered, however the closest to the current study was the case of $\alpha = 35°$ and $\beta = 26°$, which was compared with the test Case 3 from the current experiment which had $\alpha = 30°$ and $\beta = 15°$ with 1.0 cm ice thickness and with the test Case 8 which had $\alpha = 30°$, $\beta = 0°$ for 2.0 cm ice accretion. Therefore the test conditions were not identical, in terms of the vertical and horizontal inclination angles, and in order to describe the settings better the conversion to the relative angle of attack, formed between the cable axis and the wind direction, was performed for each case used in the comparison.

The experimental case with model diameter 139 mm was used for the comparison, for which the displacement of the rain-induced vibration was reported in Figure 2.12 [29].

The general formulation for the relative angle of attack can be presented as mentioned in the section 3.3 above as:

$$\cos\theta = \cos\alpha\cos\beta \quad \text{(Eq. 4.12)}$$

For the experiments conducted by He et al [29] the smallest relative angle of attack for the cable model with rain-induced vibration was:

$$\theta = \arccos(\cos 36°\cos 25°) = \arccos(0.809\times 0.90) = 43.27° \quad \text{(Eq. 4.13)}$$

For the currently performed experiment, the closest tested case of the cable model with ice accretion, in terms of the relative angle was the test Case 5 $\alpha = 30°$, $\beta = 15°$ for 1.0 cm ice accretion and the test Case 8 for $\alpha = 30°$, $\beta = 0°$ for 2.0 cm ice accretion;

$$\theta = \arccos(\cos 30°\cos 15°) = 33° \quad \text{(Eq. 4.14)}$$

$$\theta = \arccos(\cos 30°\cos 0°) = 30° \quad \text{(Eq. 4.15)}$$

Also two cable diameters were tested by He et al [29], one model had 169 mm and a second model had 139 mm. The results obtained for the cable model with diameter of 139 mm were used for the comparison with the vertical response results obtained in the current experiment for the cable model of 20 mm.

The maximum displacement for the rain-induced vibration of the cable model inclined at α =36° β = 25° (θ = 43.27°) was 10.9 mm registered at wind speed 14 m/s, as presented in Figure 4.33. The maximum vertical displacement for the stay-cable with 1.0 cm ice thickness for the case of α = 30°, β = 15° (θ = 33°) was 18.23 mm as also presented in Table 4.1, however at 14 m/s wind speed, the vertical vibration was around 11 mm as it can be seen in Figure 4.33.

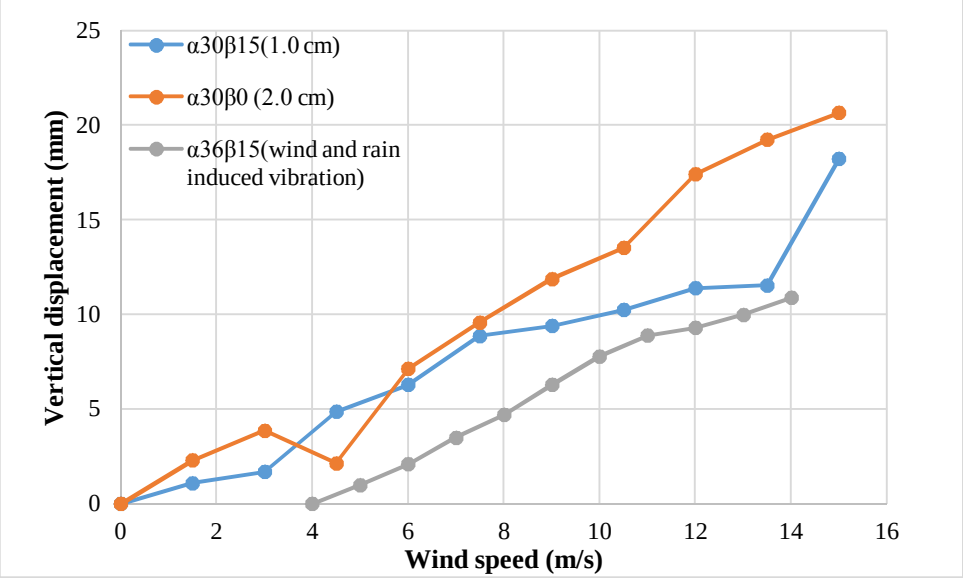

Figure 4.33 The vertical vibration for the wind and rain-induced vibration for the case α = 36°, β = 25° [14] and ice accretion for case 5 α =30°, β = 15° and case 8 α =30°, β = 0°

It can be concluded that the vertical vibration is increasing as the horizontal and vertical inclination angles α, β increase, thus for higher relative angles, and larger cable diameters, the vertical displacements for the rain-induced vibrations were still smaller than the vertical vibration of the stayed-cable with ice accretion. Therefore, it can be considered that for the tested cases, the vibration of the stay-cables with ice accretion is usually more

critical than the rain-induced vibrations of stay-cables. Also the different diameters of the cable might affect the discrepancy between the vertical vibrations of the cables models compared in Figure 4.33.

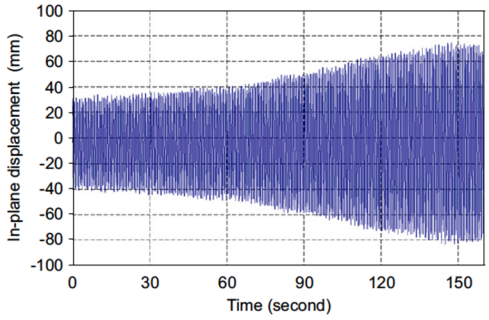

Figure 4.34 Time history of displacement for the dry inclined cable with α = 54.7° and β = 35.3°, at 32 m/s [41]

Cheng et al (2008) [41] conducted a wind tunnel experiment for simulating the vibration of dry inclined stay-cables, with a total length of the cable of 6.7 m and diameter of 160 mm; the maximum tested wind speed was 32 m/s. Figure 4.34 presents the displacement of the inclined dry cable with α = 54.7°, β = 35.3°, for which the relative angle is:

$$\cos\theta = \arccos(\cos\alpha\cos\beta) = \arccos(\cos 54.7°\cos 35.3°) = 61.96° \qquad \text{(eq. 4.16)}$$

For the currently performed wind tunnel test, the closest inclination case was α = 60°, β = 15°, for the cable model with 1.0 cm ice accretion:

$$\cos\theta_{ice} = \arccos(\cos\alpha\cos\beta) = \arccos(\cos 60°\cos 15°) = 61.31° \qquad \text{(eq. 4.17)}$$

Figure 4.6 b) represents the vertical vibration for the cable case with 1.0 cm ice thickness, for which the maximum registered displacement was 35 mm, while the minimum displacement was around 10 mm, but most of the recorded vertical displacement was

around 20 mm. Figure 4.34 shows the minimum vertical displacement for the dry cable under the effect of wind [41] was around 20 mm, and the maximum vertical displacement was around 60 mm; obviously, the displacement for the dry inclined cable is larger than the displacement for the cable with ice accretion, but the difference of displacement between the two cases is not significantly large considering the fact that the cable models diameters, the wind speeds and the lengths of the model for the dry inclined cable were much higher than these of the cable model with ice accretion, used in the current experiment. In other words, if ice accretion it is not present on the surface of the model, the difference in the wind-induced response would become even higher, therefore, the conclusion that the impact the ice profile has on the cable vibration is very significant, can be formulated.

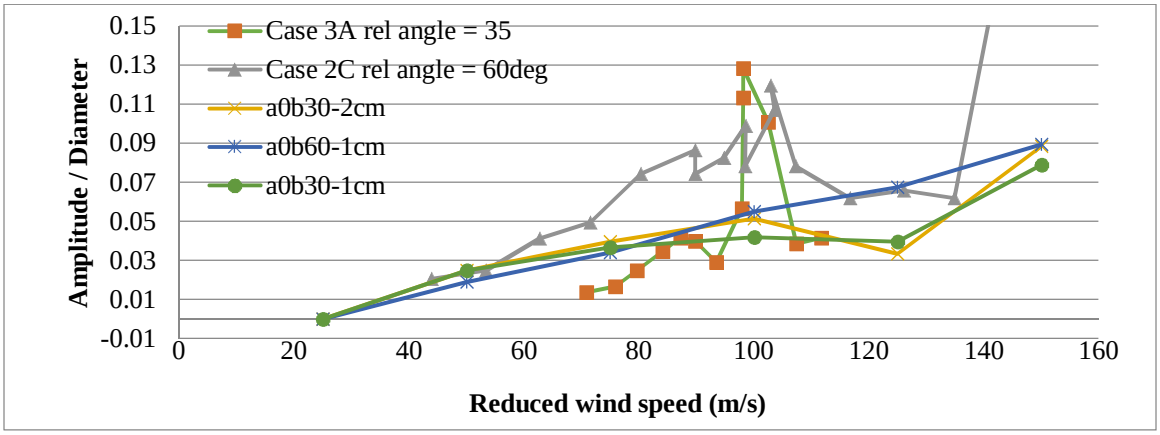

Figure 4.35 Non-dimensional vertical response for dry cables $\alpha = 35°$ $\beta = 0°$ and $\alpha = 60°$, $\beta = 54.7°$ [41] and for ice-accreted cables for $\alpha = 0°$ $\beta = 30°$, $\alpha = 0°$ $\beta = 60°$

Also the average vertical responses for $\alpha = 35°$ $\beta = 0°$ and for $\alpha = 60°$, $\beta = 54.7°$ vertical and horizontal inclination angles for the dry cable tested by Cheng et al [41] were considered when comparing with the results obtained from the current experiment, performed for the bridge cable with ice accretion. For a direct comparison the non-dimensionless vertical vibrations A/D, where A is the amplitude of the vibration and D is the diameter of the cable model, were determined and the reduced wind speed was used as B/fU (Figure 4.35); it was noticed that for the relative angle of attack of around θ =

30°, the dry cable had lower vertical response than the cable models with ice accretion of 1.0 cm and 2.0 cm, except for the reduced wind speeds of 97 to 103, for which very high amplitudes of vibrations were reported for the dry cable, of circular cross-section, as it can be noticed in Figure 4.35. Therefore the variation of the cross-section determined by the ice profiles, had the effect of stabilizing the vertical vibrations for these reduced wind speeds. For the relative angle of attack of around $\theta = 60°$, which was indicated as a critical case for the dry cable, by the study carried out by Cheng et al [41], the vertical response of the cable models with 1.0 cm and 2.0 cm ice profiles was smaller than the vertical response of the dry cable, especially for the reduced wind speeds of 62 to 107; moreover for the reduced wind speeds higher than 134, the dry cable recorded divergent vibrations, indicating the galloping instability, which was not similar to the ice accreted cable response (Figure 4.35).

The differences in the vertical response of the cables might also be caused by the fact that Cheng et al [41] considered the amplitudes as the average of the responses registered at both extremities of the cable, because the cable model they employed was longer and the extremities might be slightly offset during the recorded vibrations; in the current experiment the response was smoother, because the average was considered over time, for the time history of the responses recorded at the same extremity of the cable model, but at the ends of the steel T-bar on which the cable model was connected through the springs. This measurement method was required for estimating the rotation angle and it could be employed because the length of the cable model was much shorter. Both measuring methods are accepted, but might lead to slightly different recorded responses. Also the damping ratios used by Cheng et al [41] were smaller than the damping ratios used in the current experiments.

4.5 CFD simulation for ice accreted cable models

The drag and lift aerodynamic force coefficients were not measured in the wind tunnel experiments, due to the equipment limitations; however, these are very important parameters for the static design recommendations for the bridge stay-cables and for the galloping vibrations verification criterion. Therefore a numerical simulation employing Computational Fluid Dynamics (CFD) was conducted for determining the drag and lift

coefficients for cable model with 1.0 cm ice accretion. The 1.0 cm dimension of the ice profile was selected for the CFD study considering the available results in the literature for similar ice accretion [38]. Several experimental cases of different vertically and horizontal inclination angles were selected as follows: the case which registered the highest wind-induced response during the wind tunnel experiment (case 6 of $\alpha = 60°$, $\beta = 15°$) for the cable model with 1.0 cm ice thickness, and the case for which the smallest response was measured in the experiment (case 1 of $\alpha = 0°$, $\beta = 0°$) with 1.0 cm ice thickness. For both cases, 10 m/s wind speed and 15 m/s wind speed were used for the CFD simulation, thus in total of four cases were performed.

Besides the drag and lift coefficients, the CFD simulation provided pressure contours, each contour corresponding to the surface of the cable model or to the a plane perpendicular to the cable model; thus for the cases presented in the Figures 4.36 to Figure 4.60 below, Contour 1 presents the pressure coefficient around the surface of the cable model, Contour 2 ,Contour 3 Contour 4 and Contour 5 represent the pressure distribution in four planes intersecting the cable models at 30 cm, 60 cm and 92 cm along its length for model 1 and intersecting at 60 cm, 120 cm, 184 cm for model 3. In the last contour 5 the pressure distribution was sampled in a plane intersecting the cable model along its length and perpendicular to the incoming wind direction.

The drag and lift coefficients are defined as [48]:

$$C_D = \frac{F_D}{\frac{1}{2}\rho U^2 B} \quad C_L = \frac{F_L}{\frac{1}{2}\rho U^2 B} \qquad \text{(Eq. 4.18)}$$

F_D: drag force (N)

F_L: lift force (N)

ρ : air density, 1.29 kg/m^3 is the standard air density

B: The width (m), for this case, the diameter of the cable model.

The pressure coefficient is defined as [47]:

$$C_p = \frac{p - p_0}{\frac{1}{2}\rho U^2 B} \qquad \text{(Eq. 4.19)}$$

Where U is the mean value of the wind speed and $(p - p_0)$ is the pressure difference between the local and the far upstream pressure p_0, recorded in the CFD simulation.

4.5.1 CFD Case 6-1 α = 60°, β = 15° with 1.0 cm ice thickness at 10 m/s

The drag and lift coefficients for the case 1 of α = 60° and β = 15° were determined based on Eq. 4.18, considering that the nominal area exposed to the incoming wind speed direction was $7.03955 \times 10^{-3}\ m^2$, and the averaged lift force and drag forces for this case were -0.065 N and 0.05 N respectively. The drag and lift coefficients were obtained according to Eq. 4.18 as:

$$C_L = \frac{-0.065}{\frac{1}{2}\times 10\times 10\times 1.29\times 0.00703955} = -0.143 \qquad \text{(Eq. 4.20)}$$

$$C_D = \frac{0.05}{\frac{1}{2}\times 10\times 10\times 1.29\times 0.00703955} = 0.11 \qquad \text{(Eq. 4.21)}$$

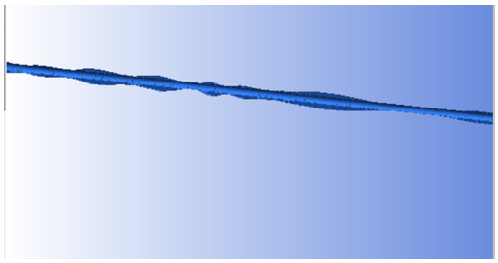

Figure 4.36 The cable model with 1.0 cm ice accretion for the case 1 of α = 60°, β = 15°

The cable model and the 1.0 cm ice accretion profile that was placed randomly along the cable for the case of α = 60°, β = 15°, with the geometry similar to the ice accretion model used in the wind tunnel experiment, is presented in Figure 4.36.

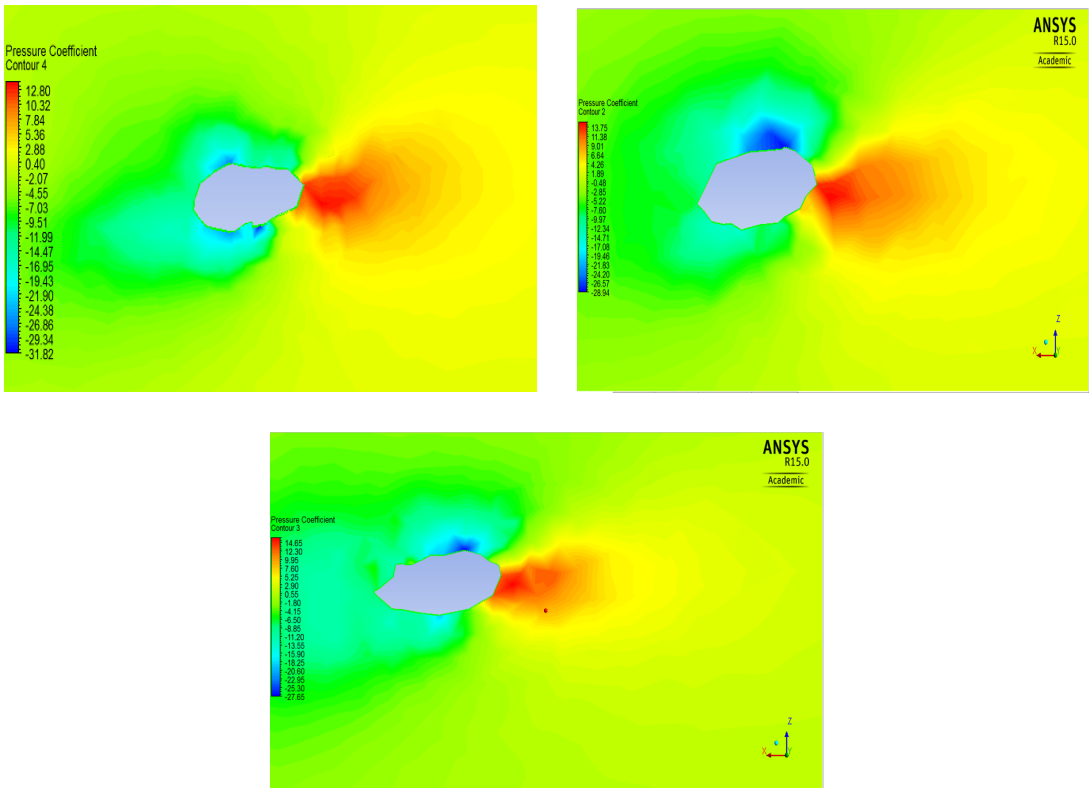

Figure 4.37 Pressure coefficient distribution on planes sectioning the cable model at 60 cm, 120 cm and 184 cm, for case 1 of $\alpha = 60°$, $\beta = 15°$ with 1.0 cm ice thickness at 10 m/s

The pressure coefficient distributions in planes perpendicular to the cable model including the ice profile, are presented in Figure 4.37. Because of the inclined direction of the cable model, the cross-section becomes an ellipse to which the un-uniform ice accretion profile shape is attached; the ice accretion shape varied along the length of the cable to better simulate the real ice accretion for cables, thus cross-sections have different shapes, depending on the plane where they were sampled. The direction of the wind speed was along the x axis, from right to left, and the surface of the cable which is in direct contact with the incoming flow has always bigger pressure coefficient of up to 14.65, as indicated by the regions of red color in Figure 4.37. Around the surface of the cable and around the ice accretion surface, which are not in direct contact with the incoming wind flow, the pressure coefficients are smaller, however because of the arrangement of the ice accretion, which is facing downwards, in the current case, on the

laterals of the cables and behind the cable, the pressure coefficient became negative indicating a suction region. The pressure coefficient varied along the length of the cable model registering higher values at the impact with the incoming wind flow, where the ice profile does not have any effect, of 12.8, 13.7 and 14.65 at 60 cm, 120 cm (middle point) and 184 cm along the cable respectively and the smallest values (higher suction) of -31.82, - 28.9 and – 27.65 for 60 cm, 120 cm (middle point) and 184 cm along the cable respectively.

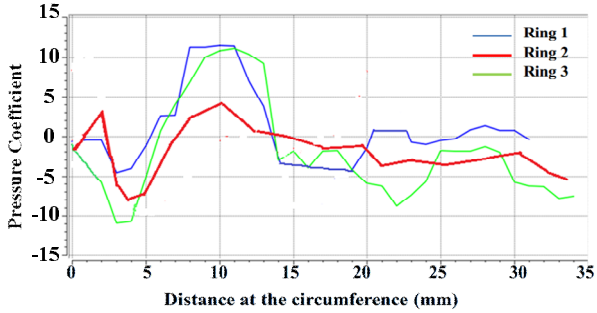

Figure 4.38 The pressure coefficient of the three planes for case α = 60°, β = 15° with 1.0 cm ice thickness at 10 m/s wind speed

Figure 4.38 shows the variation of the normalized pressure coefficient by the area of the cable model and the ice profile on which this was recorded and determined. The normalized pressure coefficient was determined at the surface of the cable model, along 3 rings obtained by intersecting the planes reported in Fig. 4.36 with the surface of the cable model. Thus the normalized pressure coefficients for the Ring 1, Ring 2 and Ring 3, at 60 cm, 120 cm (middle point) and 184 cm along the cable respectively, for the case 1 at α = 60°, β = 15° at 10 m/s wind speed is presented in Figure 4.38. A peak can be noticed which corresponds to the maximum pressure coefficient reported in Figure 4.40, on the cable surface, where the incoming wind speed impinges directly the model. Different negative values (suction) of the pressure coefficients are always noticed on the leeward side of the model surface, where the ice accretion is formed, because the cable is inclined in wind tunnel, and the ice shape is different for the 3 rings, Therefore it can be

noticed that the distribution of the pressure coefficient has negative values on the surface of the ice accretion, especially towards the lateral side of the surface of the ice profile, at the contact with the cable model, where the pressure coefficient becomes minimum. It might be concluded that due to the wind-induced pressure, the ice accretion might detach from the cable model and might fall down, for the bridge cable with 1.0 cm ice thickness, vertically and horizontal inclination at $\alpha = 60°$, $\beta = 15°$ at 10 m/s wind speed.

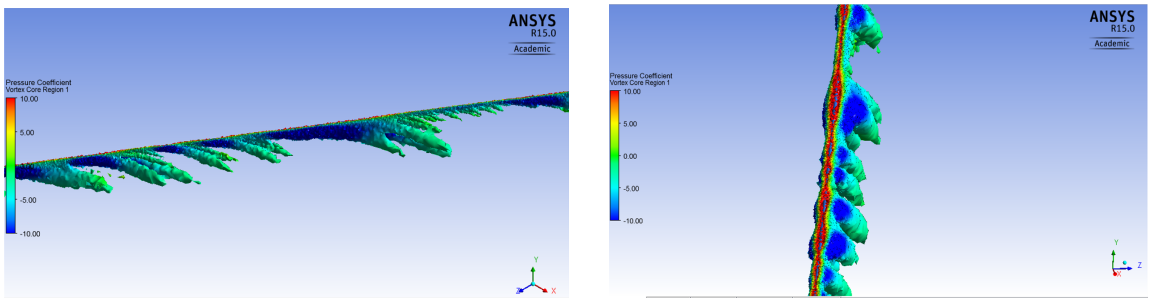

Figure 4.39 The pressure coefficient of the cable for case $\alpha = 60°$, $\beta = 15°$ with 1.0 cm ice thickness at 10 m/s wind speed

The wind flow formations detaching from the cable model are shown in Figure 4.39; the wind flow developed longitudinal vortices along the wind direction, detaching from the leeward side of the cable model, with the minimum value of the pressure coefficient within the flow vortex of -10, on the sharp area, and a maximum positive coefficient of 10 on the windward surface of the cable. Even if these are not attached to the cable surface still the very high suction might drag the leeward side of the cable model, thus having a destabilizing effect for the ice accretion formed in this region.

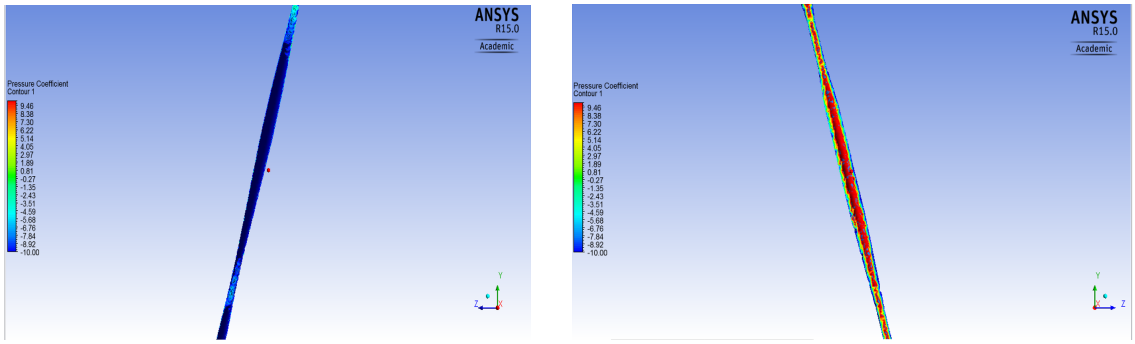

Figure 4.40 The pressure coefficient of the cable for case α = 60°, β = 15° with 1.0 cm ice thickness at 10 m/s wind speed

Figure 4.40 plotted the pressure coefficient on the windward and leeward surfaces of the cable respectively, for the case of α = 60°, β = 15° with 1.0 cm ice thickness at 10 m/s wind speed. These contours re-confirm the maximum pressure coefficient for case α = 60°, β = 15° as 9.46, and the minimum pressure coefficient is -10, as presented in the Figure 4.40.

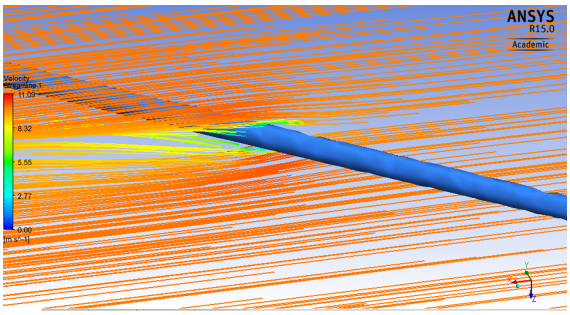

Figure 4.41 The streamlines around the cable for case α = 60°, β = 15° with 1.0 cm ice thickness at 10 m/s wind speed

The wind flow streamlines around the cable, for the case of α = 60°, β = 15° with 1.0 cm ice thickness at 10 m/s wind speed are presented in Figure 4.41. The velocity registered smaller values around the surface of the cable, because always, the wind flow is zero on

an object's surface. Thus the velocity in the vicinity of the cable's surface was around 5.55 m/s, but after the fluid passes the cable, the velocity reaches 8.32 m/s and higher up to a velocity of around 10 m/s.

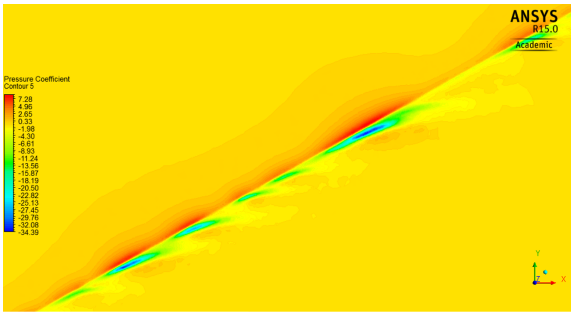

Figure 4.42 Pressure coefficient distribution within the flow formations along the cable model for the case α = 60°, β = 15° with 1.0 cm ice thickness at 10 m/s wind speed

Because the effect of the longitudinal flow formations might be decisive for the stability of the ice accretion on the surface of the cable, the pressure coefficients in a plane sectioning these flow formations, along the length of the cable was monitored in Figure 4.42. It could be noticed that, inside each of the longitudinal vortices detaching from the leeward side of the cable model, very high suction regions are formed of up to -34.39 pressure coefficients.

4.5.2 CFD Case 6-2 α = 60°, β = 15° with 1.0 cm ice thickness at 15 m/s

The nominal area of the cable model and the ice accretion profile exposed to the incoming wind speed for the case 4 of α = 60°, β = 15° with 1.0 cm ice thickness, was the same as for the case 1 modelled for the CFD simulation, namely 7.03955×10^{-3} m^2, but the lift and drag forces for this case were higher of -0.1411 N, and 0.1093 N respectively. The drag and lift coefficient were obtained according to Eq. 4.18.

$$C_L = \frac{-0.1411}{\frac{1}{2}\times 15\times 15\times 1.29\times 0.00703955} = -0.138 \qquad \text{(Eq. 4.22)}$$

$$C_D = \frac{0.1093}{\frac{1}{2}\times 15\times 15\times 1.29\times 0.00703955} = 0.107 \qquad \text{(Eq. 4.23)}$$

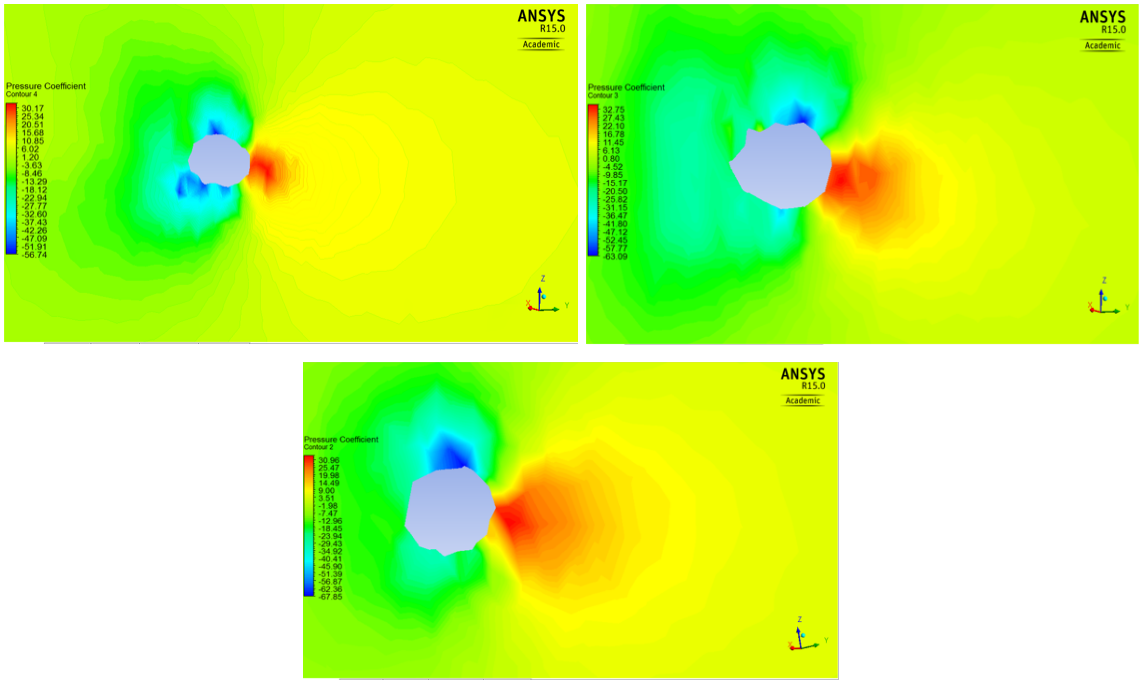

Figure 4.43 The pressure coefficient of the three planes for case α = 60°, β = 15° with 1.0 cm ice thickness at 15 m/s wind speed

Figure 4.43 represents the pressure distribution for the three planes perpendicular to the cable model at distances 60 cm 120 cm and 184 cm along the cable length, for the case of α = 60°, β = 15° with 1.0 cm ice thickness at 15 m/s wind speed. The maximum values of the pressure coefficients were signaled by the red color region in Figure 4.43, located at the contact point between the cable model and the incoming wind speed. The maximum value was 32.75 for the extremities of the cable and for the middle point of the model respectively. The pressure coefficient was positive for the surface in directly contacting the incoming wind flow, while on the leeward side of the model the pressure coefficient was negative. Because the ice shape was irregular, the value of pressure coefficient was different around each surface of the cable model. Therefore, the different ice shape could lead to more complicated wind-induced response than that of a simple dry cable vibration.

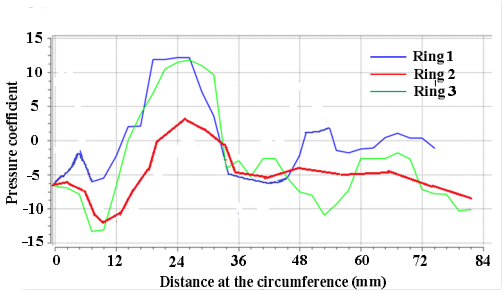

Figure 4.44 The chart for pressure coefficient of the three planes for case α = 60°, β = 15° with 1.0 cm ice thickness at 15 m/s wind speed

The variation of the pressure coefficient at the circumferences of the cable model, which is different than the pressure coefficient distribution reported for the flow domain planes in Figure 4.43 , was plotted in Figure 4.44 for the case of α = 60°, β = 15° with 1.0 cm ice thickness at 15 m/s wind speed. Ring 1 represents the pressure coefficient for the intersection line between the plane 1 located at 60 cm and the cable model, and Rings 2 and 3 represent the pressure coefficient for the intersection between the same cable model and the planes perpendicular to the cylinder, located at 120 cm and 184 cm respectively. As it can be noticed from Figure 4.44, the peak regions with positive pressure coefficients are located around the windward surface of the model where the incoming wind velocity impacts directly the model, and the minimum value for pressure coefficient is on the lateral side of the cable model from where the flow detaches; the ice accretion is situated on the leeward side of the cable model which can be observed in Figure 4.43, therefore, the ice profile might be subjected to higher suction, but this is not dominant for the ice accretion region. Also for the Ring 1, at the extremity of the cable, an increase of pressure could be noticed on the leeward side of the cable, which might be connected to the three-dimensional flow formations which are developed downstream the cable, as presented in the Figure 4.47 below

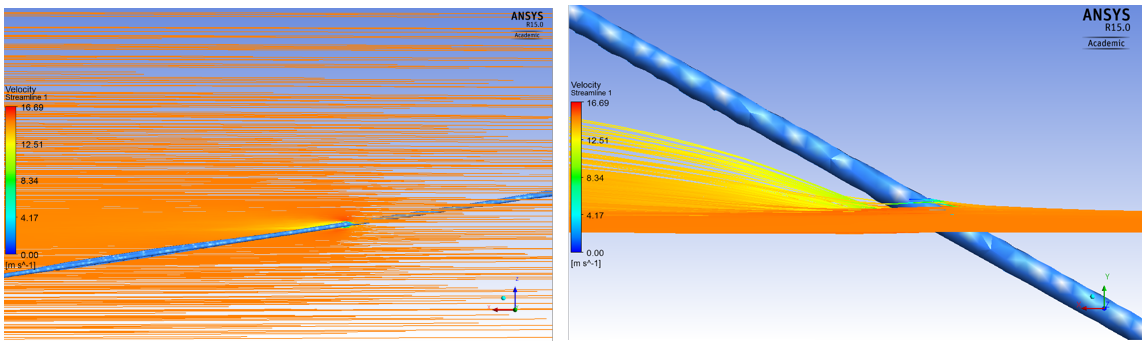

Figure 4.45 The streamlines for case α = 60°, β = 15° with 1.0 cm ice thickness at 15 m/s wind speed

The streamlines of the wind velocity, for the cable model case of α = 60°, β = 15° with 1.0 cm ice thickness is represented in Figure 4.45; it can be noticed that the velocity in the vicinity of the cable model became smaller, of around 12.5 m/s , while the average velocity is around the cable model was 16.69 m/s.

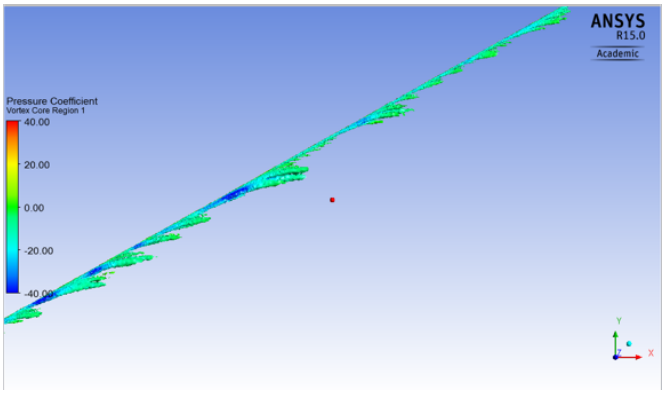

Figure 4.46 The pressure coefficient of the vortex core region for case α = 60°, β = 15° with 1.0 cm ice thickness at 15 m/s wind speed

The longitudinal vortices signaled for the case 2 of case α = 60°, β = 15° with 1.0 cm ice thickness but under the effect of the lower wind speed of 10 m/s wind speed, were noticed for the present case as well (Figure 4.46) and the pressure coefficients for three-

dimensional flow formations indicated a higher suction with pressure coefficient values of up to -40, for the leeward side of the cable model and downstream into the flow.

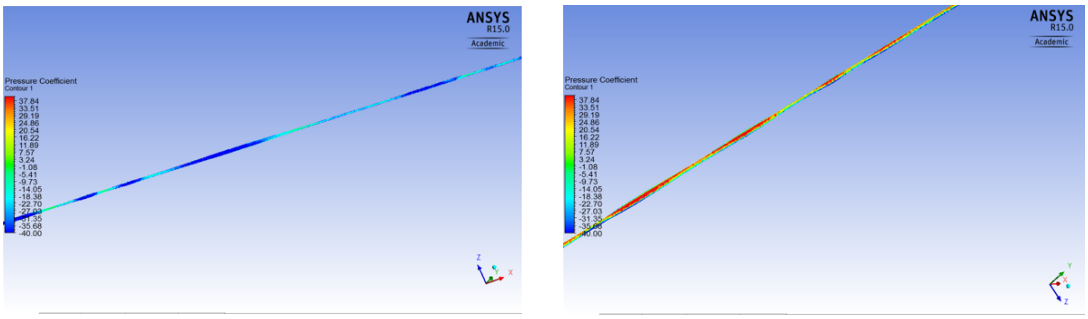

Figure 4.47 The pressure coefficient on the surface of the cable for case α = 60°, β = 15° with 1.0 cm ice thickness at 15 m/s wind speed

The pressure coefficient distribution on the windward and leeward surfaces of the cable model, for the case of α = 60°, β = 15° with 1.0 cm ice thickness at 15 m/s wind speed, as represented in Figure 4.47, showed a maximum value of 37.84, and the minimum value -40 for the pressure coefficient distributed on the windward and leeward cable surfaces respectively.

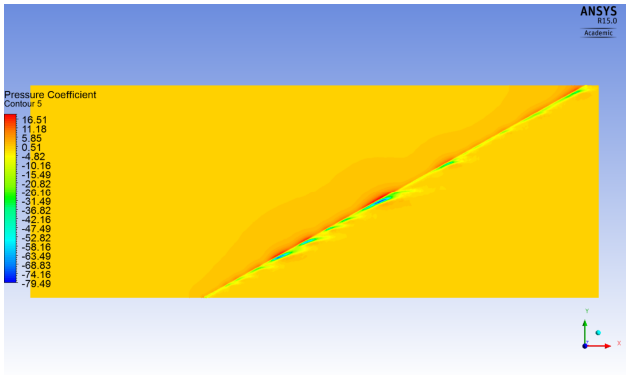

Figure 4.48 The pressure coefficient of contour 5 for case α = 60°, β = 15° with 1.0 cm ice thickness at 15 m/s wind speed

The pressure coefficient distribution in a plane sectioning the cable model and the three-dimensional flow formations developed on the leeward side of the cable is presented in Figure 4.48. The pressure coefficient is different on the surface of the cable model, along the cable axis, and it can be observed that a strong suction was formed at the center of the longitudinal vortices detaching from the leeward surface of the cable model, located in the middle part of the cable. Such uneven pressure distribution might generate instability for the ice accretion situated in this region.

4.5.3 CFD Case 1-1 α = 0°, β = 0° with 1.0 cm ice thickness at 10 m/s

For comparing the pressure coefficient distributions for the cases of highest (Case 1 presented in section 4.5.1) and lowest vertical responses registered in the wind tunnel experiments, the vertically and horizontal inclination angles of α = 0°, β = 0° with 1.0 cm ice thickness at 10 m/s were also simulated employing the same CFD laminar flow conditions. For this case, the nominal area directly exposed towards the wind direction is $3.47285 \times 10^{-3}\ m^2$, the lift force for this case was -0.60 N, and the drag force was 0.009 N. These parameters lead to the lift and drag coefficients as presented in Eq. 4.18.

$$C_L = \frac{-0.60}{\frac{1}{2}\times 10\times 10\times 1.29\times 0.00347285} = -2.68 \qquad \text{(Eq. 4.24)}$$

$$C_D = \frac{0.009}{\frac{1}{2}\times 10\times 10\times 1.29\times 0.00347285} = 0.04 \qquad \text{(Eq. 4.25)}$$

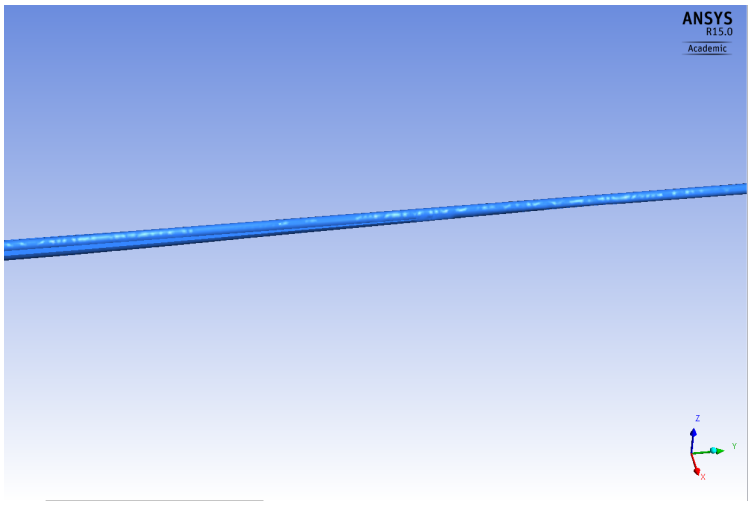

Figure 4.49 The cable model for case α = 0°, β = 0° with 1.0 cm ice thickness at 10 m/s wind speed

The cable model and the ice accretion geometry which is placed downwards around the surface of the cable, can be observed in Figure 4.49. Similar to the model used in the wind tunnel experiment, the thickness of the ice accretion was modeled randomly along the length of the cylinder, however, the average value of thickness for the ice was considered as 1.0 cm.

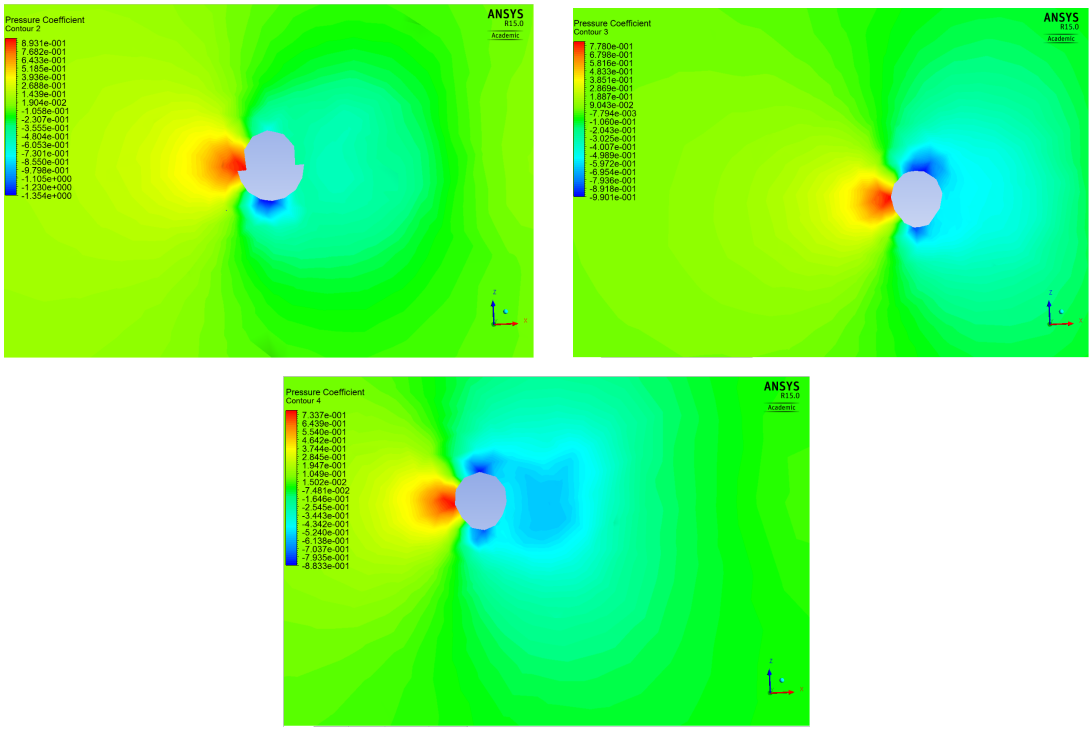

Figure 4.50 Pressure coefficient distribution on planes sectioning the cable model at 30 cm, 60 cm and 92 cm, for case 2 of $\alpha = 0°$, $\beta = 0°$ with 1.0 cm ice thickness at 10 m/s

The distribution of the pressure coefficients for the three planes located at the same distance along the length of the cable as for the previous Case 3 are presented in Figure 4.50, for the cable model case of $\alpha = 0°$, $\beta = 0°$ with 1.0 cm ice thickness at 10 m/s wind speed; the direction of wind was from left to right, along x axis. For the extremities of the cable model, where the thickness of the ice profile is not very big, the maximum pressure coefficients measured at the direct impact with the wind flow were 7.37 and 7.78 respectively and high suctions of up to -8.8 and -9.9 were noticed on both upwards and downwards surfaces of the cable. For the middle point of the cable model, where the ice profile reached is maximum height of 1.0 cm, the pressure coefficient at the impact with the wind flow was 8.93 and suctions of up to -13.5 were signaled only on the downwards surface of the model, where the ice accretion is formed.

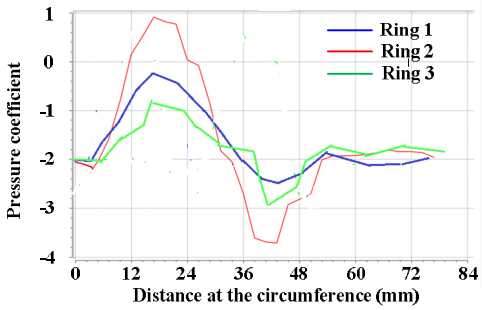

Figure 4.51 The pressure coefficient of the three planes for case α = 0°, β = 0° with 1.0 cm ice thickness at 10 m/s wind speed

The pressure coefficients for the three Rings located at the same distances along the cable length as the planes presented on Fig. 4.50, the pressure coefficient on the surface of the cable model is plotted in Fig. 4.53, for the case α = 0°, β = 0° at 10 m/s wind speed are presented in Figure 4.51. Ring 1, Ring 2 and Ring 3 show the pressure coefficients at the circumference of the cable model and the ice profile at different location along the cable model, corresponding to the distribution contours presented in Figure 4.44, namely at 30 cm, 60 cm (middle point) and 92 cm. The highest values for both high pressure and suction were registered for Ring 1 and were 9.0 and -23 respectively. Always the peaks associated with the maximum values of the pressure coefficients are signaled at the impact point between the cable model and the incoming wind flow. The pressure coefficient starts to register negative values (suction) towards the bottom side of the cable, where the minimum value of the pressure coefficients were noticed; also the ice accretion is formed on the bottom side of the cable, therefore the high suction registered in this area indicates that the ice might fall down due to the direction of the pressure; according to Figure 4.50, the part of the ice located near the extremities of the cable, registered pressure towards the surface of the cable, and this will help stabilizing the ice profile on the surface, and because of the pressure, this part of the ice accretion has less probability to fall down, when compared with the ice on the middle of the bottom surface of the cable. However the extremities of the cable bear a small part of the ice accretion, and the biggest piece situated in the middle of it might fall down due to the direction of the pressure. An interesting discussion could be conducted after the main part of the ice falls

down, and the remaining ice profile changes the entire shape of the ice accretion along the cable, which could affect the vibrations of the cable.

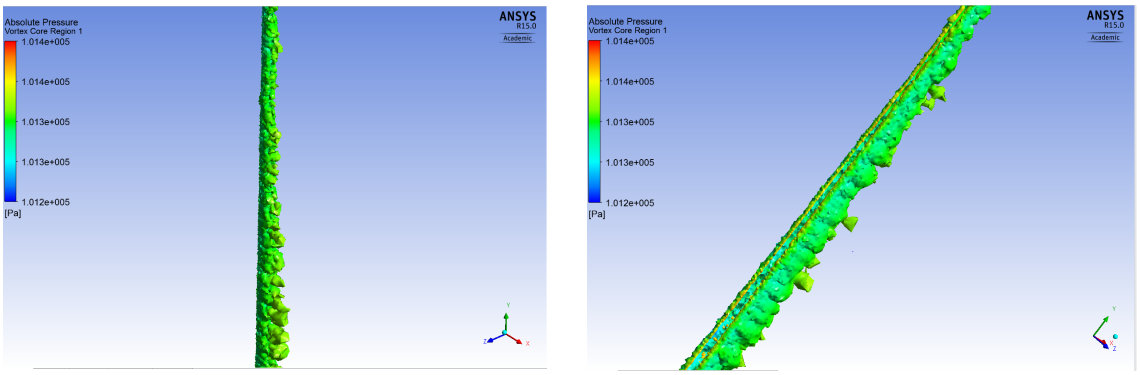

Figure 4.52 The vortex core region 1 for case α = 0°, β = 0° with 1.0 cm ice thickness at 10 m/s wind speed

The flow formations developed downstream the cable for the case of the cable model at α = 0°, β = 0° with 1.0 cm ice thickness at 10 m/s wind speed, do not resemble longitudinal vortices noticed for the case 2 above, but shows a more uniform flow detaching from the leeward side of the cable as shown in Figure 4.52. The average value of the pressure registered for the flow formations around the cable model was about 1.03×10^5 Pa.

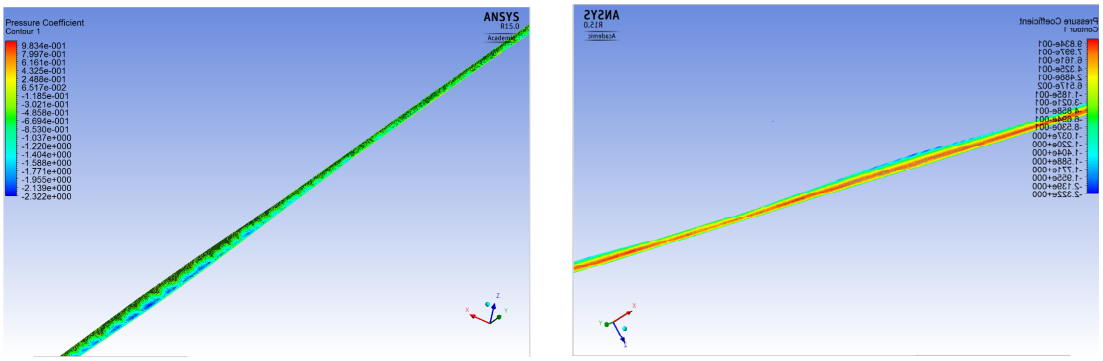

Figure 4.53 The pressure coefficient on the surface of the cable for case α = 0°, β = 0° with 1.0 cm ice thickness at 10 m/s wind speed

The variation of the pressure coefficients on the windward and leeward surfaces of the cable respectively is presented in Figure 4.53. The maximum value for pressure coefficient in this case was around 9.8, the minimum value for the case is around -23.22.

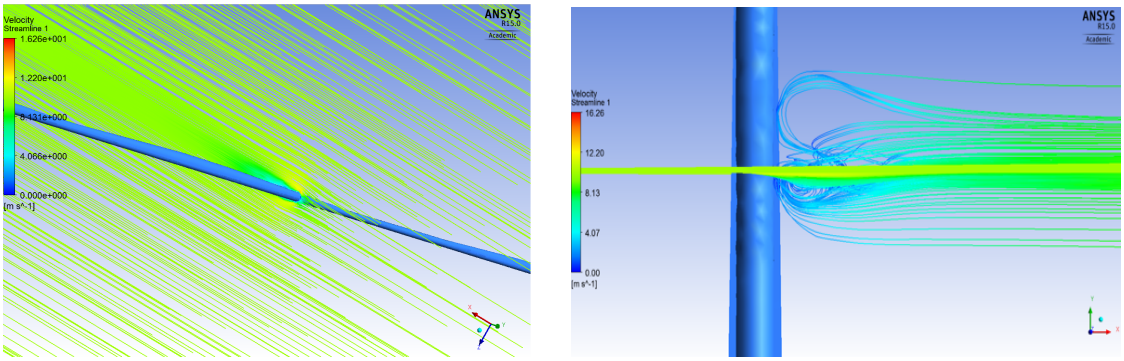

Figure 4.54 The streamlines for case α = 0°, β = 0° with 1.0 cm ice thickness at 10 m/s wind speed

Figure 4.54 shows the wind flow streamlines for the case of α = 0°, β = 0° with 1.0 cm ice thickness at 10 m/s wind speed. The average velocity of the streamline was around 8.431 m/s, but the velocity could reach up to 12.20 m/s on the lateral sides of the cable, where the wind speed is accelerated by the detachment of the flow from the cable model.

4.5.4 CFD Case 1-2 α = 0°, β = 0° with 1.0 cm ice thickness at 15 m/s

For the same cable model case of α = 0°, β = 0°, but under the effect of 15.0 m/s, the nominal area of the model exposed to the incoming wind speed was had the same value $3.4728 \times 10^{-3} m^2$, but the averaged lift and drag forces were higher registering values of -0.71 N, and 0.01 N respectively. Thus the lift and drag coefficients were obtained as follows:

$$C_L = \frac{-0.71}{\frac{1}{2} \times 15 \times 15 \times 1.29 \times 0.00347285} = -1.4 \qquad \text{(Eq. 4.26)}$$

$$C_D = \frac{0.01}{\frac{1}{2} \times 15 \times 15 \times 1.29 \times 0.00347285} = 0.0218 \qquad \text{(Eq. 4.27)}$$

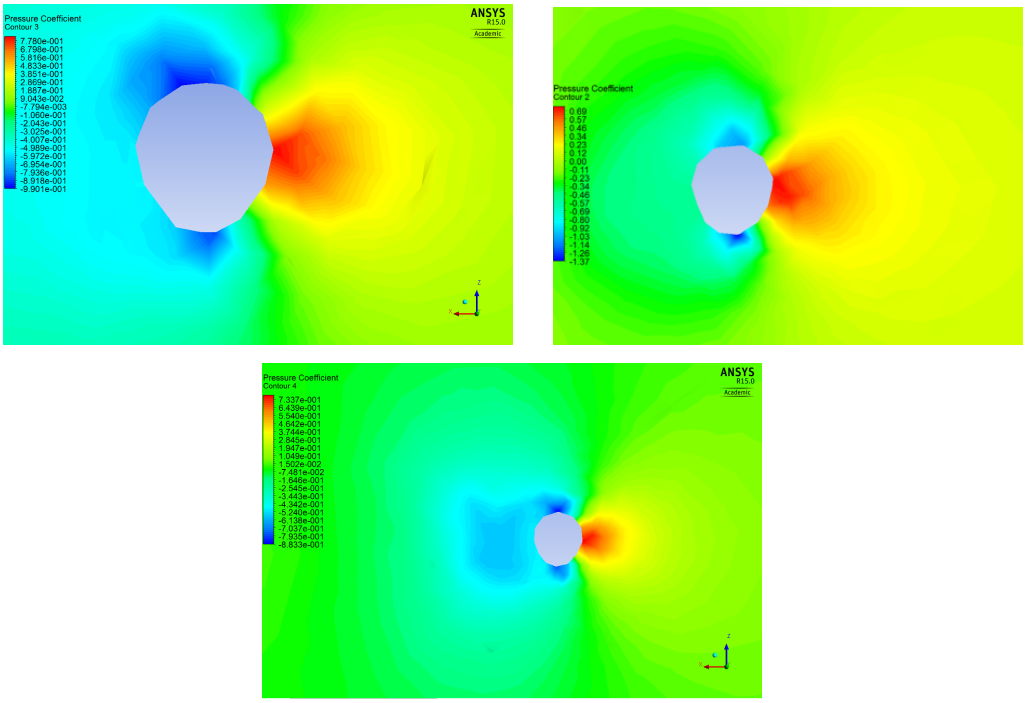

Figure 4.55 Pressure coefficient distribution on planes sectioning the cable model at 30 cm, 60 cm and 92 cm, for case 4 of α = 0°, β = 0° with 1.0 cm ice thickness at 15 m/s

The pressure coefficients distribution for different planes perpendicular to the cable model at distances 60 cm 120 cm and 184 cm along the length of the cable are plotted in Figure 4.55, for the cable model case of α = 0°, β = 0° with 1.0 cm ice thickness; the direction of the incoming wind speed was from right to left, along the x axis, while the ice profile was modeled on the downwards side of the cable. The maximum values for the pressure coefficient were registered at the impact point between the cable model and the incoming wind speed and registered values of 0.78 and 0.7337 for the extremities of the cable and 0.89 for the middle point of the cable model. High suction was noticed for the upwards and downwards sides of the cable model for the extremities of the cable, but the highest suction indicated by a pressure coefficient of -1.354 was noticed on the middle point of the cable on the downwards side of the cable mode, where the ice accretion profile was modelled.

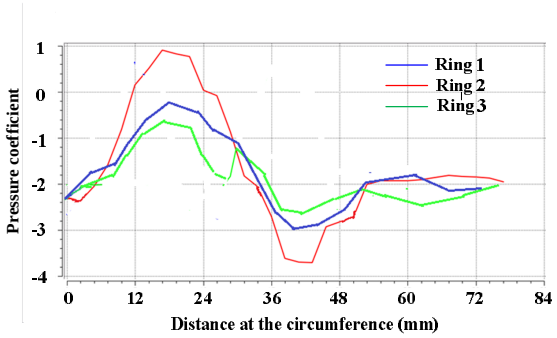

Figure 4.56 The chart for pressure coefficient of the three planes for case α = 0°, β = 0° with 1.0 cm ice thickness at 15 m/s wind speed

The pressure in the flow domain presented in Figure 4.56 is different than the actual wind-induced pressure at the surface of the cylinder, thus the variation of the pressure coefficient for the 3 Rings situated on the circumferences of the model, along the intersection lines of the three planes defined at the 60 cm 120 cm and 184 cm and the cable model for the case of α = 0°, β = 0° at 15 m/s wind speed is presented in Figure 4.49. The maximum value of the pressure coefficient, indicated by the peak in Figure 4.55, was registered for all the three regions of the cable at the same location on the surface of the model, where the incoming wind speed impacts directly the cable; the pressure coefficient decreased and became negative on the bottom surface of the cable, where the ice accretion is attached, for which the minimum pressure coefficients were negative therefore, the ice profile is under the effect of suction, and might fall down due to the wind-induced pressure.

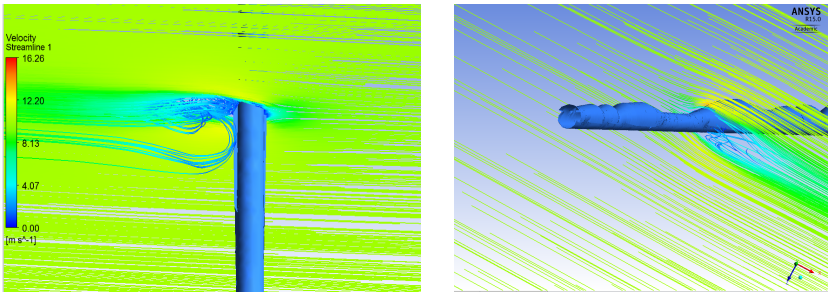

Figure 4.57 The streamlines for case α = 0°, β = 0° with 1.0 cm ice thickness at 15 m/s wind speed

Figure 4.57 shows the streamlines of the wind velocity for the cable case α = 0°, β = 0° with 1.0 cm ice thickness at 15 m/s wind speed. The wind speed approached the cable model and then detached from the lateral sides of the model; a turbulent flow formation was noticed behind the cable with streamlines suddenly changing their direction. The average velocity of the streamlines was around 8.131 m/s, and the velocity around the cable model was around 12.2 m/s.

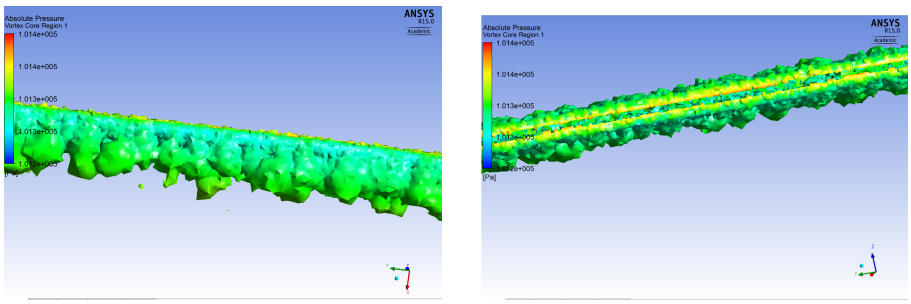

Figure 4.58 The pressure coefficient of the vortex core region for case α = 0°, β = 0° with 1.0 cm ice thickness at 15 m/s wind speed

The three-dimensional flow formations along the cable model, colored by the absolute pressure magnitude, for the case of α = 0°, β = 0° with 1.0 cm ice thickness is presented in Figure 4.58. Similar to the previous case, the flow formations are developed mainly on the leeward side of the cylinder and had a more uniform representation along the length of the cable. The maximum pressure value was around 101,400 Pa, and the minimum value was around 101,300 Pa.

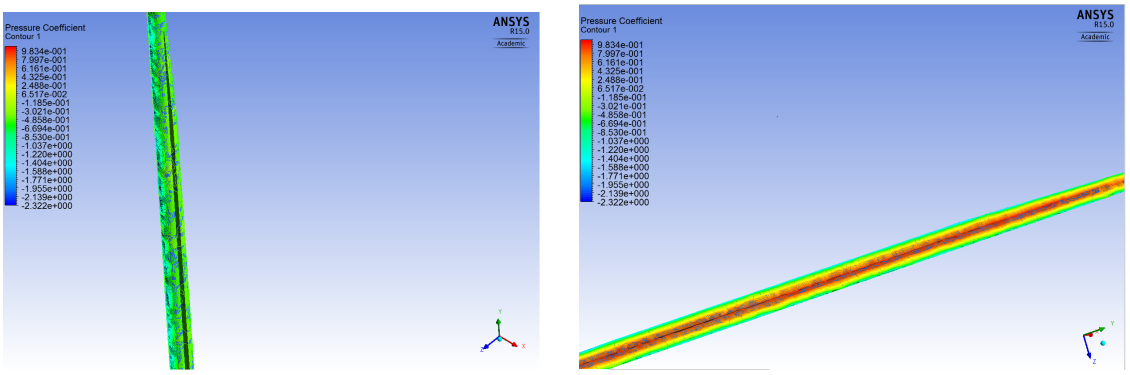

Figure 4.59 The pressure coefficient on the surface of the cable for case α = 0°, β = 0° with 1.0 cm ice thickness at 15 m/s wind speed

The pressure coefficient distributions on the surface of the windward and leeward surfaces of the cable model are plotted in Figure 4.59, for which was noticed that similar to the previous cases, the maximum pressure coefficient value of 0.983 was on the windward face, at the contact region with the incoming wind speed while the minimum value was -2.322.

4.5.5. Drag and lift coefficients and Den Hartog criterion verification

The criterion which can provide the verification for the galloping instability, as defined by Den Hartog's formulation [37] involves the variation of lift force coefficient and the drag force coefficient. Therefore, the lift and drag coefficients were determined from the CFD simulations, for the cable models with 1.0 cm ice thickness with vertical and horizontal inclination angles of α = 60°, β = 15° and at α = 0°, β = 0° for the 10 m/s and 15 m/s, and were summarized in the Table 4.2 below.

Table 4.2 Drag and lift coefficient for all cases

Modelling cases	C_D	C_L
Case 6-1 α = 60°, β = 15° (10 m/s)	0.11	- 0.143
Case 6-2 α = 60°, β = 15° (15 m/s)	0.107	-0.138
Case 1-1 α = 0°, β = 0° (10 m/s)	0.04	-2.68
Case 1-2 α = 0°, β = 0° (15 m/s)	0.02	-1.4

The values listed in Table 4.2 for the drag and lift coefficients, for all cases, were used for the galloping phenomenon verification.

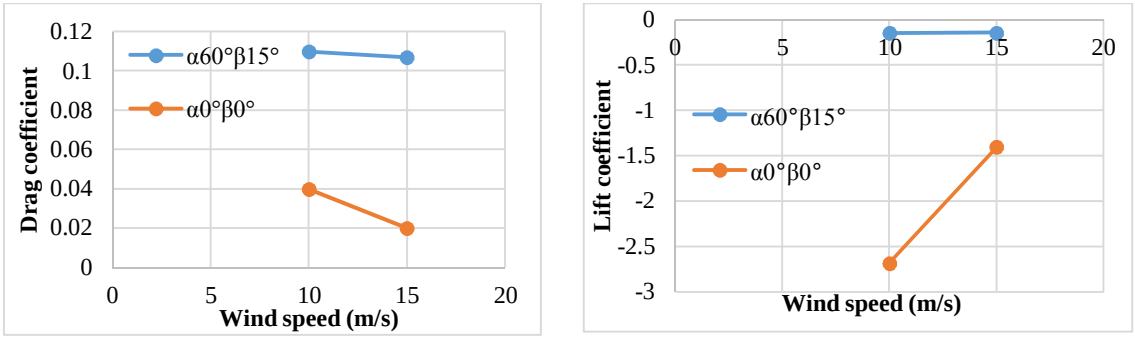

Figure 4.60 Drag coefficient and lift coefficient for the CFD cases 6 and 1 at α = 60°, β = 15° and α = 0°, β = 0°

The change of drag and lift coefficients with the increase of the wind speed is plotted in Figure 4.60, and it was noticed that in general, the horizontal and vertical inclination angles have a significant effect on the magnitude of the drag and lift coefficients, which registered very different values between the two investigated cases. For the flow perpendicular to the cable model, (Case 1, α = 0°, β = 0°), both drag and lift coefficients are higher than the cable inclined at α = 60°, β = 15° (Case 6).

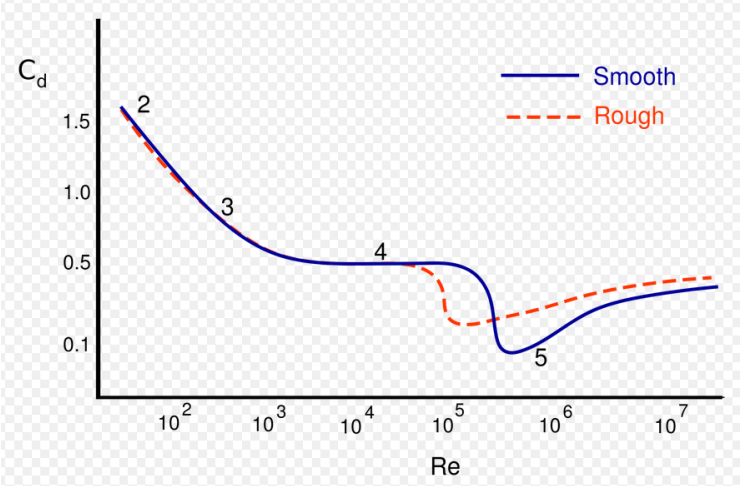

Figure 4.61 Variation of mean drag coefficient with Reynolds number for dry inclined cables [47]

Figure 4.61 shows the drag coefficient for a dry inclined cable, for two cases of smooth and rough surfaces, obtained from wind tunnel experiments [47]. For comparing with the coefficients presented in Figure 4.60, the Reynolds number of around 4×10^5 corresponds to the current CFD simulation carried out for 10 m/s; the value of the drag coefficient for Re = 4×10^5 is around 1.0, while according to the Figure 4.51, the drag coefficient for the cable models with 1.0 cm ice accretion was in the range of 0.005 to 0.04. According to Eq. 2.16 which is described in Chapter 2, Section 2.4, if $\left(\frac{\partial C_L}{\partial \alpha} + C_D\right) < 0$, then galloping instability can occur; thus considering the variation of the lift coefficient in function of the relative angle θ, it can be estimated that for the current case:

$$\cos\theta = \cos\alpha\cos\beta = \cos 60°\cos 15° = 0.48 \quad \text{(Eq. 4.28)}$$

$$\theta = 61.3° \quad \text{(Eq. 4.29)}$$

Thus, considering the slope of the lift coefficient between 0° and 61.3°, the estimation of the DenHartog criterion for the two tested wind speeds can be expressed as follows:

For 10 m/s wind speed:

$$\frac{\partial C_L}{\partial \alpha} + C_D = \frac{-2.68-(-0.143)}{61.3} + 0.11 = -0.041 + 0.04 = -0.001 < 0 \quad \text{(Eq. 4.30)}$$

Because Eq. 4.30 yielded a negative value, the galloping divergent vibration will occur for the cable model with 1.0 cm ice accretion.

For 15 m/s wind speed:

$$\frac{\partial C_L}{\partial \alpha} + C_D = \frac{-1.4-(-0.138)}{61.3} + 0.02 = -0.0205 + 0.02 = -0.0005 < 0 \quad \text{(Eq. 4.31)}$$

Occurrence of galloping vibration is also indicated by the Den Hartog formulation verified for 15 m/s wind speed, which yielded a negative value (Eq. 4.31). The actual galloping divergent vibration of the cable model cannot be identified through the CFD simulation, because only the static CFD cases were performed, for determining the static lift and drag coefficients, however the dynamic experimental test provided complete description of the wind-induced vibrations. After confirming the Den Hartog criterion, it can be concluded that the, galloping phenomenon was encountered for the inclined bridge cable with ice accretion in the wind tunnel experiments. Table 4.3 presents the aerodynamic instabilities which were recorded in the experiments and the cable inclination cases which were confirmed through the CFD simulations. Numbering of the tests and CFD case were preserved so that the inclination angles of the cable model would be the same for test Case 1 and for CFD Case 1. The main observations from the frequency analysis were also indicated for re-confirming the critical wind speed.

Table 4.3 The galloping phenomenon observed for the cases

Tested cases /CFD cases	**Aerodynamic Instability**		
	Wind tunnel experiment	**Frequency analysis**	**CFD simulations**
Case 1 $\alpha = 0°$, $\beta = 0°$, 1.0 cm (CFD case 1)	Galloping	Frequency drop at 4.5 m/s	Galloping - DenHartog
Case 2 $\alpha = 0°$, $\beta = 15°$, 1.0 cm	High-amplitude vibrations or Galloping	Frequency slight drop at 6.0 m/s	NA
Case 3 $\alpha = 30°$, $\beta = 15°$, 1.0 cm	High-amplitude vibrations	Frequency drop at 4.5 m/s	NA
Case 4 $\alpha = 30°$, $\beta = 0°$, 1.0 cm	High-amplitude vibrations	Frequency increase at 6.0 m/s	NA
Case 5 $\alpha = 60°$, $\beta = 0°$, 1.0 cm	Galloping	Frequency drop at 6.0 m/s	NA
Case 6 $\alpha = 60°$, $\beta = 15°$, 1.0 cm (CFD case 2)	Galloping	Frequency drop at 4.5 m/s	Galloping - DenHartog
Case 7 $\alpha = 0°$, $\beta = 0°$, 2.0 cm	Galloping	Frequency drop at 7.5 m/s	NA
Case 8 $\alpha = 30°$, $\beta = 0°$, 2.0 cm	High-amplitude vibrations	Frequency drop at 4.5 m/s	NA
Case 9 $\alpha = 0°$, $\beta = 15°$, 2.0 cm	High-amplitude vibrations	Frequency drop at 7.5 m/s	NA

By comparing the observations reported in Table 4.3, for the wind tunnel test and the CFD simulations, it can be noticed that the Den Hartog criterion pointed out the occurrence of galloping for the same cases for which the galloping was clearly identified

from the time history response of the vertical displacement. This can also serve as the validation of the CFD simulation against the wind tunnel results, performed for the same ice-accreted cable inclination cases. The frequency analysis indicated that the actual aerodynamic instability identified in the experiments (galloping or high-amplitude vibrations) might happen earlier than the 15 m/s which is the maximum tested wind speed for all the performed cases. Thus a change in the response frequency was noticed at 4.5 m/s for Cases 1, 3, 6 and 8, at 6.0 m/s for Cases 2, 4 and 5 and at 7.5 m/s for Cases

In conclusion, 6 cases with 1.0 cm ice thickness and 3 cases with 2.0 cm ice thickness were performed in the wind tunnel, and the vertical and torsional displacements were presented in this chapter; the vibration frequency for the vertical displacement was also plotted, and comparison was made for different vibration modes. The drag and lift static force coefficients were determined from the CFD simulation and galloping DenHartog criterion was verified. Pressure coefficient distribution along the cable and three-dimensional flow formations obtained from the CFD simulations were also discussed.

Chapter 5 Conclusions

Cable-stayed bridges' stability relies on the structural members composing these massive structures, and the stay-cables, which are the most flexible elements of the bridge, have a significant role in the overall bridge design. In recent years, it was noticed that the cross-section and shape modification brought by the ice accretion formed on cables during the cold seasons, can change the aerodynamic response of the cables, and can lead to unwanted cable vibrations.

The effect of the rain and ice accretion formed on the transmission lines was extensively analyzed, and the results indicated that the rain and ice have a major impact on the wind-induced vibrations of the transmission lines. However, researches of the ice accretion formed on bridge stay-cables of cable-stayed bridge are not yet performed in detail and are not well-understood; also the results reported for the transmission lines cannot be extended to the stay-cables, due to large differences in the scale and the geometry of the cables involved. The transmission lines usually have large sag effects as well, due to the dead or live load, which cannot be said about the bridge stay-cables, which are pre-tensioned cables, due to the self-weight of the bridge deck. Thus the wind tunnel experiment performed for cables with ice accretion, reported herewith clarify some aspects related to the galloping instability for the ice-accreted bridge stay-cables.

The galloping vibration is known as a very important phenomenon of structures in general and for bridges cables in this case; according to Den Hartog criterion, which was presented in Chapter 2, one of the assumptions is that, if the shape of the structure is symmetric, then the slope of the lift coefficient does not register any variation and the Den Hartog criterion cannot yield a negative value, which means that the galloping vibration should not occur for circular cables. However, the current experiment and the CFD studies proved that galloping can occur for the actual bridge cables; the most accepted explanation for this occurrence is that, usually the bridge cables are yawed and inclined in regard to the wind speed direction, and thus the cross-section of the cable is not a symmetric circle, but an elliptic shape, due to their placement. In this experiment, the galloping instability occurred for the dynamic response when the wind speed raised

above 4.5 m/s for the Cases 1, ($\alpha = 0°$, $\beta = 0°$ with 1.0 cm ice accretion) 3 ($\alpha = 30°$, $\beta = 15°$ with 1.0 cm ice accretion), 6 ($\alpha = 60°$, $\beta = 15°$ with 1.0 cm ice accretion) and 8, ($\alpha = 30°$, $\beta = 0°$ with 2.0 cm ice accretion), above 6.0 m/s for Cases 2 ($\alpha = 0°$, $\beta = 15°$ with 1.0 cm ice accretion), 4 ($\alpha = 30°$, $\beta = 0°$ with 1.0 cm ice accretion) and 5 ($\alpha = 60°$, $\beta = 0°$ with 1.0 cm ice accretion) and above 7.5 m/s for Cases 7 ($\alpha = 0°$, $\beta = 0°$ with 2.0 cm ice accretion) and 9 ($\alpha = 0°$, $\beta = 15°$ with 2.0 cm ice accretion).

The present research showed that the ice can change the shape of the cable, therefore even for an ideal symmetric cable, galloping vibration can occur due to ice accretion formed on cables, and this result has been confirmed through the current wind tunnel experiment.

From the experimental cases carried out for different horizontal inclination angles α and vertical inclination angles β and the dynamic test results indicated that α and β play a very important role for the vertical and torsional displacements of the ice-accreted stay-cables. When α and β increased, both vertical and torsional displacements increased, however, at low wind speeds, the effect of the inclination is relatively smaller than for the high wind speeds. Also at some wind speed points, the vibration for the cables with higher inclination angle was smaller than the cases with lower inclination, but after the wind speed reached a value higher than 7.5 m/s, the response of the cables with bigger inclination surpassed the case with lower inclination. Thus the vibrations of the cables with lower inclination never reached the vibrations of the cases with bigger inclinations. The relative angle was used to confirm the magnitude of the angles in the three-dimensional space, obtained as per the equation presented in previous chapters.

For the cables with the same inclination and the same wind speed, the difference of the ice thickness was essential in determining the wind-induced vibrations. The cables with 2.0 cm ice thickness had critical vertical and torsional vibrations and the cable with 1.0 cm ice thickness registered smaller vibrations. This result indicates that as the ice thickness is increasing, the vibration of the cables can increase, therefore, the ice on the cables should be trimmed or removed in order to avoid the increasing amplitude of the cable vibration under the effect of wind. However, the shape of the ice is difficult to identify with accuracy for the real cases because this varies with the temperature,

humidity, and different geographical regions. Researches indicate that the most important factor for the ice accretion affecting the cable vibrations is the thickness of the ice profile.

Fast Fourier Transform was performed for the displacement results obtained from the experiment, by employing a Matlab code and the vibration frequency was obtained. Also comparison of the vibration frequencies for the cables without ice, cables with rain, and cables with ice, results showed that the lowest free vibration frequency is for the ice accreted cables. However, for future analysis, the diameter, and the stiffness of the supports, the length of the model, and the wind speed should be the same to ensure accurate result.

Also results have shown that the effect of the ice is the most important for the wind-induced vibrations of cables.

A CFD simulation has been performed to obtain the pressure around the surface of the model, for the case 1 of $\alpha = 60°$, $\beta = 15°$ with 1.0 cm ice thickness, and case 2 of $\alpha = 0°$, $\beta = 0°$ with 1.0 ice thickness, at 10 m/s and 15 m/s wind speed respectively. Based on the drag and lift coefficients obtained from the CFD simulation, the occurrence of the galloping phenomenon has been verified thorough the DenHartog criterion. The distribution of pressure coefficient at different wind speeds for different cases on the surface of the model is observed through the CFD simulation.

Recommendations for future work:

The currently performed experiments and CFD simulations brought valuable information regarding the aerodynamic response of ice-accreted cables for different inclinations and have provided a consistent discussion regarding the critical wind speeds from which galloping or high-amplitude vibrations can be observed. However several aspects should be further investigated to provide even more insight regarding the wind effect on the ice-accreted bridge cables

Future research aspects for ice-accreted cables:

1. The density of the foam was much smaller than the density of the real ice, which means that the vibrations observed in the wind tunnel could be lighter than those obtained for a real ice-accreted bridge cable.

Also, the effect of the ice geometry should be separately studied to gain a better understanding of the ice accretion effect in case of strong winds.

2. For the CFD or other numerical simulations, it should be noted that the model of the irregular ice profile can be attached to the cable-body as an extension, which is the option of drawing the irregular ice in AutoCAD, but this is not working when converted to ANSYS Fluent, because the fluent software recognizes only full body when meshing is prepared. Therefore the Solidworks software should be considered for better drawing of the irregular profile of the ice at the surface of the cable.

3. An interesting discussion could be conducted if research is performed for the case when the ice-accretion partially detaches from the cable. After the main part of the ice falls down, and the remaining ice profile changes the entire shape of the ice accretion along the cable (which might happen very soon after the cable starts vibrating), the wind-induced vibrations of the cables can change entirely their characteristics and their occurrence conditions.

Reference

[1] Drivers dodge Port Mann toll bridge (with video)

http://www.vancouversun.com/Drivers+dodge+Port+Mann+toll+bridge+with+video/10752652/story.html

[2] Nicholas P.Jones Thusitha Kumarasena, Peter Irwin, and Andreas Felber. (2007). *Wind-Induced vibration of stay cables: Summary of FHWA Study*. Publication Number:FHWA-HRT-05-083.

[3] Bülah, K. Y., & Scanlan, R. H. (1991). "Resonance, Tacoma Narrows bridge failure, and undergraduate physics textbooks." *American Journal of Physics*, 59(2): 118-124.

[4] Zuo, D., & Jones, N. P. (2005). *Stay-cable Vibration Monitoring of the Fred Hartman Bridge (Houston, Texas) and the Veterans Memorial Bridge (Port Arthur, Texas)*. Center for Transportation Research, Bureau of Engineering Research, University of Texas at Austin.

[5] Fu, P., Farzaneh, M., & Bouchard, G. (2006). "Two-dimensional modelling of the ice accretion process on transmission line wires and conductors." *Cold Regions Science and Technology*, 46(2): 132-146.

[6] Duoping Zhang, Chenggen Li. (2002) *Design of the stay cables of partially cable-stayed bridge*. The 1st Survey & Design Institute of the Ministry of Railway, Lanzhou 730000, China.

[7] Wang, X., Lou, W., Shen, G., & Xu., F. (2011). "A wind tunnel study on aerodynamic characteristics of iced conductor." *Acta Aerodynamica Sinica*, 29(5).

[8] Huang., L. (2011). *Experimental Study on Bridge Stay Cable Vibration Mitigation Using External Viscous Damper*. Master's Thesis, University of Windsor.

[9] Demartino, C., & Ricciardelli, F. (2015). "Aerodynamic stability of ice-accreted bridge cables." *Journal of Fluids and Structures*, 52: 81-100.

[10] Demartino, C., Koss, H. H., Georgakis, C. T., & Ricciardelli, F. (2015). "Effects of ice accretion on the aerodynamics of bridge cables." *Journal of Wind Engineering and Industrial Aerodynamics*, 138: 98-119.

[11] Cunha, A., Caetano, E., Ribeiro, P., & Müller, G. (2014). "Prediction of the aerodynamic instability of ice-accreted bridge cables using different stability criteria. *Proceeding of the 9th International Conference on structural Dynamics*, EURODYN, 2014.

[12] Baker, P. C., Poots, G., & Rodgers, G. G. (1986). "Ice accretion on cables of various cross-sections." *IMA Journal of Applied Mathematics*, 36(1): 11-28.

[13] Wenyong Ma, Ming Gu, Yong Quan, Peng Huan. (2010). *The analyze of Galloping vibration of cable with ice on transmission line*. Journal of Tongji University. (in Chinese)

[14] Waris, M. B., Ishihara, T., & Sarwar, M. W. (2008). "Galloping response prediction of ice-accreted transmission lines." *Proceedings of the 4th International Conference on Advances in Wind and Structures*, 876-885.

[15] Jakobsen, J. B., Andersen, T. L., Macdonald, J. H. G., Nikitas, N., Larose, G. L., Savage, M. G., & McAuliffe, B. R. (2012). "Wind-induced response and excitation characteristics of an inclined cable model in the critical Reynolds number range." *Journal of Wind Engineering and Industrial Aerodynamics*, 110: 100-112.

[16] Matsumoto, M., Shiraishi, N., & Shirato, H. (1992). "Rain-induced vibration of cables of cable-stayed bridges." *Journal of Wind Engineering and Industrial Aerodynamics*, 413(1-3): 2011-2022.

[17] Matsumoto, M., Shiraishi, N., Kitazawa, M., Knisely, C., Shirato, H., Kim, Y., & Tsuijii, M. (1990). "Aerodynamic behavior of inclined circular cylinders cables aerodynamics." *Journal of Wind Engineering and Industrial Aeridynamics*, 33(1): 63-72.

[18] Liu, X. (2006). *ANSYS simulation for suspension bridge*. Doctor's Thesis, Southwest Jiaotong University, Chengdu. (in Chinese)

[19] Wujian Zhang, Bo Wang, Jinbao Yang, Xiaopeng Chai. (2012). *The characteristics analyze of the cables on Jiujiang Yangtze River bridge.*

[20] Dong, X. (2007). *Stayed Cable Vibration and Damping Measures for Extra-large Span Cable Stay Bridge*. Master's Thesis, Tongji University, Shanghai. (in Chinese)

[21] Yuan, C. (2012). *Study on Cable Vibration.* Doctoral dissertation, Sothwest Jiaotong University, Chengdu. (in Chinese)

[22] Yang, L. (2011). "Wind-induced fatigue for the longevity of suspension bridge." *Railway Survey and Design*, 2011(4): 61-67. (in Chinese)

[23] Yuan, C. (2012) *The observation of stay cables*. Master's thesis, Southwest Jiaotong University, Chengdu, China. (in Chinese)

[24] Bosch, H. (2007). *Wind induced vibration of stay cables*, FHWA-HRT-05-084.

[25] Zurell, C. (2004). *Aerodynamics of a Circular Cylinder Inclined to Airflow and Wind-induced Vibrations of Dry, Inclined Cables at High Wind Speeds*. Ph. D. Thesis, University of Ottawa.

[26] Hu J., & Ou, J. (2011). "The corrosion fatigue life analysis on hangers of long span suspension bridge under wind load." *Steel Construction*, 26(5): 63-67. (in Chinese)

[27] Wang, L., & Yi, J. (2007). "Cases analysis on cable corrosion of cable-stayed bridges." *Journal of Central South Highway Engineering*, 32(1): 93-98. (in Chinese)

[28] He, X., & Xi, S. (2006) "The vibration of stay cables due to rain-induced vibration." (in Chinese)

[29] He, X., Liao, L., Li, M., & Xi, S. (2004) "The rain-induced vibration of stay cables." *Proceedings of the 11th structure wind conference of China*. (in Chinese)

[30] Jing, D., Wen, H., & Hu, H. (2004) "The model of cable system and the control of aerodynamics." *Advances in Mechanics*, 34(3). (in Chinese)

[31] Luo, N., Liao, H., Li, M. (2009). "The rain-induced vibration and the damping ratio of stay cables in wind tunnel." *Proceedings of The 13th Structure Wind Conference of China*. (in Chinese)

[32] Li, Y., An, S., Zhao, T., & Wang, Y. (2011). "Simulation of aerodynamic characteristics of cables with rivulet by CFD." *Sichuan Building Science*, 37(5), 161-163. (in Chinese)

[33] Wang, X., Chen, Z., Gao, Z., & Ni, Y. (2002) "Study of mitigating vibration on stay cables using magneto-rheological (MR) damper". *Engineering mechanics*, 19(6): 22-28. (in Chinese)

[34] Song, H. (2007) *The vortex shedding and rain-induced vibration of stay cables*. (in Chinese)

[35] Zdero, R., & Turan, O. F. (2010). *The effect of surface strands, angle of attack, and ice accretion on the flow field around electrical power cables*. Journal of Wind Engineering and Industrial Aerodynamics, 98(10): 672-678.

[36] Li, Y., Wang, T., Liao, H. (2010). “Investigation on wake galloping of parallel cables in cable-stayed bridge by wind tunnel test.” *Engineering Mechanics* S1: 216-221+227. (in Chinese)

[37] Hao, H. (2010). *The Galloping Phenomenon and Its Control of Bridges*. Master’s Thesis, Chang’an University, Xi’an, China. (in Chinese)

[38] McComber, P., & Paradis, A. (1998). “A cable galloping model for thin ice accretions.” *Atmospheric Research* 46(1): 13-25.

[39] Koss, H. H., Gjelstrup, H., & Georgakis, C. T. (2012). “Experimental study of ice accretion on circular cylinders at moderate low temperatures.” *Journal of Wind Engineering and Industrial Aerodynamics*, 104: 540-546.

[40] Wu, W. J., Cai, C. S., & Chen, S. R. (2004). “Experiments on reduction of cable vibration using MR dampers.” *Proceedings of 17th ASCE Engineering Mechanics Conference*, Universiy of Delware, US.

[41] Cheng, S., Larose, G. L., Savage, M. G., Tanaka, H., & Irwin, P. A. (2008). “Experimental study on the wind-induced vibration of a dry inclined cable−Part I: Phenomena.” *Journal of Wind Engineering and Industrial Aerodynamics*, 96(12): 2231-2253.

[42] Michael S. Hoftyzer. (2013). *Three-dimensional turbulence and transitory flow regimes for inclined circular cyclinders.*

[43] Broström, E. (2007). *Ice storm Modelling in Transmission System Reliability Calculations*. Royal Institute of Technology, Stockholm.

[44] Wang, L. (2001). *Nonlinear vibration of a flexible cable*. Doctor’s Thesis, Hunan University, Changsha. (in Chinese)

[45] Tan, C. (2006). *ANSYS simulation for cables.* Master’s Thesis, Southwest Jiaotong University, Chengdu. (in Chinese)

[46] Zhao, Y., Zhou, H., Jin, B. & Liu, W. (2008). “Influence of bending rigidity on nonlinear natural frequency of inclined cable.” *Engineering Mechanics*, 25(1): 196-202. (in Chinese)

[47] Zhou, Y., Niu, S., Lü, J., & Zhao, L. (2012). “Meteorological conditions of ice accretion based on real-time observation of high voltage transmission line.” *Chinese Science Bulletin*, 57(7): 812-818.

[48] Simiu, E., & Scanlan, R. H. (1996). *Wind Effects on Structures: An Introduction to Wind Engineering*. John Wiley.

[49] Lnman, Daniel J. (2008). *Engineering Vibration*. Upper Saddle, NJ: Pearson Education, Inc. pp. 43–48. ISBN 0-13-228173-2.

Appendix A

Appendix A represents the original average vertical and torsional vibrations at different wind speed for all cases, hundreds of points for vibration are recorded, and the interval between the each point is 0.1 s.

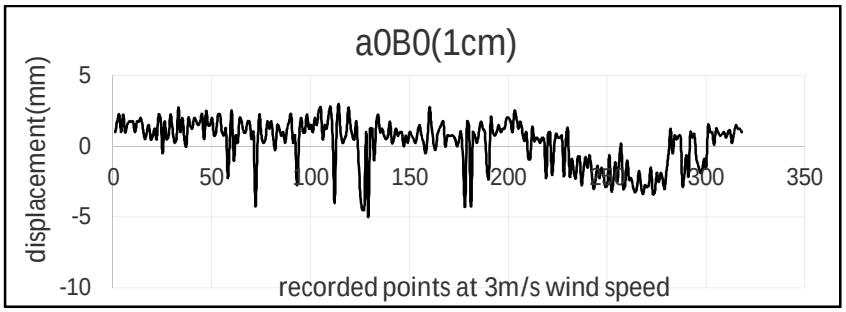

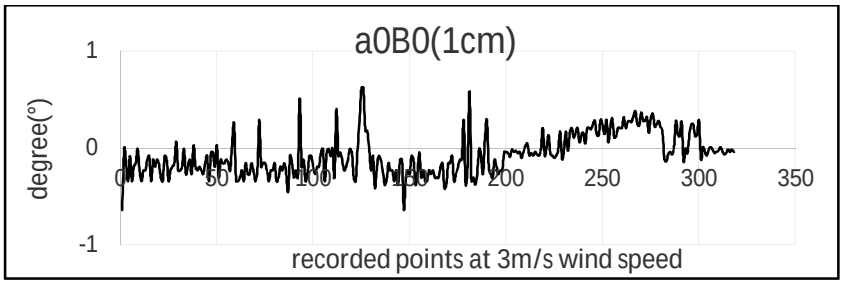

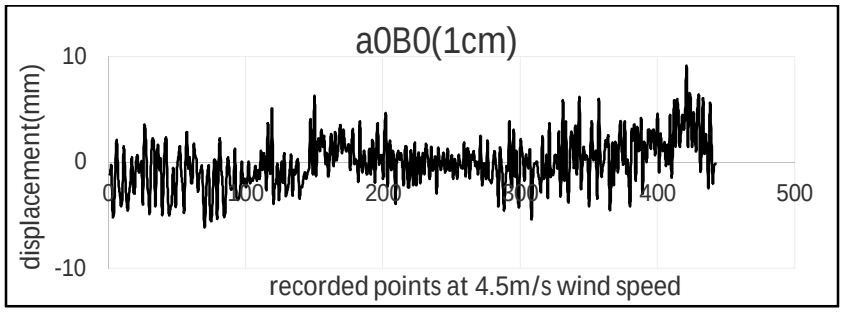

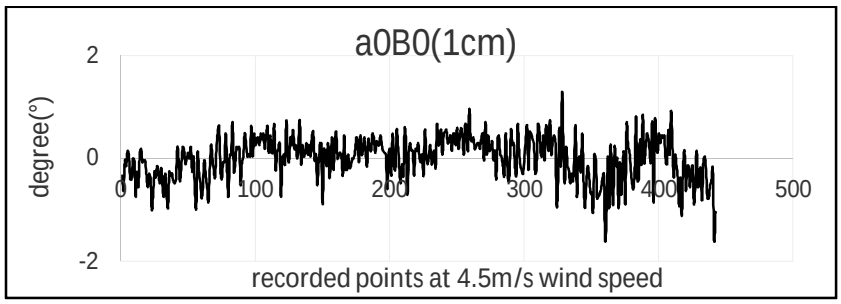

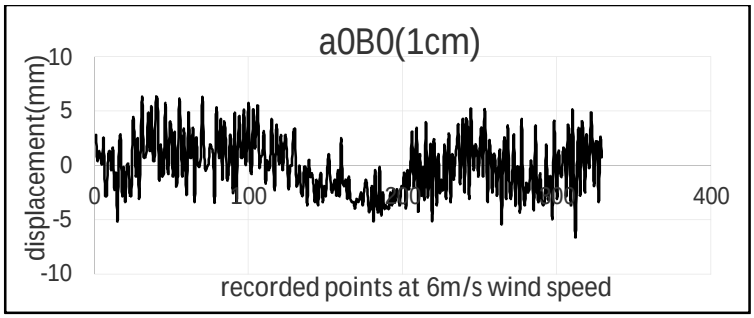
a0B0(1cm)
displacement(mm)
10
5
0
-5
-10
0
100
400
recorded points at 6m/s wind speed

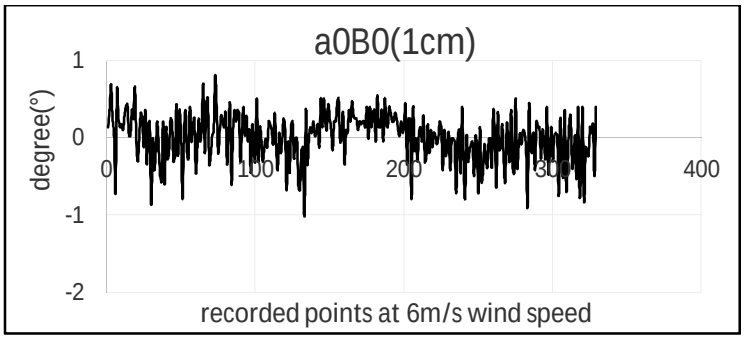
a0B0(1cm)
degree(°)
1
0
-1
-2
0
100
200
400
recorded points at 6m/s wind speed

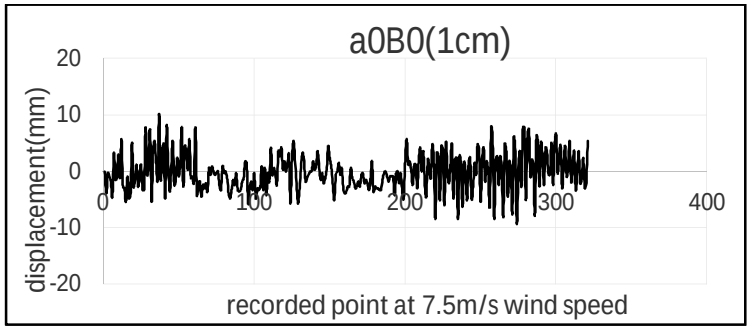
a0B0(1cm)
displacement(mm)
20
10
0
-10
-20
0
100
200
300
400
recorded point at 7.5m/s wind speed

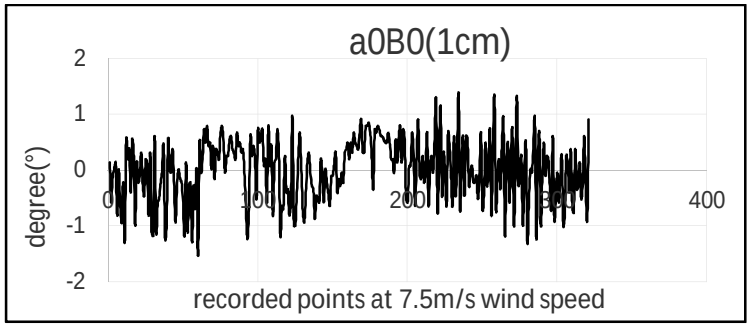
a0B0(1cm)
degree(°)
2
1
0
-1
-2
0
100
200
400
recorded points at 7.5m/s wind speed

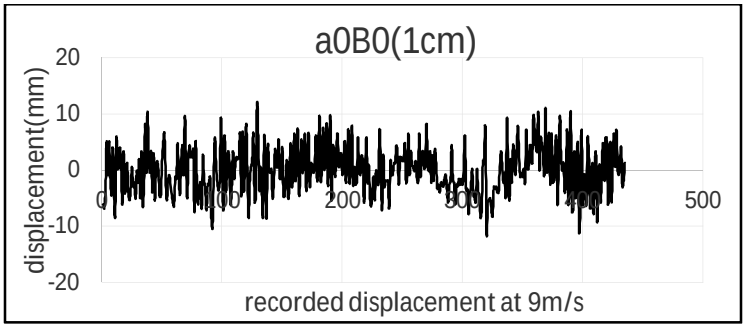
a0B0(1cm)
displacement(mm)
20
10
0
-10
-20
0
200
500
recorded displacement at 9m/s

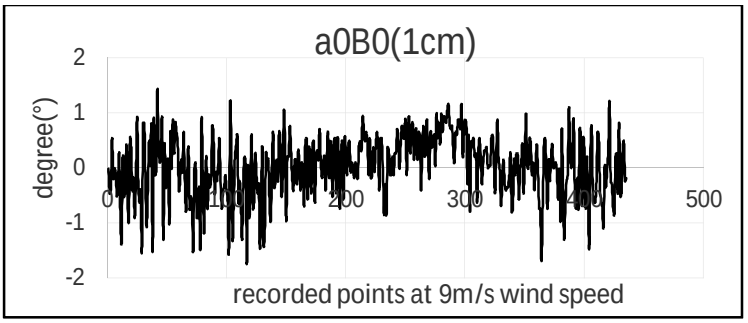
a0B0(1cm)
degree(°)
2
1
0
-1
-2
0
100
200
300
400
500
recorded points at 9m/s wind speed

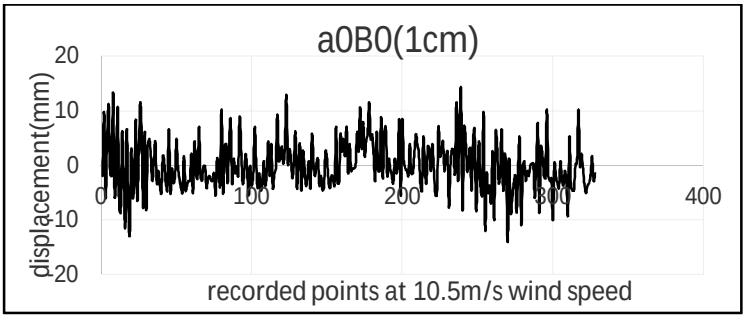
a0B0(1cm)
displacement(mm)
20
10
0
-10
-20
0
100
200
300
400
recorded points at 10.5m/s wind speed

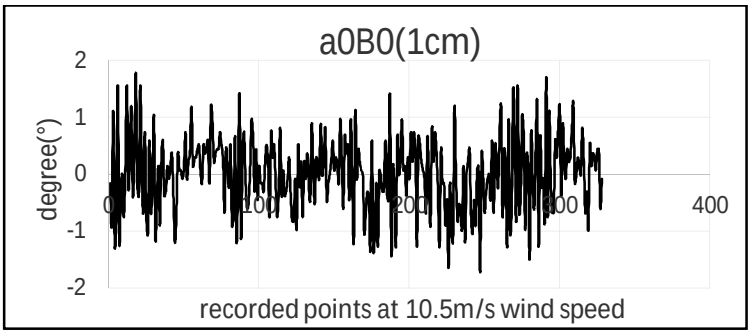
a0B0(1cm)
degree(°)
2
1
0
-1
-2
0
100
200
300
400
recorded points at 10.5m/s wind speed

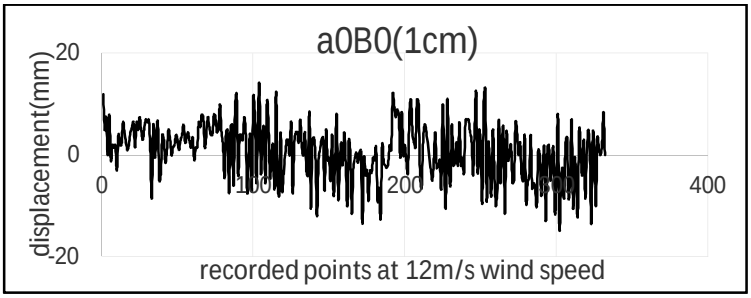
a0B0(1cm)
displacement(mm)
20
0
-20
0
100
200
300
400
recorded points at 12m/s wind speed

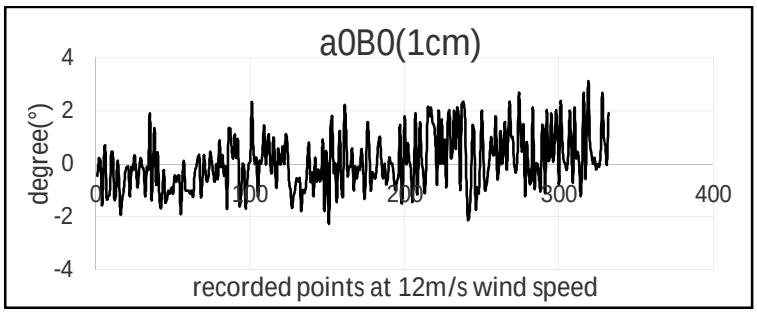
a0B0(1cm)
degree(°)
4
2
0
-2
-4
0
100
200
300
400
recorded points at 12m/s wind speed

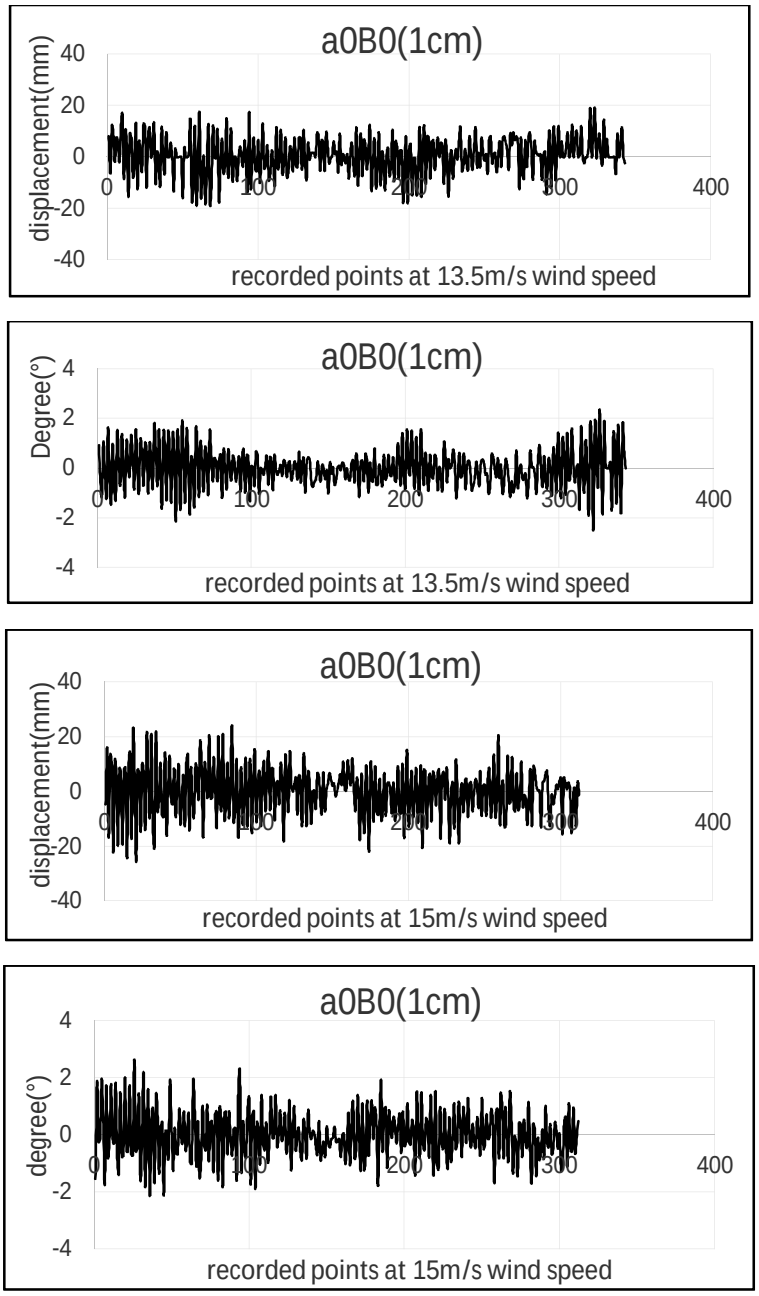

Figure A1 The vertical and Torsional Displacement from 1.5 m/s Wind speed to 15 m/s Wind speed for case $\alpha = 0°$, $\beta = 0°$ with 1 cm ice thickness

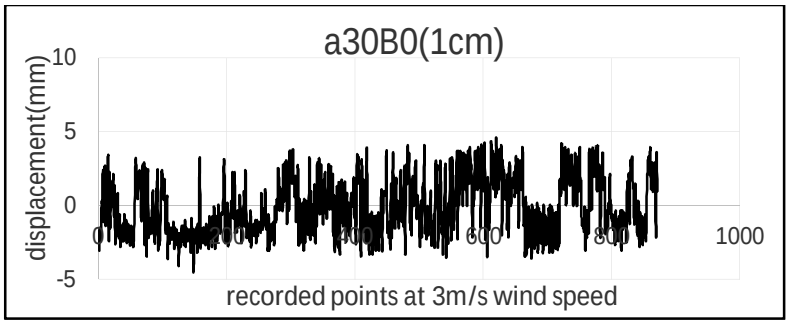
a30B0(1cm)
displacement(mm)
10
5
0
-5
0
200
400
600
800
1000
recorded points at 3m/s wind speed

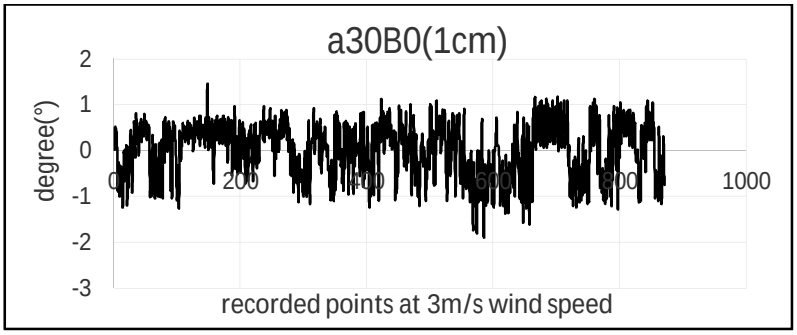
a30B0(1cm)
degree(°)
2
1
0
-1
-2
-3
0
200
400
600
800
1000
recorded points at 3m/s wind speed

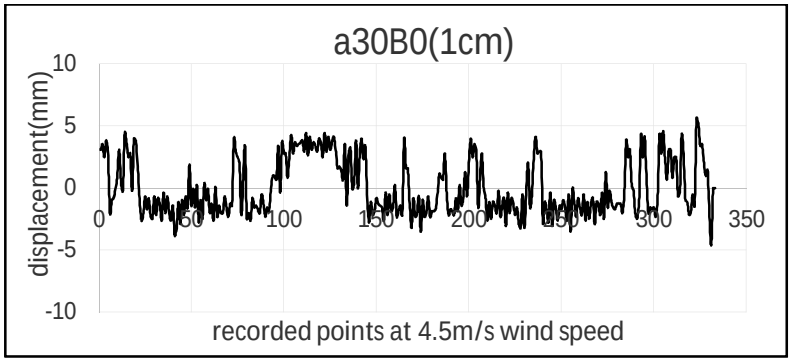
a30B0(1cm)
displacement(mm)
10
5
0
-5
-10
0
50
100
150
200
250
300
350
recorded points at 4.5m/s wind speed

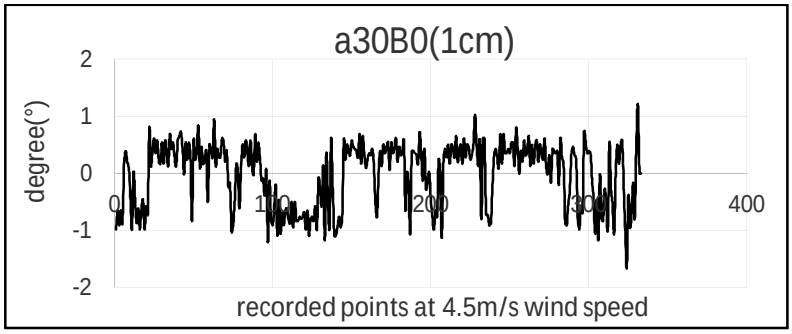
a30B0(1cm)
degree(°)
2
1
0
-1
-2
0
100
200
300
400
recorded points at 4.5m/s wind speed

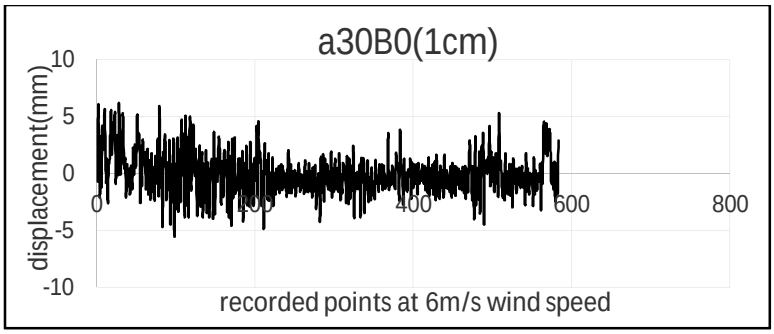
a30B0(1cm)
displacement(mm)
10
5
0
-5
-10
0
400
600
800
recorded points at 6m/s wind speed

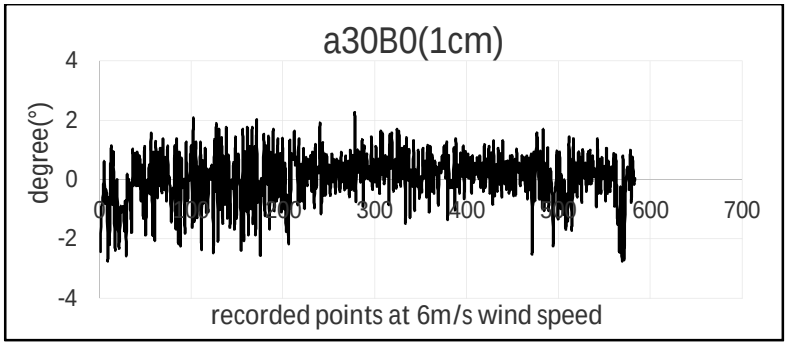
a30B0(1cm)
degree(°)
4
2
0
-2
-4
300
400
600
700
recorded points at 6m/s wind speed

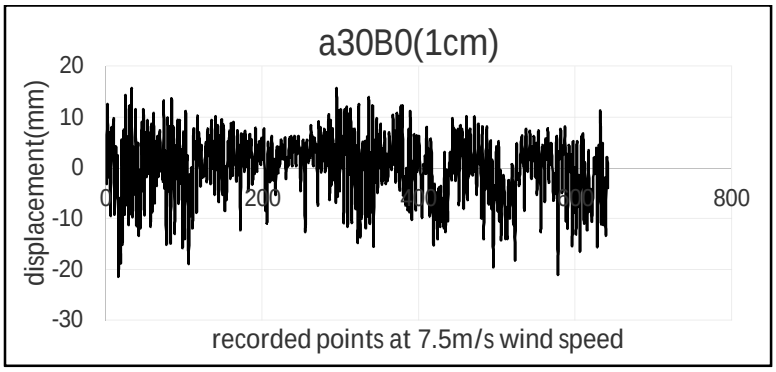
a30B0(1cm)
displacement(mm)
20
10
0
-10
-20
-30
200
800
recorded points at 7.5m/s wind speed

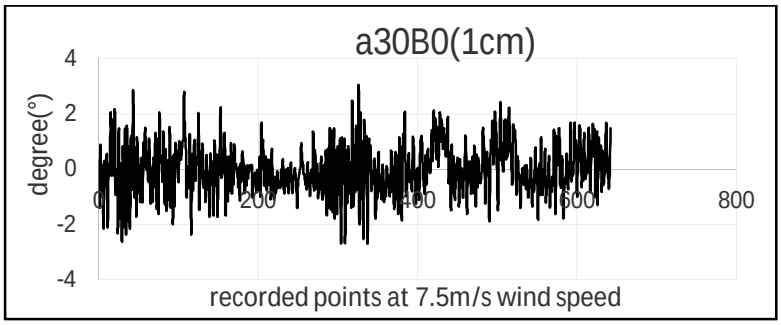
a30B0(1cm)
degree(°)
4
2
0
-2
-4
200
400
600
800
recorded points at 7.5m/s wind speed

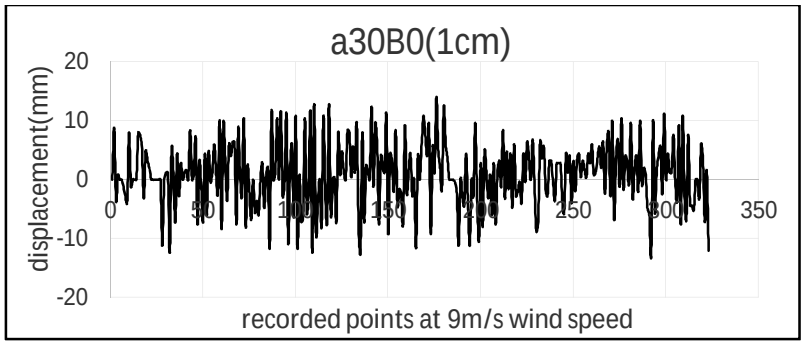
a30B0(1cm)
displacement(mm)
20
10
0
-10
-20
0
50
100
150
200
250
300
350
recorded points at 9m/s wind speed

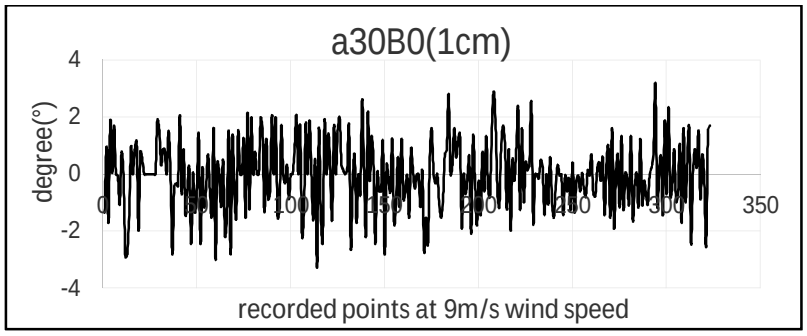
a30B0(1cm)
degree(°)
4
2
0
-2
-4
0
50
100
150
200
250
300
350
recorded points at 9m/s wind speed

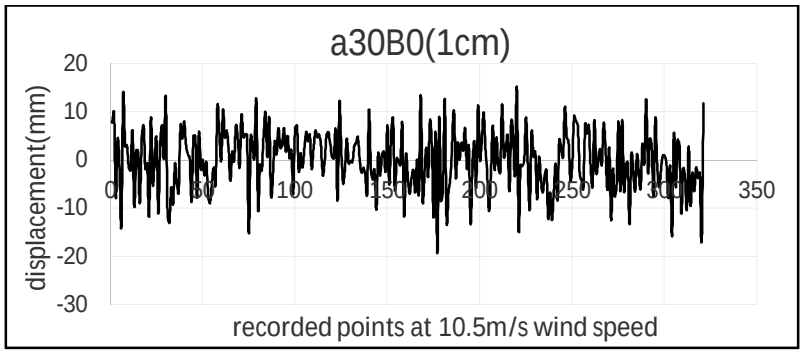
a30B0(1cm)
displacement(mm)
20
10
0
-10
-20
-30
0
50
100
150
200
250
300
350
recorded points at 10.5m/s wind speed

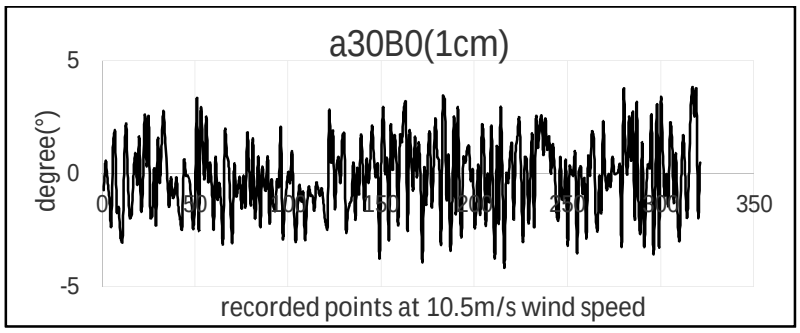
a30B0(1cm)
degree(°)
5
0
-5
0
50
100
150
200
250
300
350
recorded points at 10.5m/s wind speed

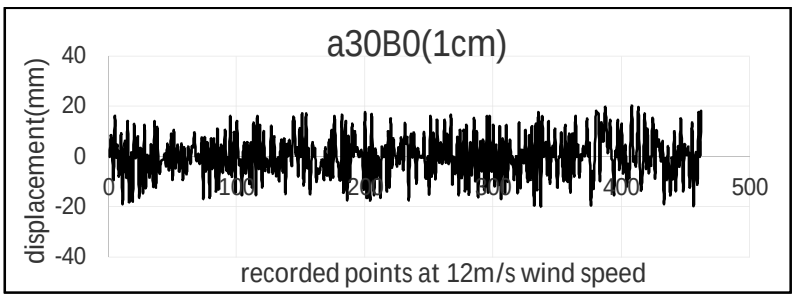
a30B0(1cm)
displacement(mm)
40
20
0
-20
-40
0
100
200
300
400
500
recorded points at 12m/s wind speed

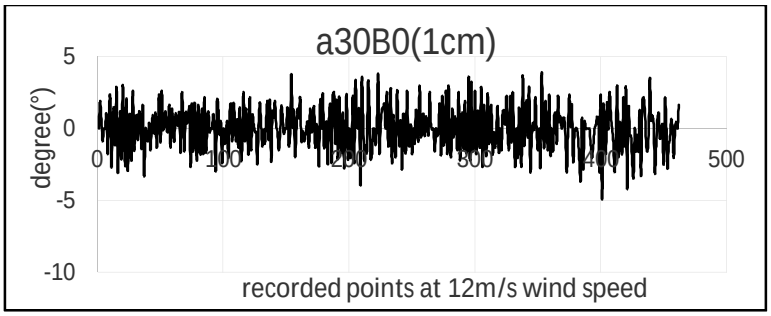
a30B0(1cm)
degree(°)
5
0
-5
-10
0
100
500
recorded points at 12m/s wind speed

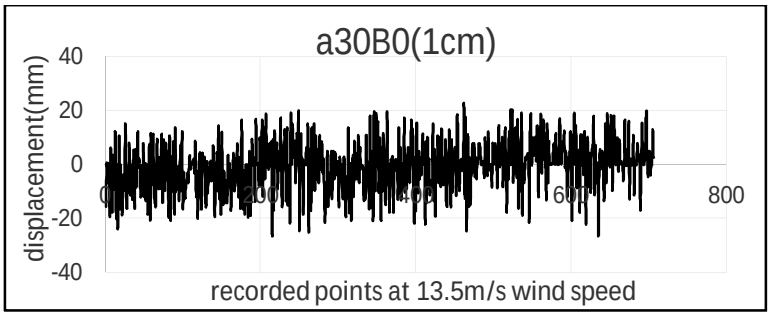
a30B0(1cm)
displacement(mm)
40
20
0
-20
-40
800
recorded points at 13.5m/s wind speed

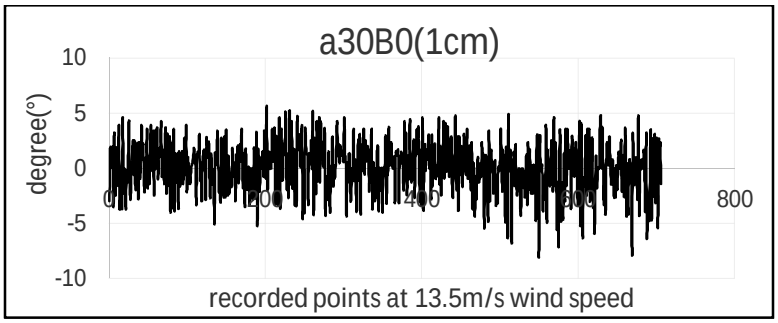
a30B0(1cm)
degree(°)
10
5
0
-5
-10
800
recorded points at 13.5m/s wind speed

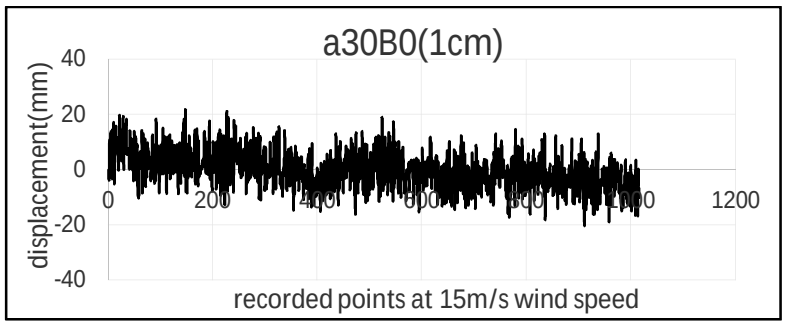
a30B0(1cm)
displacement(mm)
40
20
0
-20
-40
0
200
1200
recorded points at 15m/s wind speed

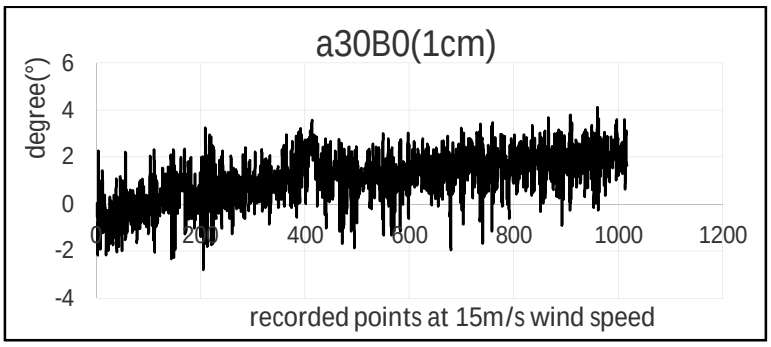
a30B0(1cm)
degree(°)
6
4
2
0
-2
-4
0
400
600
800
1000
1200
recorded points at 15m/s wind speed

Figure A2 The vertical and Torsional Displacement from 1.5 m/s Wind speed to 15 m/s Wind speed for case $\alpha = 30°$, $\beta = 0°$ with 1 cm ice thickness

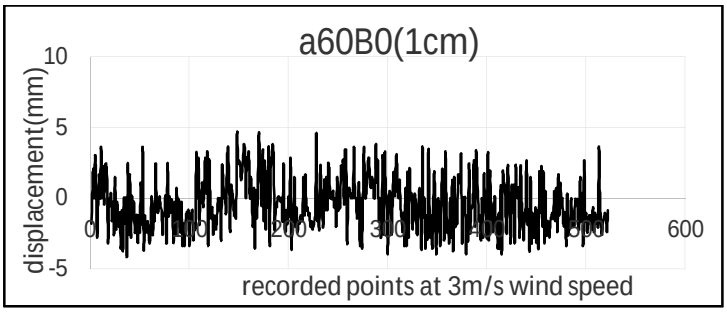

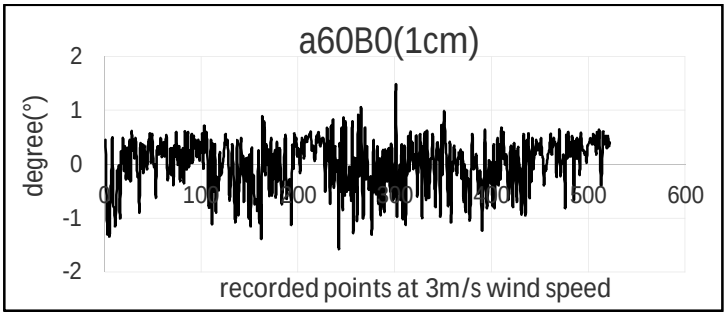

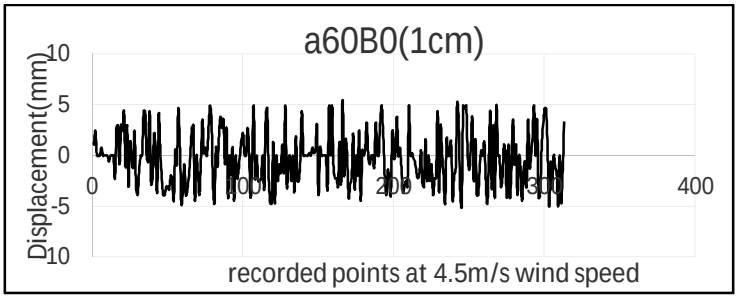

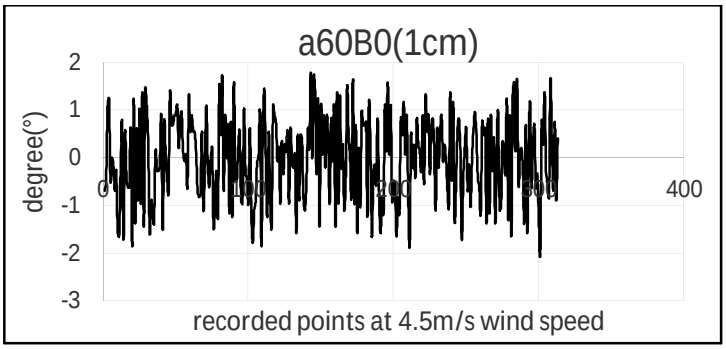

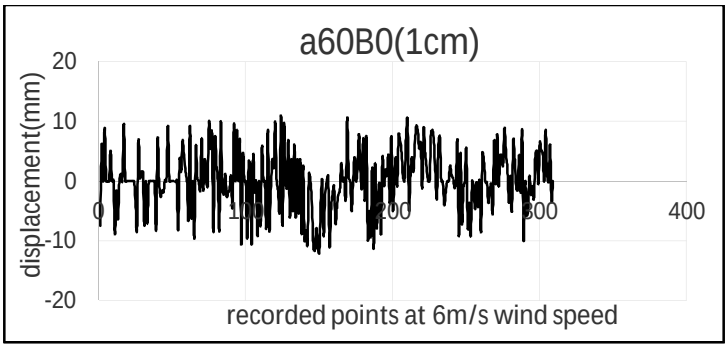
a60B0(1cm)
displacement(mm)
20
10
0
-10
-20
0
100
200
300
400
recorded points at 6m/s wind speed

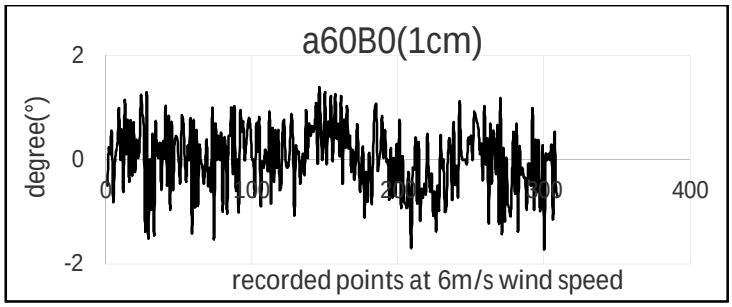
a60B0(1cm)
degree(°)
2
0
-2
0
100
200
300
400
recorded points at 6m/s wind speed

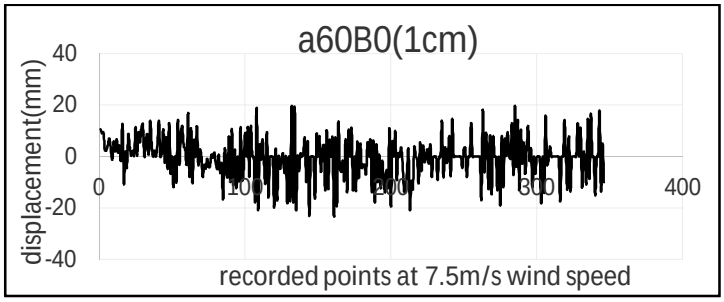
a60B0(1cm)
displacement(mm)
40
20
0
-20
-40
0
100
200
300
400
recorded points at 7.5m/s wind speed

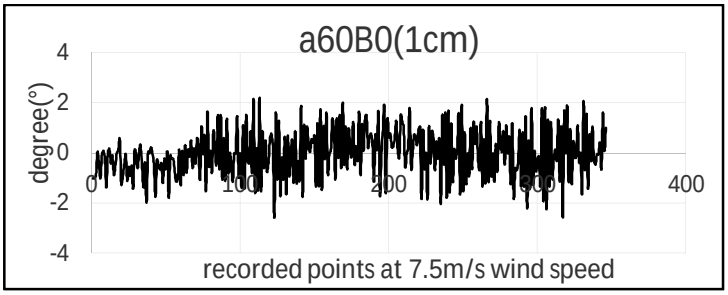
a60B0(1cm)
degree(°)
4
2
0
-2
-4
0
100
200
300
400
recorded points at 7.5m/s wind speed

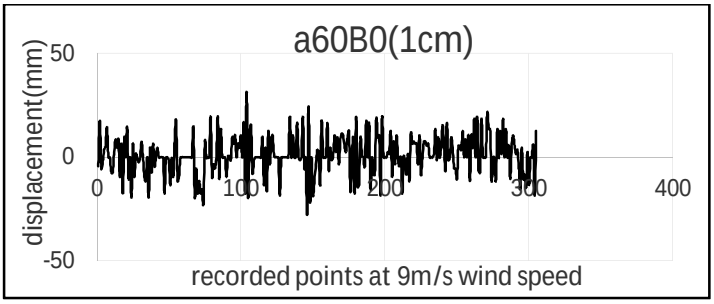
a60B0(1cm)
displacement(mm)
50
0
-50
0
100
200
300
400
recorded points at 9m/s wind speed

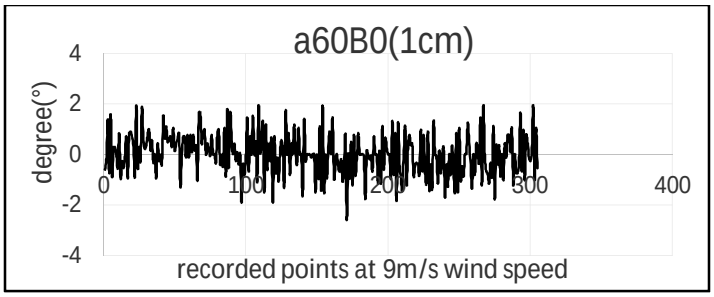
a60B0(1cm)
degree(°)
4
2
0
-2
-4
0
100
200
300
400
recorded points at 9m/s wind speed

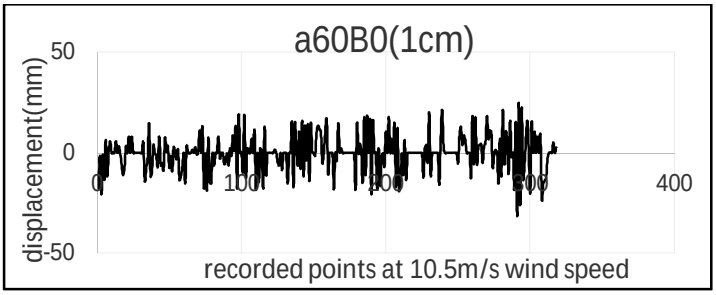
a60B0(1cm)
displacement(mm)
50
0
-50
0
100
200
300
400
recorded points at 10.5m/s wind speed

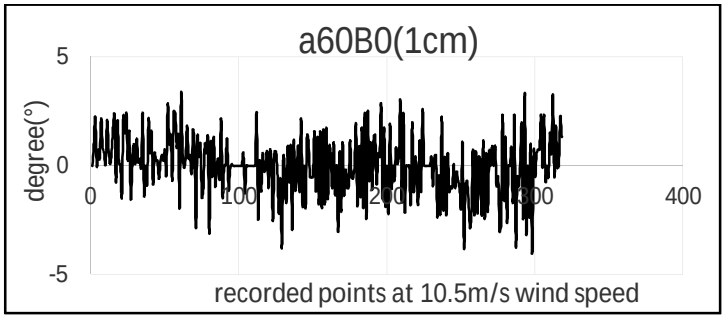
a60B0(1cm)
degree(°)
5
0
-5
0
100
200
300
400
recorded points at 10.5m/s wind speed

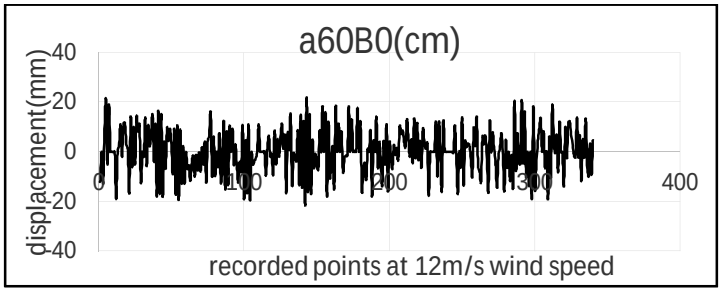
a60B0(cm)
displacement(mm)
40
20
0
-20
-40
0
100
200
300
400
recorded points at 12m/s wind speed

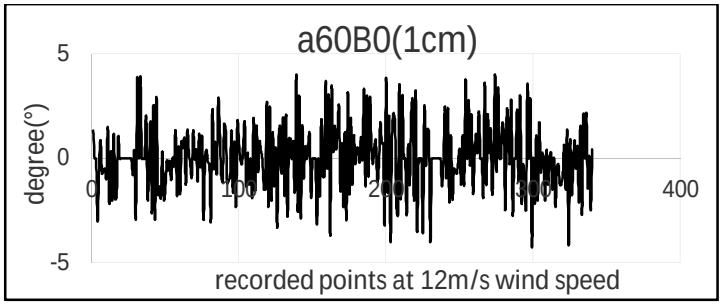
a60B0(1cm)
degree(°)
5
0
-5
0
100
200
300
400
recorded points at 12m/s wind speed

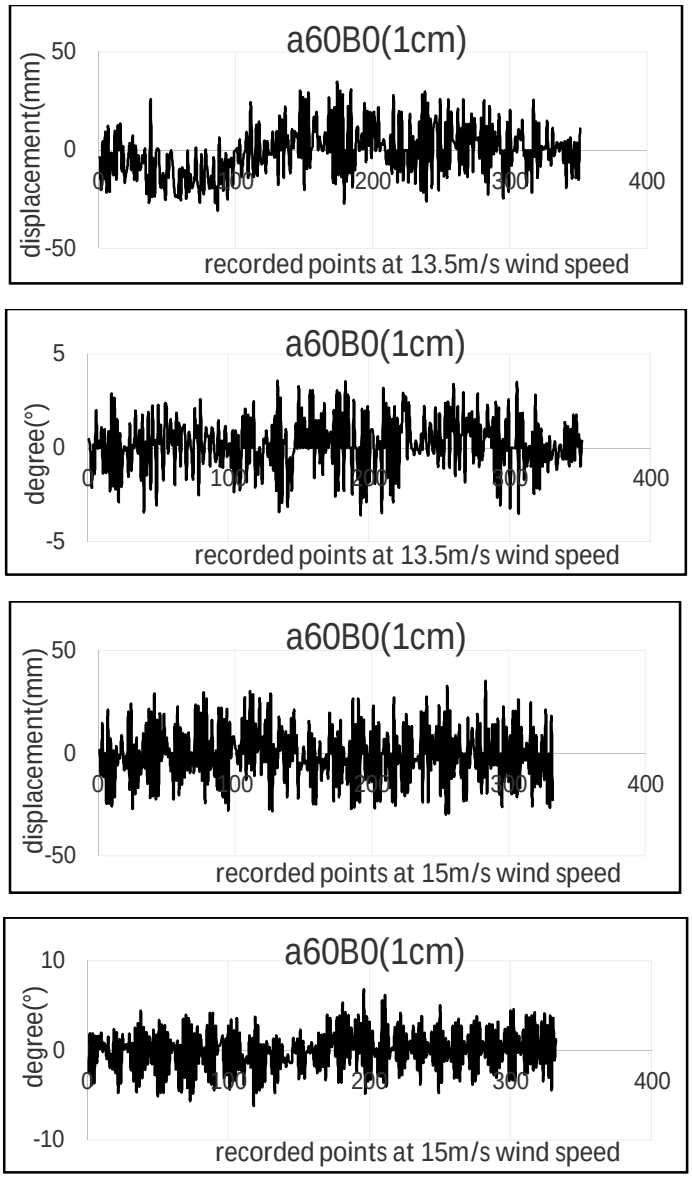

Figure A3 The vertical and Torsional Displacement from 1.5 m/s Wind speed to 15 m/s Wind speed for case $\alpha = 60°$, $\beta = 0°$ with 1 cm ice thickness

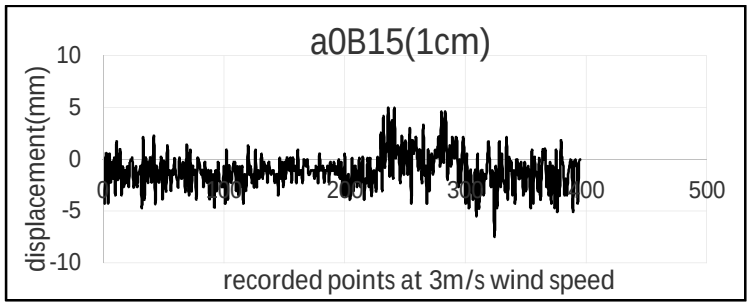

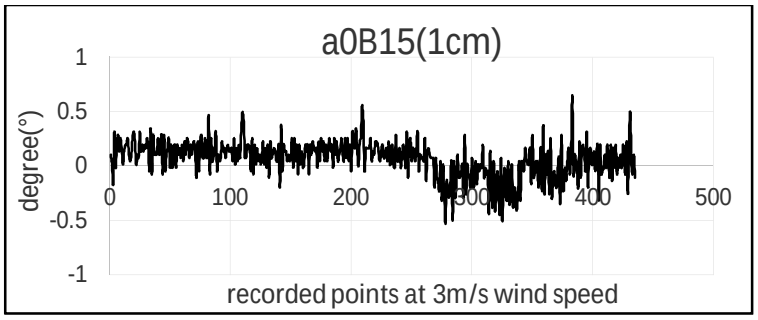
a0B15(1cm)
degree(°)
1
0.5
0
-0.5
-1
0
100
200
300
400
500
recorded points at 3m/s wind speed

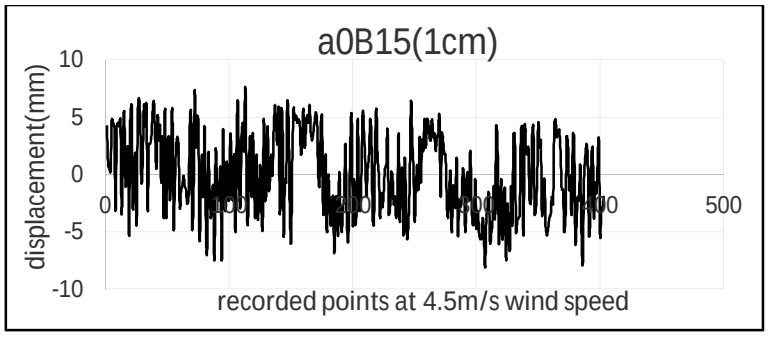
a0B15(1cm)
displacement(mm)
10
5
0
-5
-10
0
500
recorded points at 4.5m/s wind speed

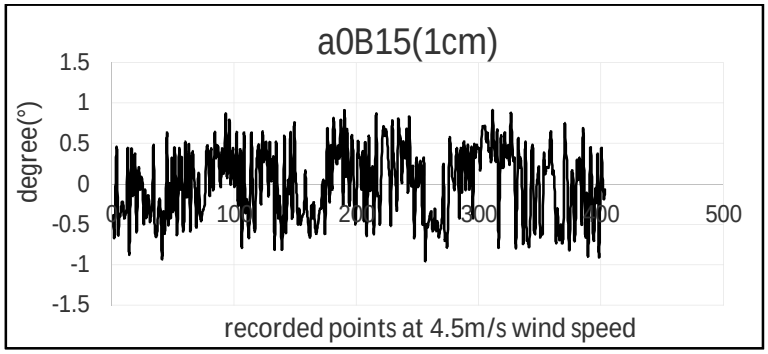
a0B15(1cm)
degree(°)
1.5
1
0.5
0
-0.5
-1
-1.5
500
recorded points at 4.5m/s wind speed

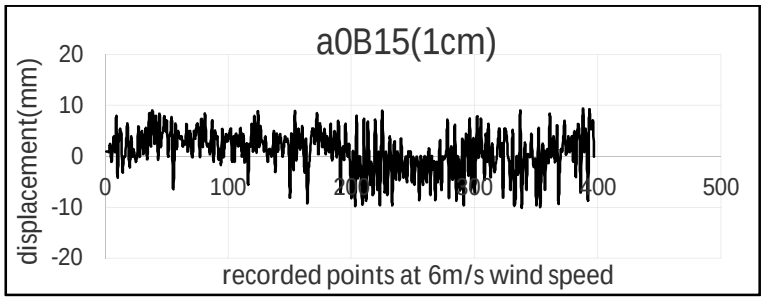
a0B15(1cm)
displacement(mm)
20
10
0
-10
-20
0
100
400
500
recorded points at 6m/s wind speed

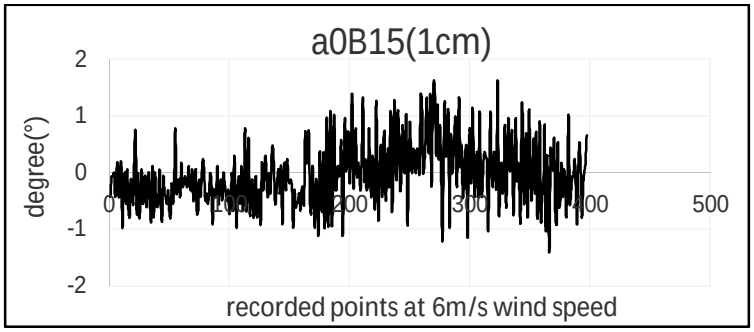
a0B15(1cm)
degree(°)
2
1
0
-1
-2
0
500
recorded points at 6m/s wind speed

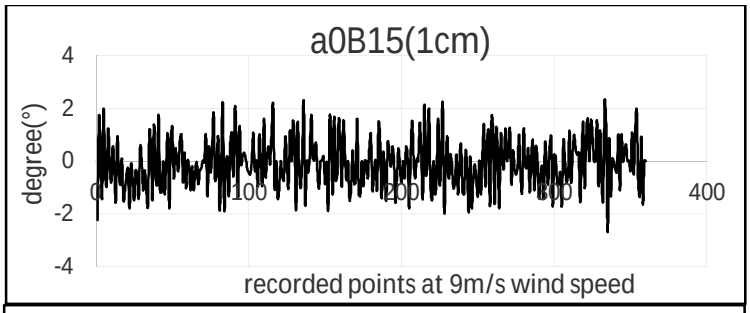
a0B15(1cm)
degree(°)
4
2
0
-2
-4
0
100
200
300
400
recorded points at 9m/s wind speed

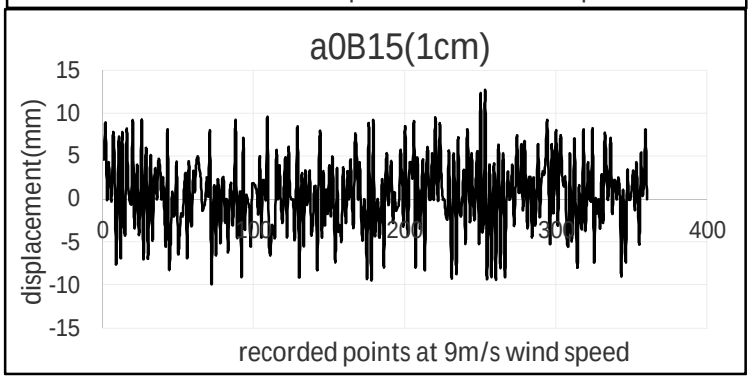
a0B15(1cm)
displacement(mm)
15
10
5
0
-5
-10
-15
0
200
300
400
recorded points at 9m/s wind speed

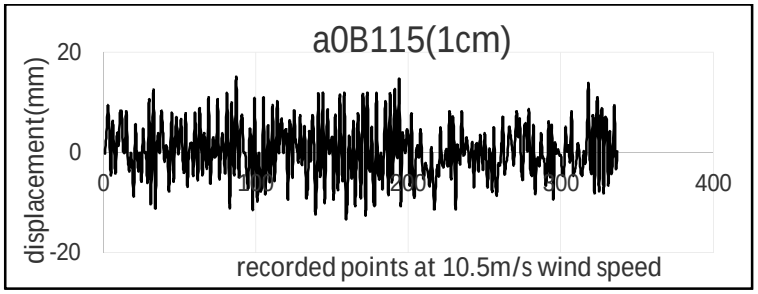
a0B115(1cm)
displacement(mm)
20
0
-20
0
200
400
recorded points at 10.5m/s wind speed

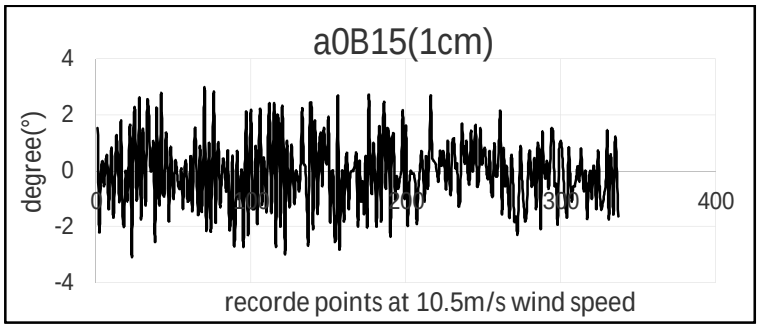
a0B15(1cm)
degree(°)
4
2
0
-2
-4
0
200
300
400
recorde points at 10.5m/s wind speed

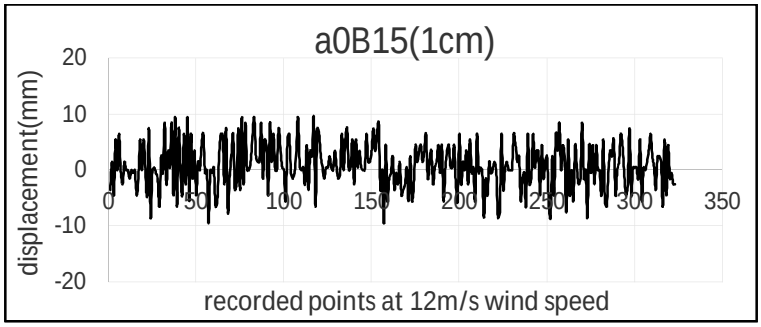
a0B15(1cm)
displacement(mm)
20
10
0
-10
-20
0
50
100
150
200
250
300
350
recorded points at 12m/s wind speed

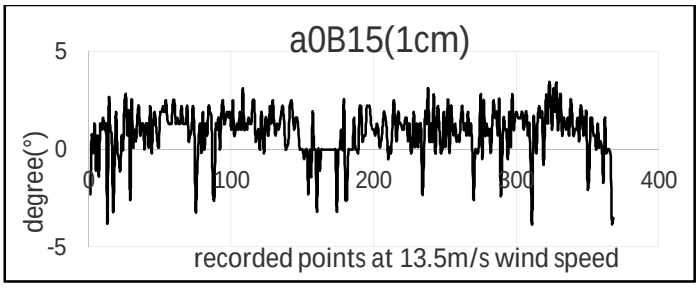

Figure A4 The vertical and Torsional Displacement from 1.5 m/s Wind speed to 15 m/s Wind speed for case $\alpha = 0°$, $\beta = 15°$ with 1 cm ice thickness

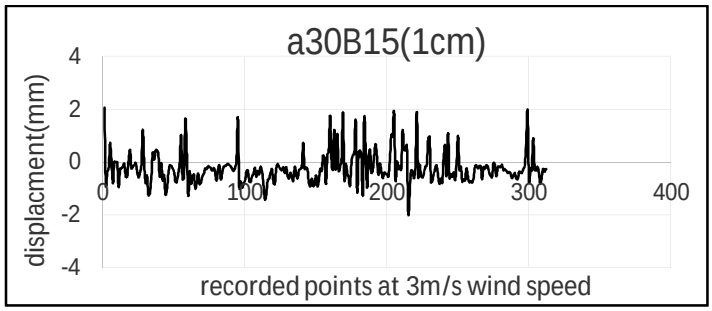

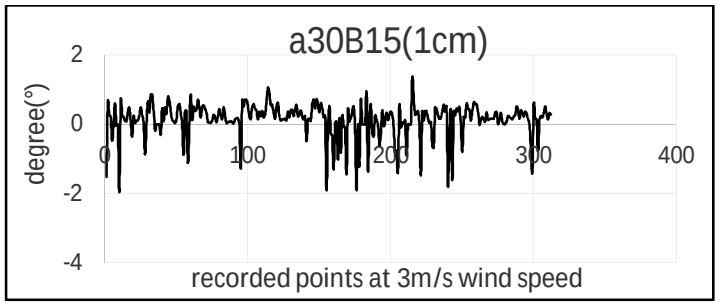

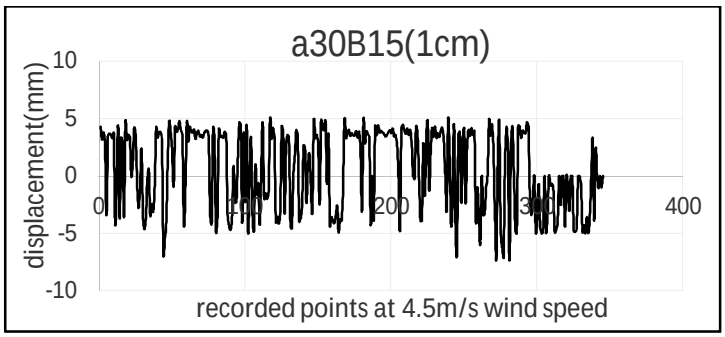

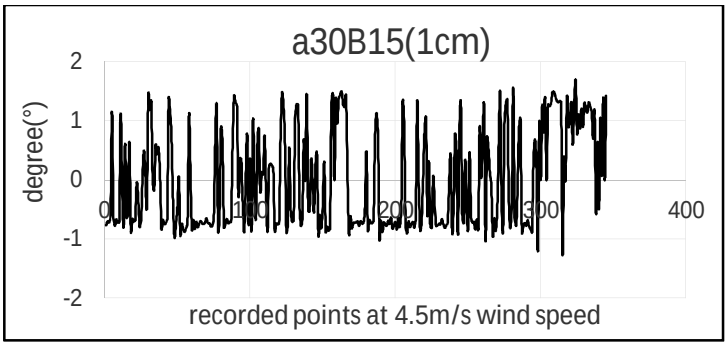
a30B15(1cm)
degree(°)
2
1
0
-1
-2
0
100
200
300
400
recorded points at 4.5m/s wind speed

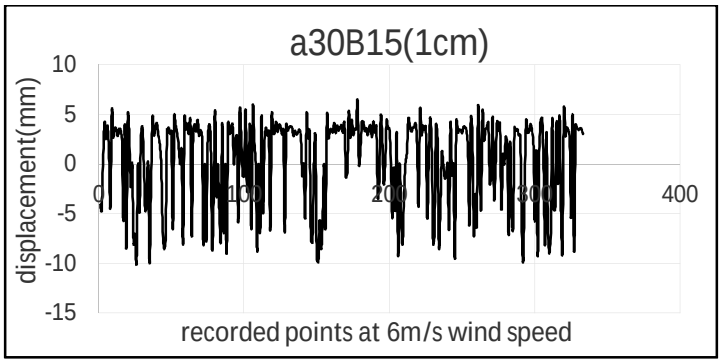
a30B15(1cm)
displacement(mm)
10
5
0
-5
-10
-15
400
recorded points at 6m/s wind speed

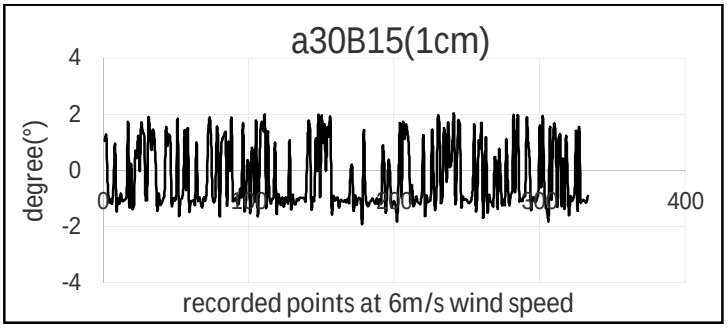
a30B15(1cm)
degree(°)
4
2
0
-2
-4
400
recorded points at 6m/s wind speed

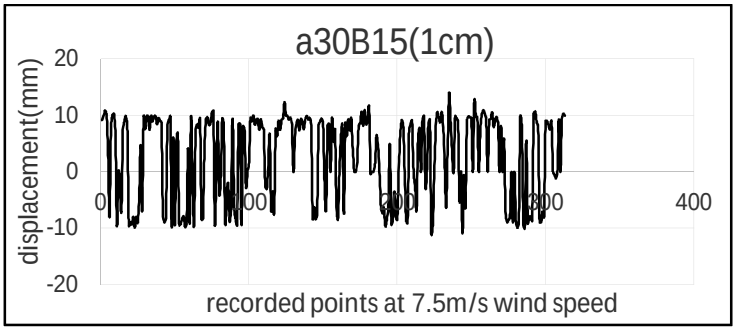
a30B15(1cm)
displacement(mm)
20
10
0
-10
-20
400
recorded points at 7.5m/s wind speed

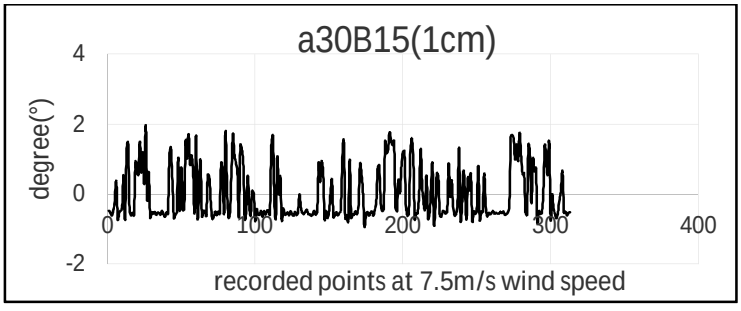
a30B15(1cm)
degree(°)
4
2
0
-2
0
100
200
300
400
recorded points at 7.5m/s wind speed

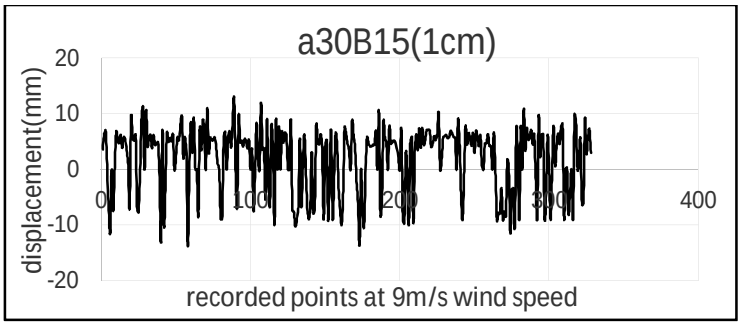
a30B15(1cm)
displacement(mm)
20
10
0
-10
-20
0
100
200
300
400
recorded points at 9m/s wind speed

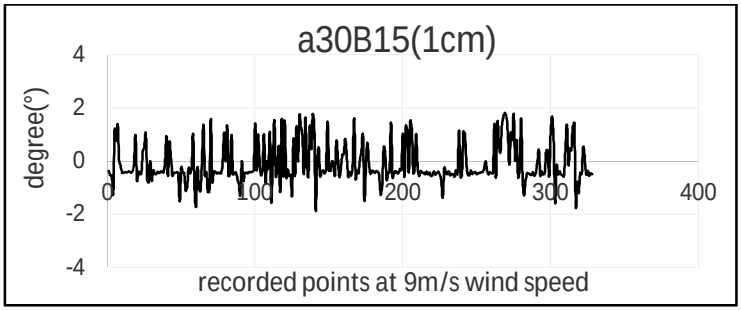
a30B15(1cm)
degree(°)
4
2
0
-2
-4
0
100
200
300
400
recorded points at 9m/s wind speed

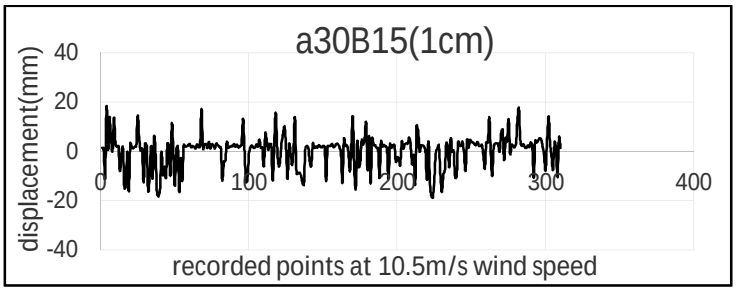
a30B15(1cm)
displacement(mm)
40
20
0
-20
-40
0
100
200
300
400
recorded points at 10.5m/s wind speed

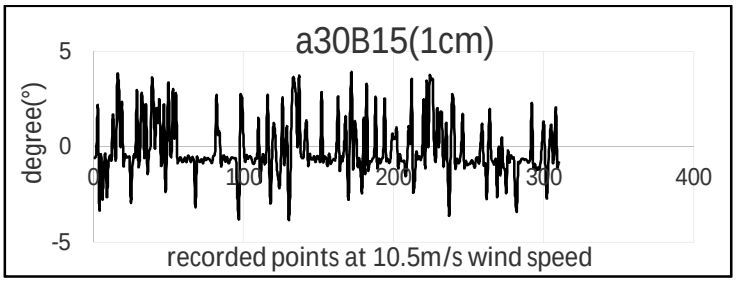
a30B15(1cm)
degree(°)
5
0
-5
0
100
200
300
400
recorded points at 10.5m/s wind speed

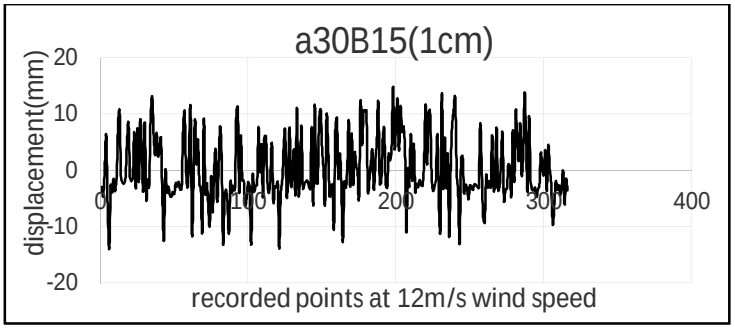
a30B15(1cm)
displacement(mm)
20
10
0
-10
-20
0
100
200
300
400
recorded points at 12m/s wind speed

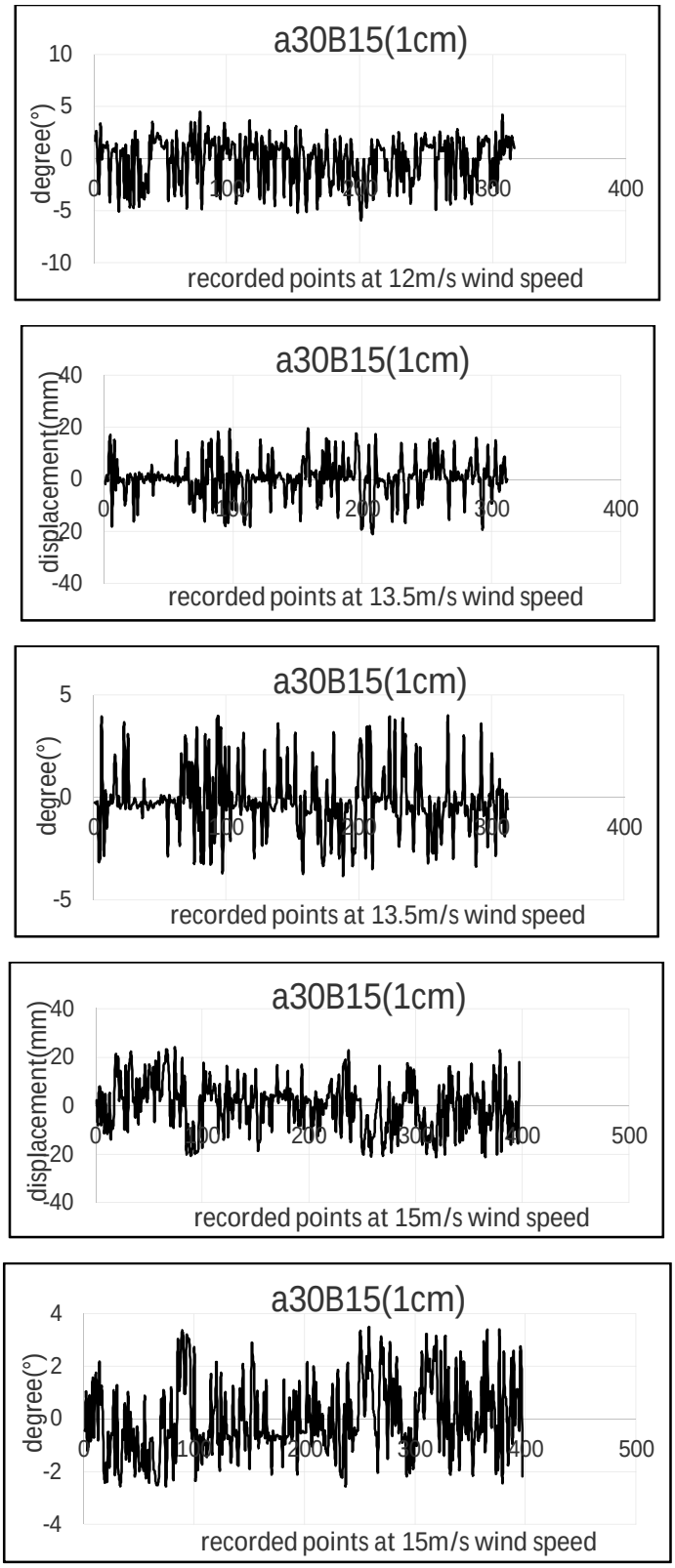

Figure A5 The vertical and Torsional Displacement from 1.5 m/s Wind speed to 15 m/s Wind speed for case $\alpha = 30°$, $\beta = 15°$ with 1 cm ice thickness

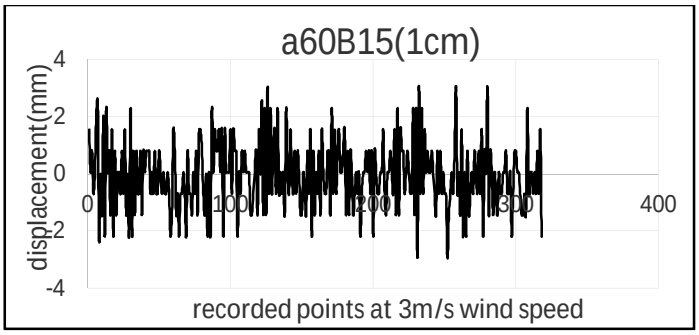
a60B15(1cm)
displacement(mm)
4
2
0
-2
-4
0
100
200
300
400
recorded points at 3m/s wind speed

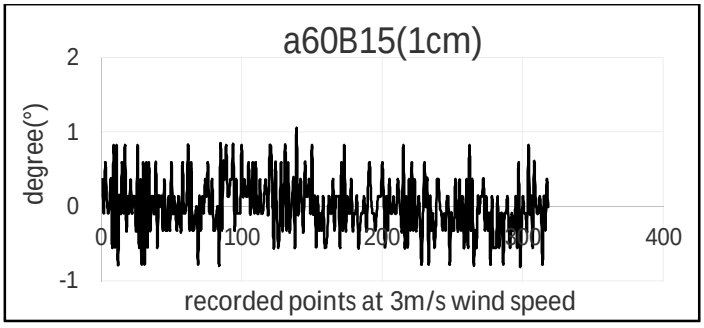
a60B15(1cm)
degree(°)
2
1
0
-1
0
100
200
300
400
recorded points at 3m/s wind speed

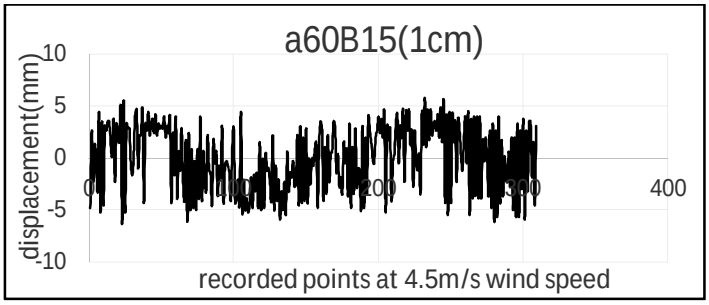
a60B15(1cm)
displacement(mm)
10
5
0
-5
-10
0
100
200
300
400
recorded points at 4.5m/s wind speed

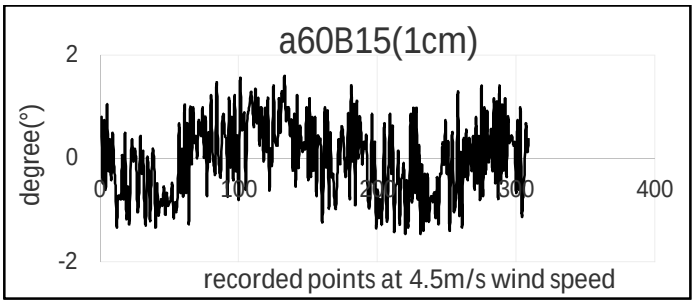
a60B15(1cm)
degree(°)
2
0
-2
0
100
200
300
400
recorded points at 4.5m/s wind speed

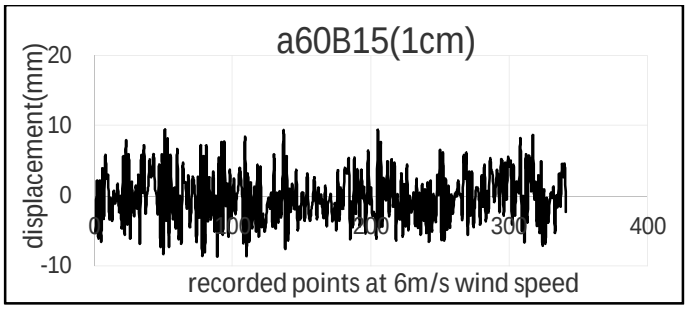
a60B15(1cm)
displacement(mm)
20
10
0
-10
0
100
200
300
400
recorded points at 6m/s wind speed

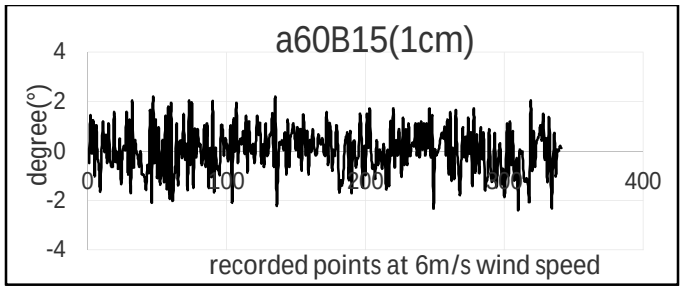
a60B15(1cm)
degree(°)
4
2
0
-2
-4
0
100
200
300
400
recorded points at 6m/s wind speed

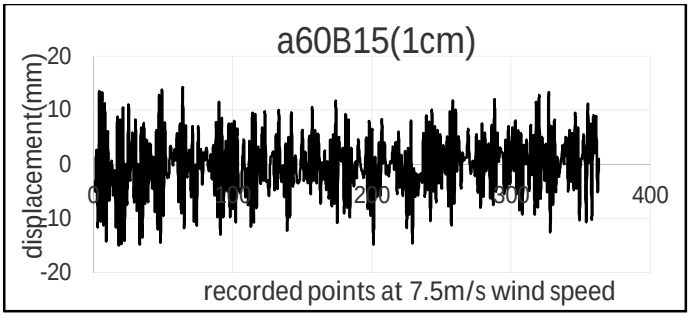
a60B15(1cm)
displacement(mm)
20
10
0
-10
-20
0
100
200
300
400
recorded points at 7.5m/s wind speed

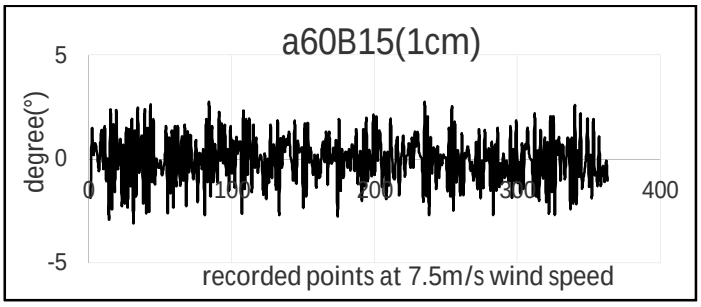
a60B15(1cm)
degree(°)
5
0
-5
0
100
200
300
400
recorded points at 7.5m/s wind speed

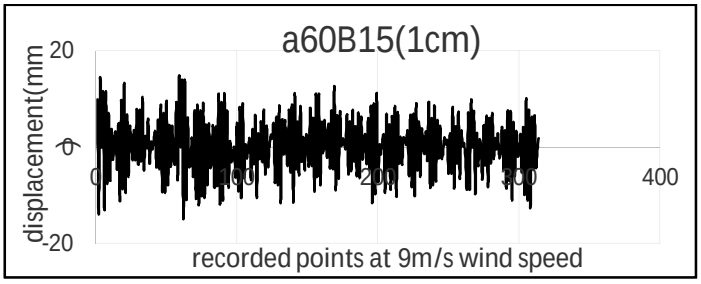
a60B15(1cm)
displacement(mm
20
0
-20
0
100
200
300
400
recorded points at 9m/s wind speed

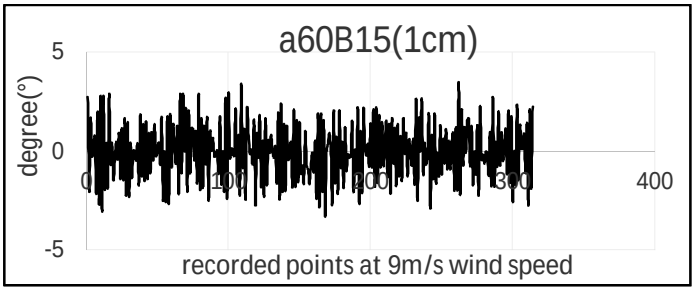
a60B15(1cm)
degree(°)
5
0
-5
0
100
200
300
400
recorded points at 9m/s wind speed

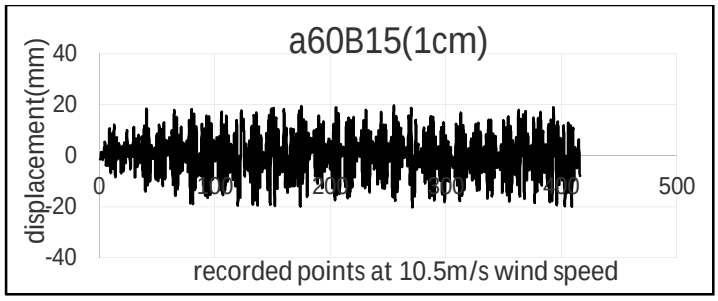
a60B15(1cm)
displacement(mm)
40
20
0
-20
-40
0
500
recorded points at 10.5m/s wind speed

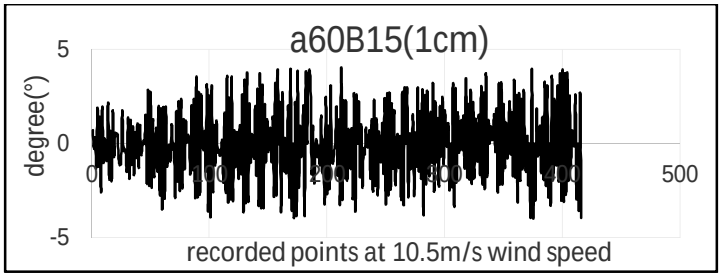
a60B15(1cm)
degree(°)
5
0
-5
0
500
recorded points at 10.5m/s wind speed

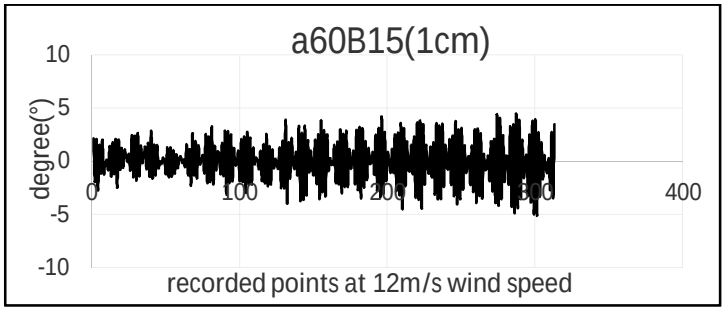
a60B15(1cm)
degree(°)
10
5
0
-5
-10
0
100
200
300
400
recorded points at 12m/s wind speed

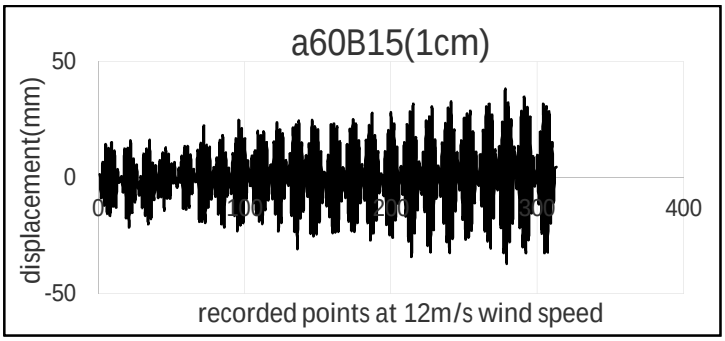
a60B15(1cm)
displacement(mm)
50
0
-50
0
100
200
300
400
recorded points at 12m/s wind speed

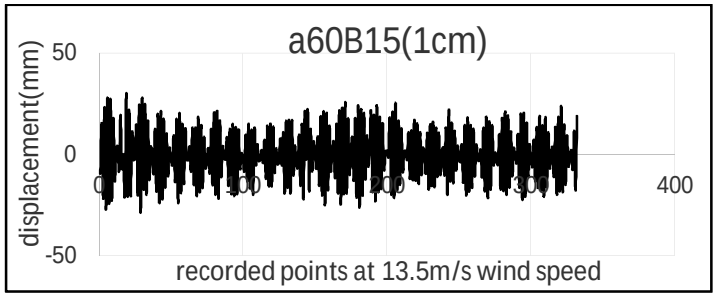
a60B15(1cm)
displacement(mm)
50
0
-50
0
100
200
300
400
recorded points at 13.5m/s wind speed

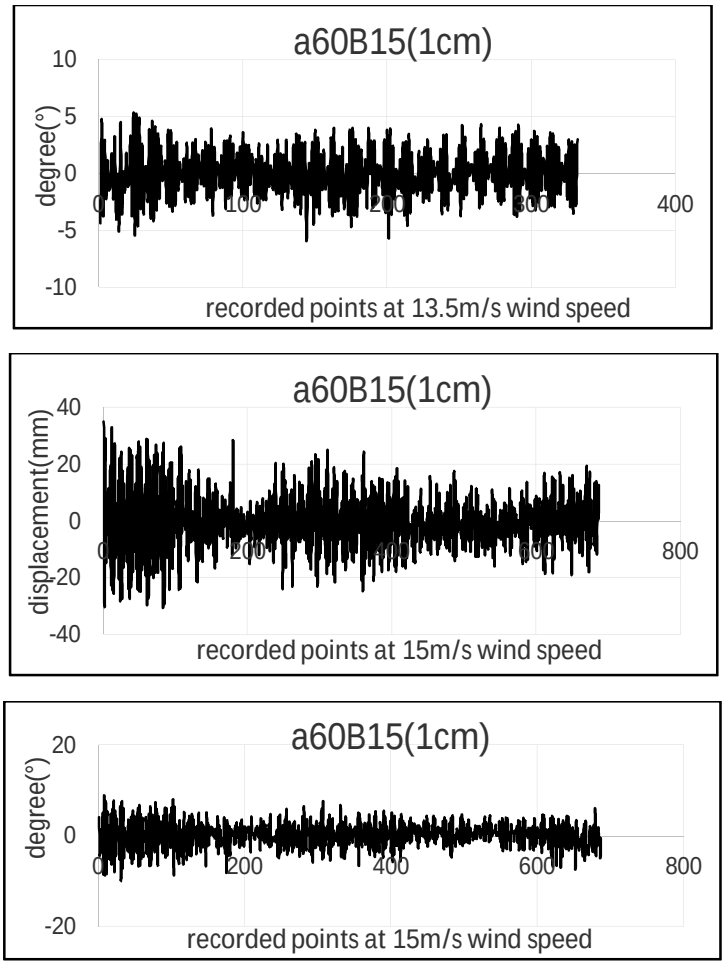

Figure A6 The vertical and Torsional Displacement from 1.5 m/s Wind speed to 15 m/s Wind speed for case $\alpha = 60°$, $\beta = 15°$ with 1 cm ice thickness

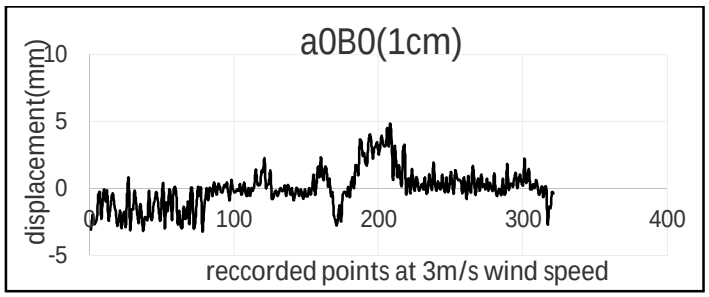

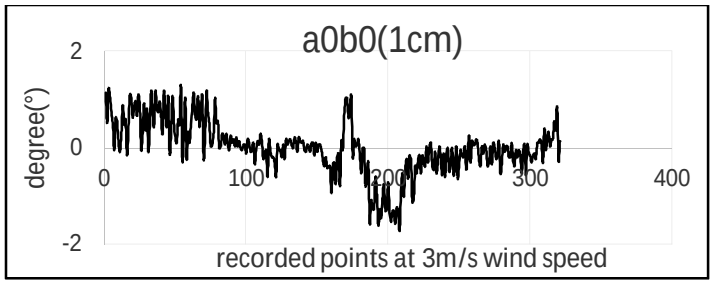
a0b0(1cm)
degree(°)
2
0
-2
0
100
200
300
400
recorded points at 3m/s wind speed

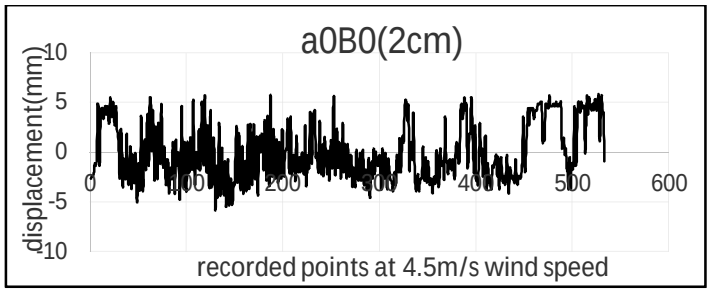
a0B0(2cm)
displacement(mm)
10
5
0
-5
-10
0
100
200
300
400
500
600
recorded points at 4.5m/s wind speed

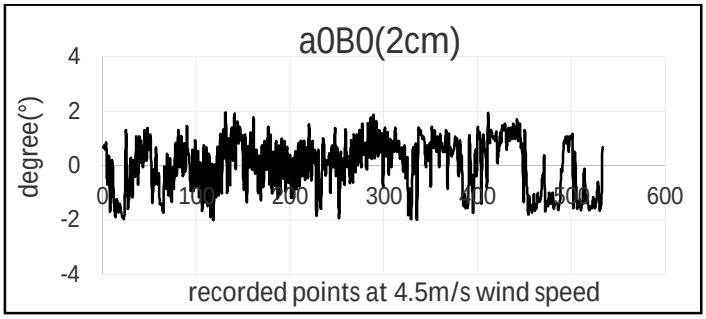
a0B0(2cm)
degree(°)
4
2
0
-2
-4
0
100
200
300
400
500
600
recorded points at 4.5m/s wind speed

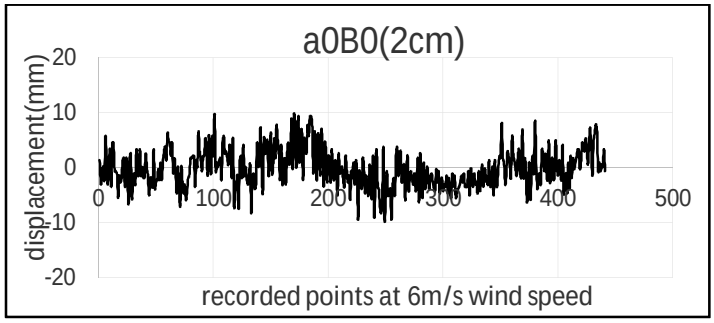
a0B0(2cm)
displacement(mm)
20
10
0
-10
-20
0
100
200
300
400
500
recorded points at 6m/s wind speed

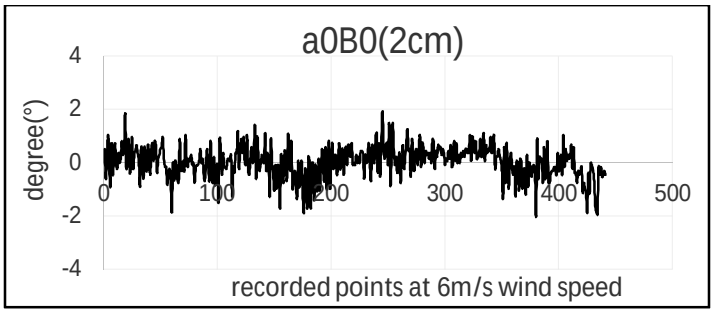
a0B0(2cm)
degree(°)
4
2
0
-2
-4
0
100
200
300
400
500
recorded points at 6m/s wind speed

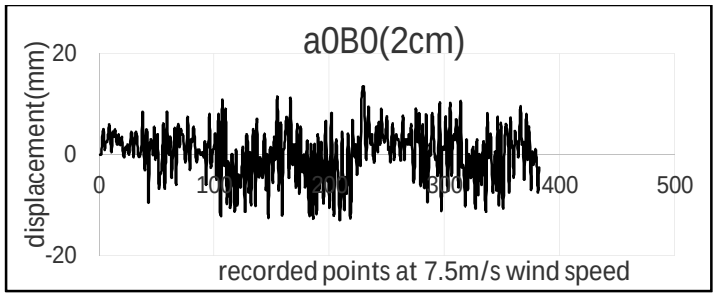
a0B0(2cm)
displacement(mm)
20
0
-20
0
100
200
300
400
500
recorded points at 7.5m/s wind speed

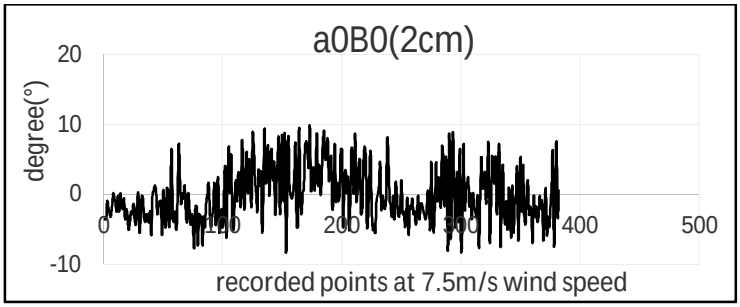
a0B0(2cm)
degree(°)
20
10
0
-10
0
100
200
300
400
500
recorded points at 7.5m/s wind speed

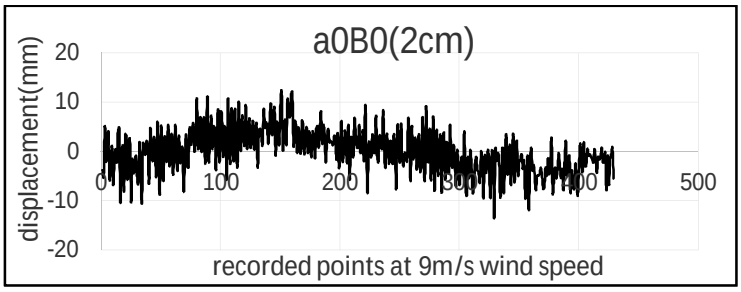
a0B0(2cm)
displacement(mm)
20
10
0
-10
-20
0
100
200
300
400
500
recorded points at 9m/s wind speed

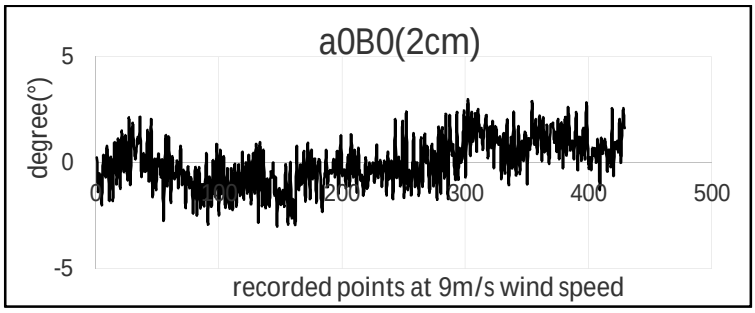
a0B0(2cm)
degree(°)
5
0
-5
0
100
200
300
400
500
recorded points at 9m/s wind speed

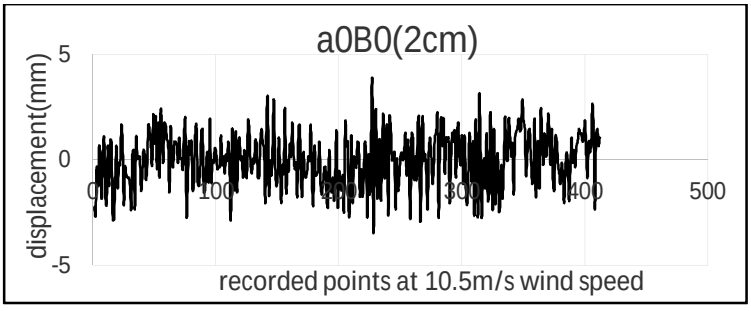
a0B0(2cm)
displacement(mm)
5
0
-5
0
100
200
300
400
500
recorded points at 10.5m/s wind speed

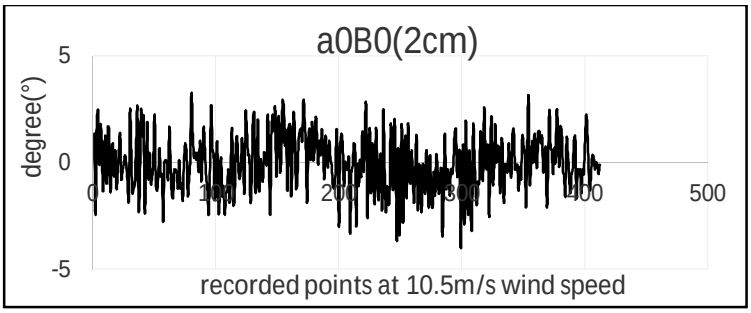
a0B0(2cm)
degree(°)
5
0
-5
0
100
200
300
400
500
recorded points at 10.5m/s wind speed

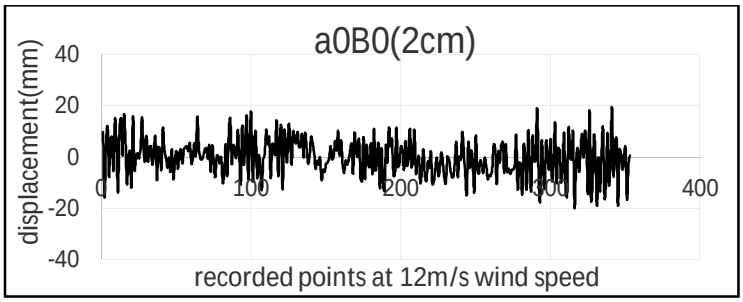
a0B0(2cm)
displacement(mm)
40
20
0
-20
-40
0
100
200
300
400
recorded points at 12m/s wind speed

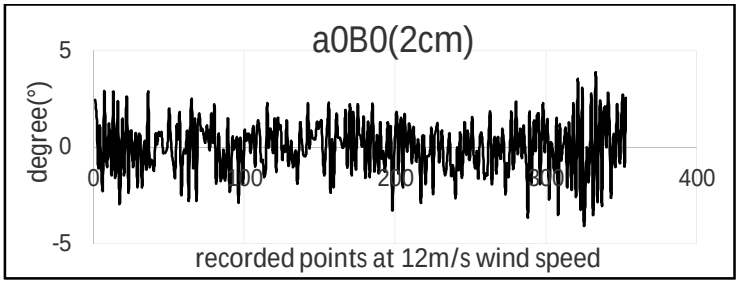
a0B0(2cm)
degree(°)
5
0
-5
0
100
200
300
400
recorded points at 12m/s wind speed

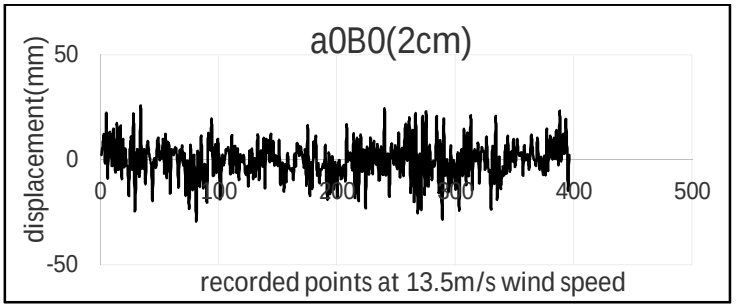
a0B0(2cm)
displacement(mm)
50
0
-50
0
100
200
300
400
500
recorded points at 13.5m/s wind speed

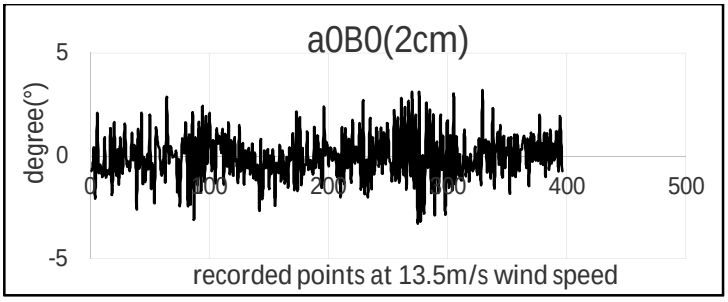
a0B0(2cm)
degree(°)
5
0
-5
0
100
200
300
400
500
recorded points at 13.5m/s wind speed

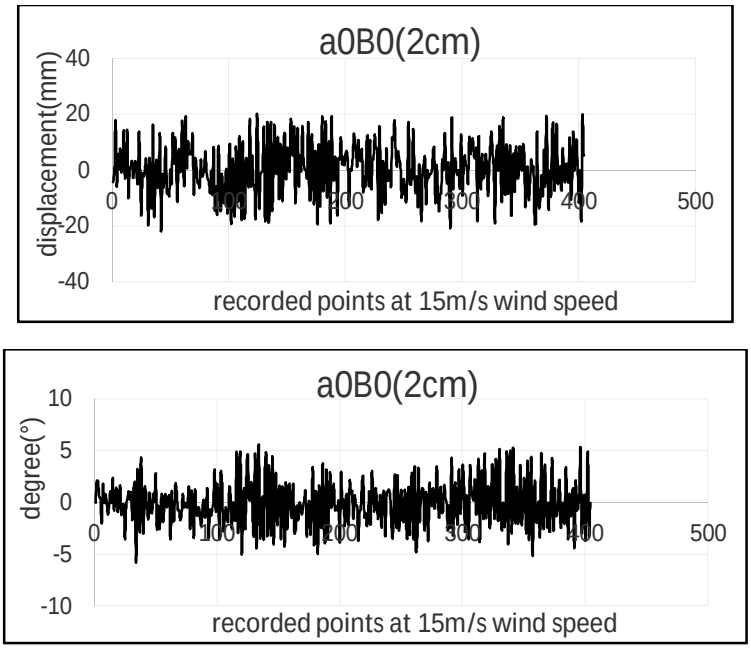

Figure A7 The vertical and Torsional Displacement from 1.5 m/s Wind speed to 15 m/s Wind speed for case $\alpha = 0°$, $\beta = 0°$ with 2 cm ice thickness

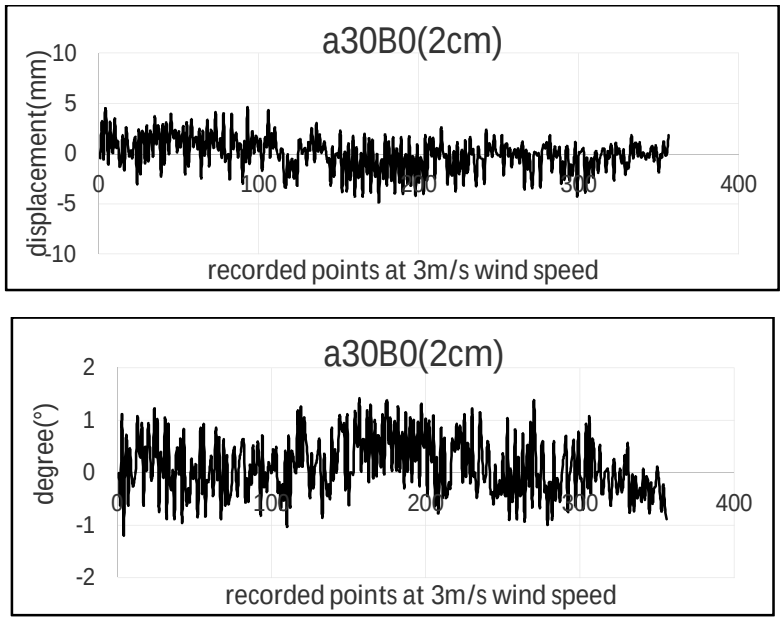

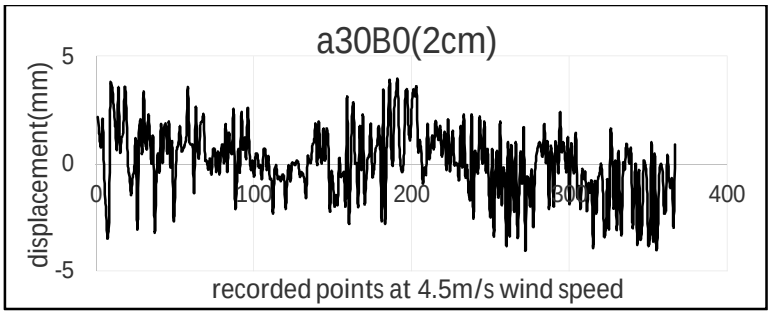
a30B0(2cm)
displacement(mm)
5
0
-5
0
100
200
300
400
recorded points at 4.5m/s wind speed

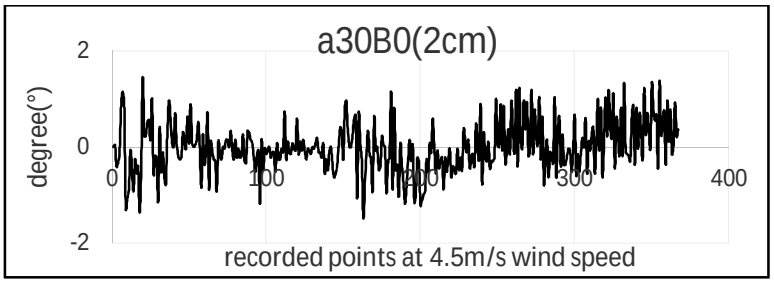
a30B0(2cm)
degree(°)
2
0
-2
0
100
200
300
400
recorded points at 4.5m/s wind speed

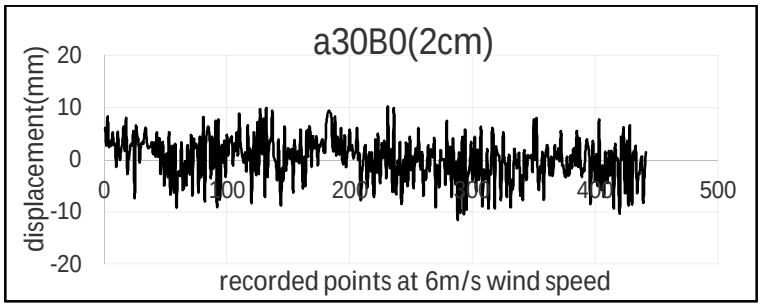
a30B0(2cm)
displacement(mm)
20
10
0
-10
-20
0
100
200
300
400
500
recorded points at 6m/s wind speed

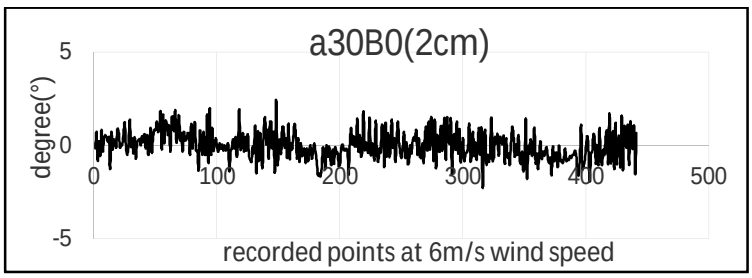
a30B0(2cm)
degree(°)
5
0
-5
0
100
200
300
400
500
recorded points at 6m/s wind speed

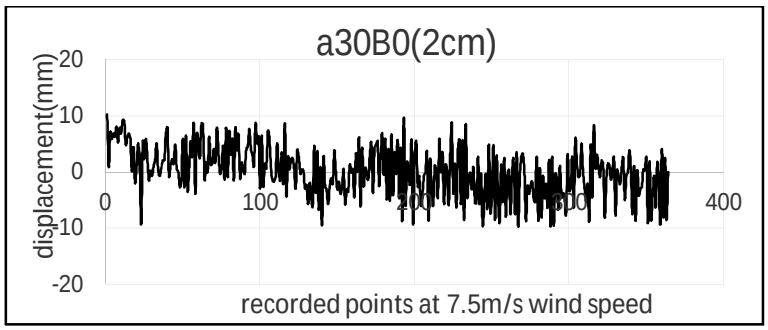
a30B0(2cm)
displacement(mm)
20
10
0
-10
-20
0
100
200
300
400
recorded points at 7.5m/s wind speed

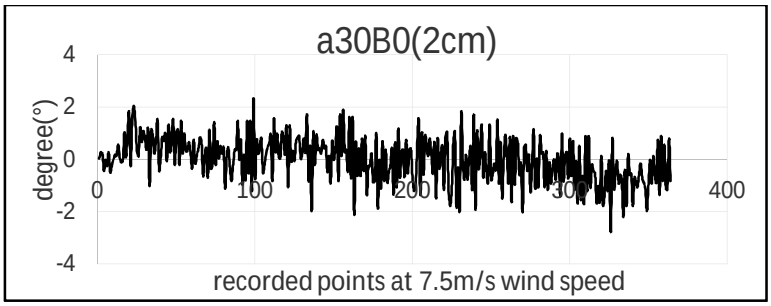
a30B0(2cm)
degree(°)
4
2
0
-2
-4
0
100
200
300
400
recorded points at 7.5m/s wind speed

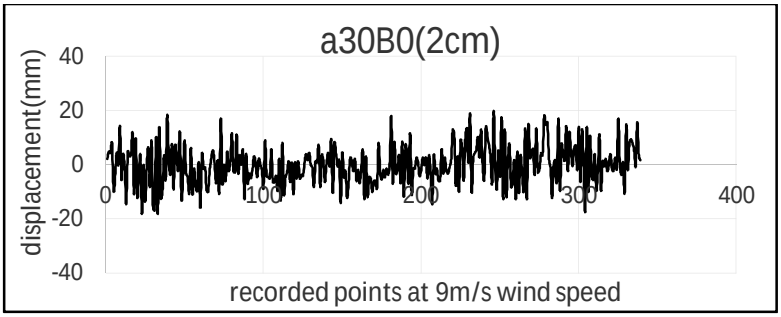
a30B0(2cm)
displacement(mm)
40
20
0
-20
-40
0
100
200
300
400
recorded points at 9m/s wind speed

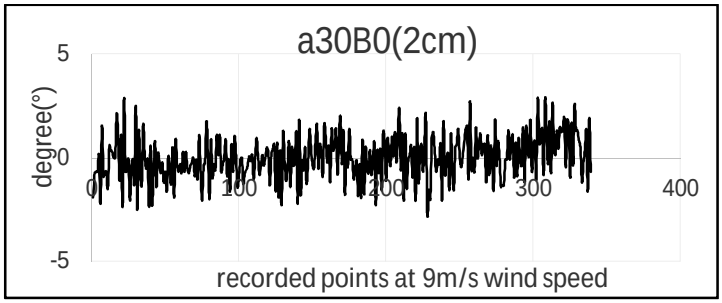
a30B0(2cm)
degree(°)
5
0
-5
0
100
200
300
400
recorded points at 9m/s wind speed

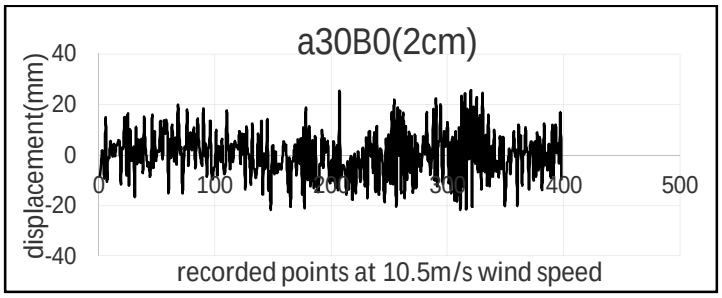
a30B0(2cm)
displacement(mm)
40
20
0
-20
-40
0
100
200
300
400
500
recorded points at 10.5m/s wind speed

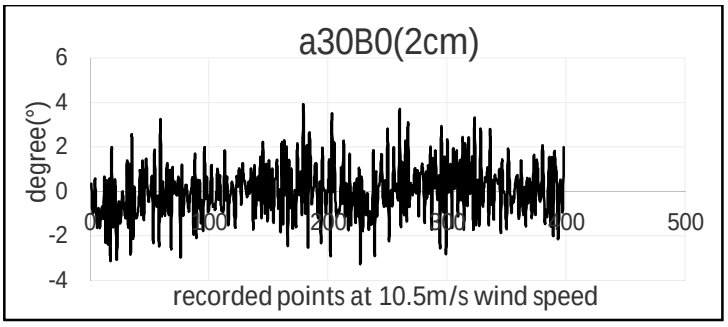
a30B0(2cm)
degree(°)
6
4
2
0
-2
-4
0
100
200
300
400
500
recorded points at 10.5m/s wind speed

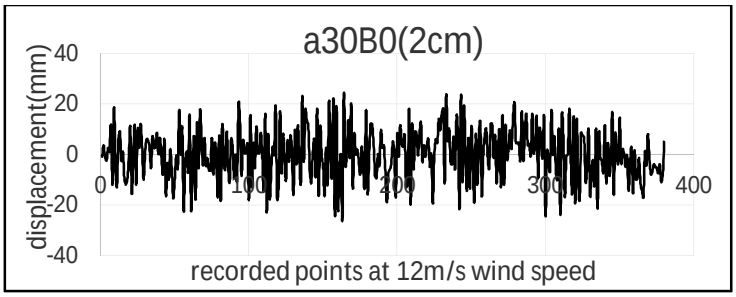
a30B0(2cm)
displacement(mm)
40
20
0
-20
-40
0
100
200
300
400
recorded points at 12m/s wind speed

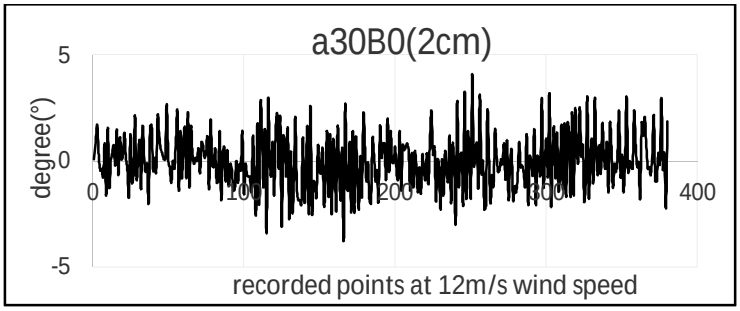
a30B0(2cm)
degree(°)
5
0
-5
0
100
200
300
400
recorded points at 12m/s wind speed

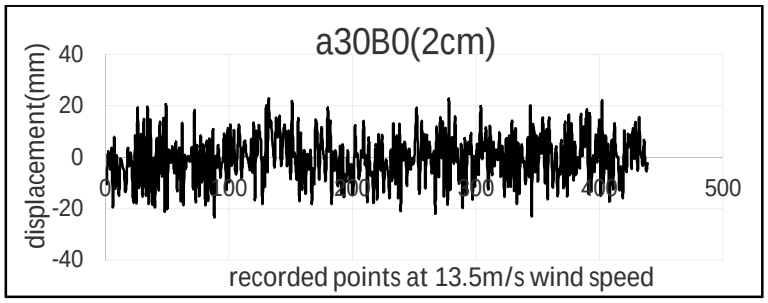
a30B0(2cm)
displacement(mm)
40
20
0
-20
-40
0
100
200
300
400
500
recorded points at 13.5m/s wind speed

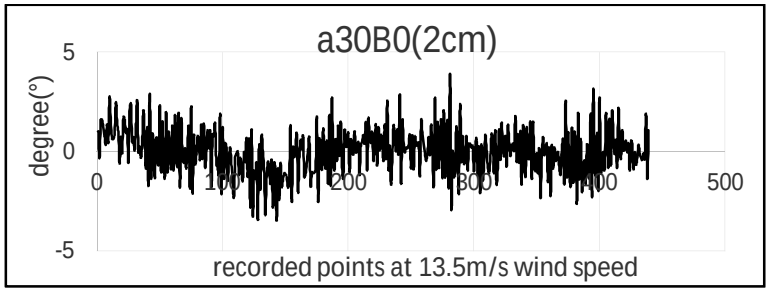
a30B0(2cm)
degree(°)
5
0
-5
0
100
200
300
400
500
recorded points at 13.5m/s wind speed

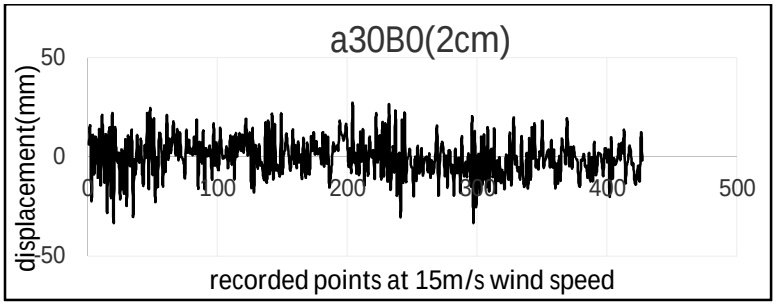
a30B0(2cm)
displacement(mm)
50
0
-50
0
100
200
300
400
500
recorded points at 15m/s wind speed

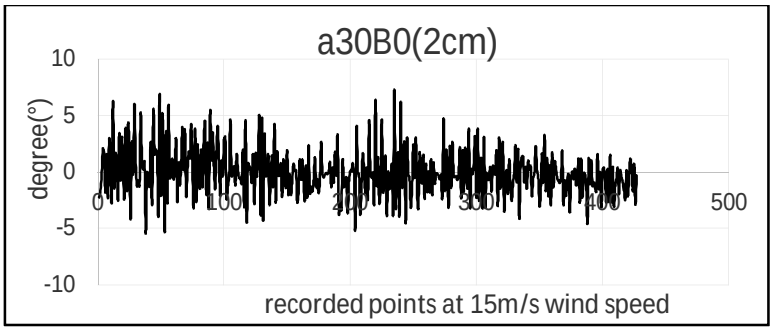

Figure A8 The vertical and Torsional Displacement from 1.5 m/s Wind speed to 15 m/s Wind speed for case $\alpha = 30°$, $\beta = 0°$ with 2 cm ice thickness

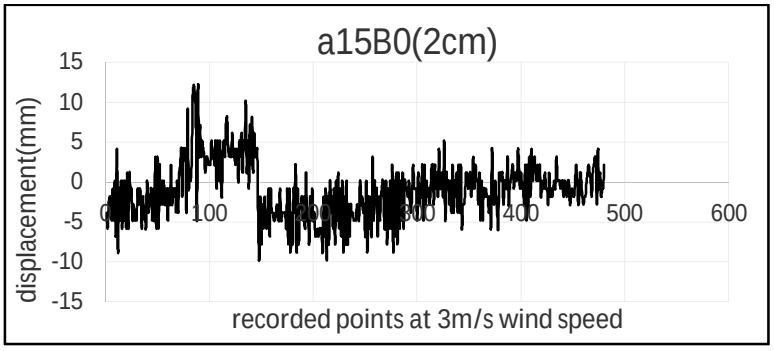

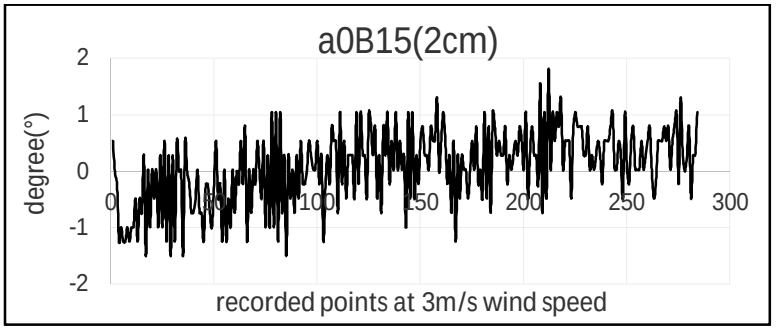

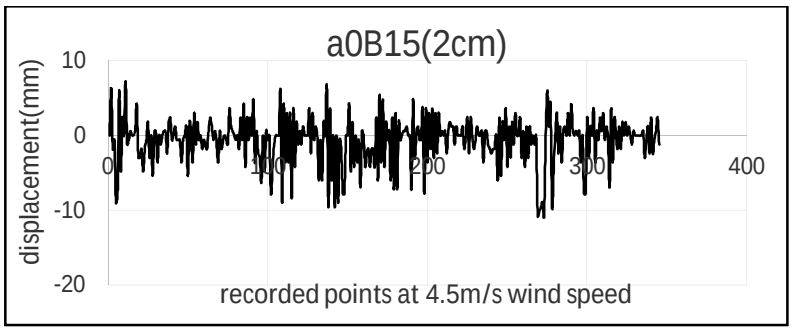

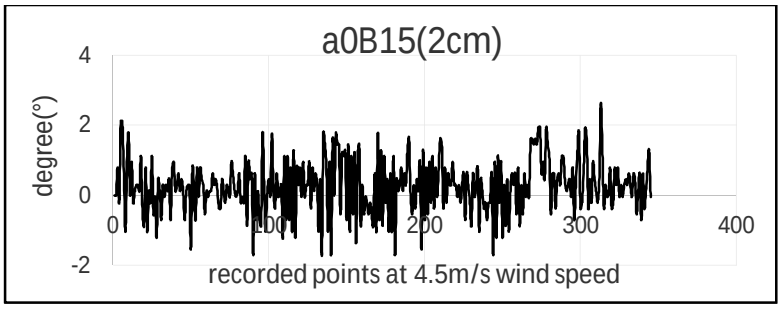
a0B15(2cm)
degree(°)
4
2
0
-2
0
100
200
300
400
recorded points at 4.5m/s wind speed

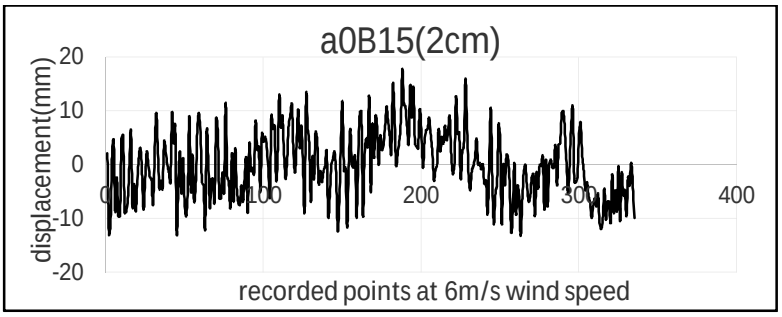
a0B15(2cm)
displacement(mm)
20
10
0
-10
-20
0
100
200
300
400
recorded points at 6m/s wind speed

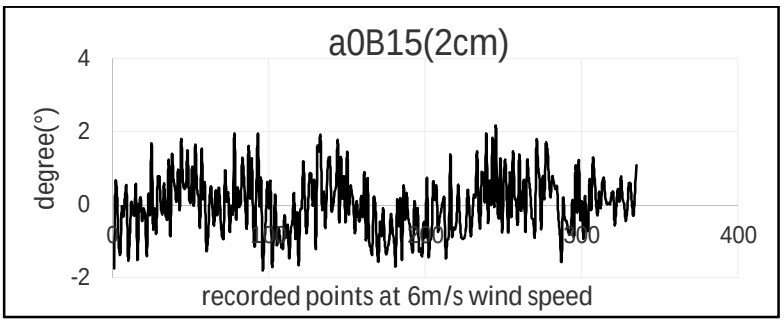
a0B15(2cm)
degree(°)
4
2
0
-2
400
recorded points at 6m/s wind speed

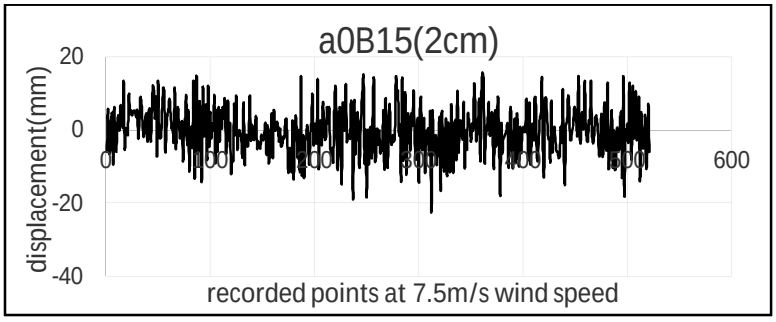
a0B15(2cm)
displacement(mm)
20
0
-20
-40
600
recorded points at 7.5m/s wind speed

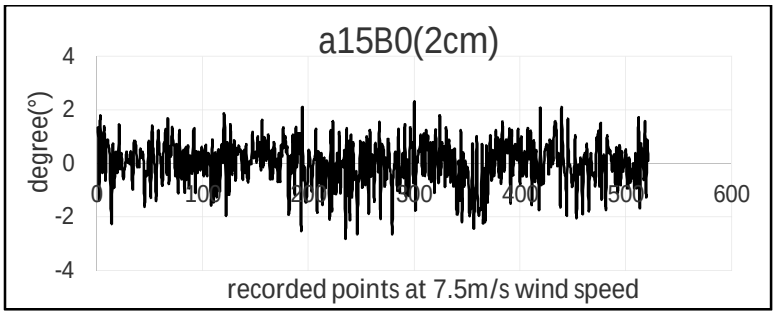
a15B0(2cm)
degree(°)
4
2
0
-2
-4
600
recorded points at 7.5m/s wind speed

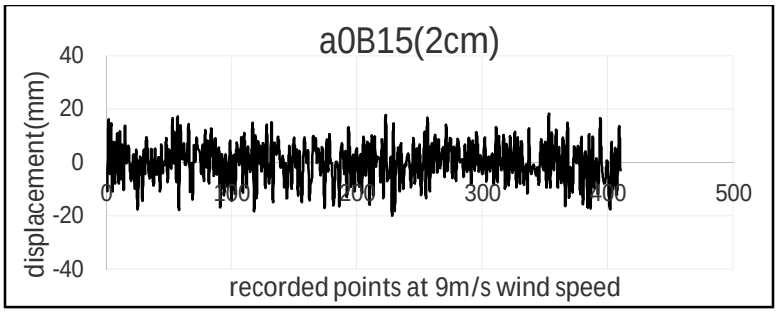
a0B15(2cm)
displacement(mm)
40
20
0
-20
-40
0
100
200
300
400
500
recorded points at 9m/s wind speed

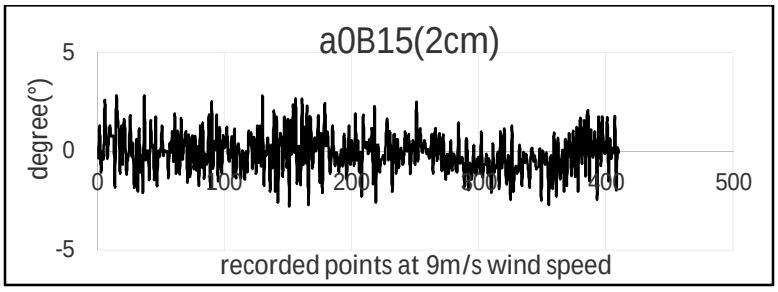
a0B15(2cm)
degree(°)
5
0
-5
0
100
200
300
400
500
recorded points at 9m/s wind speed

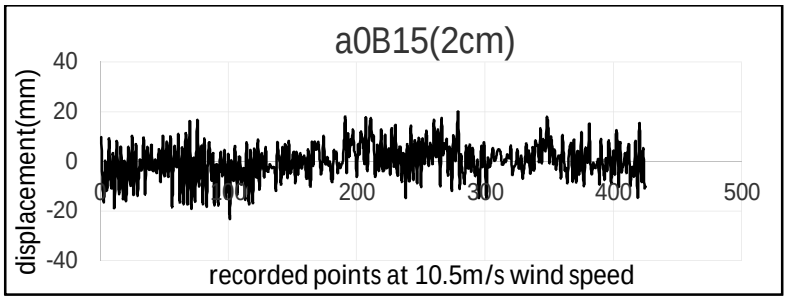
a0B15(2cm)
displacement(mm)
40
20
0
-20
-40
0
100
200
300
400
500
recorded points at 10.5m/s wind speed

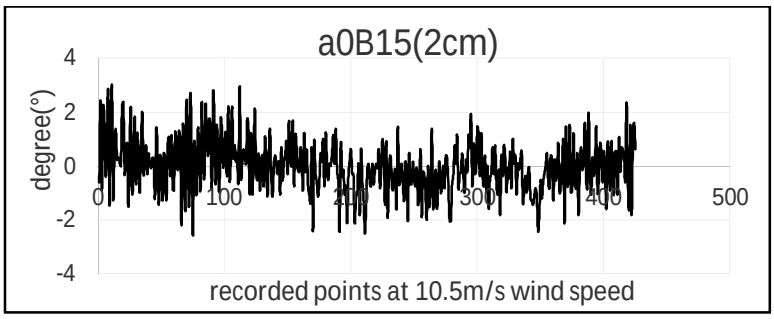
a0B15(2cm)
degree(°)
4
2
0
-2
-4
0
100
200
300
400
500
recorded points at 10.5m/s wind speed

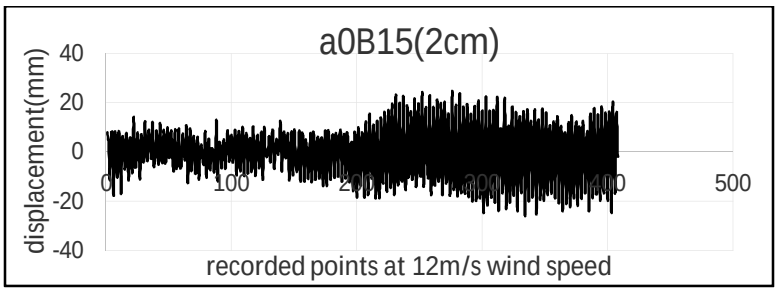
a0B15(2cm)
displacement(mm)
40
20
0
-20
-40
0
100
200
300
400
500
recorded points at 12m/s wind speed

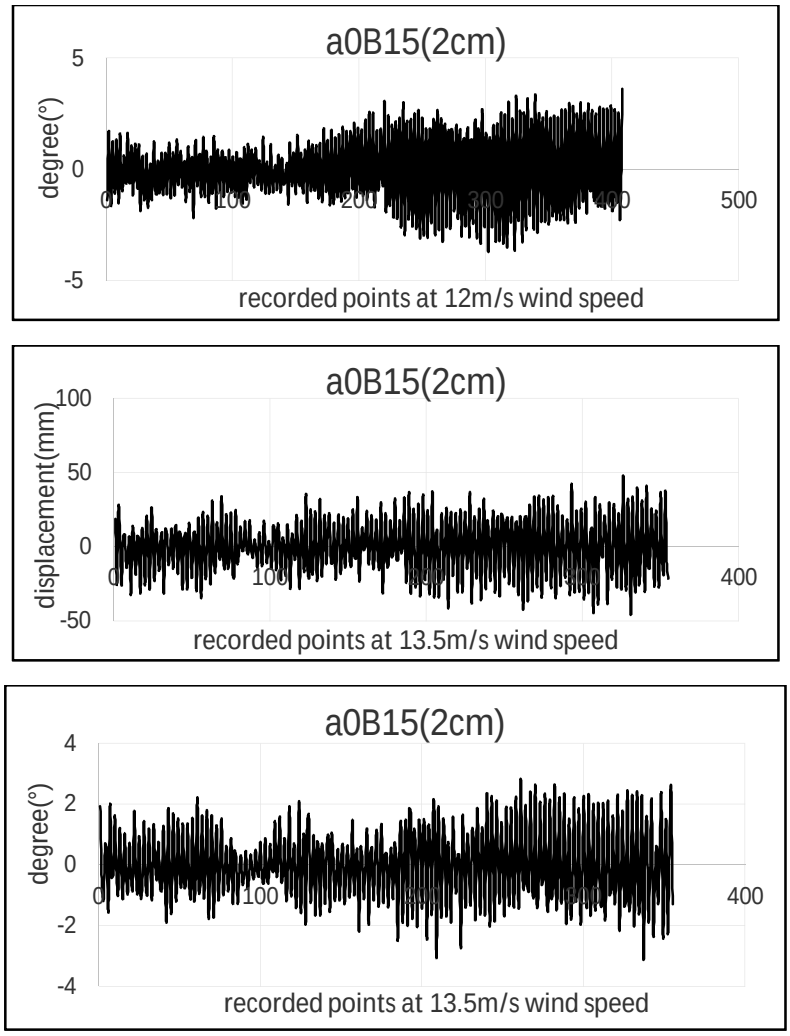

Figure A9 The vertical and Torsional Displacement from 1.5 m/s Wind speed to 15 m/s Wind speed for case $\alpha = 0°$, $\beta = 15°$ with 2 cm ice thickness

Appendix B

The final average vertical and torsional displacements are plotted in Appendix B.

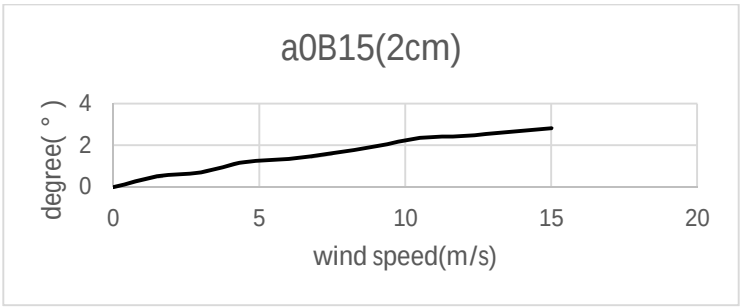

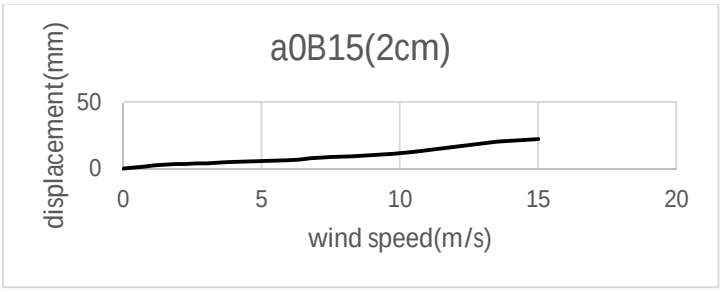

Figure B1 Average vertical and Torsional vibration for case α = 0°, β = 15° with 2 cm ice thickness

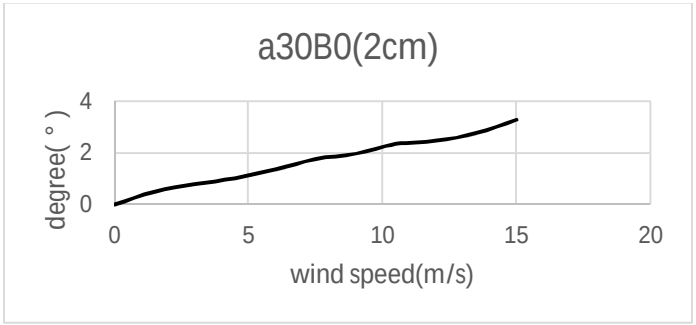

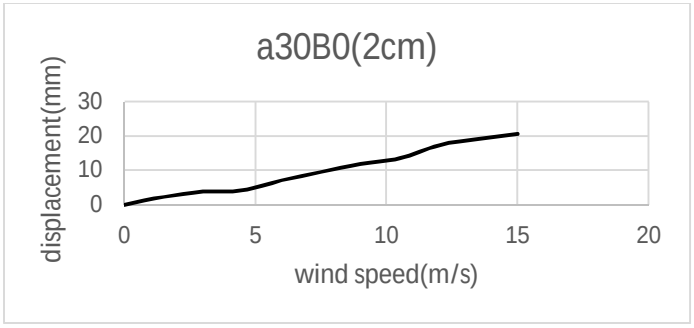

Figure B2 Average vertical and Torsional vibration for case α = 30°, β = 0° with 2 cm ice thickness

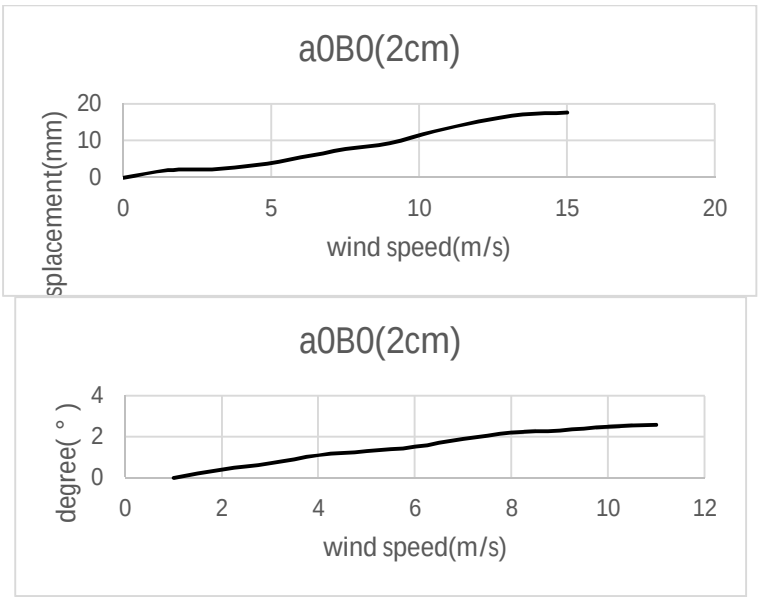

Figure B3 Average vertical and Torsional vibration for case α = 0°, β = 0° with 2 cm ice thickness

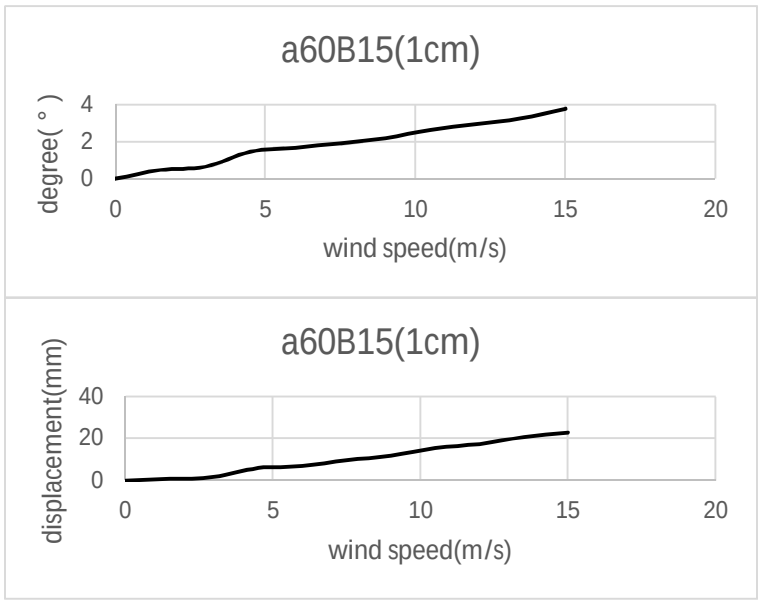

Figure B4 Average vertical and Torsional vibration for case α = 60°, β = 15° with 1 cm ice thickness

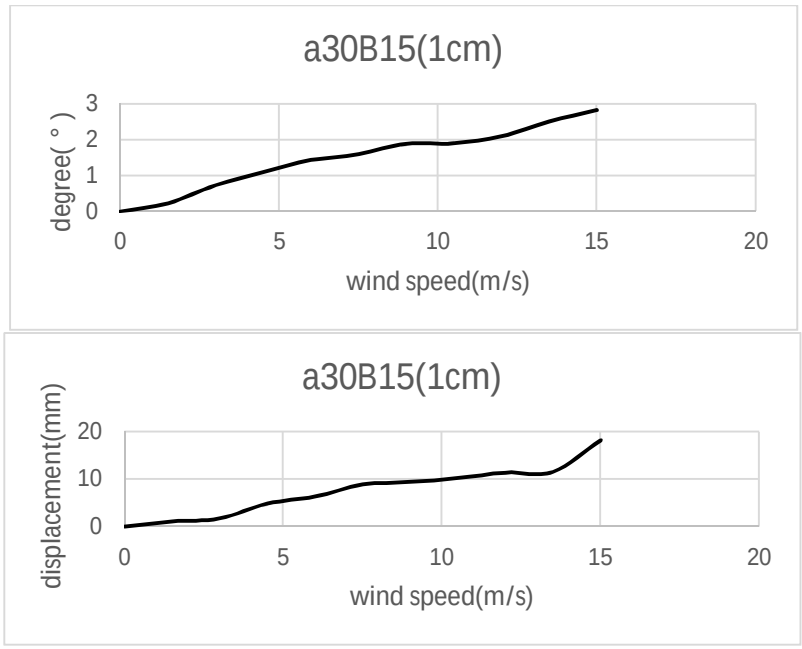

Figure B5 Average vertical and Torsional vibration for case α = 30°, β = 15° with 1 cm ice thickness

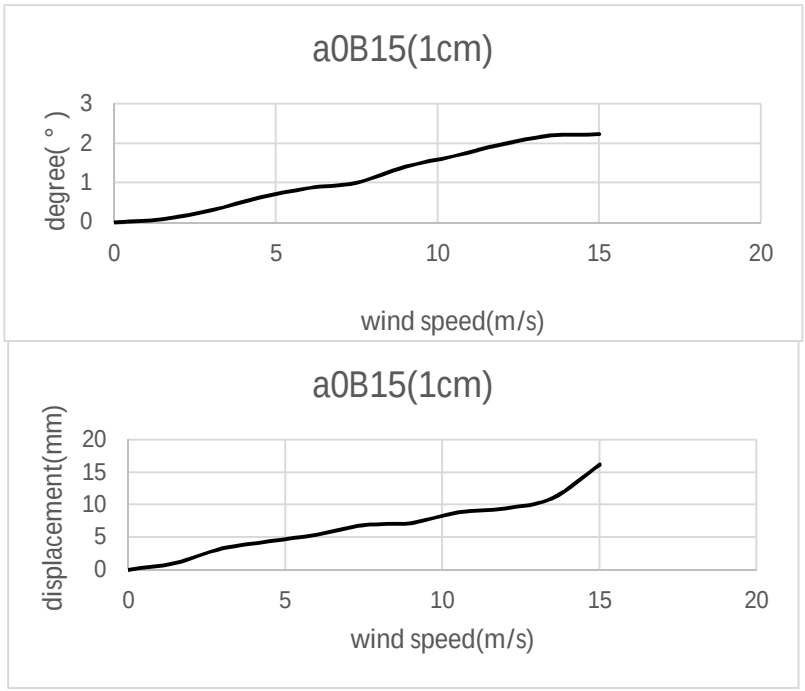

Figure B6 Average vertical and Torsional vibration for case α = 0°, β = 15° with 1 cm ice thickness

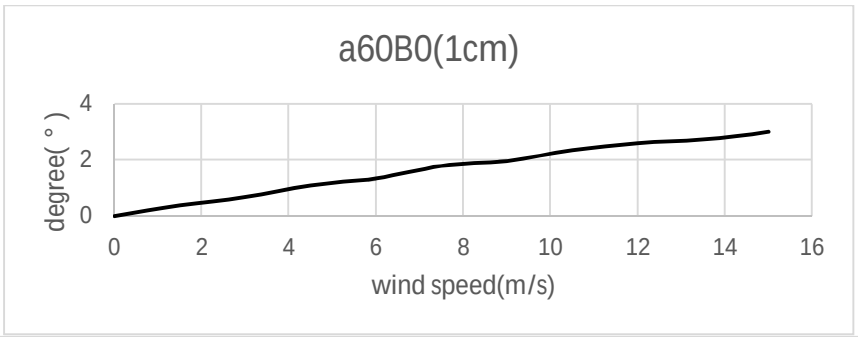

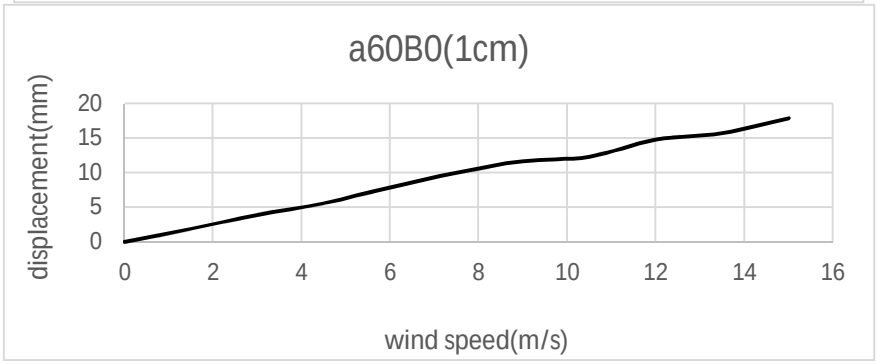

Figure B7 Average vertical and Torsional vibration for case α = 60°, β = 0° with 1 cm ice thickness

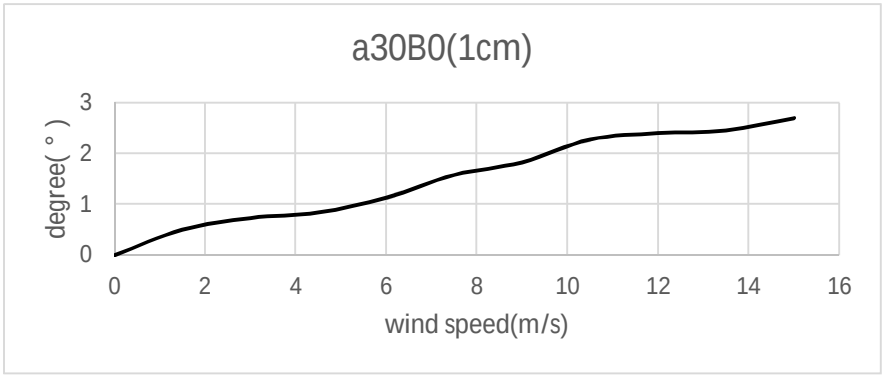

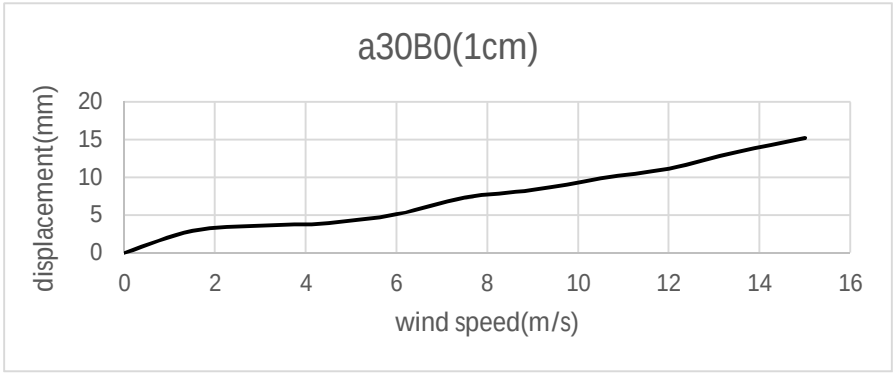

Figure B8 Average vertical and Torsional vibration for case α = 30°, β = 0° with 1 cm ice thickness

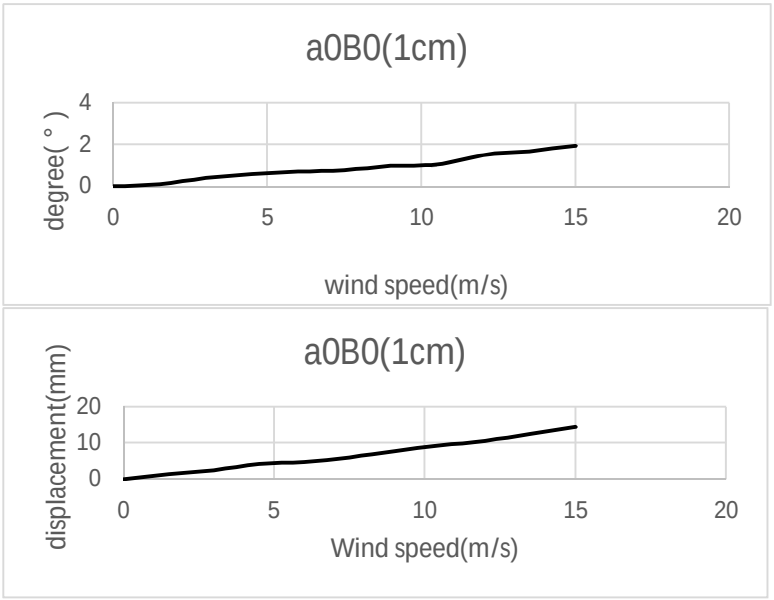

Figure B9 Average vertical and Torsional vibration for case $\alpha = 0°$, $\beta = 0°$ with 1 cm ice thickness